Beamforming Techniques for Environmental Noise

Master's Thesis

by

Elisabet Tiana Roig

October 8, 2009

Supervisors

Finn Jacobsen and Efrén Fernández Grande

Technical University of Denmark
Acoustic Technology, DTU Elektro
Ørsteds Plads, Building 352
DK–2800 Kongens Lyngby

Karim Haddad and Jørgen Hald

Brüel & Kjær
Sound & Vibration Measurement A/S
Skodsborgvej 307
DK–2850 Nærum

DTU Technical University of Denmark
DTU Electrical Engineering
Department of Electrical Engineering

Brüel & Kjær

Abstract:

A problem of practical interest when dealing with outdoor acoustic measurements is to estimate the noise contributions from different directions around the measurement point. This estimation can be done by means of microphone arrays. More specifically, circular arrays are suitable for this purpose as, in combination with proper signal processing techniques, they are capable of mapping the sound field in a plane over 360°.

Two processing techniques meant to be used with circular arrays are implemented: the 'classical' Delay-and-Sum beamforming and a novel technique called Circular Harmonics beamforming. The latter is based on the decomposition of the sound field in series of circular harmonics. The performance of these beamforming techniques is analyzed by means of simulations and evaluated by two parameters, the resolution and the maximum side lobe level.

Making use of the results of the simulations, a circular array has been designed for the localization of environmental noise sources around a measurement point. Finally, a prototype implemented in accordance with the design has been tested in anechoic conditions. The results, which agree very well with the simulations, reveal that the array is suitable for the purpose of concern.

Keywords: Beamforming, Circular Arrays, Delay-and-Sum, Circular Harmonics, Environmental Noise

Preface

This Master's Thesis presents the final project of the Master of Science in Engineering Acoustics at the Technical University of Denmark (DTU). The work, carried out at the Acoustic Technology department between March and October of 2009, has been supervised by Finn Jacobsen and Efrén Fernández Grande.

The project has been done in collaboration with Brüel & Kjær, under supervision of Karim Haddad and Jørgen Hald.

Acknowledgments

First of all, I would like to thank Finn Jacobsen and Efrén Fernández for their guidance, their suggestions, their corrections... and for their patience. Being supervised by them has been a pleasure. I am also grateful to Karim Haddad and Jørgen Hald for their help and for making it possible to have a prototype array based on my investigations.

I would like to express my gratitude to the technicians of the Acoustic Technology department, Jørgen Rasmussen and Tom Petersen, who helped me a lot with the measurement equipment. Many thanks also to all the professors, students and staff of the department for creating a very nice atmosphere.

I am very indebted to Björn Ohl not only for his help with LaTeX and Matlab, but also, and most important, for bringing my laptop back to life two months before the thesis deadline.

I would also like to thank my mother for her advice concerning the design of the document and my brother for his useful and funny corrections. In fact, this thesis would not have been possible without the support and love of my family, who have always made their best for giving me education and studies. For this reason, this thesis is dedicated to them.

Finally, my deepest thanks go to Toni Torras for always being there, for his infinite patience, for cheering me up many times, for preparing very useful Matlab functions, for sitting next to me hours and hours and helping me with some ugly mathematics, for coming with me to perform outdoor measurements, for taking care of me, for making me happy... and for many other reasons. This thesis is also dedicated to him.

Elisabet Tiana Roig

Contents

1

Introduction

Acoustical beamforming is a signal processing technique used to localize sound sources using microphone arrays. Unlike other array techniques such as NAH or SONAH which are based on near-field measurements [1, 2], beamforming is based on far-field measurements, i. e. the array must be placed relatively far from the sources in order to determine their 'position' by processing the signals captured by the microphones [3].

In the literature, beamforming techniques are traditionally classified in two categories, conventional beamforming and adaptive beamforming [4, 5]. In the first case, the beamformers do not change their features during the measurement, whereas adaptive beamformers adapt their response during the measurement in order to improve the performance. Besides the processing techniques, the shape of the array is also of great importance depending on the application of concern. For example, relatively small rectangular or spherical arrays are appropriate for the localization of noise sources in car or aircrafts interiors, whereas other purposes may require large arrays or irregular arrays.

One of the goals in the present work is the design of an array for a new application: the localization of environmental noise sources. In outdoors measurements, the sound field is basically generated by sources placed far from the measurement point which create waves with a direction of propagation rather parallel to the ground. Hence, the sound field can be assumed to be two-dimensional. This implies on the one hand that beamforming techniques should be used for this purpose as they are meant to be used in far-field measurements, and on the other hand that circular arrays can be used as they are suitable for two-dimensional fields.

Two beamforming techniques will be developed and analyzed for this application when circular arrays are used. These techniques are Delay-and-Sum beamforming and Circular Harmonics beamforming. The first technique is the 'classical' beamforming technique that belongs to the category of conventional beamformers. It is the most basic technique and has been widely used for many applications due to the fact that it is very robust in the presence of background noise. By contrast, Circular Harmonics

beamforming is a novel technique that can be classified in a category that has been recently created called Eigenbeamforming. All the techniques that belong to this group are based on the decomposition of the sound field into a summation of harmonics. Some examples are Spherical Harmonics beamforming which decompose the sound field in three-dimensions by means of spherical arrays [6, 7, 8], or the techniques called EB-ESPIRIT and EB-DETECT that use circular arrays [9]. One of the main challenges in the present thesis is the derivation of Circular Harmonics beamforming. This is done by adapting the theory behind Spherical Harmonics beamforming to the two-dimensional case using circular arrays.

Delay-and-Sum and Circular Harmonics beamforming will be analyzed by means of simulations. Furthermore, several features will be taken into account, such as the array dimensions or the influence of being mounted on a cylindrical baffle. The design of the prototype array used for localization of environmental noise will be based on the simulation results. Finally, the prototype will be tested in anechoic conditions and the results will be compared to the theoretical ones.

This document is structured as follows: the wave equation in cylindrical coordinates and the basic background for the following chapters are given in chapter 2. In chapter 3, the sound field is decomposed using as a first step circular apertures and circular arrays afterwards. This concept is used in the following chapter where the mentioned beamforming techniques are developed. In chapter 5, the results of several simulations are presented and the array design is carried out. The measurements with the implemented array are shown in chapter 6. The last chapter presents the conclusions drawn from the simulations and the measurement results.

2

The Sound Field in Cylindrical Coordinates

2.1 The Wave Equation and its General Solution

The wave equation is defined and solved in the following sections for systems described in cylindrical coordinates r, φ and z. Figure 2.1 illustrates this coordinate system.

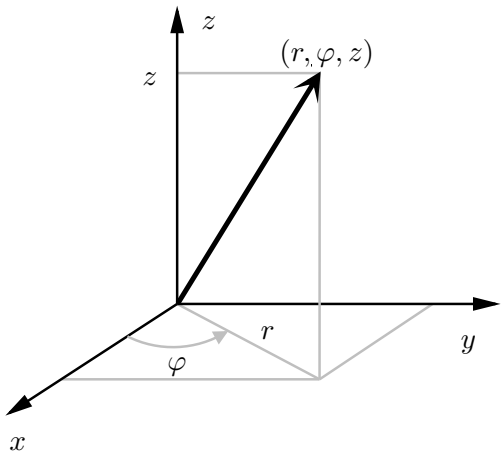

Figure 2.1: Cylindrical coordinate system.

The relationship between cylindrical and Cartesian coordinates follows

$$x = r\cos\varphi, \tag{2.1}$$

$$y = r\sin\varphi, \tag{2.2}$$

$$z = z. \tag{2.3}$$

2.1.1 The Wave Equation

The acoustical wave equation describes the variation of sound pressure p with time and space as follows

$$\nabla^2 p - \frac{1}{c^2}\frac{\partial^2 p}{\partial t^2} = 0, \tag{2.4}$$

where c is the speed of sound and ∇^2 is the Laplace operator which in cylindrical coordinates is given by

$$\nabla^2 = \frac{\partial^2}{\partial r^2} + \frac{1}{r}\frac{\partial}{\partial r} + \frac{1}{r^2}\frac{\partial^2}{\partial \varphi^2} + \frac{\partial^2}{\partial z^2}. \tag{2.5}$$

The definition given for the wave equation is valid when the sound field behaves linearly [10]. When the sound pressure varies harmonically (i. e. sinusoidally) with time and frequency at all positions, it is possible to represent the sound field using complex notation. The complex pressure $\hat{p}$ can be defined as

$$\hat{p} = |\hat{p}|\, \mathrm{e}^{-\mathrm{j}(\omega t + \phi)}, \tag{2.6}$$

where ω is the angular frequency and ϕ is the phase of the complex sound pressure at $t = 0$. The time dependence is represented by the factor $-\mathrm{j}\omega t$. The sound pressure p is then obtained with the real part of $\hat{p}$

$$p = \mathrm{Re}\{\hat{p}\} = \mathrm{Re}\left\{|\hat{p}|\, \mathrm{e}^{-\mathrm{j}(\omega t + \phi)}\right\} = |\hat{p}| \cos(\omega t + \phi). \tag{2.7}$$

The use of complex notation is convenient as it simplifies the calculation when solving the wave equation.

The wave equation written using the complex pressure is

$$\nabla^2 \hat{p} + \left(\frac{\omega}{c}\right)^2 \hat{p} = 0. \tag{2.8}$$

This equation is called the Helmholtz equation, and is usually expressed as follows

$$\nabla^2 \hat{p} + k^2 \hat{p} = 0, \tag{2.9}$$

where k is the wavenumber,

$$k = \frac{\omega}{c}. \tag{2.10}$$

2.1.2 General Solution

In order to solve the Helmholtz equation, it is assumed that the complex pressure is a product of independent functions that depend on one single variable

$$\hat{p} = \hat{p}(r, \varphi, z, t) = \underbrace{p_r(r) p_\varphi(\varphi) p_z(z)}_{p(r,\varphi,z)}\, \mathrm{e}^{-\mathrm{j}\omega t}, \tag{2.11}$$

where the spatial terms can be distinguished from the temporal term

$$\hat{p}(r,\varphi,z,t) = p(r,\varphi,z)\mathrm{e}^{-\mathrm{j}\omega t}. \tag{2.12}$$

Inserting the latter expression into the Helmholtz equation, it is revealed that the solution only depends on the spatial term

$$\nabla^2 p(r,\varphi,z) + k^2 p(r,\varphi,z) = 0 \tag{2.13}$$

The latter equation results, after inserting equation (2.11), in

$$\begin{aligned} p_\varphi(\varphi)p_z(z)\left(\frac{\partial^2 p_r(r)}{\partial r^2} + \frac{1}{r}\frac{\partial p_r(r)}{\partial r}\right) + \frac{1}{r^2}p_r(r)p_z(z)\frac{\partial^2 p_\varphi(\varphi)}{\partial \varphi^2} \\ + p_r(r)p_\varphi(\varphi)\frac{\partial^2 p_z(z)}{\partial z^2} + k^2 p_r(r)p_\varphi(\varphi)p_z(z) = 0, \end{aligned} \tag{2.14}$$

Dividing equation (2.14) by the term $p_r(r)p_\varphi(\varphi)p_z(z)$ yields

$$\frac{1}{p_r(r)}\left(\frac{\partial^2 p_r(r)}{\partial r^2} + \frac{1}{r}\frac{\partial p_r(r)}{\partial r}\right) + \frac{1}{r^2}\frac{1}{p_\varphi(\varphi)}\frac{\partial^2 p_\varphi}{\partial \varphi^2} + \frac{1}{p_z(z)}\frac{\partial^2 p_z(z)}{\partial z^2} + k^2 = 0. \tag{2.15}$$

The third term of the latter equation only depends on z and equals a sum of terms that are independent of z

$$\frac{1}{p_z(z)}\frac{\partial^2 p_z(z)}{\partial z^2} = -\frac{1}{p_r(r)}\left(\frac{\partial^2 p_r(r)}{\partial r^2} + \frac{1}{r}\frac{\partial p_r(r)}{\partial r}\right) - \frac{1}{r^2}\frac{1}{p_\varphi(\varphi)}\frac{\partial^2 p_\varphi}{\partial \varphi^2} - k^2, \tag{2.16}$$

which leads to the conclusion that this term must be a constant $-k_z^2$. Then,

$$\frac{1}{p_z(z)}\frac{\mathrm{d}^2 p_z(z)}{\mathrm{d}z^2} + k_z^2 = 0. \tag{2.17}$$

Multiplying with the term r^2, equation (2.15) can now be rewritten as

$$\frac{r^2}{p_r(r)}\frac{\partial^2 p_r(r)}{\partial r^2} + \frac{r}{p_r(r)}\frac{\partial p_r(r)}{\partial r} + \frac{1}{p_\varphi(\varphi)}\frac{\partial^2 p_\varphi}{\partial \varphi^2} + r^2\left(k^2 - k_z^2\right) = 0. \tag{2.18}$$

This equation reveals that the third term only depends on the φ coordinate and equals a sum of terms that are independent. Using the same argumentation that in the case of p_z in equations (2.16) and (2.17), it is shown that

$$\frac{1}{p_\varphi(\varphi)}\frac{\mathrm{d}^2 p_\varphi(\varphi)}{\mathrm{d}\varphi^2} + k_\varphi^2 = 0, \tag{2.19}$$

where $-k_\varphi^2$ is a constant. Using this value, equation (2.18) results in

$$\frac{r^2}{p_r(r)}\frac{\partial^2 p_r(r)}{\partial r^2} + \frac{r}{p_r(r)}\frac{\partial p_r(r)}{\partial r} + r^2\left(k^2 - k_z^2 - \frac{k_\varphi^2}{r^2}\right) = 0. \tag{2.20}$$

Equations (2.17) and (2.19) are identified as one-dimensional Helmholtz equation. They have the general solutions

$$p_z(z) = A\mathrm{e}^{\mathrm{j}k_z z} + B\mathrm{e}^{-\mathrm{j}k_z z}, \tag{2.21}$$

$$p_\varphi(\varphi) = C\mathrm{e}^{\mathrm{j}k_\varphi \varphi} + D\mathrm{e}^{-\mathrm{j}k_\varphi \varphi}. \tag{2.22}$$

Besides, due to the symmetry of the problem $p_\varphi(\varphi)$ must be 2π-periodic, which leads to the conclusion that k_φ must be an integer n.

Using $k_\varphi = n$ and the definition of the transversal wavenumber k_r

$$k_r^2 = k^2 - k_z^2, \tag{2.23}$$

equation (2.20) can finally be written as

$$\frac{r^2}{p_r(r)}\frac{\partial^2 p_r(r)}{\partial r^2} + \frac{r}{p_r(r)}\frac{\partial p_r(r)}{\partial r} + r^2\left(k_r^2 - \frac{n^2}{r^2}\right) = 0. \tag{2.24}$$

This equation is recognized as the one that defines a Bessel equation (see appendix A.1). Its the general solution follows

$$p_r(r) = E\mathrm{J}_n(k_r r) + F\mathrm{Y}_n(k_r r), \tag{2.25}$$

where J_n and Y_n are the Bessel and the Neumann functions of order n, respectively. Further details about these functions can be found in appendix A.1

Now the solutions of the independent variables can be combined together. This yields solutions of the form

$$\begin{aligned} p(r,\varphi,z) \propto &\left(A\mathrm{e}^{\mathrm{j}k_z z} + B\mathrm{e}^{-\mathrm{j}k_z z}\right)\left(C\mathrm{e}^{\mathrm{j}n\varphi} + D\mathrm{e}^{-\mathrm{j}n\varphi}\right) \\ &\times \Big(E\mathrm{J}_n(k_r r) + F\mathrm{Y}_n(k_r r)\Big). \end{aligned} \tag{2.26}$$

All combinations provided by the latter equation must be included in the general solution of the Helmholtz equation. Therefore, all possible values of n and k_z must be taken into account

$$\begin{aligned} p(r,\varphi,z) = &\sum_{n=0}^{\infty}\Big(C_n\mathrm{e}^{\mathrm{j}n\varphi} + D_n\mathrm{e}^{-\mathrm{j}n\varphi}\Big) \\ &\times \int_{-\infty}^{\infty}\left(A\mathrm{e}^{\mathrm{j}k_z z} + B\mathrm{e}^{-\mathrm{j}k_z z}\right)\Big(E\mathrm{J}_n(k_r r) + F\mathrm{Y}_n(k_r r)\Big)\mathrm{d}k_z. \end{aligned} \tag{2.27}$$

The discrete summation over all n can be rewritten as

$$\sum_{n=0}^{\infty}\Big(C_n\mathrm{e}^{\mathrm{j}n\varphi} + D_n\mathrm{e}^{-\mathrm{j}n\varphi}\Big) = \sum_{n=-\infty}^{\infty} G_n\mathrm{e}^{\mathrm{j}n\varphi}. \tag{2.28}$$

Using this equivalence, the general solution yields after some rearrangement

$$p(r,\varphi,z) = \sum_{n=-\infty}^{\infty}\mathrm{e}^{\mathrm{j}n\varphi}\int_{-\infty}^{\infty}\Big(A_n\mathrm{J}_n(k_r r) + B_n\mathrm{Y}_n(k_r r)\Big)\mathrm{e}^{\mathrm{j}k_z z}\mathrm{d}k_z. \tag{2.29}$$

Alternatively, the general solution can be given using Hankel functions

$$p(r,\varphi,z) = \sum_{n=-\infty}^{\infty} \mathrm{e}^{\mathrm{j}n\varphi} \int_{-\infty}^{\infty} \Big(C_n \mathrm{H}_n^{(1)}(k_r r) + D_n \mathrm{H}_n^{(2)}(k_r r) \Big) \mathrm{e}^{\mathrm{j}k_z z} \mathrm{d}k_z, \tag{2.30}$$

where $\mathrm{H}_n^{(1)}$ and $\mathrm{H}_n^{(2)}$ are the Hankel functions of first and second kind and order n, respectively. These are defined as follows

$$\mathrm{H}_n^{(1)}(x) = \mathrm{J}_n(x) + \mathrm{j}\mathrm{Y}_n(x), \tag{2.31}$$

$$\mathrm{H}_n^{(2)}(x) = \mathrm{J}_n(x) - \mathrm{j}\mathrm{Y}_n(x). \tag{2.32}$$

The values A_n, B_n, C_n and D_n in the equations of the general solution are determined by means of the boundary conditions of the problem under analysis. Of special interest are the interior and the exterior problems described in the following section.

2.1.3 Interior and Exterior Boundary Value Problems

The interior and the exterior boundary value problem are characterized by both the region where the wave equation is valid and the location of the sound sources with respect to the region of validity. A sketch of these problems is shown in figure 2.2.

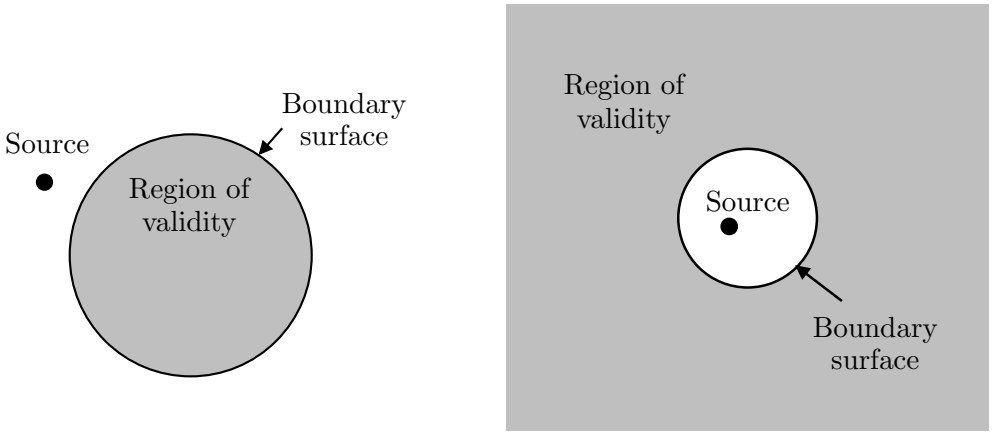

(a) Interior problem. **(b)** Exterior problem.

Figure 2.2: Interior and exterior problems. The region of validity of the wave equation is represented by the gray area.

These two boundary problems are described as follows

- **Interior problems.** The sources are located completely outside the boundary surface, which is the limit of the region of validity. This implies that the sound pressure must be finite at the origin. This behavior is not easily described by means of equation (2.30) since the Hankel functions are infinite at the origin. Therefore, equation (2.29) must be used instead. Whereas the term J_n is finite at the origin, the term Y_n is infinite as can be seen in figure A.1 in appendix A.1. As a consequence, B_n must be set to zero. In this case, the general solution simplifies

to

$$p(r,\varphi,z) = \sum_{n=-\infty}^{\infty} \mathrm{e}^{\mathrm{j}n\varphi} \int_{-\infty}^{\infty} A_n \mathrm{J}_n(k_r r)\mathrm{e}^{\mathrm{j}k_z z}\mathrm{d}k_z. \tag{2.33}$$

This boundary problem is the case, for example, of the sound field inside a cylindrical duct [10].

- **Exterior problems.** In this case, the boundary surface totally encloses all the sources. Now, equation (2.30) is used as the condition for a finite field at the origin is no longer valid.

  The boundary condition at infinity, is in this case given by the Sommerfeld radiation condition[1] which states that only outgoing waves can exist [12]. The asymptotic behavior of the Hankel functions for large arguments, i. e. at $r \to \infty$, follows

$$\lim_{r\to\infty} \mathrm{H}_n^{(1)}(k_r r) = \sqrt{\frac{2}{\pi k_r r}}\mathrm{e}^{\mathrm{j}(k_r r - n\pi/2 - \pi/4)}, \tag{2.34}$$

$$\lim_{r\to\infty} \mathrm{H}_n^{(2)}(k_r r) = \sqrt{\frac{2}{\pi k_r r}}\mathrm{e}^{-\mathrm{j}(k_r r - n\pi/2 - \pi/4)}. \tag{2.35}$$

  Using the convention $\mathrm{e}^{-\mathrm{j}\omega t}$, it becomes obvious that equation (2.34) represents outgoing waves, whereas equation (2.35) represents incoming waves [13]. Therefore, to fulfill the Sommerfeld condition it must be imposed that $D_n = 0$, and the solution of the wave equation becomes

$$p(r,\varphi,z) = \sum_{n=-\infty}^{\infty} \mathrm{e}^{\mathrm{j}n\varphi} \int_{-\infty}^{\infty} C_n \mathrm{H}_n^{(1)}(k_r r)\mathrm{e}^{\mathrm{j}k_z z}\mathrm{d}k_z. \tag{2.36}$$

  The exterior problem is of interest when dealing with scattering from rigid cylinders, as will be seen in the following section.

2.2 Scattering from Rigid Cylinders

When a sound wave encounters an obstacle, some of the wave is deflected from its original path. For linear problems, the difference between the actual sound field and the sound field that would be present if the obstacle was not there is the scattered wave. Hence, the total pressure can be written as the sum of the incident and the scattered pressure,

$$p_{\mathrm{total}} = p_{\mathrm{i}} + p_{\mathrm{sc}}. \tag{2.37}$$

In this section it is considered that the incoming waves are created by a point source in the far-field, which implies that the waves that interact with the obstacle can be regarded as plane waves [14]. The obstacle that creates scattering is assumed to be a cylinder with a rigid surface. Due to the stiffness, the total radial particle velocity at the surface of the cylinder must be zero.

[1] The Sommerfeld radiation condition is given in detail in [11] for spherical waves.

In addition, it is also assumed that the vibration of the cylindrical surface is independent of the axial coordinate. This assumption corresponds to a symmetric setup that simplifies further derivations, and in effect, reduces the problem to two dimensions.

The scattering from cylinders is here described for cylinders of finite and infinite length. The geometry of the problem, depicted in figure 2.3, shows an incident wave, characterized by a plane wave moving along the direction of the wavenumber $\vec{k}_\mathrm{i}$, that is obstructed by a cylinder of radius R and length $2L$. Note that cylinders of infinite length are represented when $L \to \infty$.

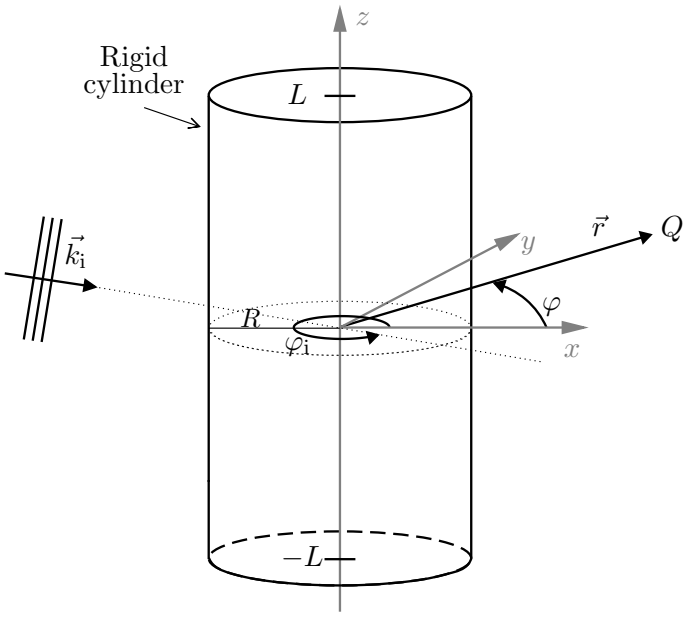

Figure 2.3: Geometrical model considered for the scattering problem. The incident waves impinge on a rigid cylinder of radius R and length $2L$.

2.2.1 Cylindrical Scatterer of Infinite Length

Consider a plane wave created by a source that travels perpendicularly to the axis of the cylinder, i. e. perpendicular to the z-axis. In the absence of the cylinder, the incident wave traveling in the direction $\vec{k}_\mathrm{i}$ is, at a point $Q(r, \varphi)$,

$$\hat{p}_\mathrm{i}(\vec{r}) = P_0 \mathrm{e}^{\mathrm{j}\left(\vec{k}_\mathrm{i} \cdot \vec{r} - \omega t\right)}, \tag{2.38}$$

where P_0 is the amplitude of the plane wave and $\vec{r}$ is the position vector in a cylindrical coordinate system. For mathematical simplicity, and due to the symmetry of the problem, the z-coordinate of the vectors $\vec{k}_\mathrm{i}$ and $\vec{r}$ is set to zero. In Cartesian coordinates the wavenumber vector $\vec{k}_\mathrm{i}$ is

$$\vec{k}_\mathrm{i} = k \left(\cos\varphi_\mathrm{i} \vec{\boldsymbol{e}}_{\boldsymbol{x}} + \sin\varphi_\mathrm{i} \vec{\boldsymbol{e}}_{\boldsymbol{y}} + 0 \vec{\boldsymbol{e}}_{\boldsymbol{z}}\right), \tag{2.39}$$

where φ_i is the angle of incidence of the plane wave in the xy-plane (see figure 2.3) and $\vec{\boldsymbol{e}}_{\boldsymbol{x}}$, $\vec{\boldsymbol{e}}_{\boldsymbol{y}}$ and $\vec{\boldsymbol{e}}_{\boldsymbol{z}}$ represent the unit vectors along the x, y and z-axis, respectively. The

position vector $\vec{r}$ is, in Cartesian coordinates,

$$\vec{r} = r\left(\cos\varphi\vec{\boldsymbol{e}}_{\boldsymbol{x}} + \sin\varphi\vec{\boldsymbol{e}}_{\boldsymbol{y}} + 0\vec{\boldsymbol{e}}_{\boldsymbol{z}}\right). \tag{2.40}$$

Now, using the previous expressions in Cartesian coordinates, the pressure of the incident wave becomes

$$\hat{p}_{\mathrm{i}}(r,\varphi,t) = P_0 \mathrm{e}^{\mathrm{j}\left(kr(\cos\varphi_{\mathrm{i}}\cos\varphi+\sin\varphi_{\mathrm{i}}\sin\varphi)-\omega t\right)} = P_0 \mathrm{e}^{\mathrm{j}\left(kr\cos(\varphi-\varphi_{\mathrm{i}})-\omega t\right)}. \tag{2.41}$$

As the incident plane wave is created far from the cylinder and approaches the cylinder placed at the origin, the situation can be regarded as an interior boundary problem according to section 2.1.3. Therefore, the sound field created by the incident wave must be expressible in terms of equation (2.33). Taking into account that the plane wave travels perpendicularly to the z-axis, k_z must be zero meaning that $k = k_r$ (see equation (2.23)). Going back to section 2.1.2, the particular solution for $\hat{p}_z(z)$ given in equation (2.21) is reduced to a constant since $k_z = 0$. This implies that the general solution does not present the integral with respect to k_z. As a consequence, the pressure in the case of the interior boundary problem becomes

$$\hat{p}_{\mathrm{i}}(r,\varphi,t) = \mathrm{e}^{-\mathrm{j}\omega t} \sum_{n=-\infty}^{\infty} \mathrm{e}^{\mathrm{j}n\varphi} A_n \mathrm{J}_n(kr). \tag{2.42}$$

Note that in the latter equation the pressure is expressed in complex notation so the temporal term must be present. Equation (2.41) must equal equation (2.42)

$$P_0 \mathrm{e}^{\mathrm{j}\left(kr\cos(\varphi-\varphi_{\mathrm{i}})-\omega t\right)} = \mathrm{e}^{-\mathrm{j}\omega t} \sum_{n=-\infty}^{\infty} \mathrm{e}^{\mathrm{j}n\varphi} A_n \mathrm{J}_n(kr). \tag{2.43}$$

The coefficients A_n are obtained by multiplying both sides of the latter equation with $e^{-\mathrm{j}\nu\varphi}$ and integrating over φ

$$\int_0^{2\pi} \mathrm{e}^{-\mathrm{j}\nu\varphi} P_0 \mathrm{e}^{\mathrm{j}kr\cos(\varphi-\varphi_{\mathrm{i}})} \mathrm{d}\varphi = \int_0^{2\pi} \mathrm{e}^{-\mathrm{j}\nu\varphi} \sum_{n=-\infty}^{\infty} \mathrm{e}^{\mathrm{j}n\varphi} A_n \mathrm{J}_n(kr) \mathrm{d}\varphi, \tag{2.44}$$

then,

$$P_0 \int_0^{2\pi} \mathrm{e}^{\mathrm{j}kr\cos(\varphi-\varphi_{\mathrm{i}})} \mathrm{e}^{-\mathrm{j}\nu\varphi} \mathrm{d}\varphi = \sum_{n=-\infty}^{\infty} A_n \mathrm{J}_n(kr) \int_0^{2\pi} \mathrm{e}^{-\mathrm{j}\nu\varphi} \mathrm{e}^{\mathrm{j}n\varphi} \mathrm{d}\varphi. \tag{2.45}$$

The functions of the form $\mathrm{e}^{\mathrm{j}n\varphi}$ are orthogonal, which implies that the integral of the right side term equals 0 when $n \neq \nu$ or 2π when $n = \nu$. More details about these functions are given in section 3.1. Therefore, equation (2.45) is simplified to

$$P_0 \int_0^{2\pi} \mathrm{e}^{\mathrm{j}\left(kr\cos(\varphi-\varphi_{\mathrm{i}})-n\varphi\right)} \mathrm{d}\varphi = 2\pi A_n \mathrm{J}_n(kr). \tag{2.46}$$

Applying the change of variables $\psi = \varphi - \varphi_\mathrm{i}$ at the left side term of the latter equation yields

$$P_0 \mathrm{e}^{-\mathrm{j}n\varphi_\mathrm{i}} \int_0^{2\pi} \mathrm{e}^{\mathrm{j}(kr\cos\psi - n\psi)} \mathrm{d}\psi = 2\pi A_n \mathrm{J}_n(kr). \tag{2.47}$$

According to equation (A.4) given in appendix A.1, the integral at the left side of the previous equation equals

$$\int_0^{2\pi} \mathrm{e}^{\mathrm{j}(kr\cos\psi - n\psi)} \mathrm{d}\psi = 2\pi(\mathrm{j})^{-n} \mathrm{J}_{-n}(kr). \tag{2.48}$$

Using the property found in the previous equation and the relationship between J_{-n} and J_n given in equation (A.6), the coefficients A_n can be isolated from equation (2.47)

$$A_n = P_0 \mathrm{j}^n \mathrm{e}^{-\mathrm{j}n\varphi_\mathrm{i}}. \tag{2.49}$$

Finally, inserting this value into equation (2.42), the incident pressure is given by

$$\hat{p}_\mathrm{i}(r,\varphi,t) = P_0 \mathrm{e}^{-\mathrm{j}\omega t} \sum_{n=-\infty}^{\infty} \mathrm{j}^n \mathrm{J}_n(kr) \mathrm{e}^{\mathrm{j}n(\varphi-\varphi_\mathrm{i})}. \tag{2.50}$$

As mentioned previously, the radial velocity vanishes on the surface of a rigid cylinder at $r = R$

$$\hat{u}_{\mathrm{total},r}(R,\varphi,t) = \hat{u}_{\mathrm{i},r}(R,\varphi,t) + \hat{u}_{\mathrm{sc},r}(R,\varphi,t) = 0. \tag{2.51}$$

Therefore, $u_{\mathrm{sc},r}(R,\varphi,t) = -u_{\mathrm{i},r}(R,\varphi,t)$. The particle velocity in the radial direction due to the incoming wave is

$$\hat{u}_{\mathrm{i},r}(R,\varphi,t) = \frac{1}{\mathrm{j}\omega\rho_0} \frac{\mathrm{d}\hat{p}_\mathrm{i}(r,\varphi,t)}{\mathrm{d}r}\bigg|_{r=R} = \frac{P_0 \mathrm{e}^{-\mathrm{j}\omega t}}{\mathrm{j}\omega\rho_0} \sum_{n=-\infty}^{\infty} \mathrm{j}^n \frac{\mathrm{dJ}_n(kr)}{\mathrm{d}r} \mathrm{e}^{\mathrm{j}n(\varphi-\varphi_\mathrm{i})}\bigg|_{r=R}, \tag{2.52}$$

where ρ_0 is the equilibrium density of the medium. The scattered pressure can be regarded as an exterior boundary problem, and consequently it can be written by the sum of outgoing waves described in equation (2.36). However, the integral with respect to k_z can be removed from the equation due to the fact that it has been assumed that the vibration of the cylindrical surface is independent of the axial coordinate. Similarly to the derivation of $\hat{p}_\mathrm{i}$, this implies that $k_z = 0$, hence the solution of $p_z(z)$ yields a constant (see equation (2.21)), and the general solution does not depend on k_z. The scattered pressure is then

$$\hat{p}_\mathrm{sc}(r,\varphi,t) = \mathrm{e}^{-\mathrm{j}\omega t} \sum_{n=-\infty}^{\infty} \mathrm{e}^{\mathrm{j}n\varphi} C_n \mathrm{H}_n^{(1)}(kr). \tag{2.53}$$

The scattered particle velocity in the radial direction is given by

$$\hat{u}_{\mathrm{sc},r}(r,\varphi,t) = \frac{1}{\mathrm{j}\omega\rho_0} \frac{\mathrm{d}\hat{p}_\mathrm{sc}(r,\varphi)}{\mathrm{d}r} = \frac{\mathrm{e}^{-\mathrm{j}\omega t}}{\mathrm{j}\omega\rho_0} \sum_{n=-\infty}^{\infty} \mathrm{e}^{\mathrm{j}n\varphi} C_n \frac{\mathrm{dH}_n^{(1)}(kr)}{\mathrm{d}r}. \tag{2.54}$$

Equation (2.52) can be related to the latter expression evaluated at $r = R$, according to equation (2.51),

$$\mathrm{e}^{-\mathrm{j}\omega t} \sum_{n=-\infty}^{\infty} \mathrm{e}^{\mathrm{j}n\varphi} C_n \mathrm{H}_n'^{(1)}(kR) = -P_0 \mathrm{e}^{-\mathrm{j}\omega t} \sum_{n=-\infty}^{\infty} \mathrm{j}^n \mathrm{J}_n'(kR) \mathrm{e}^{\mathrm{j}n(\varphi-\varphi_\mathrm{i})}, \tag{2.55}$$

where $\mathrm{J}_n'(kR)$ and $\mathrm{H}_n'^{(1)}(kR)$ are given by

$$\mathrm{J}_n'(kR) = \left.\frac{\mathrm{d}\mathrm{J}_n(kr)}{\mathrm{d}r}\right|_{r=R}, \tag{2.56}$$

$$\mathrm{H}_n'^{(1)}(kR) = \left.\frac{\mathrm{d}\mathrm{H}_n^{(1)}(kr)}{\mathrm{d}r}\right|_{r=R}. \tag{2.57}$$

Now, the coefficients C_n can be isolated from equation (2.55)

$$C_n = -P_0 \mathrm{j}^n \frac{\mathrm{J}_n'(kR)}{\mathrm{H}_n'^{(1)}(kR)} \mathrm{e}^{-\mathrm{j}n\varphi_\mathrm{i}}. \tag{2.58}$$

Making use of C_n, the scattered pressure and the total pressure result in

$$\hat{p}_\mathrm{sc}(r,\varphi,t) = -P_0 \mathrm{e}^{-\mathrm{j}\omega t} \sum_{n=-\infty}^{\infty} \mathrm{j}^n \frac{\mathrm{J}_n'(kR)\mathrm{H}_n^{(1)}(kr)}{\mathrm{H}_n'^{(1)}(kR)} \mathrm{e}^{\mathrm{j}n(\varphi-\varphi_\mathrm{i})}, \tag{2.59}$$

and

$$\hat{p}_\mathrm{total}(r,\varphi,t) = P_0 \mathrm{e}^{-\mathrm{j}\omega t} \sum_{n=-\infty}^{\infty} \mathrm{j}^n \left(\mathrm{J}_n(kr) - \frac{\mathrm{J}_n'(kR)\mathrm{H}_n^{(1)}(kr)}{\mathrm{H}_n'^{(1)}(kR)} \right) \mathrm{e}^{\mathrm{j}n(\varphi-\varphi_\mathrm{i})}. \tag{2.60}$$

Of special interest will be the sound field on the surface of the cylinder of infinite length

$$\hat{p}_\mathrm{total}(R,\varphi,t) = P_0 \mathrm{e}^{-\mathrm{j}\omega t} \sum_{n=-\infty}^{\infty} \mathrm{j}^n \left(\mathrm{J}_n(kR) - \frac{\mathrm{J}_n'(kR)\mathrm{H}_n^{(1)}(kR)}{\mathrm{H}_n'^{(1)}(kR)} \right) \mathrm{e}^{\mathrm{j}n(\varphi-\varphi_\mathrm{i})}. \tag{2.61}$$

2.2.2 Cylindrical Scatterer of Finite Length

The total sound field when a cylinder of finite length is present is usually difficult to solve analytically. As in the case of the infinite-length cylinder, an incident plane wave with amplitude P_0 traveling in the direction $\vec{k}_\mathrm{i}$ is assumed (see equation (2.38)). This impinges on the finite-length rigid scatterer orthogonally to the cylindrical axis. Therefore, the expression of the incident pressure derived for the case of an infinitely long cylinder (given in equation (2.50)) is still valid.

Neglecting the boundary conditions at the end caps of the cylinder (at $z = L$ and $z = -L$), the following approximation for the scattered sound pressure[2] is given in [15]

$$\hat{p}_{\mathrm{sc}}(r,\varphi,z,t) = -P_0 \mathrm{e}^{-\mathrm{j}\omega t}\frac{kL}{\pi}\sum_{n=-\infty}^{\infty}\mathrm{j}^n \mathrm{J}'_n(kR)\mathrm{e}^{\mathrm{j}n(\varphi-\varphi_\mathrm{i})} \times \int_{-\infty}^{\infty}\frac{\mathrm{H}_n^{(1)}(\sqrt{k^2-k_z^2}r)\mathrm{sinc}(k_zL)}{\sqrt{k^2-k_z^2}\mathrm{H}_n'^{(1)}(\sqrt{k^2-k_z^2}R)}\mathrm{e}^{\mathrm{j}k_z z}\mathrm{d}k_z, \tag{2.62}$$

where the sinc function is defined as

$$\mathrm{sinc}(k_zL) = \frac{\sin(k_zL)}{k_zL}. \tag{2.63}$$

The scattered pressure due to a cylinder of infinite length can be derived from the finite-length cylinder case. At $L \to \infty$, only the term $L\mathrm{sinc}(k_zL)$ of equation (2.62) is affected. Using the relationship [16]

$$\delta(k_z) = \lim_{L\to\infty}\frac{1}{\pi k_z}\sin(k_zL), \tag{2.64}$$

the upper limit of the term $L\mathrm{sinc}(k_zL)$ follows

$$\lim_{L\to\infty} L\mathrm{sinc}(k_zL) = \lim_{L\to\infty}\frac{\sin(k_zL)}{k_z} = \lim_{L\to\infty}\frac{\pi}{\pi k_z}\sin(k_zL) = \pi\delta(k_z). \tag{2.65}$$

The result of inserting the latter relation into equation (2.62) is the same as the one obtained for the infinite-length cylinder in equation (2.59).

The total sound pressure, given by the summation of the incident and the scattered pressures, is

$$\hat{p}_{\mathrm{total}}(r,\varphi,z,t) = P_0\sum_{n=-\infty}^{\infty}\mathrm{j}^n\mathrm{e}^{\mathrm{j}n(\varphi-\varphi_\mathrm{i})}\left(\mathrm{J}_n(kr) - \frac{kL}{\pi}\mathrm{J}'_n(kR) \times \int_{-\infty}^{\infty}\frac{\mathrm{H}_n^{(1)}(\sqrt{k^2-k_z^2}r)\mathrm{sinc}(k_zL)}{\sqrt{k^2-k_z^2}\mathrm{H}_n'^{(1)}(\sqrt{k^2-k_z^2}R)}\mathrm{e}^{\mathrm{j}k_z z}\mathrm{d}k_z\right)\mathrm{e}^{-\mathrm{j}\omega t}. \tag{2.66}$$

Of special importance will be the pressure on the surface of a rigid cylinder of finite length in the xy-plane, i. e. at $z = 0$

$$\hat{p}_{\mathrm{total}}(R,\varphi,t) = P_0\sum_{n=-\infty}^{\infty}\mathrm{j}^n\mathrm{e}^{\mathrm{j}n(\varphi-\varphi_\mathrm{i})}\left(\mathrm{J}_n(kR) - \frac{kL}{\pi}\mathrm{J}'_n(kR) \times \int_{-\infty}^{\infty}\frac{\mathrm{H}_n^{(1)}(\sqrt{k^2-k_z^2}R)\mathrm{sinc}(k_zL)}{\sqrt{k^2-k_z^2}\mathrm{H}_n'^{(1)}(\sqrt{k^2-k_z^2}R)}\mathrm{d}k_z\right)\mathrm{e}^{-\mathrm{j}\omega t}. \tag{2.67}$$

[2] The derivation of the scattered sound pressure from a finite cylinder is beyond the scope of this document. Details about it are given in [15].

3

Sound Field Decomposition

3.1 Fourier Series

The decomposition of a function in a Fourier Series is of great utility when dealing with functions that present circular symmetry. A function defined in polar coordinates (r and φ) can be represented in a Fourier series in the φ coordinate as [17]

$$f(r,\varphi) = \sum_{n=-\infty}^{\infty} \mathcal{C}_n(r) \mathrm{e}^{\mathrm{j}n\varphi}, \tag{3.1}$$

where the coefficient functions $\mathcal{C}_n(r)$ are given by

$$\mathcal{C}_n(r) = \frac{1}{2\pi} \int_0^{2\pi} f(r,\varphi) \mathrm{e}^{-\mathrm{j}n\varphi} \mathrm{d}\varphi. \tag{3.2}$$

The representation in terms of Fourier series is in fact a summation modes of the form

$$f_n(r,\varphi) = \mathcal{C}_n(r) \mathrm{e}^{\mathrm{j}n\varphi}. \tag{3.3}$$

The terms $\mathrm{e}^{\mathrm{j}n\varphi}$ are referred to as circular harmonics (CH). In the literature, other names can be found, e. g. circumferential harmonics. Figure 3.1 shows the magnitude of the real part of the first six harmonics, $\left|\mathrm{Re}\left\{\mathrm{e}^{\mathrm{j}n\varphi}\right\}\right|$, as a function of φ. As can be seen, these harmonics correspond to multipoles: order 0 yields a monopole, order 1 a dipole, etc. An important property of the CH is that they are orthogonal, which means that they satisfy

$$\frac{1}{2\pi} \int_0^{2\pi} \mathrm{e}^{\mathrm{j}n\varphi} (\mathrm{e}^{\mathrm{j}\nu\varphi})^* \mathrm{d}\varphi = \delta_{n\nu}, \tag{3.4}$$

where $\delta_{n\nu}$ is the Kronecker function which equals unity when $n = \nu$ and it is zero otherwise.

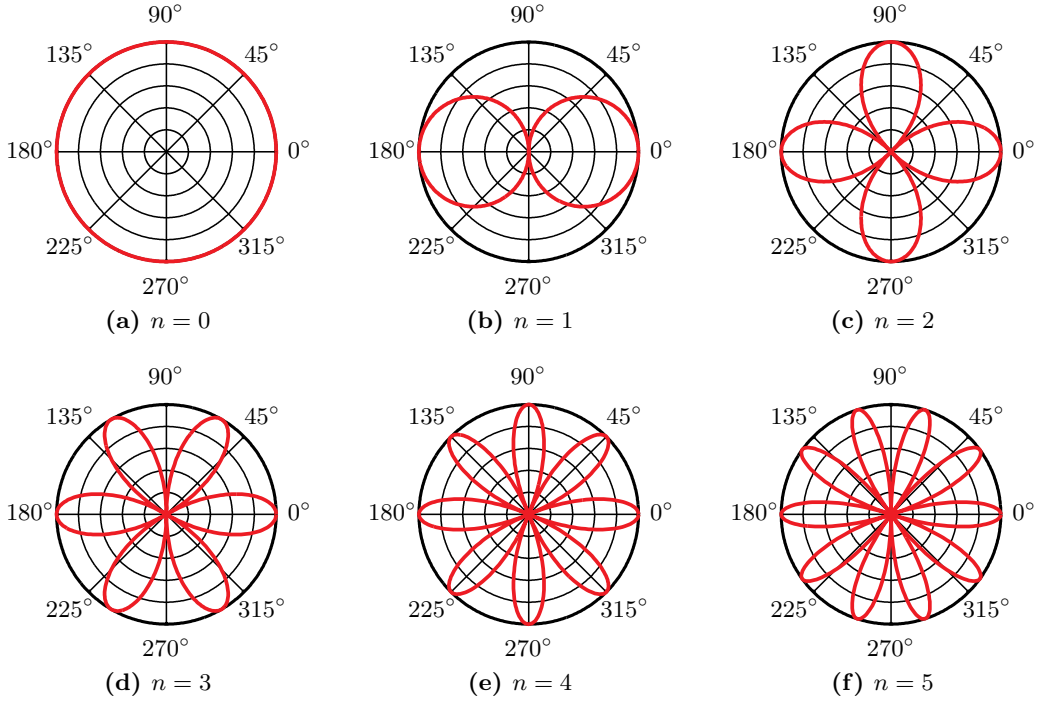

(a) $n = 0$ **(b)** $n = 1$ **(c)** $n = 2$

(d) $n = 3$ **(e)** $n = 4$ **(f)** $n = 5$

Figure 3.1: Magnitude of the real part of the CH as a function of φ, for the first six orders. The outer circle corresponds to a level of 0 dB.

3.2 Sound Field Decomposition using Circular Apertures

In this section the sound field captured by a circular aperture is decomposed in a Fourier series, and its modal response is analyzed in two configurations. The first one, namely the *unbaffled* case, consists of a circular aperture that is not mounted on any baffle. For the second setup, the aperture is mounted on a rigid cylindrical baffle and is referred to as a *baffled* circular aperture.

3.2.1 Unbaffled Circular Apertures

In the following, the modal properties of an unbaffled circular array are analyzed. As shown in figure 3.2, a circular aperture of radius R that lies on the xy-plane is considered as well as a plane wave that impinges on the aperture perpendicularly to the z-axis. The aperture is not regarded as an obstacle by the impinging wave, and therefore, the pressure on the aperture is only due to the wave itself. In other words, no scattered sound field is created. The incident pressure at any point of the aperture is, according to equation (2.50) on page 11,

$$p(kR, \varphi) = P_0 \mathrm{e}^{\mathrm{j}\vec{k_\mathrm{i}} \cdot \vec{r}}\Big|_{r=R} = P_0 \sum_{n=-\infty}^{\infty} \mathrm{j}^n \mathrm{J}_n(kR) \mathrm{e}^{\mathrm{j}n(\varphi - \varphi_\mathrm{i})}, \tag{3.5}$$

where the product of the wavenumber k and the radius of th aperture R, i. e. kR, is referred to as spatial frequency. Note that the temporal term $\mathrm{e}^{-\mathrm{j}\omega t}$ is not shown in

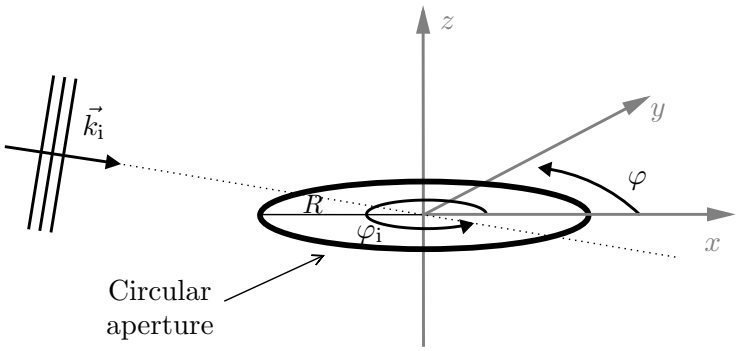

Figure 3.2: Plane wave impinging on a circular aperture.

the latter equation in order to simplify following derivations. The pressure can now be decomposed by an infinite number of modes (harmonics) using the principles of the Fourier series given in equations (3.1) and (3.2)

$$p(kR,\varphi) = \sum_{n=-\infty}^{\infty} \mathcal{C}_n^\circ(kR)\mathrm{e}^{\mathrm{j}n\varphi}, \tag{3.6}$$

$$\mathcal{C}_n^\circ(kR) = \frac{1}{2\pi}\int_0^{2\pi} p(kR,\varphi)\mathrm{e}^{-\mathrm{j}n\varphi}\mathrm{d}\varphi. \tag{3.7}$$

The superscript $\circ$ in the coefficient functions denotes that an *unbaffled* circular aperture is under consideration. The coefficients $\mathcal{C}_n^\circ$ are found after inserting equation (3.5) into equation (3.7)

$$\mathcal{C}_n^\circ(kR) = \frac{1}{2\pi}\int_0^{2\pi} P_0 \sum_{\nu=-\infty}^{\infty} \mathrm{j}^\nu \mathrm{J}_\nu(kR)\mathrm{e}^{\mathrm{j}\nu(\varphi-\varphi_\mathrm{i})}\mathrm{e}^{-\mathrm{j}n\varphi}\mathrm{d}\varphi. \tag{3.8}$$

Due to the fact that the CH are orthogonal, as stated previously in equation (3.4), the coefficients result in

$$\mathcal{C}_n^\circ(kR) = P_0\mathrm{j}^n\mathrm{J}_n(kR)\mathrm{e}^{-\mathrm{j}n\varphi_\mathrm{i}}. \tag{3.9}$$

The magnitude of the first five coefficients $\mathcal{C}_n^\circ$ is shown in figure 3.3. At low spatial frequencies kR, the zeroth order mode is constant and equals 0 dB, whereas all the other modes present a slope of $10 \times n$ dB per decade. This means that the zeroth order is the order that has more strength in this range of spatial frequencies. With the increase of kR more and more harmonics gain strength, but around some values they present dips. The consequence is that signals that have components around these dips cannot be totally resolved. As shown in the next section, this problem can be solved by mounting the aperture on a rigid scatterer. Due to the geometry of the aperture, the scatterer should be a rigid cylindrical baffle.

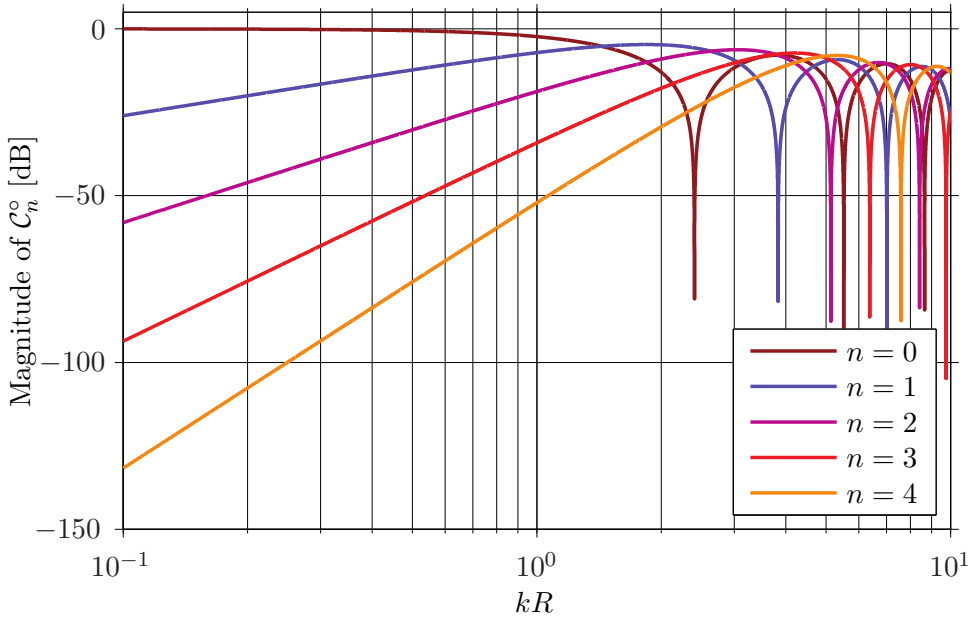

Figure 3.3: Magnitude of the Fourier coefficients of an unbaffled circular aperture, $\mathcal{C}_n^\circ$, when $P_0 = 1$ Pa. The first five modes are shown.

3.2.2 Circular Apertures Mounted on a Rigid Cylindrical Baffle

It is considered that the aperture of the previous section is now mounted on a rigid cylindrical baffle as can be seen in figure 3.4. The assumptions made for the unbaffled aperture regarding the features of the impinging wave are still valid. However, now the presence of the cylinder causes scattering. The theory given for cylindrical scatterers in section 2.2.2 is therefore of great utility in this section. The modal response the baffled apertures is analyzed for cylindrical scatterers of finite and infinite length.

3.2.2.1 Baffle of Infinite Length

The pressure captured by an aperture mounted on a rigid cylindrical baffle of infinite length corresponds to the pressure on the surface of a rigid cylindrical scatterer of infinite length derived in section 2.2.1. The modal response such aperture is obtained by means of the pressure given in equation (2.61) on page 12

$$\mathcal{C}_n^\bullet(kR) = \frac{1}{2\pi}\int_0^{2\pi} P_0 \sum_{n=-\infty}^{\infty} \mathrm{j}^\nu \left(\mathrm{J}_\nu(kR) - \frac{\mathrm{J}'_\nu(kR)\mathrm{H}_\nu^{(1)}(kR)}{\mathrm{H}_\nu'^{(1)}(kR)} \right) \mathrm{e}^{\mathrm{j}\nu(\varphi-\varphi_\mathrm{i})} \mathrm{e}^{-\mathrm{j}n\varphi} \mathrm{d}\varphi. \quad (3.10)$$

The superscript $\bullet$ denotes that the aperture is mounted on a cylindrical baffle of infinite length. Due to the orthogonality property of the CH, the coefficients result in

$$\mathcal{C}_n^\bullet(kR) = P_0 \mathrm{j}^n \left(\mathrm{J}_n(kR) - \frac{\mathrm{J}'_n(kR)\mathrm{H}_n^{(1)}(kR)}{\mathrm{H}_n'^{(1)}(kR)} \right) \mathrm{e}^{-\mathrm{j}n\varphi_\mathrm{i}}. \quad (3.11)$$

In figure 3.5, the magnitude of the first five Fourier coefficients $\mathcal{C}_n^\bullet$ is shown. At first sight, one can see that at low spatial frequencies the response is rather similar to the

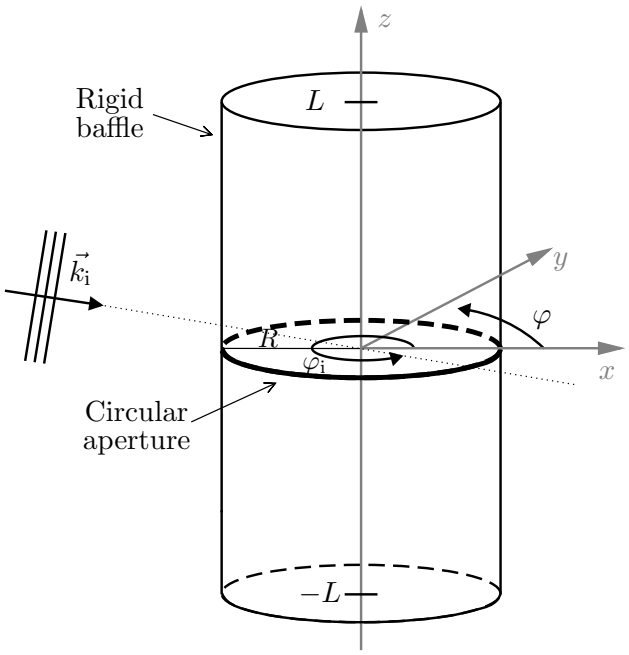

Figure 3.4: Circular aperture of radius R mounted on a cylindrical baffle of the same radius and length $2L$.

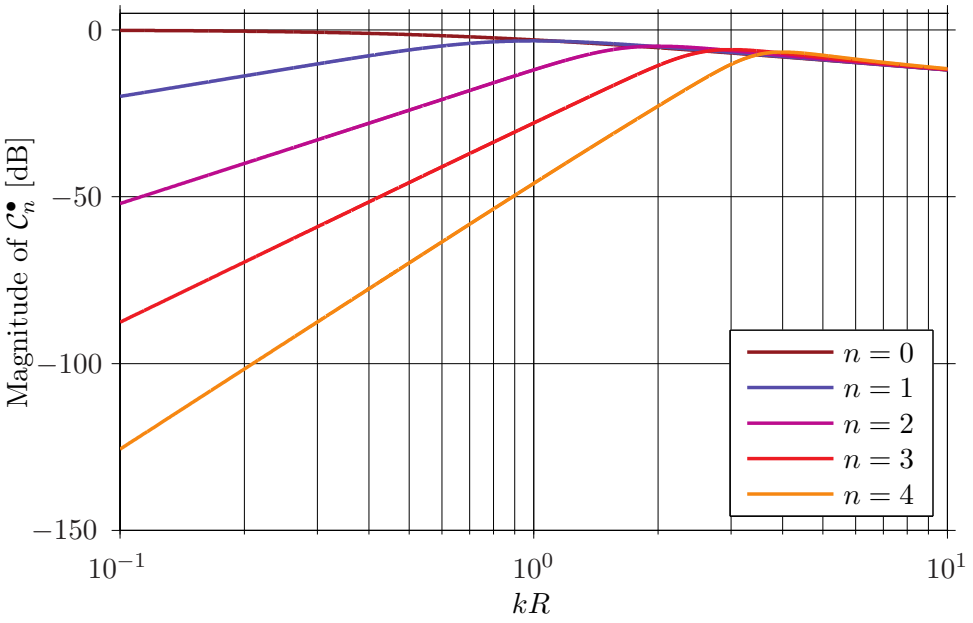

Figure 3.5: Magnitude of the Fourier coefficients of a circular aperture mounted on a rigid cylindrical baffle of infinite length, $\mathcal{C}_n^\bullet$, when $P_0 = 1$ Pa. The first five modes are shown.

one of the unbaffled aperture since the slope of $10 \times n$ dB per decade is also present, see figure 3.3. The only difference is that the response is offset by 6 dB with respect to the unbaffled aperture response. This offset is caused by the stiffness of the cylinder. As its impedance is high, the radial particle velocity is canceled and the sound pressure is doubled. On the other hand, at high values of kR the problem presented for the unbaffled aperture is totally solved, i. e. the dips are canceled, and all the spatial frequencies can be successfully resolved. Furthermore, at these frequencies all the modes present the same response, which means that all of them have the same strength.

3.2.2.2 Baffle of Finite Length

Obviously, for real implementations it is not possible to use cylindrical baffles of infinite length, and hence, finite-length scatterers with a reasonable length must be used instead. The pressure on the surface of a cylindrical scatterer of finite length has been given in section 2.2.2. The pressure that an aperture captures when it is mounted on this scatterer at $z = 0$ (given in equation (2.67) on page 2.67) is decomposed in CH as follows

$$\begin{aligned}\mathcal{C}_n^{\mathrm{L}}(kR) =& \frac{1}{2\pi}\int_0^{2\pi} P_0 \sum_{\nu=-\infty}^{\infty} \mathrm{j}^{\nu}\Bigg(\mathrm{J}_n(kR) - \frac{kL}{\pi}\mathrm{J}'_{\nu}(kR) \\ &\times \int_{-\infty}^{\infty} \frac{\mathrm{H}_{\nu}^{(1)}(\sqrt{k^2-k_z^2}R)\mathrm{sinc}(k_zL)}{\sqrt{k^2-k_z^2}\mathrm{H}_{\nu}^{\prime(1)}(\sqrt{k^2-k_z^2}R)}\mathrm{d}k_z\Bigg)\mathrm{e}^{\mathrm{j}\nu(\varphi-\varphi_{\mathrm{i}})}\mathrm{e}^{-\mathrm{j}n\varphi}\mathrm{d}\varphi. \end{aligned} \tag{3.12}$$

In the coefficients $\mathcal{C}_n^{\mathrm{L}}$ the superscript 'L' denotes that the baffle has a finite length. After solving the integral with respect to φ, the coefficients yield

$$\begin{aligned}\mathcal{C}_n^{\mathrm{L}}(kR) =& P_0\mathrm{j}^n\Bigg(\mathrm{J}_n(kR) - \frac{kL}{\pi}\mathrm{J}'_n(kR) \\ &\times \int_{-\infty}^{\infty} \frac{\mathrm{H}_n^{(1)}(\sqrt{k^2-k_z^2}R)\mathrm{sinc}(k_zL)}{\sqrt{k^2-k_z^2}\mathrm{H}_n^{\prime(1)}(\sqrt{k^2-k_z^2}R)}\mathrm{d}k_z\Bigg)\mathrm{e}^{-\mathrm{j}n\varphi_{\mathrm{i}}}. \end{aligned} \tag{3.13}$$

In figure 3.6, the magnitude of the first four modes is shown for various ratios of L/R. These results were presented by Teutsch in [9] and [15]. The unbaffled case is represented when $L/R = 0$ and the infinite baffle case, when $L/R = \infty$. At low spatial frequencies all curves in all the panels of the figure are parallel, presenting a slope of $10 \times n$ dB per decade independently of the ratio L/R. Note that the difference of 6 dB in offset between the infinite baffle and the unbaffled cases becomes clear. For very small ratios, dips are still present at high values of kR but they vanish progressively when the ratio increases due to the fact that the response becomes more similar to the one obtained with the infinite baffle. Teutsch concludes that with a ratio of 1.4 the modal response is fairly similar to the one of the infinite baffle case. This is a very convenient result for a real implementation of the system, because for ratios $L/R > 1.4$ the coefficients $\mathcal{C}_n^{\mathrm{L}}$ can be approximated to the expression presented for the infinite-length baffle in equation (3.11), which agrees in high level with the actual result and is computationally simpler.

To verify Teutsch results, the modal response for a baffle of finite length has been

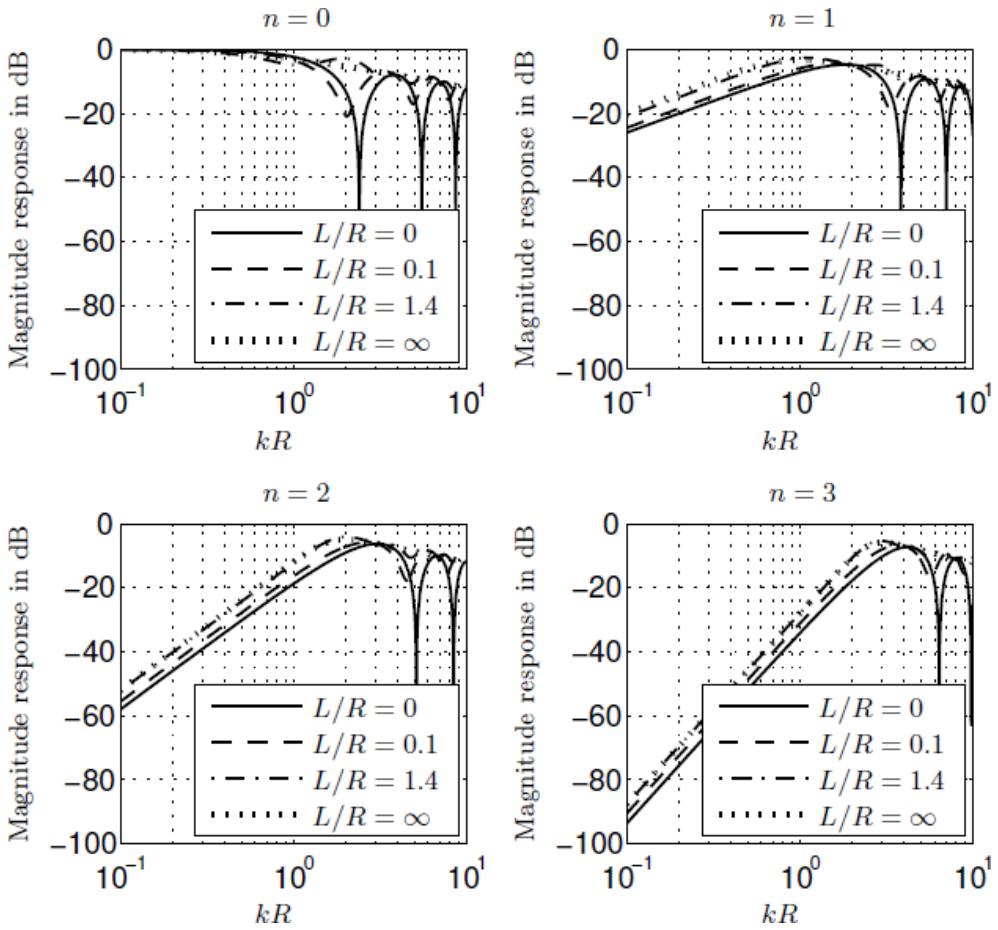

Figure 3.6: Magnitude of the Fourier coefficients of a circular aperture mounted on a rigid cylindrical baffle of finite length. The first four modes are shown for different values of L/R. Taken from [15].

implemented. The results, shown in figure 3.7, reveal significant differences from his results. Comparing the two sets of results, it can be seen that the modal response for the unbaffled aperture and for the aperture mounted on an infinitely-long baffle agree with Teutsch results shown in figure 3.6, in all the spatial frequency range. However, the results deviate when dealing with finite baffles. The obtained curves present a slope at low values of kR that differs of $10 \times n$ dB per decade, which was the value obtained by Teutsch. At higher frequencies, the differences also become apparent, mostly for $L/R = 1.4$. Unlike Teutsch results, this curve is not that similar to the one obtained in the infinite baffle case, as some boosts and dips are now present. Therefore, in this case, one cannot say that with a ratio of $L/R = 1.4$ the aperture can be considered to be mounted into an infinite baffle.[1] Even though it is not shown here, the curves only get closer to the case of the infinite baffle for rather high ratios of L/R (around $L/R \approx 20$). The *Matlab* scripts implemented for the aperture mounted on a finite baffle are given in appendix B.1

[1] Teutsch was contacted during the realization of this project in order to find out the reason for the difference in the results. However, no solution came out from the correspondence.

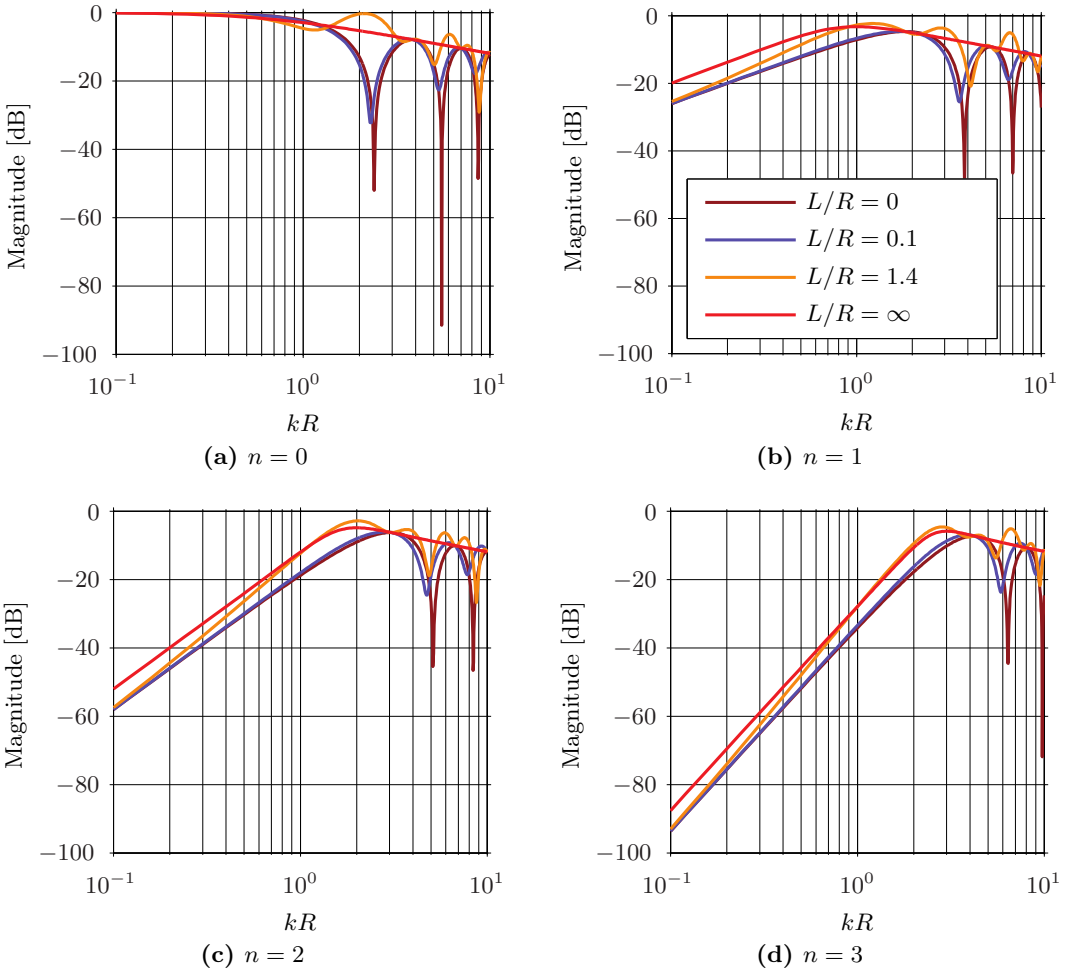

(a) $n = 0$ **(b)** $n = 1$ **(c)** $n = 2$ **(d)** $n = 3$

Figure 3.7: Magnitude of the Fourier coefficients of a circular aperture when $P_0 = 1$ Pa. The first four modes are shown for the values of L/R stated in panel (b). Note that $L/R = 0$ corresponds to an unbaffled aperture, $L/R = \infty$ is the case of an aperture mounted on a baffle of infinite length, whereas the cases where the aperture is mounted on a baffle of finite length are represented by L/R equal to 0.1 and 1.4. The latter two cases, i. e. when the aperture is mounted on a baffle of finite length, are obtained with the *Matlab* scripts given in appendix B.1.

3.3 Error due to Truncation

The sound field can be decomposed in CH, where the superposition of all the modes yields the sound field under analysis. However, in practice, only a certain number of harmonics can be used, and therefore, the sound field is approximated by

$$p(kR, \varphi) \approx \sum_{n=-N}^{N} \mathcal{C}_n(kR) \mathrm{e}^{\mathrm{j}n\varphi}, \tag{3.14}$$

where N is the maximum order. As a consequence, the so-called truncation error arises. In the case of unbaffled circular apertures, this error is

$$\begin{aligned}\mathcal{E}^{\circ}_{\mathrm{t},n}(kR) &= \sum_{n=-\infty}^{\infty} \mathrm{j}^n \mathrm{J}_n(kR)\mathrm{e}^{\mathrm{j}n(\varphi-\varphi_\mathrm{i})} - \sum_{n=-N}^{N} \mathrm{j}^n \mathrm{J}_n(kR)\mathrm{e}^{\mathrm{j}n(\varphi-\varphi_\mathrm{i})} \\ &= \sum_{|n|>N} \mathrm{j}^n \mathrm{J}_n(kR)\mathrm{e}^{\mathrm{j}n(\varphi-\varphi_\mathrm{i})}. \end{aligned} \tag{3.15}$$

By analogy, the expression for circular apertures mounted on a rigid cylindrical baffle of infinite length is obtained

$$\begin{aligned}\mathcal{E}^{\bullet}_{\mathrm{t},n}(kR) &= \sum_{n=-\infty}^{\infty} \mathrm{j}^n \left(\mathrm{J}_n(kR) - \frac{\mathrm{J}'_n(kR)\mathrm{H}_n(kR)}{\mathrm{H}'_n(kR)}\right) \mathrm{e}^{\mathrm{j}n(\varphi-\varphi_\mathrm{i})} \\ &\quad - \sum_{n=-N}^{N} \mathrm{j}^n \left(\mathrm{J}_n(kR) - \frac{\mathrm{J}'_n(kR)\mathrm{H}_n(kR)}{\mathrm{H}'_n(kR)}\right) \mathrm{e}^{\mathrm{j}n(\varphi-\varphi_\mathrm{i})} \\ &= \sum_{|n|>N} \mathrm{j}^n \left(\mathrm{J}_n(kR) - \frac{\mathrm{J}'_n(kR)\mathrm{H}_n(kR)}{\mathrm{H}'_n(kR)}\right) \mathrm{e}^{\mathrm{j}n(\varphi-\varphi_\mathrm{i})}. \end{aligned} \tag{3.16}$$

According to [15], the mean square truncation error of an unbaffled circular aperture follows

$$\bar{\mathcal{E}}^{2\circ}_{\mathrm{t},n} = \frac{1}{2\pi}\int_0^{2\pi} \left| \sum_{|n|>N} \mathrm{j}^n \mathrm{J}_n(kR)\mathrm{e}^{\mathrm{j}n(\varphi-\varphi_\mathrm{i})} \right|^2 \mathrm{d}\varphi = 2\cdot \sum_{n=N+1}^{\infty} \mathrm{J}_n^2(kR). \tag{3.17}$$

For a circular aperture mounted on a cylindrical baffle of infinite length, it is given by

$$\begin{aligned}\bar{\mathcal{E}}^{2\bullet}_{\mathrm{t},n} &= \frac{1}{2\pi}\int_0^{2\pi} \left| \sum_{|n|>N} \mathrm{j}^n \left(\mathrm{J}_n(kR) - \frac{\mathrm{J}'_n(kR)\mathrm{H}_n(kR)}{\mathrm{H}'_n(kR)}\right) \mathrm{e}^{\mathrm{j}n(\varphi-\varphi_\mathrm{i})} \right|^2 \mathrm{d}\varphi \\ &= 2\cdot \sum_{n=N+1}^{\infty} \left(\mathrm{J}_n(kR) - \frac{\mathrm{J}'_n(kR)\mathrm{H}_n(kR)}{\mathrm{H}'_n(kR)}\right)^2. \end{aligned} \tag{3.18}$$

Figure 3.8 shows the magnitude of the truncation error for unbaffled circular apertures. As can be seen, at low spatial frequencies each order presents smaller error than at high frequencies. Besides, at low spatial frequencies the error is reduced when the number of orders taken into account increases. However, at the highest frequencies the truncation error becomes similar independently of the number of orders that are used.

For a fixed error, the results reveal that for low spatial frequencies a small number of orders can be used, whereas with increasing kR the number of orders used to achieve the same error has to be increased. This means that the sound field can be represented rather accurately with few harmonics at low spatial frequencies, whereas to represent it with the same accuracy at higher frequencies, the maximum order of harmonics needs to be increased.

According to the previous reasoning, it turns out that the sound field can be described

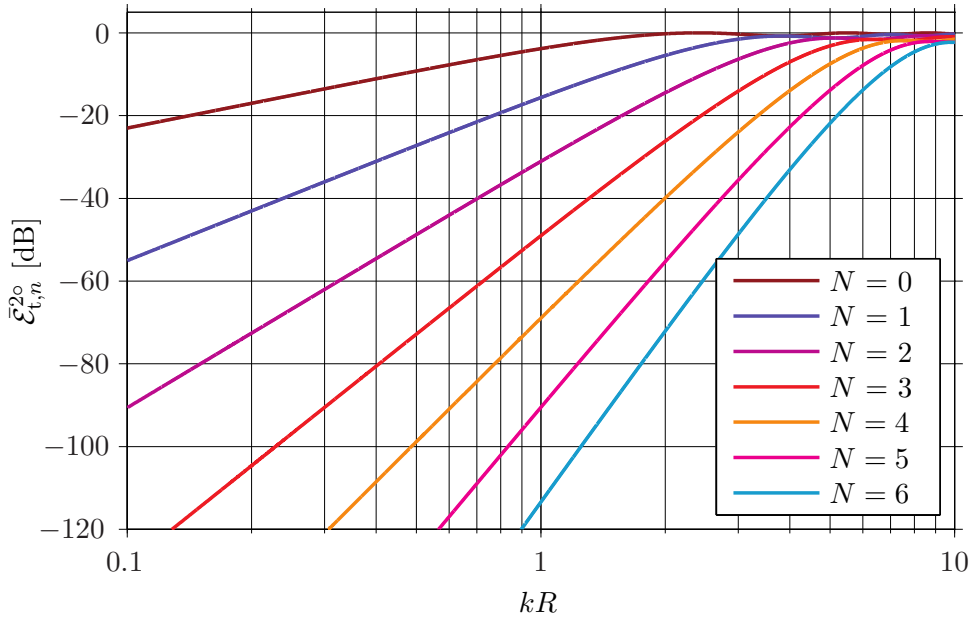

Figure 3.8: Sound field truncation error using unbaffled circular apertures.

rather accurately by choosing $N \approx kR$ [15, 18]. More specifically, N is chosen to be

$$N = \lceil kR \rceil \,, \tag{3.19}$$

where $\lceil \cdot \rceil$ is the ceiling function. The reason for this is that kR is the argument of the Bessel functions in the modal response (see equations (3.9) and (3.11)) and a Bessel function of order different from zero becomes very small when the order exceeds the argument.

For ease of understanding, an example is given in figure 3.9, where it is assumed that the spatial frequency of interest is $kR = 2$. At this point, the Bessel functions of orders 0, 1 and 2 present higher amplitude than the rest of orders. Even though higher orders than 4 are not shown in figure 3.9, their amplitudes get smaller with increasing order at $kR = 2$. Therefore, it is perhaps reasonable to neglect all the functions of order higher than 2.

3.4 Sound Field Decomposition using Circular Microphone Arrays – Sampling Error

So far, continuous circular apertures have been analyzed. However, for real-world applications one can only use microphone arrays instead of 'ideal' continuous apertures. This is done by sampling the aperture with microphones positioned at discrete points. It is assumed that the aperture is sampled with M omnidirectional microphones placed equidistantly. This procedure introduces an error due to sampling.

Considering that the maximum spatial frequency of interest is $k_{\max}R$, the spatial sampling frequency, $k_{\mathrm{s}}R$, must satisfy $k_{\mathrm{s}}R \geq 2k_{\max}R$. According to [18], this function

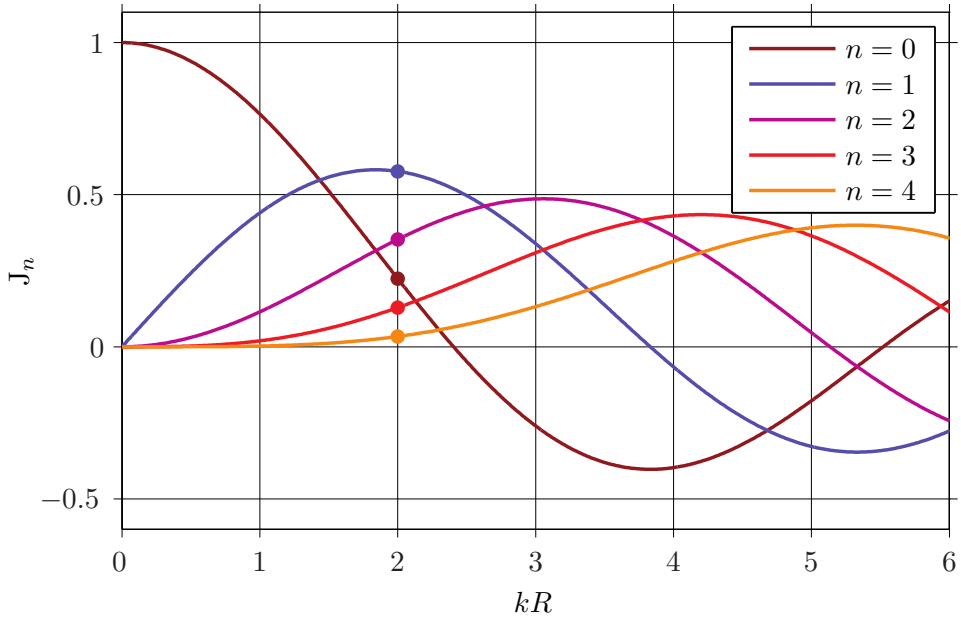

Figure 3.9: Magnitude of the Bessel functions, where the values at $kR = 2$ are highlighted with a dot. Up to order 2, these functions present significant amplitude, whereas for higher orders the amplitude can be neglected as it gets smaller.

is, in two-dimensions,

$$\begin{aligned} S(\varphi) &= \sum_{p=-\infty}^{\infty} \delta(\varphi - p\varphi_{\mathrm{si}}) \\ &= \frac{1}{\varphi_{\mathrm{si}}} \sum_{q=-\infty}^{\infty} \mathrm{e}^{\mathrm{j}qM\varphi} \\ &= \frac{1}{\varphi_{\mathrm{si}}} \left(1 + \sum_{q=1}^{\infty} \left(\mathrm{e}^{\mathrm{j}qM\varphi} + \mathrm{e}^{-\mathrm{j}qM\varphi} \right) \right), \end{aligned} \tag{3.20}$$

where the sampling interval along the circle, φ_{si}, is

$$\varphi_{\mathrm{si}} = \frac{\pi}{k_{\max} R}. \tag{3.21}$$

Applying the sampling function on the Fourier coefficients obtained with an unbaffled aperture (see equation (3.9)), the sampled coefficients become

$$\tilde{\mathcal{C}}_n^{\circ}(kR) = \underbrace{\mathrm{j}^n \mathrm{J}_n(kR) \mathrm{e}^{-\mathrm{j}n\varphi_{\mathrm{i}}}}_{\mathcal{C}_n^{\circ}(kR)} + \underbrace{\sum_{q=1}^{\infty} \left(\mathrm{j}^g \mathrm{J}_g(kR) \mathrm{e}^{\mathrm{j}g\varphi_{\mathrm{i}}} + \mathrm{j}^h \mathrm{J}_h(kR) \mathrm{e}^{-\mathrm{j}h\varphi_{\mathrm{i}}} \right)}_{\mathcal{C}_{\mathrm{e},n}^{\circ}(kR)}, \tag{3.22}$$

where $g = (Mq - n)$ and $h = (Mq + n)$. The tilde in $\tilde{\mathcal{C}}_n^{\circ}$ is used to emphasize that these coefficients are approximated by using microphone arrays instead of apertures. By analyzing the sampled coefficients, one can see that the first term corresponds to the

coefficients of an unbaffled circular aperture $\mathcal{C}_n^\circ$, whereas the second term gives the error due to sampling $\mathcal{C}_{\mathrm{e},n}^\circ$. The error, which is a series of Bessel functions, can be minimized recalling the idea that the Bessel functions become negligible when the order exceeds the argument. In this sense, if the smallest order has a negligible amplitude, it can be ensured that the rest of modes will have even smaller amplitude. This is satisfied when the smallest order, $M - n$ (when $q = 1$), exceeds the maximum argument; that is

$$M - n > \lceil k_{\max} R \rceil \,. \tag{3.23}$$

Since according to section 3.3, the maximum order should follow $N_{\max} = \lceil k_{\max} R \rceil$ in order to minimize the error due to truncation, n must be

$$n \leq N_{\max} = \lceil k_{\max} R \rceil \,. \tag{3.24}$$

Inserting the maximum value of n, i. e. $n = N_{\max} = \lceil k_{\max} R \rceil$, into equation (3.23) yields

$$\begin{aligned} M - N_{\max} &> \lceil k_{\max} R \rceil \quad \Leftrightarrow \\ M - \lceil k_{\max} R \rceil &> \lceil k_{\max} R \rceil \quad \Leftrightarrow \\ M &> 2 \lceil k_{\max} R \rceil \,. \end{aligned} \tag{3.25}$$

In conclusion, the sampling error is minimized when the number of microphones follows

$$M > 2 \lceil k_{\max} R \rceil \qquad \Leftrightarrow \qquad M > 2 N_{\max}. \tag{3.26}$$

This condition is satisfied when the distance between microphones along the arc of the circle is

$$\begin{aligned} d_{\mathrm{arc}} &= \frac{2\pi R}{M} \quad \Leftrightarrow \\ M &= \frac{2\pi R}{d_{\mathrm{arc}}} > 2 N_{\max} \quad \Leftrightarrow \\ d_{\mathrm{arc}} &< \frac{2\pi R}{2 N_{\max}} = \frac{2\pi R}{2 \lceil k_{\max} R \rceil} \quad \Leftrightarrow \\ d_{\mathrm{arc}} &< \frac{2\pi R}{2 k_{\max} R} \Leftrightarrow \\ d_{\mathrm{arc}} &< \frac{\lambda_{\min}}{2}. \end{aligned} \tag{3.27}$$

By analogy, the sampled coefficients obtained with a circular array mounted on baffle

of infinite length are given by

$$\begin{aligned}\tilde{\mathcal{C}}_n^{\bullet}(kR) = \mathrm{j}^n \left(\mathrm{J}_n(kR) - \frac{\mathrm{J}'_n(kR)\mathrm{H}_n(kR)}{\mathrm{H}'_n(kR)}\right) \mathrm{e}^{-\mathrm{j}n\varphi_\mathrm{i}} \\ + \sum_{q=1}^{\infty} \mathrm{j}^g \left(\mathrm{J}_g(kR) - \frac{\mathrm{J}'_g(kR)\mathrm{H}_g(kR)}{\mathrm{H}'_g(kR)}\right) \mathrm{e}^{\mathrm{j}g\varphi_\mathrm{i}} \\ + \sum_{q=1}^{\infty} \mathrm{j}^h \left(\mathrm{J}_h(kR) - \frac{\mathrm{J}'_h(kR)\mathrm{H}_h(kR)}{\mathrm{H}'_h(kR)}\right) \mathrm{e}^{-\mathrm{j}h\varphi_\mathrm{i}},\end{aligned} \tag{3.28}$$

where the first term corresponds to the Fourier coefficients of an aperture mounted on an infinite baffle, and the second and third terms are the error due to the sampling operation,

$$\begin{aligned}\mathcal{C}_{\mathrm{e},n}^{\bullet}(kR) = \sum_{q=1}^{\infty} \mathrm{j}^g \left(\mathrm{J}_g(kR) - \frac{\mathrm{J}'_g(kR)\mathrm{H}_g(kR)}{\mathrm{H}'_g(kR)}\right) \mathrm{e}^{\mathrm{j}g\varphi_\mathrm{i}} \\ + \sum_{q=1}^{\infty} \mathrm{j}^h \left(\mathrm{J}_h(kR) - \frac{\mathrm{J}'_h(kR)\mathrm{H}_h(kR)}{\mathrm{H}'_h(kR)}\right) \mathrm{e}^{-\mathrm{j}h\varphi_\mathrm{i}}.\end{aligned} \tag{3.29}$$

In figure 3.11, the first six theoretical coefficients of an unbaffled aperture are compared to the approximated coefficients obtained with an unbaffled array of 12 microphones. As can be seen, the theoretical coefficients and the approximated ones are identical, for each order, in almost the entire spatial frequency range. Just at the higher values of kR, deviations between them are observed, which are caused by the sampling error. In fact, the error is present at a lower value of kR with increasing order, which agrees with equation (3.23). Therefore, the most restrictive case is found for the highest order shown, $n = 5$, where the error appears at about $kR = 5$, see panel (f). This is indeed what we expect from equation (3.26). In this equation the maximum value kR that can be represented without having sampling error is related to the number of microphones. In the present case, M is 12, then, $\lceil k_{\max}R \rceil < 12/2$, and hence $k_{\max}R$=5. According to equation (3.19), this also means that the sound field can be represented very accurately up to order 5, i. e. $N_{\max} = 5$. In contrast with this, when the order of the coefficients exceeds $N_{\max}$, the approximated coefficients do not match the theoretical ones due to the sampling error. This is illustrated in figure 3.11, for $n = 6$ and $n = 7$.

To sum up, the sound field decomposed with a circular array of M microphones is very similar to the decomposition that would be obtained with an aperture of the same radius, up to a maximum spatial frequency $\lceil k_{\max}R \rceil < M/2$. Above this value, sampling error occurs. Furthermore, the maximum order that can be represented accurately follows $N_{\max} = \lceil k_{\max}R \rceil$.

The foregoing ideas can also be examined by means of the relative error due to the sampling process. This is defined as [15]

$$\mathcal{E}_{\mathrm{s},n}(kR) = \left| \frac{\mathcal{C}_{\mathrm{e},n}(kR)}{\tilde{\mathcal{C}}_n(kR)} \right|^2. \tag{3.30}$$

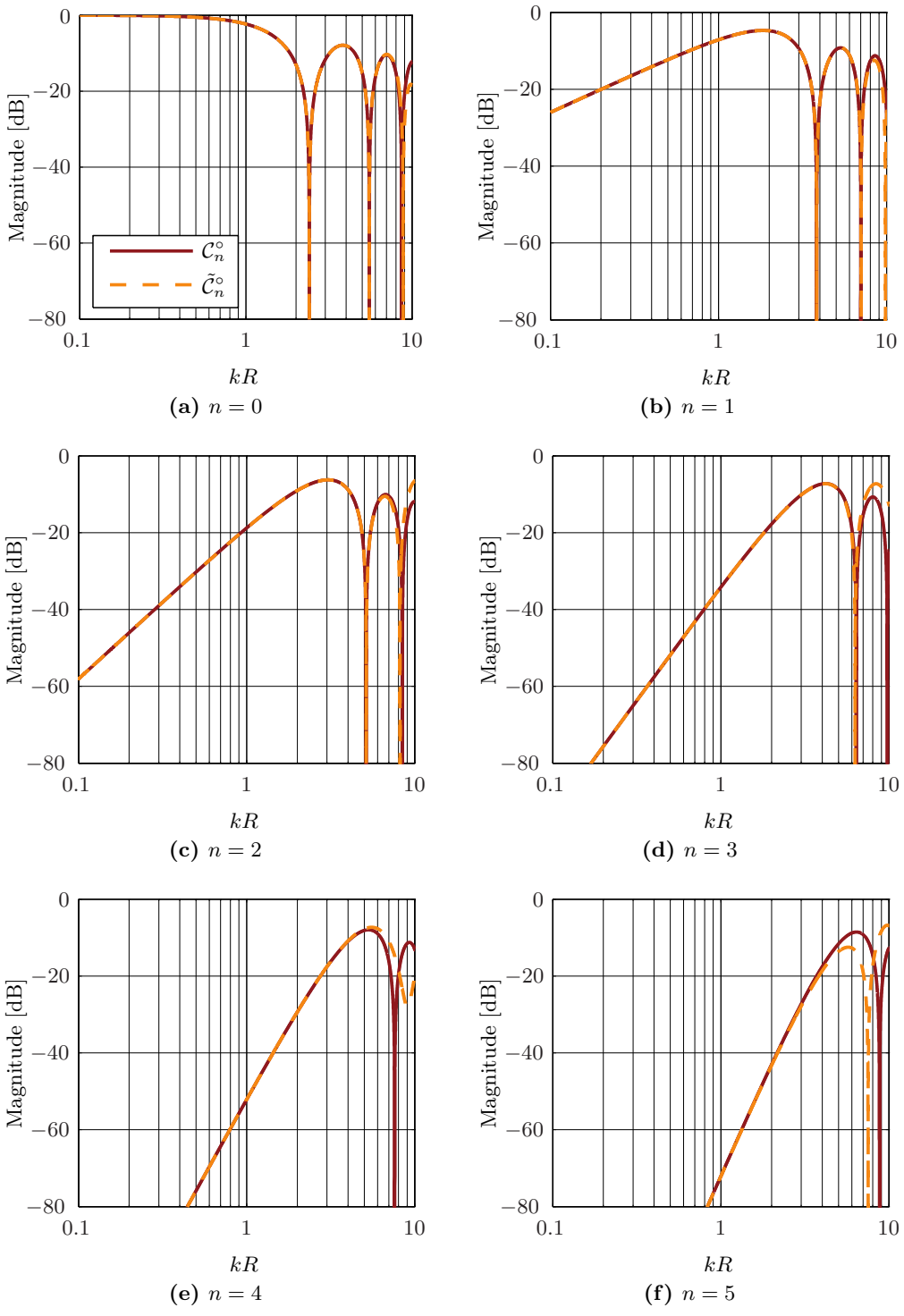

(a) $n = 0$ **(b)** $n = 1$

(c) $n = 2$ **(d)** $n = 3$

(e) $n = 4$ **(f)** $n = 5$

Figure 3.10: Comparison between the theoretical coefficients of an unbaffled aperture, $\mathcal{C}_n^\circ$, and the approximated coefficients, $\tilde{\mathcal{C}}_n^\circ$, that result from sampling the aperture with an array of 12 microphones. The first six orders are shown, i. e. $n = 0$ to 5. The theoretical coefficients correspond to the maroon-continuous lines, whereas the approximated ones correspond to the orange-dashed lines.

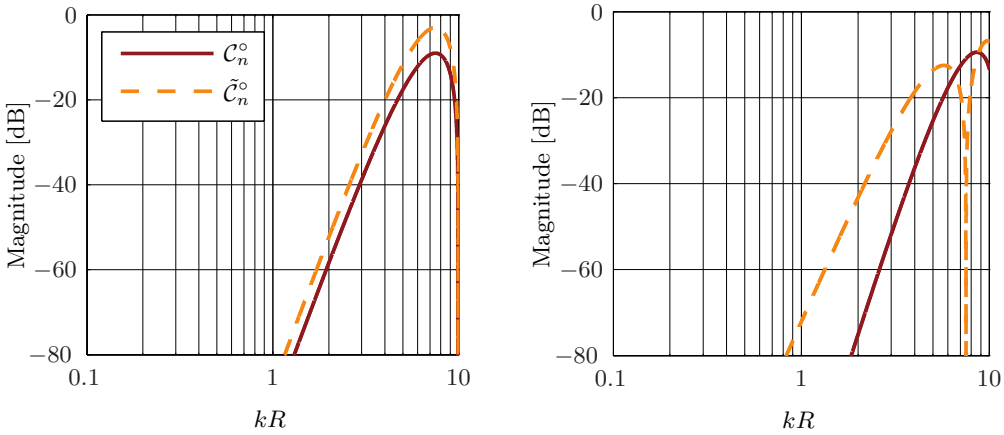

(a) $n = 6$ **(b)** $n = 7$

Figure 3.11: Comparison between the theoretical coefficients of an unbaffled aperture, $\mathcal{C}_n^\circ$, and the approximated coefficients, $\tilde{\mathcal{C}}_n^\circ$, that result from sampling the aperture with an array of 12 microphones. Orders 6 and 7 are shown as these are the first two orders where the sampling error is visible in all the frequency range. The theoretical coefficients correspond to the maroon-continuous lines, whereas the approximated ones correspond to the orange-dashed lines.

This is shown in figure 3.12 for two unbaffled circular arrays with the same radius, one conformed by 12 microphones and the other one by 15. The maximum order that can be used in order to minimize the error is, according to equation (3.26), $N_{\max} = 5$ for 12 microphones and $N_{\max} = 7$ for 15 microphones. As can be seen, independently of the number of microphones, for a particular order the error increases with increasing values of kR. Besides, it also increases with increasing order. When the number of microphones is increased, the error is lower for all orders in comparison with the array with smaller number of microphones. This is due to the fact that using more and more microphones the array becomes more similar to the case of a continuous circular aperture, and therefore, the distortion caused by the sampling process is reduced.

At high spatial frequencies, all modes present severe error. In order to avoid this as much as possible, the maximum value of spatial frequency that should be taken into account must fulfill the condition $N = \lceil kR \rceil$, according to equation (3.19). This value is $k_{\max}R = 5$ in the case of 12 microphones and $k_{\max}R = 7$ for 15 microphones.

The peaks that can be seen at high spatial frequencies are due to the unresolved frequencies found in the calculation of the Fourier coefficients using an unbaffled circular aperture (see figure 3.3). These would be avoided if the array were mounted on a cylindrical baffle of infinite length. Even though this case is not shown here, the overall behavior of the error in terms of kR and number of microphones has the same tendency that has been found for the unbaffled array.

When higher orders than the maximum allowed $N_{\max}$ are taken, a constant and severe error appears along all values $kR \leq N_{\max}$. The error becomes even higher (and peaky) at higher spatial frequencies due to the unresolved frequencies, since the array is unbaffled. This is illustrated in figure 3.13 where the relative error due to sampling using the array of 12 microphones is given for several orders higher than $N_{\max}$. As can

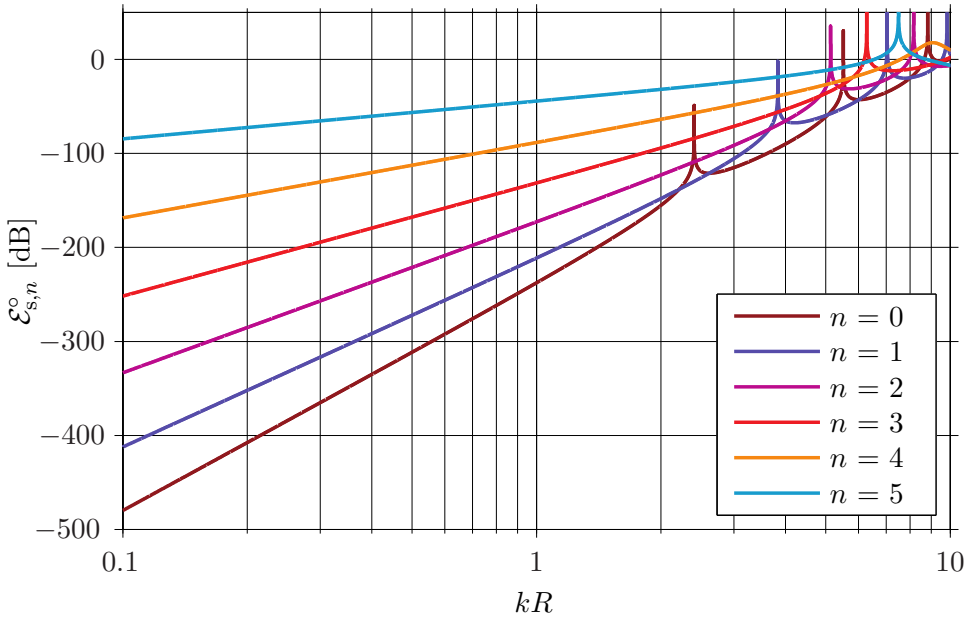

(a) Using 12 microphones.

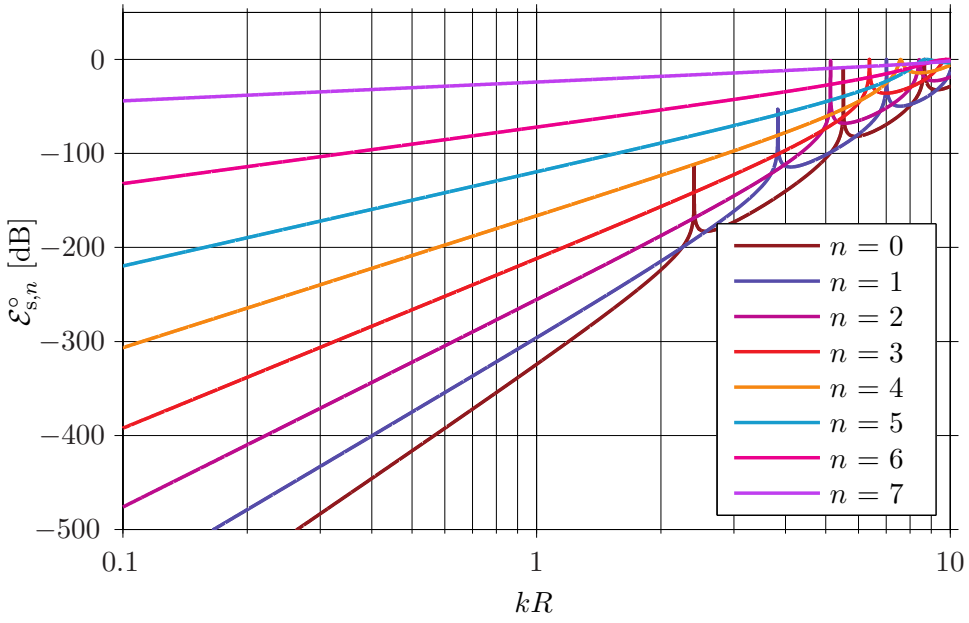

(b) Using 15 microphones.

Figure 3.12: Relative error due to sampling an unbaffled circular aperture using 12 or 15 microphones when $\varphi_{\mathrm{i}} = 0$.

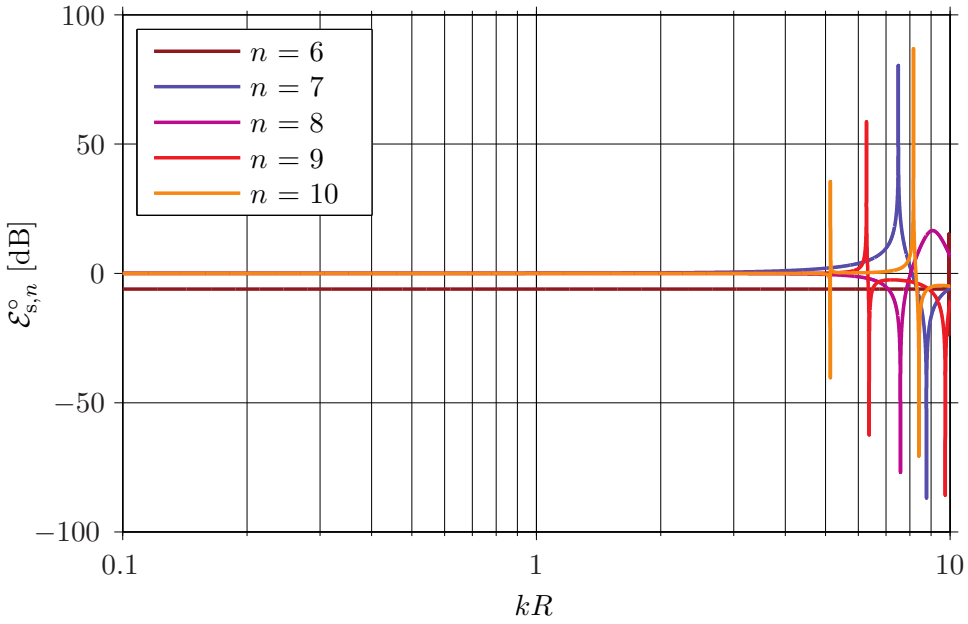

Figure 3.13: Relative error due to sampling an unbaffled circular aperture using an unbaffled array with 12 microphones, for $n > N_{\max}$ where $N_{\max} = \lceil k_{\max} R \rceil < M/2$.

be seen, at $kR \leq 5$ the error is constant and equals -6 dB for $n = 6$ and 0 dB for $n > 6$. This behavior can be deduced from equations (3.22) and (3.30). For example, for $n = 6$,

$$\begin{aligned}
\mathcal{C}^{\circ}_{\mathrm{e},6} &= \sum_{q=1}^{\infty} \left(\mathrm{j}^{(12q-6)} \mathrm{J}_{(12q-6)}(kR) \mathrm{e}^{\mathrm{j}(12q-6)\varphi_{\mathrm{i}}} + \mathrm{j}^{(12q+6)} \mathrm{J}_{(12q+6)}(kR) \mathrm{e}^{-\mathrm{j}(12q+6)\varphi_{\mathrm{i}}} \right) \\
&= \mathrm{j}^{(12-6)} \mathrm{J}_{(12-6)}(kR) \mathrm{e}^{\mathrm{j}(12-6)\varphi_{\mathrm{i}}} + \mathrm{j}^{(2\cdot 12-6)} \mathrm{J}_{(2\cdot 12-6)}(kR) \mathrm{e}^{\mathrm{j}(2\cdot 12-6)\varphi_{\mathrm{i}}} \\
&+ \mathrm{j}^{(3\cdot 12-6)} \mathrm{J}_{(3\cdot 12-6)}(kR) \mathrm{e}^{\mathrm{j}(3\cdot 12-6)\varphi_{\mathrm{i}}} + \ldots \\
&+ \mathrm{j}^{(12+6)} \mathrm{J}_{(12+6)}(kR) \mathrm{e}^{\mathrm{j}(12+6)\varphi_{\mathrm{i}}} + \mathrm{j}^{(2\cdot 12+6)} \mathrm{J}_{(2\cdot 12-6)}(kR) \mathrm{e}^{\mathrm{j}(2\cdot 12+6)\varphi_{\mathrm{i}}} \\
&+ \mathrm{j}^{(3\cdot 12+6)} \mathrm{J}_{(3\cdot 12+6)}(kR) \mathrm{e}^{\mathrm{j}(3\cdot 12+6)\varphi_{\mathrm{i}}} + \ldots
\end{aligned} \tag{3.31}$$

Taking into account the condition given in equation (3.19), all the arguments that follow $kR \leq N_{\max} = 5$ will vanish. Only the first term in equation (3.31) presents a Bessel function of order comparable to the argument, whereas all the other terms can be neglected. Then, equation (3.31) is, approximately

$$\mathcal{C}^{\circ}_{\mathrm{e},6} \approx \mathrm{j}^{6} \mathrm{J}_{6}(kR) \mathrm{e}^{\mathrm{j}6\varphi_{\mathrm{i}}}. \tag{3.32}$$

Inserting this relationship into equation (3.22) the Fourier coefficient is, for $n = 6$,

$$\begin{aligned}
\mathcal{C}^{\circ}_{\mathrm{s},6}(kR) &= \mathcal{C}^{\circ}_{6}(kR) + \mathcal{C}^{\circ}_{\mathrm{e},6}(kR) \\
&\approx \mathrm{j}^{6} \mathrm{J}_{6}(kR) \mathrm{e}^{-\mathrm{j}6\varphi_{\mathrm{i}}} + \mathrm{j}^{6} \mathrm{J}_{6}(kR) \mathrm{e}^{\mathrm{j}6\varphi_{\mathrm{i}}} \\
&\approx 2\mathrm{j}^{7} \mathrm{J}_{6}(kR) \cos(6\varphi_{\mathrm{i}}).
\end{aligned} \tag{3.33}$$

Finally, the relative error follows

$$\mathcal{E}^{\circ}_{\mathrm{s},6}(kR) = \frac{|\mathcal{C}_{\mathrm{e},6}(kR)|^2}{|\mathcal{C}_{\mathrm{s},6}(kR)|^2} \approx \frac{\left|\mathrm{j}^6 \mathrm{J}_6(kR)\mathrm{e}^{\mathrm{j}6\varphi_\mathrm{i}}\right|^2}{|2\mathrm{j}^7 \mathrm{J}_6(kR)\cos(6\varphi_\mathrm{i})|^2} \approx \frac{1}{4\cos^2(6\varphi_\mathrm{i})}. \tag{3.34}$$

This result reveals that the error is constant for all values of kR when $M = 12$ and $n = 6$. If $\varphi_\mathrm{i} = 0$, $\mathcal{E}^{\circ}_{\mathrm{s},6}(kR) = -6$ dB as seen in panel (a) of figure 3.13. The errors for $n > 6$ can be derived using the same procedure. In these cases, it can be proved that the error equals 0 dB and is independent of the angle φ_i.

4

Beamforming Techniques

4.1 Introduction

Two beamforming techniques used to localize sound in two dimensions by means of circular arrays are derived in this chapter. The first one is a novel technique that is referred to as Circular Harmonics beamforming (CHB). This is a technique that can be included in the so-called Eigenbeamforming techniques, which are based on the decomposition of the sound field in series of harmonics. The second technique is called Delay-and-Sum beamforming (DSB) and is considered the 'classical' beamforming technique.

These techniques are implemented for circular arrays in two different cases, when they are mounted on cylindrical baffles of infinite length and when they are unbaffled.

Before focusing on the details of each technique, it is convenient to give a theoretical background in which circular apertures are considered as a first approach, and real circular arrays are derived afterwards.

4.2 Theoretical Basis

The sound pressure on a circular aperture of radius R can be expanded into a series of CH, $\mathrm{e}^{\mathrm{j}n\varphi}$, using the principles of the Fourier Series given in section 3.1,

$$p(kR,\varphi) = \sum_{n=-\infty}^{\infty} \mathcal{C}_n(kR)\mathrm{e}^{\mathrm{j}n\varphi}, \tag{4.1}$$

where

$$\mathcal{C}_n(kR) = \frac{1}{2\pi}\int_0^{2\pi} p(kR,\varphi)\mathrm{e}^{-\mathrm{j}n\varphi}\mathrm{d}\varphi. \tag{4.2}$$

Assuming that the pressure at each point of the circular aperture is due to a source

in the far-field, the waves that impinge on the aperture can be considered to be planar [15]. Under these circumstances, the Fourier coefficients follow the expressions given in equations (3.9) on page 17 and (3.13) on page 20, for unbaffled apertures and for apertures mounted on a rigid cylindrical baffle of infinite length, respectively.

It is convenient to define the general expression for the coefficients

$$\mathcal{C}_n(kR) = P_0 R_n(kR) \mathrm{e}^{-\mathrm{j}n\varphi_\mathrm{i}}, \tag{4.3}$$

where R_n is given by

$$R_n(kR) = \begin{cases} \mathrm{j}^n \mathrm{J}_n(kR) & \text{if unbaffled,} \\ \mathrm{j}^n \left(\mathrm{J}_n(kR) - \dfrac{\mathrm{J}'_n(kR)\mathrm{H}_n(kR)}{\mathrm{H}'_n(kR)} \right) & \text{if infinitely-long baffle.} \end{cases} \tag{4.4}$$

Using equations (4.1) and (4.3) the sound pressure at each point of the aperture can be rewritten as

$$p(kR, \varphi) = P_0 \sum_{n=-\infty}^{\infty} R_n(kR) \mathrm{e}^{\mathrm{j}n(\varphi - \varphi_\mathrm{i})}. \tag{4.5}$$

As in real-world implementations it is not feasible to use apertures, the circular aperture must be sampled with an array of M of microphones. Therefore, the pressure is only known at the microphones position. The Fourier coefficients given in equation (4.2) are then approximated by

$$\tilde{\mathcal{C}}_n(kR) = \sum_{m=1}^{M} a_m p(kR, \varphi_m) \mathrm{e}^{-\mathrm{j}n\varphi_m}, \tag{4.6}$$

where the coefficients a_m provide the closest values to the real integration of equation (4.2) and φ_m are the angles on the xy-plane of the microphone positions. The a_m coefficients can be obtained by applying the condition of orthogonality of the CH similarly to equation (3.4)

$$\sum_{m=0}^{M} a_m \mathrm{e}^{\mathrm{j}n\varphi_m} (\mathrm{e}^{\mathrm{j}\nu\varphi_m})^* \approx \delta_{n\nu}. \tag{4.7}$$

This equation is verified when a_m equal $1/M$.

Obviously, the approximated coefficients obtained with equation (4.6) coincide with the analytical expressions given in section 3.4 that followed from sampling apertures with microphone arrays. This is illustrated in figure 4.1, where the first four coefficients obtained with an unbaffled array of 12 microphones are shown. The maroon-continuous curves result from applying equation (3.22) given on page 25, whereas the orange-dashed curves are given by equation (4.6).

The differences between the approximated coefficients and the ones that would be obtained with an unbaffled aperture can be seen in figure 3.11 on page 29.

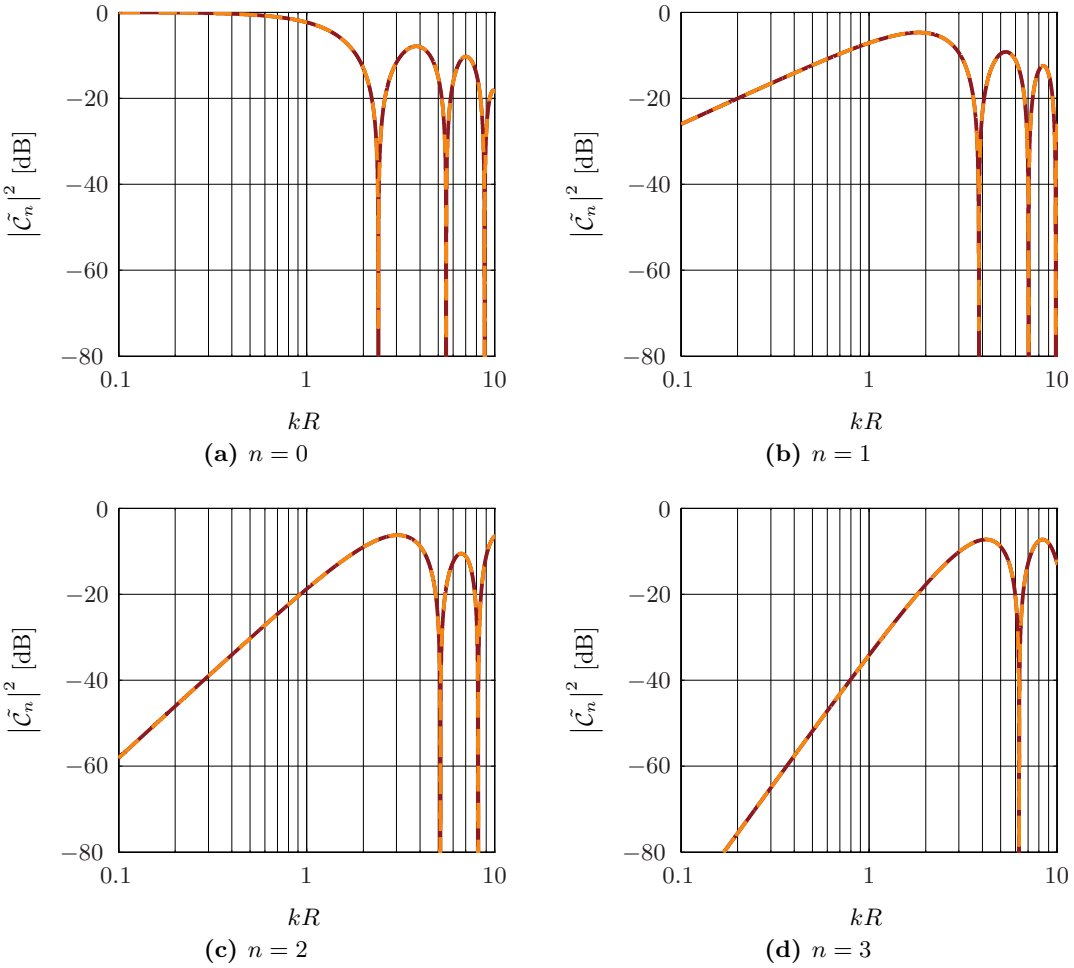

(a) $n = 0$ **(b)** $n = 1$

(c) $n = 2$ **(d)** $n = 3$

Figure 4.1: Approximated Fourier coefficients obtained by decomposing the sound field with an unbaffled circular array of 12 microphones. The maroon-continuous curves result from applying equation (3.22) given on page 25, whereas the orange-dashed curves are given by equation (4.6).

The sound pressure in each microphone of the array is, according to equation (4.5),

$$p(kR, \varphi_m) = P_0 \sum_{n=-N}^{N} R_n(kR) \mathrm{e}^{\mathrm{j}n(\varphi_m - \varphi_\mathrm{i})}. \tag{4.8}$$

Recall that the number of modes must be truncated up to a finite number N, and this introduces some error. In section 3.3 on page 22, it was shown that this error is minimized when $N = \lceil kR \rceil$. Besides, according to section 3.4, the number of microphones must follow $M > 2N$, in order to minimize the error that the sampling procedure introduces.

4.3 Circular Harmonics Beamforming

The beamformer response describes the output of the beamformer as a function of the steering angle, i. e. the angle in which the main beam of the beamformer is 'pointing out'. Ideally, the beamformer response obtained by means of a circular array provides a maximum value only when the beamformer is steered towards the position of the source φ_s, and zero in all other directions; that is

$$b_\mathrm{ideal}(\varphi) = A\delta(\varphi - \varphi_\mathrm{s}), \tag{4.9}$$

where A is a scale factor. On the other hand, the beamformer output can be described by means of CH using the principles of the Fourier series

$$b_\mathrm{ideal}(\varphi) = \sum_{n=-\infty}^{\infty} \mathcal{I}_n \mathrm{e}^{\mathrm{j}n\varphi}, \tag{4.10}$$

where $\mathcal{I}_n$ are the Fourier coefficients of the ideal beamformer due to a source located at φ_s. These are given by

$$\begin{aligned}
\mathcal{I}_n &= \frac{1}{2\pi}\int_0^{2\pi} b_\mathrm{ideal}(\varphi)\mathrm{e}^{-\mathrm{j}n\varphi}\mathrm{d}\varphi \\
&= \frac{1}{2\pi}\int_0^{2\pi} A\delta(\varphi-\varphi_\mathrm{s})\mathrm{e}^{-\mathrm{j}n\varphi}\mathrm{d}\varphi \\
&= \frac{1}{2\pi}\int_0^{2\pi} A\delta(\varphi-\varphi_\mathrm{s})\mathrm{e}^{-\mathrm{j}n\varphi_\mathrm{s}}\mathrm{d}\varphi \\
&= A\mathrm{e}^{-\mathrm{j}n\varphi_\mathrm{s}}.
\end{aligned} \tag{4.11}$$

Inserting equation (4.11) into equation (4.10) yields

$$b_\mathrm{ideal}(\varphi) = A\sum_{n=-\infty}^{\infty} \mathrm{e}^{-\mathrm{j}n\varphi_\mathrm{s}}\mathrm{e}^{\mathrm{j}n\varphi}. \tag{4.12}$$

From equation (4.3) we have

$$\mathrm{e}^{-\mathrm{j}n\varphi_\mathrm{i}} = \frac{\mathcal{C}_n(kR)}{P_0 R_n(kR)}. \tag{4.13}$$

Applying the relationship between the angle of the impinging waves and the angle of the source, $\varphi_\mathrm{i} = \varphi_\mathrm{s} + \pi$, into equation (4.13)

$$\mathrm{e}^{-\mathrm{j}n\varphi_\mathrm{s}} = \frac{\mathcal{C}_n(kR)}{(-1)^n P_0 R_n(kR)}. \tag{4.14}$$

Using the latter expression, the output of the ideal beamformer yields

$$b_\mathrm{ideal}(kR,\varphi) = A\sum_{n=-\infty}^{\infty} \frac{\mathcal{C}_n(kR)}{(-1)^n P_0 R_n(kR)}\mathrm{e}^{\mathrm{j}n\varphi}. \tag{4.15}$$

However, for real-life implementations, the number of modes used must be truncated at a reasonable value N and the aperture must be sampled by a number of microphones M. This implies that the coefficients $\mathcal{C}_n$ must be approximated by the values $\tilde{\mathcal{C}}_n$

$$b_{N,\mathrm{CH}}(kR,\varphi) = A \sum_{n=-N}^{N} \frac{\tilde{\mathcal{C}}_n(kR)}{(-1)^n P_0 R_n(kR)} \mathrm{e}^{\mathrm{j}n\varphi}. \tag{4.16}$$

Further analysis of this expression reveals that

$$b_{N,\mathrm{CH}}(kR,\varphi) = A \sum_{n=-N}^{N} \frac{\tilde{\mathcal{C}}_n(kR)}{(-1)^n P_0 R_n(kR) \mathrm{e}^{-\mathrm{j}n\varphi}}, \tag{4.17}$$

so the term that divides $\tilde{\mathcal{C}}_n$ is, according to equation (4.3), a coefficient $\mathcal{C}_n$ obtained when the sound field created by a source located at φ is decomposed with a circular aperture

$$\mathcal{C}_n(kR,\varphi) = (-1)^n P_0 R_n(kR) \mathrm{e}^{-\mathrm{j}n\varphi}. \tag{4.18}$$

In this equation, the argument φ in $\mathcal{C}_n(kR,\varphi)$ is used to emphasize that the coefficients depend on φ. Therefore, the output of the beamformer can be rewritten as

$$b_{N,\mathrm{CH}}(kR,\varphi) = A \sum_{n=-N}^{N} \frac{\tilde{\mathcal{C}}_n(kR,\varphi_\mathrm{s})}{\mathcal{C}_n(kR,\varphi)}, \tag{4.19}$$

where the argument of the approximated coefficients $\tilde{\mathcal{C}}_n$ is used to recall that they are obtained by decomposing the sound pressure created by a source located at φ_s. Then, the output of the beamformer is maximum when φ equals φ_s as the quotient in the latter equation approximates unity. Note that, when using unbaffled apertures, the latter equation yields a singularity at those frequencies where the Fourier coefficients present dips, see figure 3.3 on page 18. Hence, in such frequencies the CH beamformer is not capable to resolve the location of the source properly.

Inserting the approximated coefficients given in equation (4.6) into equation (4.16), the final implementation of a CH beamformer follows

$$b_{N,\mathrm{CH}}(kR,\varphi) = \frac{A}{P_0} \sum_{m=1}^{M} p(kR,\varphi_m) \sum_{n=-N}^{N} \frac{1}{(-1)^n R_n(kR)} \mathrm{e}^{-\mathrm{j}n(\varphi_m-\varphi)}. \tag{4.20}$$

Ideally, the output is expected to be zero for all the angles different from φ_s. However, due to the fact that a limited number of microphones is used and the number of modes is truncated, the response presents a main lobe around $\varphi = \varphi_\mathrm{s}$ and side lobes (or secondary lobes) in the rest of angles.

The maximum number of orders used for the CHB algorithm will follow $N = \lceil kR \rceil$, according to equation (3.19) on page 24. This feature will be further analyzed in section 5.3.2.

For clarity sake, some examples are given for a CH beamformer using an unbaffled circular array of radius 11.9 cm with $M = 12$ microphones. As a first step, it is considered that a plane wave with frequency 1.5 kHz created by a source at 180° impinges on

the array. The signal captured by the array is considered to be ideal, meaning that it is not contaminated with background noise. According to equation (3.26) on page 26, the maximum number of orders that can be used with this array is 5, so the maximum frequency that the array can capture without significant error is about 2.3 kHz. When the beamformer is tuned at 1.5 kHz the output shown in figure 4.2 is obtained. Note that the number of harmonics used for this frequency is 4, as

$$N = \lceil kR \rceil = \left\lceil \frac{2\pi f}{c} \cdot R \right\rceil = \left\lceil \frac{2\pi \cdot 1.5 \cdot 10^3}{343} \cdot 11.9 \cdot 10^{-2} \right\rceil = \lceil 3.27 \rceil = 4. \tag{4.21}$$

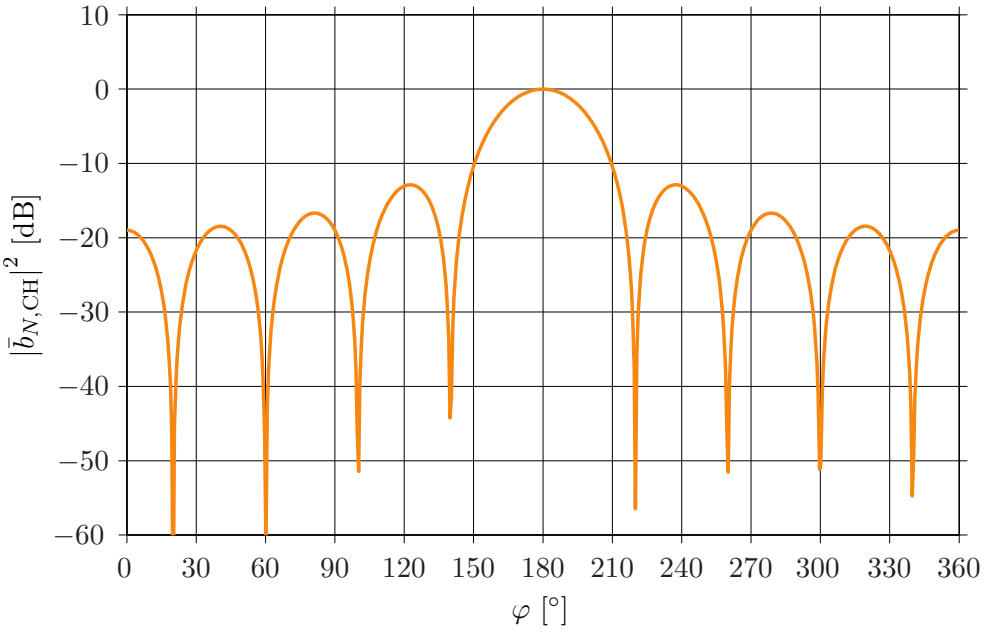

Figure 4.2: Magnitude of the normalized output of the CH beamformer tuned at 1.5 kHz. The maximum order used for this frequency is $N = 4$. The array used is an unbaffled circular array with radius 11.9 cm.

As can be seen, the magnitude of the normalized beamformer output, $\bar{b}_{N,\mathrm{CH}}$, presents a main lobe around $\varphi = 180°$, meaning that the source is localized. The presence of the side lobes around the main lobe can be interpreted as waves from various sources located at different directions from the real source (at φ_s) that impinge on the array. These sources do not exist in reality, and for this reason they are called 'ghost sources'. This is one of the main problems of beamforming techniques.

Now, a source presenting a broadband spectrum is assumed to be located at 0° in the far-field with respect to the array of the previous example. The normalized beamformer output at four different frequencies is shown in polar diagrams in figure 4.3. The maximum order N used in each case is stated in the caption of each panel.

As can be seen, tuning the beamformer at different frequencies, the output always presents a main lobe around 0°, and therefore, the location of the source is recognized independently of the frequency. However, the pattern of the beamformer varies with frequency. At 100 Hz a broad main lobe and just one side lobe can be observed, whereas

for higher frequencies the main lobe gets narrower and more side lobes appear. At first glance, the total number of lobes (or maxima) and the number of minima between lobes seems to be related to the maximum order N. Indeed, the number of lobes is in all cases twice the maximum order used for a particular frequency. In chapter 5, this relationship will be further analyzed through simulations.

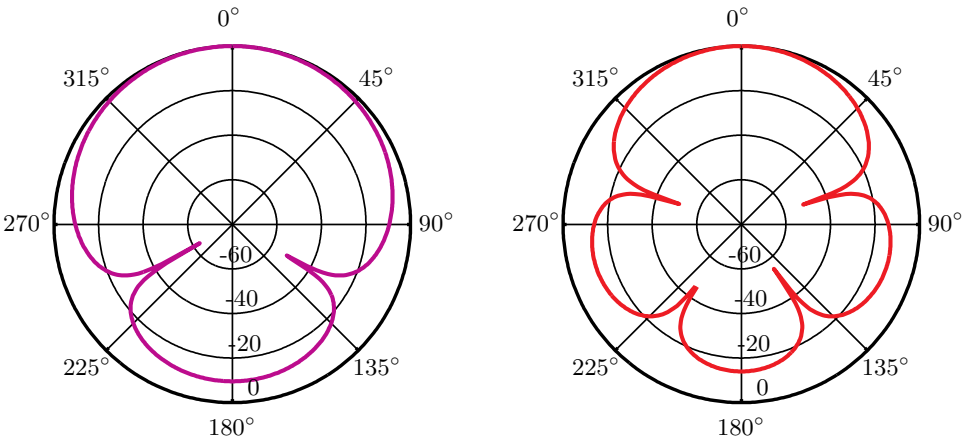

(a) $f = 100$ Hz; $N = 1$.

(b) $f = 500$ Hz; $N = 2$.

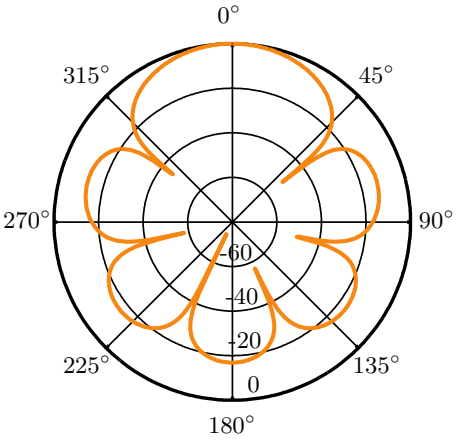

(c) $f = 1000$ Hz; $N = 3$.

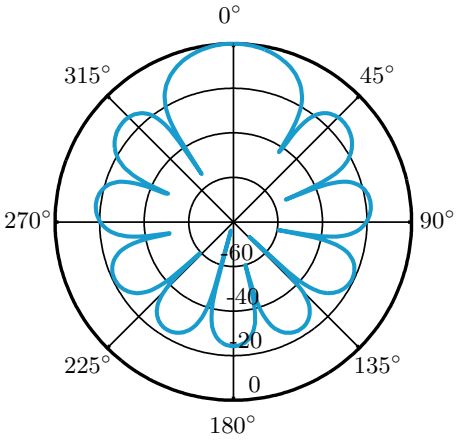

(d) $f = 2000$ Hz; $N = 5$.

Figure 4.3: Magnitude in dB of the normalized output of the CH beamformer at four different frequencies, when an unbaffled circular array with radius 11.9 cm is used. The maximum order used for the processing is given below each response. All the outputs detect the presence of a source placed at 0°.

4.4 Delay-and-Sum Beamforming

The beamforming response of an ideal Delay-and-Sum (DS) beamformer provides maximum output when the beamformer points towards the direction of the source and zero otherwise, as in the case of the CHB.

This technique takes the set of signals captured by the microphones of the array, delays them and finally adds them together. The value of the delays is determined by

the steering direction of the array [3, 4, 19]. The DS beamformer output is maximum when the focusing direction coincides with the position of the source.

For simplicity, in the present project the DSB is implemented in the frequency domain, using matched field processing [8, 20]. This method uses phase shifts to align all signal components in phase. Instead of time delays, phase shifts between microphones are obtained by focusing the array to a certain direction. Then, the opposite phase shifts are applied to the microphones signals and finally, all the signals are added up. The maximum output is achieved when the wave propagates from the steered direction.

Assuming the beamformer is steered towards the source direction φ_s, the beamformer output is

$$b_{N,\mathrm{DS}}(kR,\varphi_\mathrm{s}) = A\sum_{m=1}^{M} w_m \underbrace{p(kR,\varphi_m)}_{\text{measured}}\underbrace{p^*(kR,\varphi_m)}_{\text{theoretical}}, \tag{4.22}$$

where A is a scaling factor, w_m is the weighting coefficient of the m'th microphone, $p(kR,\varphi_m)$ is the pressure captured at each microphone position due to a plane wave created by a source at φ_s, and $p^*(kR,\varphi_m)$ is equal in magnitude than $p(kR,\varphi_m)$ but with the phase shifted. As the array is steered towards the source direction, $p(kR,\varphi_m)$ and $p^*(kR,\varphi_m)$ are equal in magnitude but have opposite phase, and hence, when all components are added the beamformer response becomes maximum. The key point is that the first term in equation (4.22) is the 'real' signal that the microphones capture, whereas the second term is the theoretical pressure that would be captured having a source at φ_s. This is defined according to equation (4.8) but using the angle of the source instead of the angle of the incident wave, $\varphi_\mathrm{s} = \varphi_\mathrm{i} - \pi$,

$$\begin{aligned} p(kR,\varphi_m) &= P_0 \sum_{n=-N}^{N} R_n(kR)\mathrm{e}^{\mathrm{j}n(\varphi_m-\varphi_\mathrm{s}+\pi)} \\ &= P_0 \sum_{n=-N}^{N} (-1)^n R_n(kR)\mathrm{e}^{\mathrm{j}n(\varphi_m-\varphi_\mathrm{s})}. \end{aligned} \tag{4.23}$$

Introducing the latter expression into equation (4.22), the beamformer output results in

$$b_{N,\mathrm{DS}}(kR,\varphi_\mathrm{s}) = AP_0\sum_{m=1}^{M} p(kR,\varphi_m)\sum_{n=-N}^{N}(-1)^n R_n^*(kR)\mathrm{e}^{-\mathrm{j}n(\varphi_m-\varphi_\mathrm{s})}, \tag{4.24}$$

when the beamformer is steered towards the source position. Note that the weights w_m have been set to 1 as all microphones have equal 'importance'.

In general, the source position is unknown, and therefore the beamformer must map over all possible source positions, i. e. $0 \le \varphi \le 2\pi$. The general expression is then given by

$$b_{N,\mathrm{DS}}(kR,\varphi) = AP_0\sum_{m=1}^{M} p(kR,\varphi_m)\sum_{n=-N}^{N}(-1)^n R_n^*(kR)\mathrm{e}^{-\mathrm{j}n(\varphi_m-\varphi)}. \tag{4.25}$$

As mentioned previously, the maximum output is reached when the beamformer focuses in the direction of the source. A further analysis of the latter equation reveals that the

beamformer output can be written, according to equations (4.6) and (4.18), as

$$b_{N,\mathrm{DS}}(kR,\varphi) = A \sum_{n=-N}^{N} \tilde{\mathcal{C}}_n(kR,\varphi_\mathrm{s}) \cdot \mathcal{C}_n^*(kR,\varphi). \tag{4.26}$$

In contrast with CHB, where the beamformer output was given by the division of the approximated coefficients with the theoretical ones (see equation (4.19)), the DS beamformer presents a multiplication of these terms. Therefore, in the case of unbaffled apertures, the singularities that can be present in CHB due to the dips of the Fourier coefficients are totally solved with the DS beamformer. This idea will be further examined in chapter 5.

The number of orders used for the DS beamformer follows

$$N = \lceil kR \rceil + 1. \tag{4.27}$$

The use of this expression, instead of the one used for CHB, will be clarified in section 5.3.3.

The magnitude of a normalized beamformer output $\bar{b}_{N,\mathrm{DS}}$ is shown in figure 4.4, using the same example given for CHB, i. e. plane waves coming from a source located at 180° impinge on an unbaffled circular array of radius 11.9 cm.

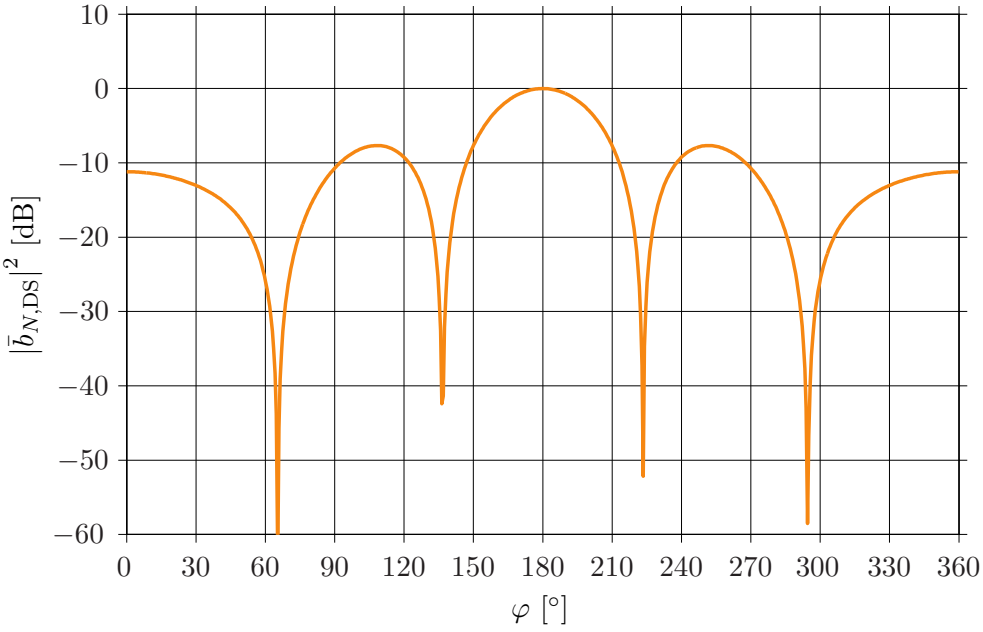

Figure 4.4: Magnitude of the normalized output of the DS beamformer at 1.5 kHz. The maximum order used for this frequency is $N = 5$. The array used is an unbaffled circular array with radius 11.9 cm.

Like in the case of CHB, the pattern reveals a maximum contained in a main lobe which is surrounded by side lobes. As expected, the main lobe is centered at 180° which is the position of the source. The pattern presents several differences with the one obtained with CHB in figure 4.2, such as the width of the main lobe and the number of side lobes.

Now a broadband source located at 0° is captured by the same array like in the example given in figure 4.3 for CHB. The output of the DS beamformer tuned at several frequencies is shown in figure 4.5. The number of modes used in each case is given in the captions of each panel.

As can be seen, at low frequencies the output is practically omnidirectional showing a single lobe. With increasing frequency the number of side lobes increases and the main lobe gets narrower. Note that all the outputs differ from the ones obtained with CHB shown in figure 4.3. Besides, the relationship between number of maxima (and minima) and N found for CHB is no longer valid when DSB is used.

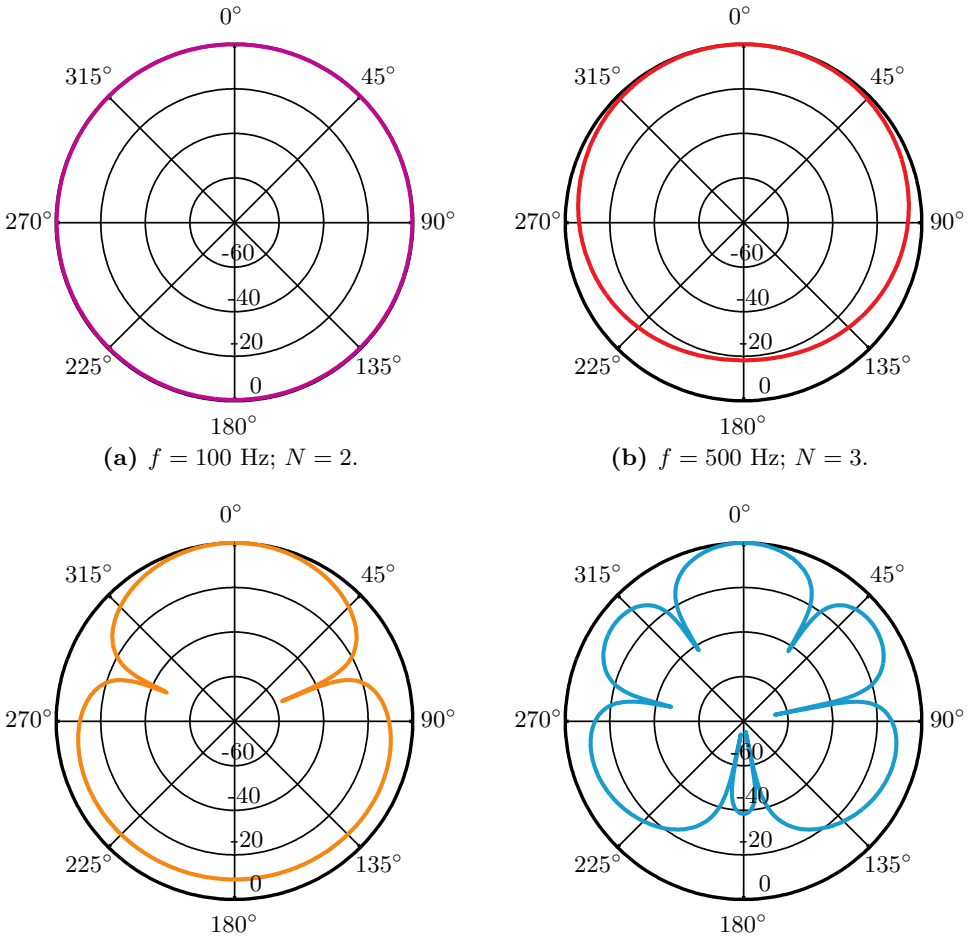

(a) $f = 100$ Hz; $N = 2$.

(b) $f = 500$ Hz; $N = 3$.

(c) $f = 1000$ Hz; $N = 4$.

(d) $f = 2000$ Hz; $N = 6$.

Figure 4.5: Magnitude in dB of the normalized output of the DS beamformer at four different frequencies, when an unbaffled circular array with radius 11.9 cm is used. The maximum order used for the processing is given in the captions of each panel. All the outputs detect the presence of a source placed at 0°.

4.5 Beamformer Performance

Throughout the examples given for CHB and DSB it has been seen that the pattern of the output of a beamformer varies from one technique to the other and also varies just by changing the frequency. For these reasons, it is necessary to evaluate the performance of a beamformer. This is done by means of the following measures: the resolution and the maximum side lobe level (MSL).

4.5.1 Resolution

The resolution of a beamformer is defined as the -3 dB width of the main lobe of the beampattern [20]. In figure 4.6, the resolution is calculated from the output of a beamformer that captures the sound from a source placed at $\varphi_{s1} = 150°$. As expected,

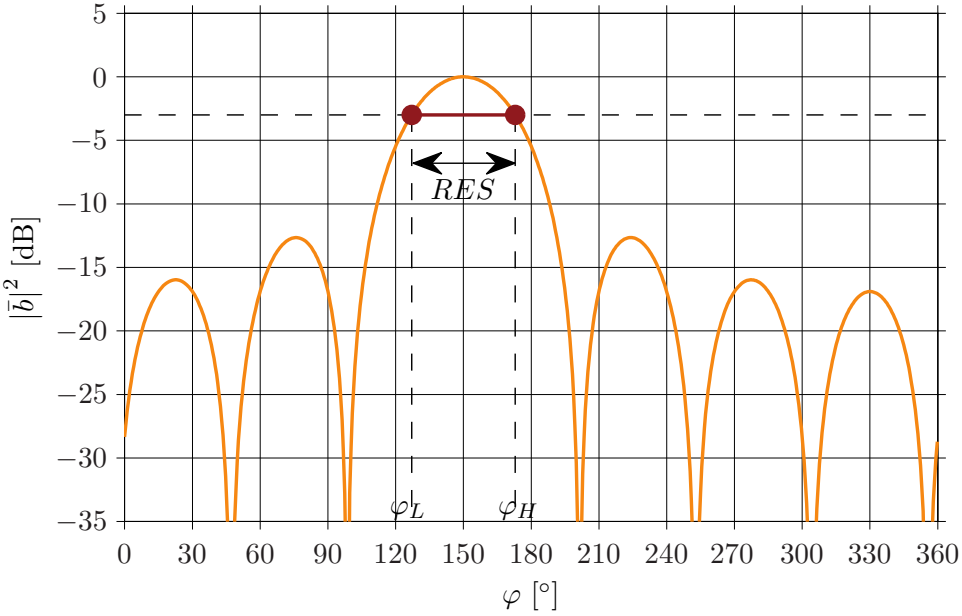

Figure 4.6: Calculation of the resolution for a given beamformer output.

the beampattern presents a main lobe with a maximum in the direction of the source φ_{s1}. In the main lobe, there are two angles φ_L and φ_H at which the magnitude with respect to the position of the maximum has decreased by -3 dB. These two angles determine the resolution as follows

$$RES = \varphi_H - \varphi_L. \tag{4.28}$$

This parameter is of interest because it gives an approximation to the minimum angular difference between two incoherent sources that is necessary in order for them to be distinguished. In other words, if the angular difference between the sources is equal or exceeds the resolution, the beampattern presents two maxima that correspond to the source positions, and hence they can be resolved. Panel (a) in figure 4.7 shows the beampattern that is measured when two incoherent sources with the same characteris-

tics are active. One of the sources is placed at $\varphi_{s1} = 150°$, like in the above example, whereas the second one is placed at $\varphi_{s2} = \varphi_{s1} + RES$.

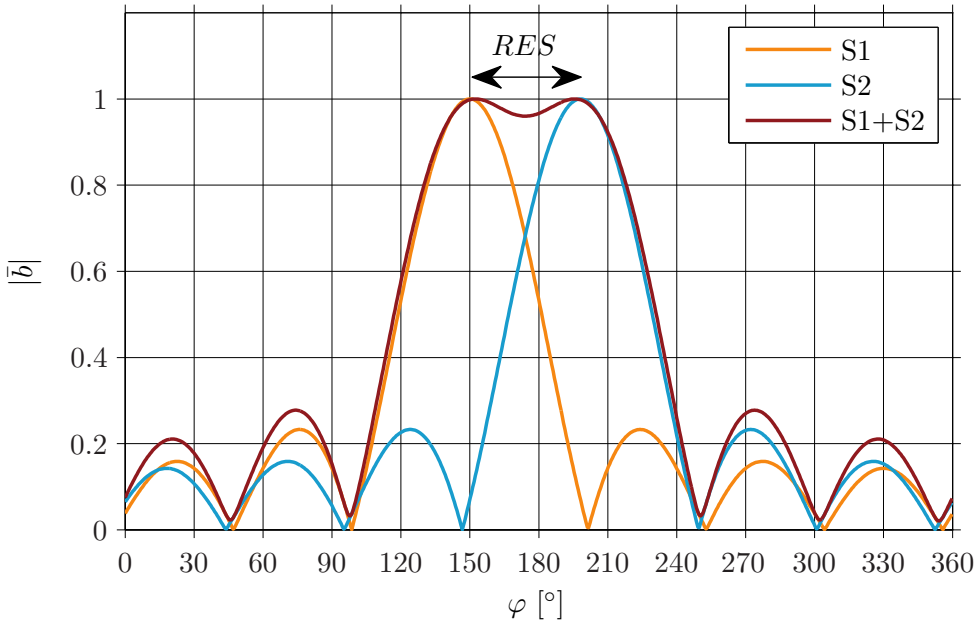

(a) $\Delta_s = RES$.

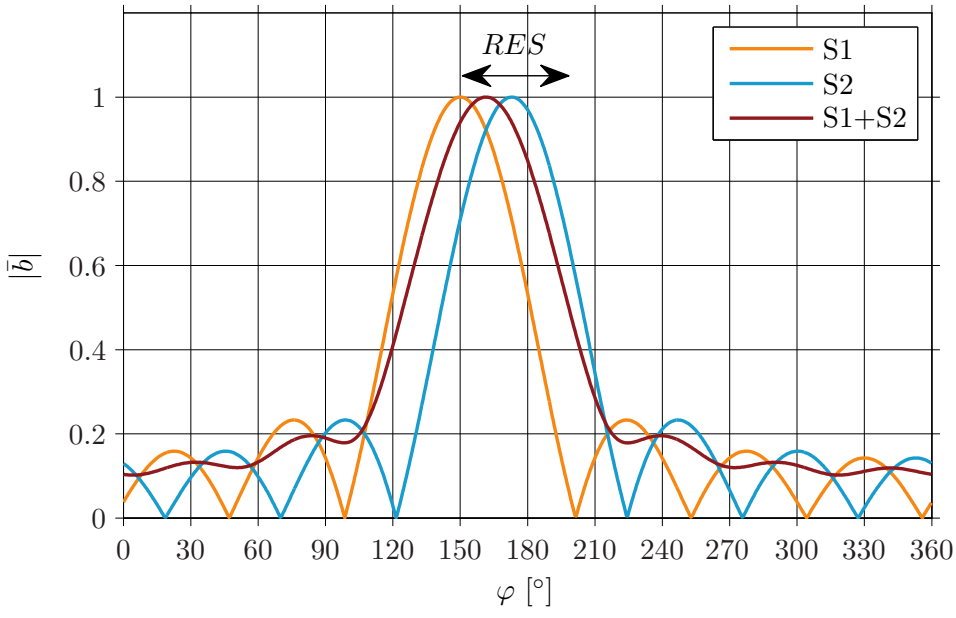

(b) $\Delta_s < RES$.

Figure 4.7: Normalized beamformer output measured when two incoherent sources (S1+S2) are active. In the top panel, the sources are away from each other with an angular distance (Δ_s) that equals the resolution, whereas in the bottom panel the angular distance is smaller than the resolution. The normalized beamformer outputs are also shown for the sources being active separately.

In such situation, it can be seen that the beamformer output reveals two maxima that coincide with the maxima that would be obtained with each source being active independently. On the contrary, when the angular difference between the sources is smaller than the resolution they cannot be resolved. This is shown in panel (b) in figure 4.7. As can be seen, the beamformer output gives a single maximum located in between the angles of the sources, and therefore, just one 'non-existent' source is identified instead of the two actual sources.

A *Matlab* function that calculates the resolution for a given beamformer output can be found in appendix B.3.1.

4.5.2 Maximum Side Lobe Level

As mentioned previously, the beamformer output usually presents side lobes around the main lobe. This is an unwanted effect as the beamformer seems to be sensitive not only in the focusing direction, i. e. the direction of the 'real source', but also in the direction of 'ghost sources'. For this reason, it is useful to evaluate the beamformer response by means of the MSL. This parameter is given by the difference between the peak of the main lobe and the peak of the highest side lobe [21]. The calculation of the MSL is illustrated in figure 4.8.

In appendix B.3.2, the source code implemented for the calculation of the MSL can be seen.

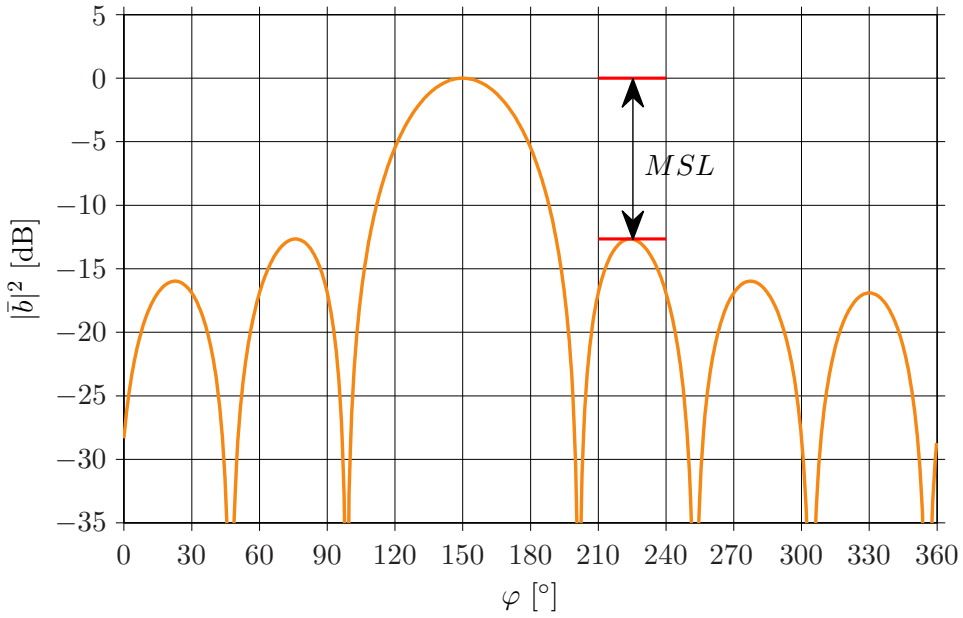

Figure 4.8: Calculation of the MSL for a given beamformer output.

5

Array Design and Simulations

5.1 Introduction

The design of any array is mainly determined by the purpose of the array and the signal processing techniques that are used. In our case, the aim of the array is the localization of environmental noise sources, e. g. motorways, trains, etc. This means that the array is placed outdoors, under free-field conditions. In such case, we assume that the array captures the sound field created by sources placed in the far-field. This makes it possible to consider that the waves that impinge on the array are planar and that they propagate in parallel to the ground, perpendicularly to the z-axis, i. e. reflections from the sky are inexistent and reflections from the ground are sufficiently attenuated. This requirement is fulfilled by circular arrays since they can be deployed in situations where the sound field is two-dimensional. In the actual case, the array should be placed in parallel to the ground to capture the sound field in the xy-plane, as depicted in figure 5.1. Besides, all the directions in this plane have the same importance, which implies that the array microphones must be omnidirectional.

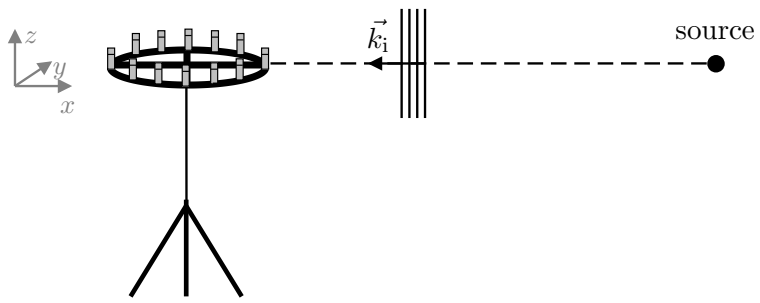

Figure 5.1: Layout of a circular array used to localize environmental noise sources. The waves that impinge on the array are planar and their direction of propagation is parallel to ground.

Concerning environmental noise, the frequency range under consideration is often broadband. The problem is that the frequency range of arrays is limited. Therefore, the array should be sensitive at those frequencies where the presence of noise is more severe. In this sense, the frequency range of the array is chosen in section 5.2, where the spectral behavior of some sources of interest is presented.

There are two main requirements in the design of the array:

- It must be relatively small and portable, since it is meant to be used in outdoor measurements. According to this, the maximum radius of the array that is taken into account is 20 cm.
- The number of microphones must be moderate in order to lower expenses.

In terms of signal processing it is convenient to use beamforming techniques as they are suitable for far-field measurements. The techniques that will be analyzed are CHB and DSB. As mentioned in chapters 3 and 4, several parameters play a role when dealing with CHB and DSB, namely the radius of the array, the number of microphones, the number of modes used to decompose the sound field or the dynamic range in terms of kR. Therefore, it becomes necessary to make use of simulations and base the final design of the array on their results.

5.2 Environmental Noise Sources

The frequency content of the noise created by several environmental sources has been measured with a Brüel & Kjær Hand-held sound level meter *B&K Type 2250*. A short description of the measured sources and the measurement procedure is given in the following:

- **Motorway.** The sound from the motorway from Helsingør to Copenhagen has been measured in the surroundings of Kgs. Lyngby at about 4 m away from the motorway. Ten measurements of one minute each have been performed.
- **Airports.** The sound from several airplanes taking off has been measured in Dragør in front of one of the main lanes of Copenhagen Airport. The distance to the airplanes is about 40 m in the moment of the taking off. Each measurement has been started when the airplane started to accelerate before the taking off and has been stopped when the sound is no longer perceived at the measurement point.
- **Trains.** The sound produced by S-tog trains when they arrive or leave Lyngby Station has been measured at a distance of 50 cm away from the railway at the station. In the case of trains arriving, the measurements start when the sound is perceived for the first time and stop after the trains stop in the station. For trains leaving the station, the measurements start after the trains doors are closed and they are stopped when the sound totally vanishes.

  Besides, the sound of trains passing by has been also measured in the surroundings of Lyngby Sø, in Kgs. Lyngby. The measurement position is about 2 m away from the railway. The measurements start when the sound of trains is heard for the first time and stop when the sound vanishes.

All the measurements of equivalent sound pressure level performed in each situation have been averaged. Figures 5.2 to 5.4 show the averaged equivalent sound pressure level of each kind of source, with and without A-weighting.

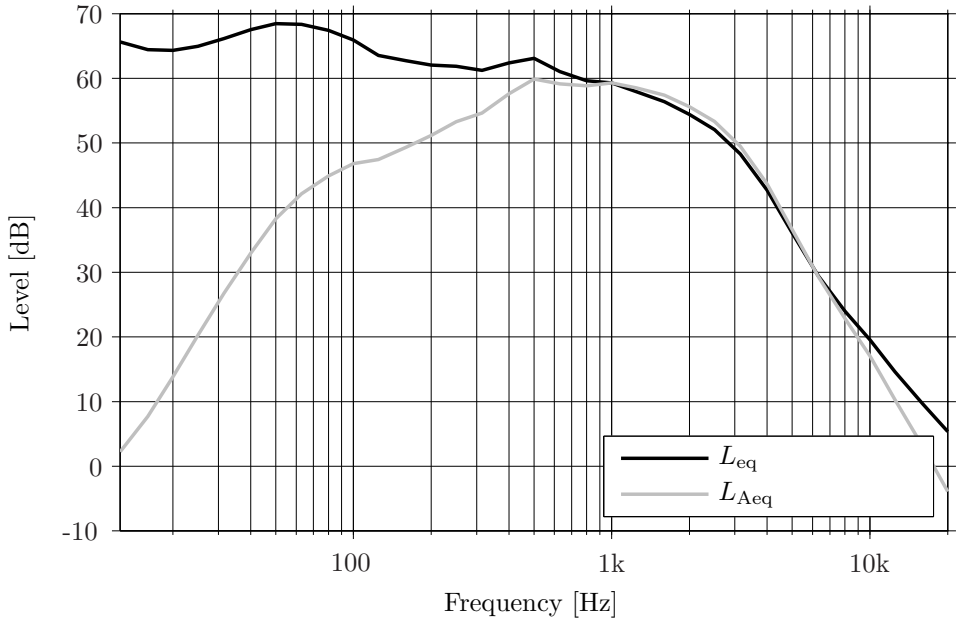

Figure 5.2: Equivalent sound pressure of airplanes taking off. This is the result of averaging 10 measurements of 10 min each.

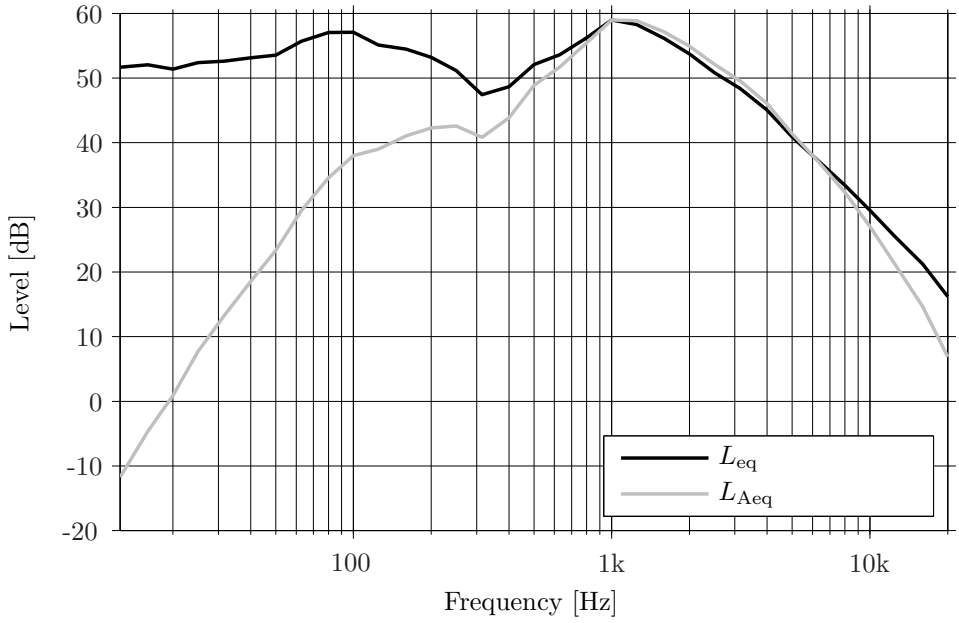

Figure 5.3: Equivalent sound pressure of a motorway. This is the result of averaging 10 measurements of 10 min each.

In the case of train, the spectrum in all three situations (passing by, arriving and leaving the station) presents frequency content in the same frequency range. For this

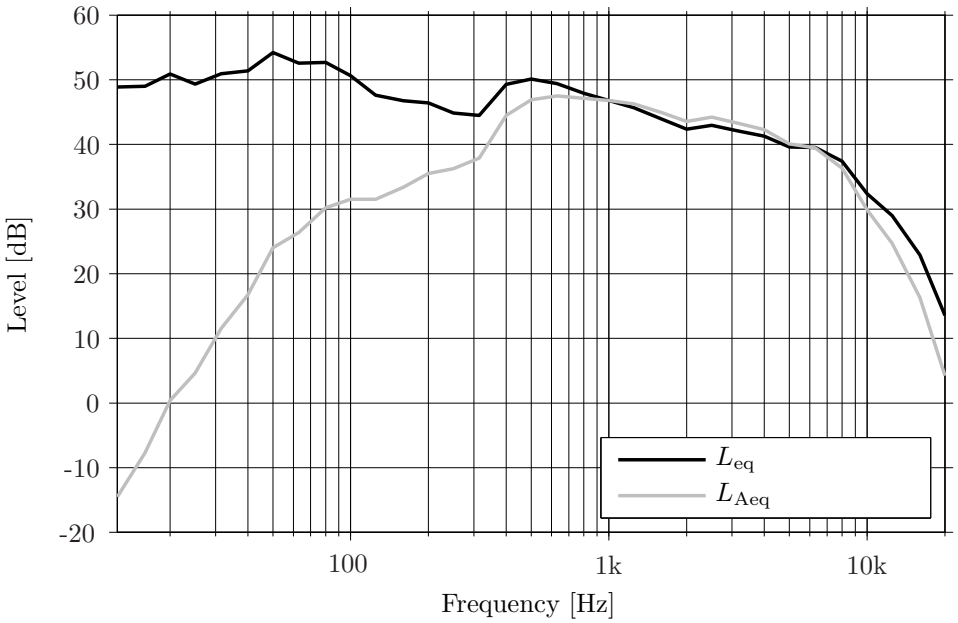

Figure 5.4: Equivalent sound pressure of trains passing by. This is the result of averaging 10 measurements of 10 min each.

reason only the case of trains passing by is shown in this section, whereas the spectrum of trains arriving and leaving the station can be seen in appendix A.4.

Comparing the measurements, it can be seen that the frequency content at lower frequencies is similar in all cases. At higher frequencies, the case of trains presents a wider range, up to 8 kHz, and from this frequency on it decreases. In the case of aircraft, the most relevant content is up to about 3 kHz and decays afterwards. Similar results are obtained for the motorway, in which the content reaches 3–4 kHz and decreases at higher frequencies.

Taking all these ideas into account, it would be desirable to have an array with a dynamic range up to 8 kHz, since this is the extreme case that has been measured. The number of microphones of a circular array is, according to section 3.4, given by $M > 2N_{\max}$, where $N_{\max} = \lceil k_{\max} R \rceil$. Considering arrays of radius 5 cm, 10 cm and 20 cm, the minimum number of microphones that should be used in order to cover the frequency range up to 8 kHz is 16, 31 and 60, respectively. Such high number of microphones requires high expenses, and hence this does not fulfill the established requirements. In addition to this, in the case of arrays mounted on a baffle, the fact that the microphones are embedded in the baffle as can be seen in figure 5.5 implies that they are placed in a rather small space. Then, if the number of microphones is too high the implementation can be rather complicated, if not impossible. For these reasons the number of microphones must be reduced. A compromise between the frequency range and both the size of the array and the number of microphones should be found.

Finally, it is decided that a fair design accounts for an array with a dynamic range from 100 Hz to around 2–3 kHz, since all noise sources present a high content in this range. In such case, the maximum frequency required can be set to 2.5 kHz, which results in a minimum number of microphones of 7, 11 and 21 for arrays with radius 5,

Figure 5.5: Ten-sensor circular array mounted into a rigid cylindrical baffle of length of 11.3 cm and radius of 4 cm. Picture taken from [15].

10 and 20 cm. These values are considered to be reasonable for the implementation of the array.

5.3 Beamforming Simulations

5.3.1 Simulations Procedure

All the simulations carried out in this chapter take into account that a circular array is placed at the origin of coordinates. The sound field is composed by plane waves in the frequency range from 1 Hz to 3 kHz, created by a source placed at an angle φ_s. The direction of propagation of the waves is parallel to the ground. This setup is shown in figure 5.6. The pressure of the waves that impinge on the array has been implemented

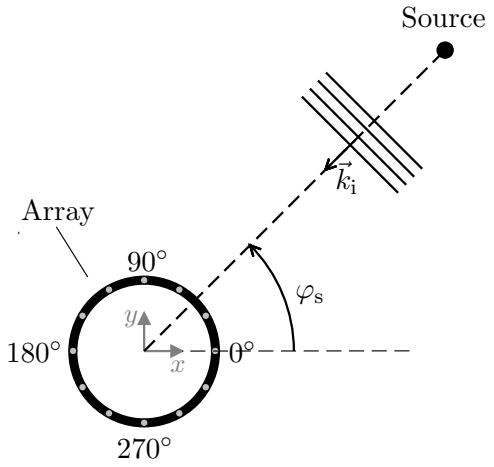

Figure 5.6: Setup used for the simulations. The pressure captured by a circular array is due to plane waves generated by a source in the direction of φ_s.

in *Matlab*, for both unbaffled arrays and arrays mounted on a rigid cylindrical baffle of infinite length. The source code is given in appendix B.4.1.

The performance of beamformers that use DSB and CHB is analyzed in the absence

of noise, i. e. in ideal conditions, as a first approach. Afterwards, the influence of background noise is investigated. The response of the beamformers is calculated in the frequency range of interest, with a resolution of 1 Hz. Besides, the beamformers response is obtained for all the angles φ from 0 to 2π rad, with an angular resolution of 0.005 rad (or 0.286°).

The arrays under test are unbaffled and mounted on a rigid cylindrical baffle of infinite length. According to the previous sections, the radius of the arrays must be 20 cm at most and their dynamic range should be from 100 Hz up to 2–3 kHz. Following these requirements, arrays of radius 5, 10 and 20 cm are used for the simulations. The highest frequency is set to be at least 2.5 kHz. Inserting this frequency into the relationship $N = \lceil kR \rceil$ by means of the wavenumber k ($k = 2\pi f/c$), the maximum order needed for the beamforming algorithms (see equations (4.20) and (4.25)) follows

$$N_{\max} = \left\lceil \frac{2\pi f_{\text{req}}}{c} R \right\rceil . \tag{5.1}$$

As the number of microphones must fulfill $M > 2N_{\max}$, the minimum number of microphones needed for each array is $M = 2N_{\max} + 1$. When the condition $M > 2N_{\max}$ is not respected, a sampling error arises. An approximation of the maximum frequency that can be used without having severe error due to sampling is determined by means of the higher value kR

$$N_{\max} = k_{\max} R \qquad \Rightarrow \qquad f_{\max} = \frac{N_{\max} c}{2\pi R}.$$

Table 5.1 states the characteristics of the arrays used in the simulations that follow from the previous relationships, in terms of radius, maximum number of orders, number of microphones and maximum frequency allowed to avoid sampling error.

Table 5.1: Features of the arrays used in the simulations. Note that the number of microphones is the minimum required.

	R [cm]	$N_{\max}$	M	$f_{\max}$ [Hz]
Array 1	5	3	7	3275
Array 2	10	5	11	2729
Array 3	20	10	21	2729

5.3.2 Circular Harmonics Beamforming

5.3.2.1 Performance in Ideal Conditions

In this section, the results of several simulations carried out without the influence of background noise are shown. In order to compare the beamforming techniques and the cases of baffled and unbaffled arrays, a source placed at 180° has been used in all the simulations. In all cases, the displayed frequency range is up to 3 kHz which corresponds to the frequency content of the source. It is assumed that the amplitude of the waves is the same for all frequencies.

The directivity patterns obtained with CHB when the arrays of table 5.1 are unbaffled are shown in figure 5.7. As can be seen, all the responses present a main lobe in the direction of the source at 180°. The patterns of the three arrays are similar as in all cases they remain constant for a certain interval and then change. Besides, these intervals are compressed when the radius increases. It turns out that this behavior is caused by the ceiling function in the calculation of N, i. e. in $N = \lceil kR \rceil$. For example, in the case of an array of 5 cm, the pattern is constant up to 1091 Hz as $N = 1$ in this interval, and varies when N changes to 2, and varies a third time when $N = 3$. Accordingly, the total number of intervals where the pattern is constant is given by the value $N_{\max}$, which is stated in table 5.1 for each array under analysis. In addition to this, the main lobe gets narrower and the number of side lobes raises progressively with increasing N. As the array of 20 cm of radius presents the highest value of $N_{\max}$, its response is the most directive.

Certain frequencies present an 'unexpected' response, as can be seen around 2.6 kHz for the array of radius of 5 cm in panel (a) or around 2.1 kHz and 2.8 kHz for the array of 10 cm, in panel (b). This phenomenon is due to the fact that the Fourier coefficients obtained with unbaffled arrays present some dips at certain values kR (see section 3.2.1). For example, in the case of the array of 5 cm, the problem occurs at 2.6 kHz which leads to a spatial frequency of $kR \approx 2.4$. According to figure 3.3 on page 18, this value corresponds to the first dip of $\mathcal{C}_0^\circ$. Those frequencies where this phenomenon occurs cannot be resolved with precision. This effect is avoided when the arrays are mounted on a rigid cylindrical baffle of infinite length. The overall behavior of the beamformers output when baffled arrays are used is qualitatively identical to the unbaffled case but without the problem of unresolved frequencies. This can be seen in appendix A.2.1.

As mentioned in the previous section, the arrays can be used up to a maximum frequency $f_{\max}$ without having the influence of the error due to sampling. In the cases of the arrays of radius of 10 and 20 cm this value is around 2.7 kHz. From this frequency on, the effect of the sampling error can be seen in the beampatterns through the magnitude of the side lobes which are higher than in the previous interval of frequencies.

All these ideas are reflected in the resolution and the MSL. These parameters are shown for unbaffled arrays, using a logarithmic scale from 50 Hz to 3 kHz, in figure 5.8.

As can be seen, the resolution and the MSL are constant for a certain interval. For each array, these intervals correspond to the ones observed in the beamformers patterns. The fact that the main lobe gets narrower from interval to interval results in the improvement of the resolution that can be observed. More intervals result in a better resolution, which is the case of the array of largest radius. The MSL follows the same behavior than the resolution, improving when the number of orders is raised. The staircase pattern in the resolution and the MSL is also obtained with spherical harmonics beamforming [20].

Both measures get worse in those frequencies that coincide with the dips in the Fourier coefficients. Besides, at those frequencies that exceed $f_{\max}$, the MSL is dramatically affected by the sampling error. In contrast to this, the resolution keeps constant an unaltered at the very same frequencies.

The resolution and the MSL obtained with baffled arrays is shown in figures A.3 and

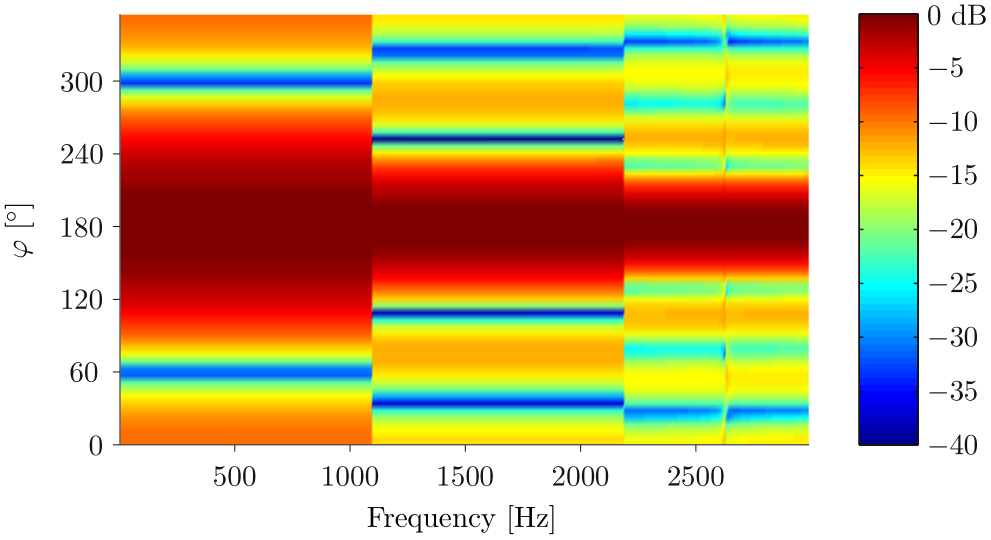

(a) CHB, $R = 5$ cm, Unbaffled.

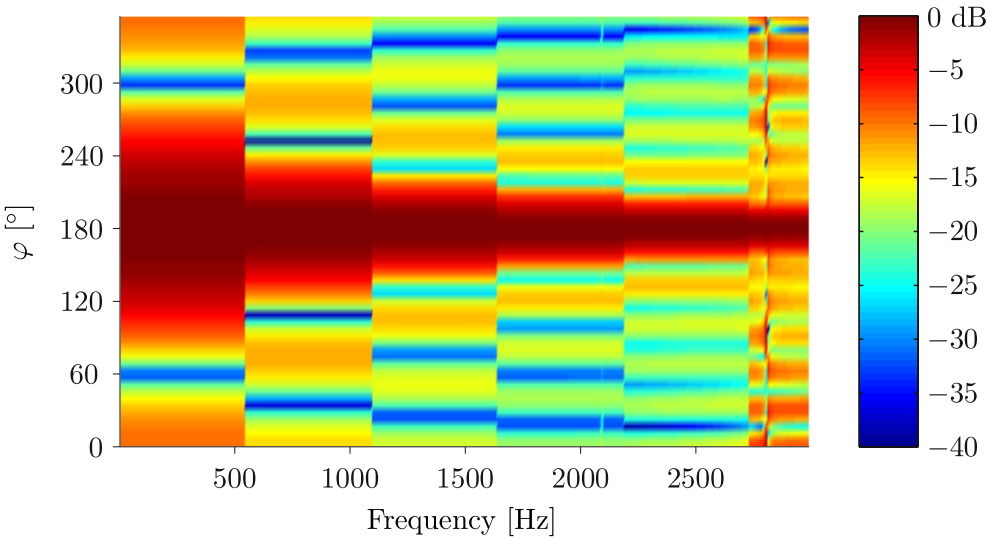

(b) CHB, $R = 10$ cm, Unbaffled.

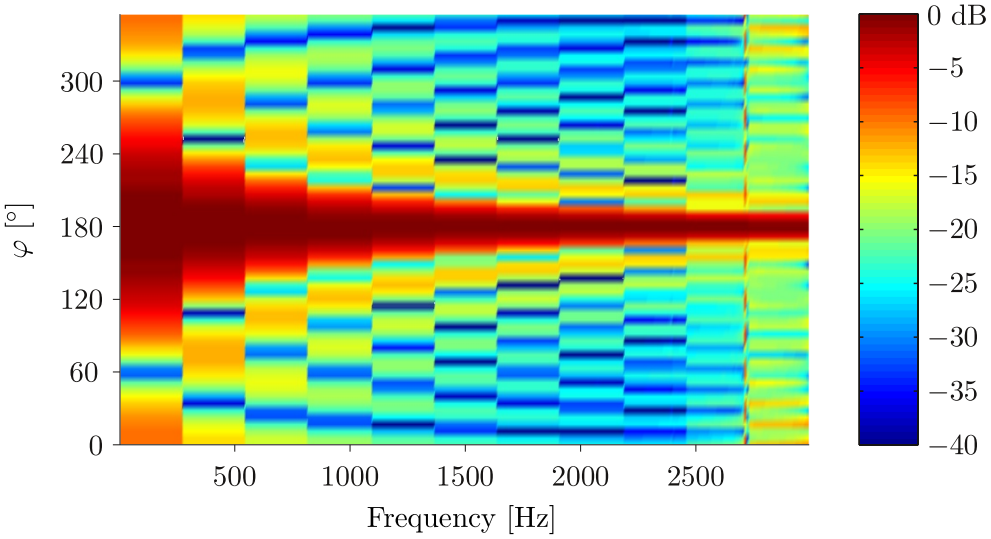

(c) CHB, $R = 20$ cm, Unbaffled.

Figure 5.7: Normalized outputs of three CH beamformers that use unbaffled circular arrays of radius 5, 10 and 20 cm, when a source is placed at 180°. The features of each array are shown in table 5.1.

A.4 in appendix A.2.1. These parameters are identical to the ones of the unbaffled arrays, but with the problem of the singularities at high frequencies solved.

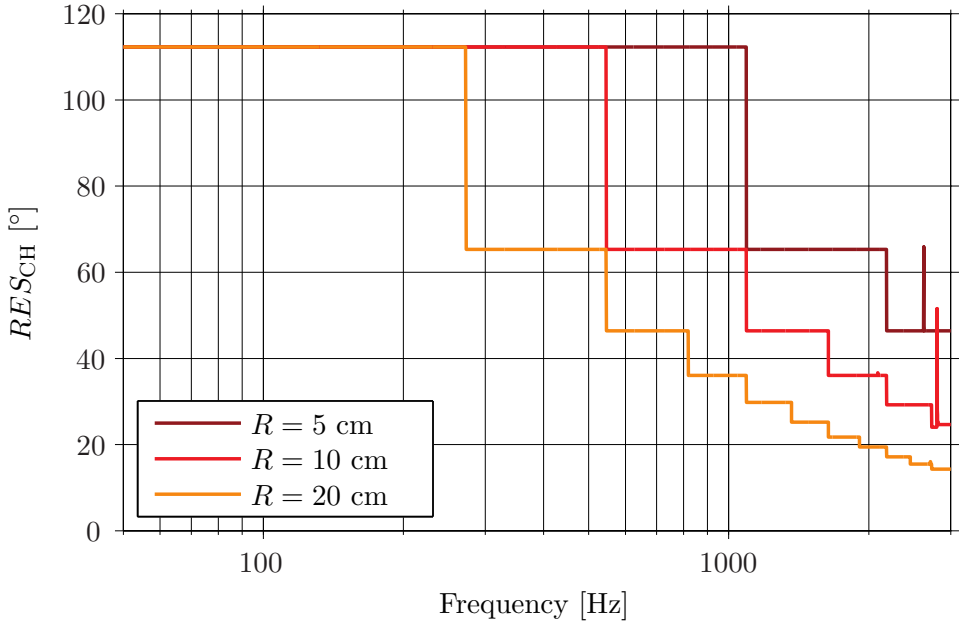

(a)

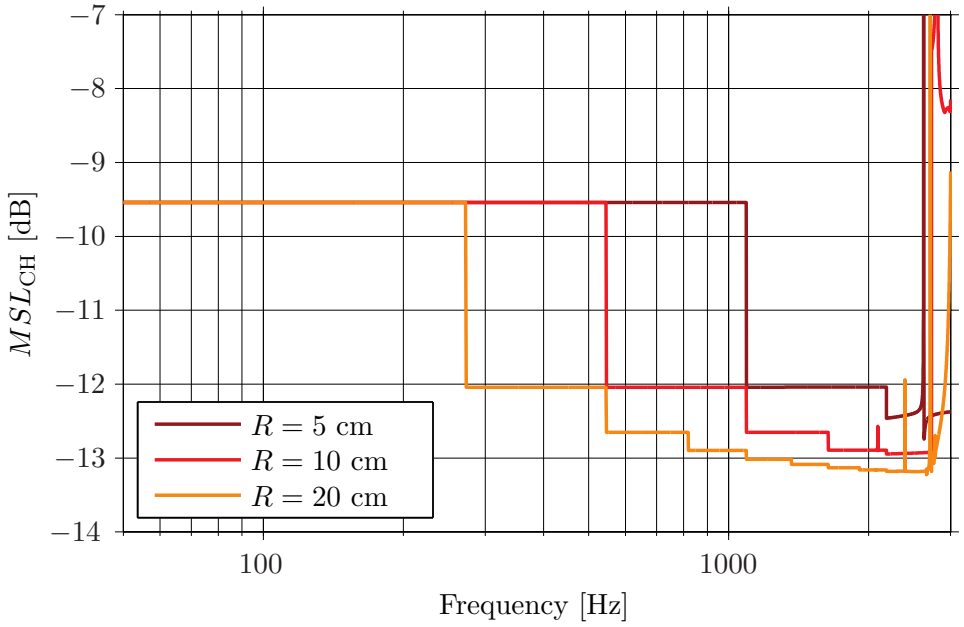

(b)

Figure 5.8: Resolution and MSL of three CH beamformers that use unbaffled circular arrays of radius 5, 10 and 20 cm, when a source is placed at 180°. The features of each array are given in table 5.1.

In order to analyze the dependency of resolution and MSL on the position of the source, some simulations have been carried out for several frequencies as a function of the angle of the source φ_s. The resolution chosen for φ_s is 0.005 rad. The results are

shown in figure 5.9 for the unbaffled array of 10 cm of radius. The frequencies used are 100 Hz, 700 Hz, 1.2 kHz, 2 kHz and 2.5 kHz. For each frequency, the number of orders needed for the beamforming processing is different, which implies that the resolution and the MSL are different in each case.

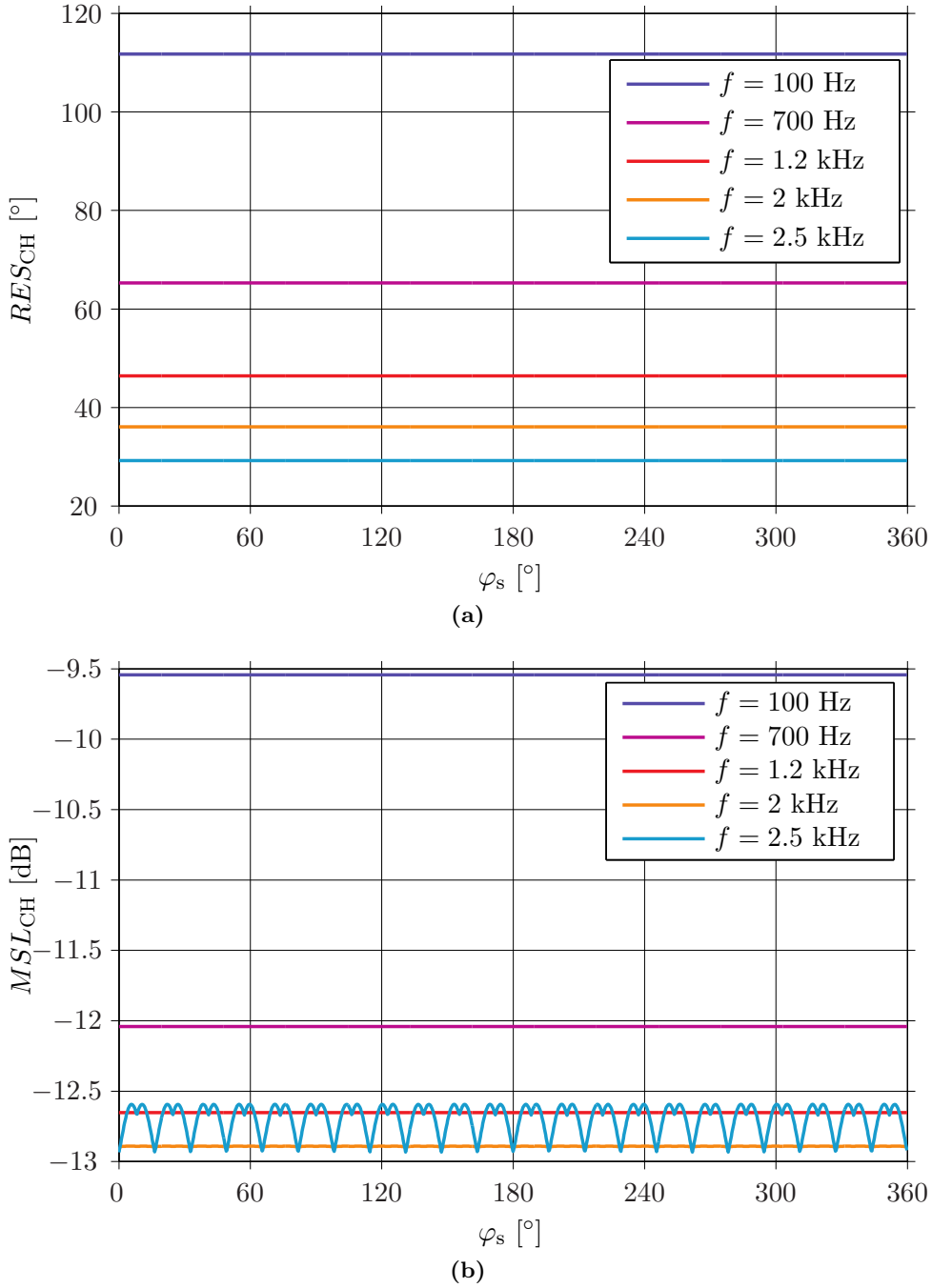

Figure 5.9: Resolution and MSL as a function of the angular position of the source obtained with CHB and an unbaffled array of radius 10 cm at five different frequencies. The features of the array are given in table 5.1.

As can be seen, for each frequency the resolution is constant for all values of φ_s. The MSL results are also constant except for the case of 2.5 kHz. This effect can be caused by the sampling error that starts to arise around $f_{max} = 2.7$ kHz. In the case of a baffled array with the same radius, which can be seen in appendix A.2.1, the resolution slightly varies with φ_s at 2 kHz and 2.5 kHz, and the MSL presents more variation at these precise frequencies.

The number of side lobes, shown in figure 5.10, has also been obtained for the same unbaffled array as a function of source position. Like in the case of the MSL, the number

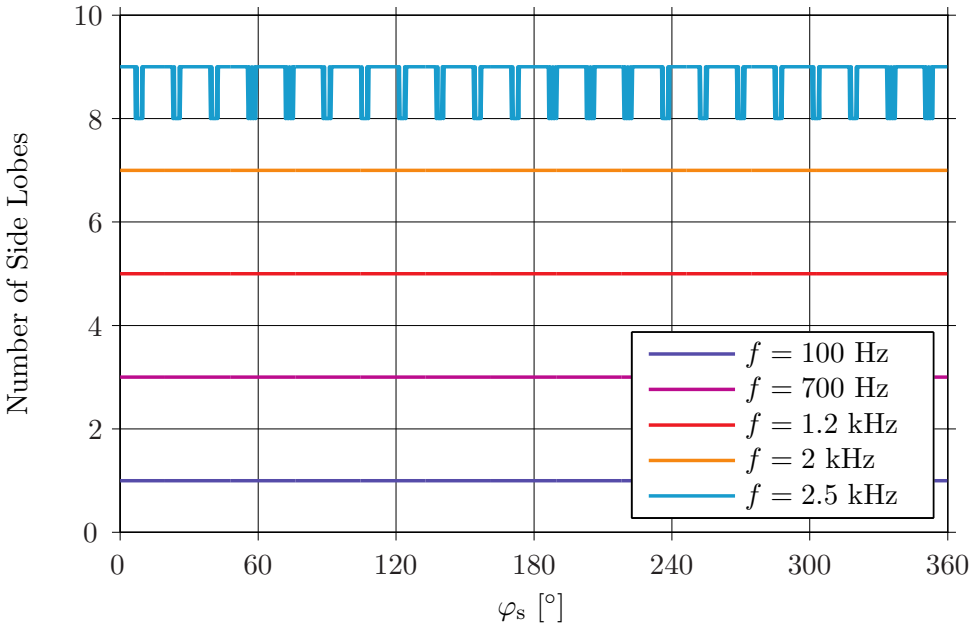

Figure 5.10: Number of side lobes as a function of the angular position of the source obtained with CHB and an unbaffled array of radius 10 cm at five different frequencies. The features of the array are given in table 5.1.

of side lobes is independent of φ_s except for the case of 2.5 Hz. At those frequencies where the number of side lobes is independent of φ_s, the number of side lobes follows

$$\text{Number of Side Lobes} = 2N - 1. \tag{5.2}$$

For example, at 100 Hz, $N = 1$ and the pattern presents one side lobe; at 700 Hz, $N = 2$ and the number of side lobes is 3, etc. This behavior is also observed for baffled arrays (see figure A.5 in appendix A.2.1).

Even though it is not shown here, the same behavior is observed with arrays of different radius. From these results, one can say that the resolution, the MSL and the number of side lobes obtained with CHB are independent of the source position in almost all the frequency range of interest.

5.3.2.2 Performance with Influence of Background Noise

In order to analyze the beamformers performance in a more realistic situation, background noise is introduced. The pressure captured by each microphone is then con-

taminated with additive noise. The Signal-to-Noise ratio (SNR) in each microphone of the array is the ratio of the power of the signal without being contaminated with noise over the power of the noise. It is considered that the spectral components of the noise captured by the microphones have the same magnitude. On the contrary, the noise phase, which is uniformly distributed from 0 to 2π rad, varies from one microphone to the other. Therefore, the noise signals in the various microphones are uncorrelated. Then, at a given frequency, the SNR at each microphone follows

$$\mathrm{SNR}_m(f) = \frac{P_{\mathrm{signal}}(f)}{P_{\mathrm{noise}}(f)} = \frac{|A_{\mathrm{signal}}|^2}{|A_{\mathrm{noise}}|^2}, \tag{5.3}$$

where $|A_{\mathrm{signal}}|$ and $|A_{\mathrm{noise}}|$ are the magnitudes of the spectral components of the signal and the noise for a certain frequency. Note that they are independent of the frequency as they have been assumed to be constant. For the simulations, an $\mathrm{SNR}_m = 30$ dB has been used. A function that generates background noise for a required SNR has been implemented for the simulations and is provided in appendix B.4.2.

The simulations performed in ideal conditions are now repeated but inserting background noise. A broadband source placed at 180° is again used. In figures 5.11 and 5.12, the resolution and MSL obtained with unbaffled arrays are shown. At first

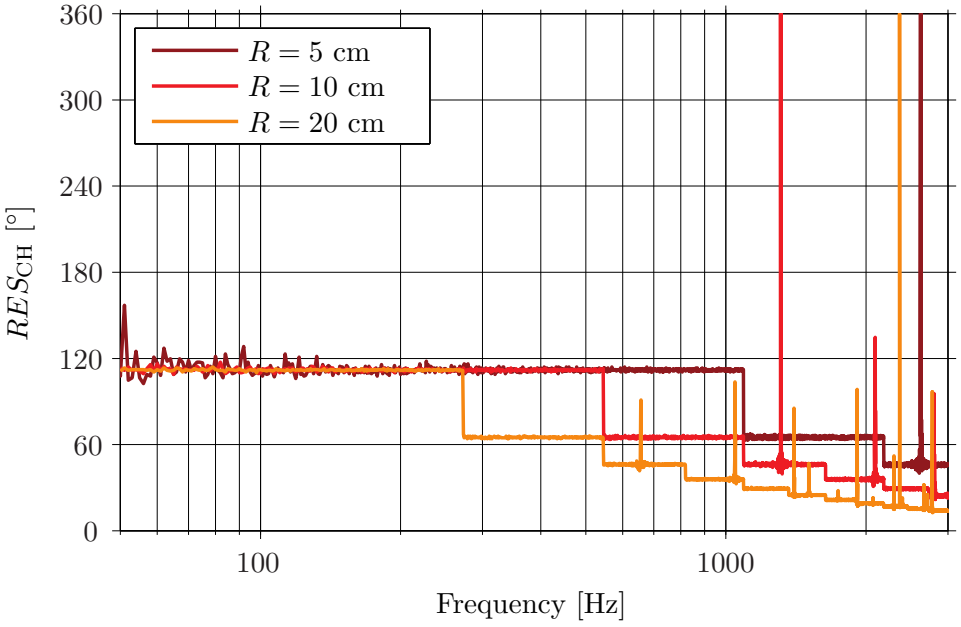

Figure 5.11: Resolution of three CH beamformers that use unbaffled circular arrays of radius 5, 10 and 20 cm, when a source is placed at 180° and the SNR in the array microphones is 30 dB. The features of each array are given in table 5.1.

glance, it can be seen that the resolution resembles the ideal case, with the difference that instead of having continuous values in each interval, the responses present small fluctuations caused by the presence of noise. At low frequencies, the amplitude of these fluctuations is higher than in high frequencies. Besides, the response is poorer for the array with the shortest radius.

The results obtained for MSL reveal that this measure is more sensitive to noise

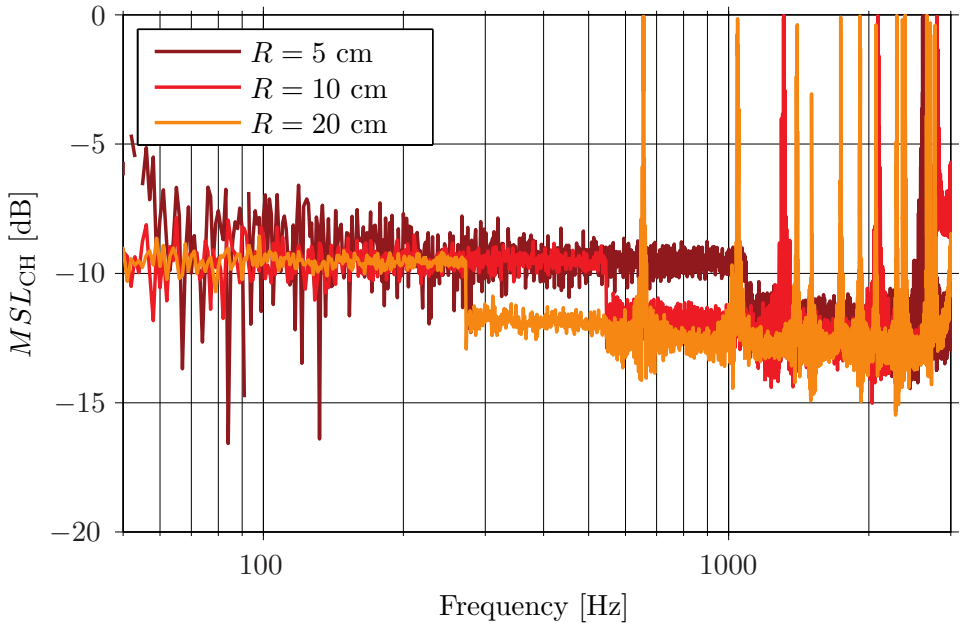

Figure 5.12: MSL of three CH beamformers that use unbaffled circular arrays of radius 5, 10 and 20 cm, when a source is placed at 180° and the SNR in the array microphones is 30 dB. The features of each array are given in table 5.1.

since the response has large fluctuations around the ideal curves. Again, the lower frequencies are the most affected. Like in the ideal case, the MSL worsens considerably at those frequencies that exceed $f_{\max}$.

At those frequencies that coincide with a dip of the modal response, the resolution and the MSL get worse than in the ideal case and in some cases the resolution is 360° and the MSL reaches 0 dB approximately. When this happens, the response is practically omnidirectional at that particular frequency and therefore, the direction of the source cannot be resolved. This is shown in figure 5.13 when the unbaffled array of 10 cm is tuned at the frequency of the first peak. This phenomenon is completely

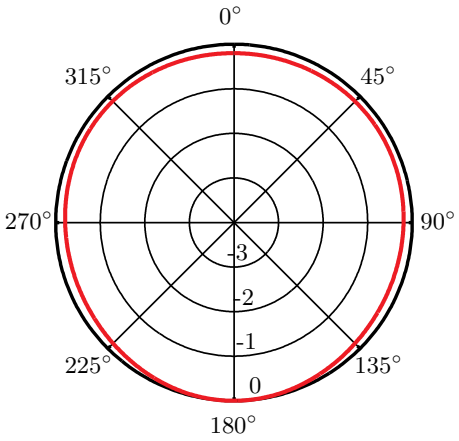

Figure 5.13: Normalized output of a beamformer tuned at 1313 Hz, when an unbaffled array of 10 cm of radius is used. The output, given in dB, reveals that at this frequency the resolution is 360° and the MSL is practically 0 dB.

solved when baffled arrays are used instead. In these cases, the resolution and the MSL, which are shown in appendix A.2.1, are practically the same as the ones obtained with unbaffled arrays and do not warrant a separate discussion.

The influence of noise can be analyzed by means of the CH beamformer response. When background noise contaminates the measurement, the pressure in each microphone is the summation of the pressure due to the source and the pressure of the noise

$$p_{\text{total}}(kR, \varphi_m) = p(kR, \varphi_m) + n(kR, \varphi_m). \tag{5.4}$$

Then, according to equation (4.19) on page 37, the output of the beamformer is

$$b_{N,\text{CH}}(kR, \varphi) = A \sum_{n=-N}^{N} \frac{\tilde{\mathcal{C}}_n(kR, \varphi_\text{s})}{\mathcal{C}_n(kR, \varphi)} + \frac{\mathcal{N}_n}{\mathcal{C}_n(kR, \varphi)}, \tag{5.5}$$

where $\mathcal{N}_n$ are the coefficients obtained by decomposing the noise in CH with the array using equation (4.6) on page 34

$$\mathcal{N}_n = \frac{1}{M} \sum_{m=1}^{M} n(kR, \varphi_m) \mathrm{e}^{-\mathrm{j}n\varphi_m}. \tag{5.6}$$

Let us suppose that the beamformer is steered to φ_s, so the first term in equation (5.5) approximates unity for all orders n as the theoretical and the approximated coefficients become very similar. However, the coefficients of the noise do not have anything in common with $\mathcal{C}_n$. This can be seen in figure 5.14 where the coefficients of the noise and the term $1/\mathcal{C}_n$ are shown for orders up to 3 when an unbaffled array of 10 cm and 11 microphones is used. The negative orders of $1/\mathcal{C}_n$ are not given because they are exactly the same as the positive ones.

The noise coefficients $\mathcal{N}_n$ are just random noise uniformly distributed, whereas the terms $1/\mathcal{C}_n$ do vary with order and kR. As can be seen, the zeroth order is constant at low values of kR. By contrast, higher orders present higher magnitudes which decay with increasing kR. With increasing order, the decay becomes faster. At high values kR, all orders present similar and rather small amplitudes, with the exception of some peaks that correspond to those frequencies that cannot be resolved. As mentioned before, these can be removed by mounting the array on a baffle. According to equation (5.5) the noise coefficients multiply the terms $1/\mathcal{C}_n$. As can be seen from figure 5.14, at low values kR, or equivalently at low frequencies, the noise coefficients of order different from 0 are amplified. Then the noise gain more strength than the signal and this contaminates the beamformer processing. This explains why the resolution and mostly the MSL are more influenced by noise at low frequencies. Besides this, there are other ideas concerning noise that must be analyzed in the following:

- The curves obtained for $1/\mathcal{C}_n$ are independent of the array size. However, for a given frequency range, arrays with short radius present lower values kR in comparison with larger arrays. Taking into account that at lower values of kR the noise is more amplified, it becomes obvious that smaller arrays are more affected by noise. Because of this, the array with smallest radius is more influenced than the other arrays as observed in figures 5.11 and 5.12.
- According to the previous item, the terms $1/\mathcal{C}_n$ are of greater amplitude with increasing order, at low frequencies. Then, if the calculation of the beamformer output is done with more orders than necessary, the noise becomes more amplified. It has been seen that using $N = \lceil kR \rceil$ the results in terms of MSL and resolution

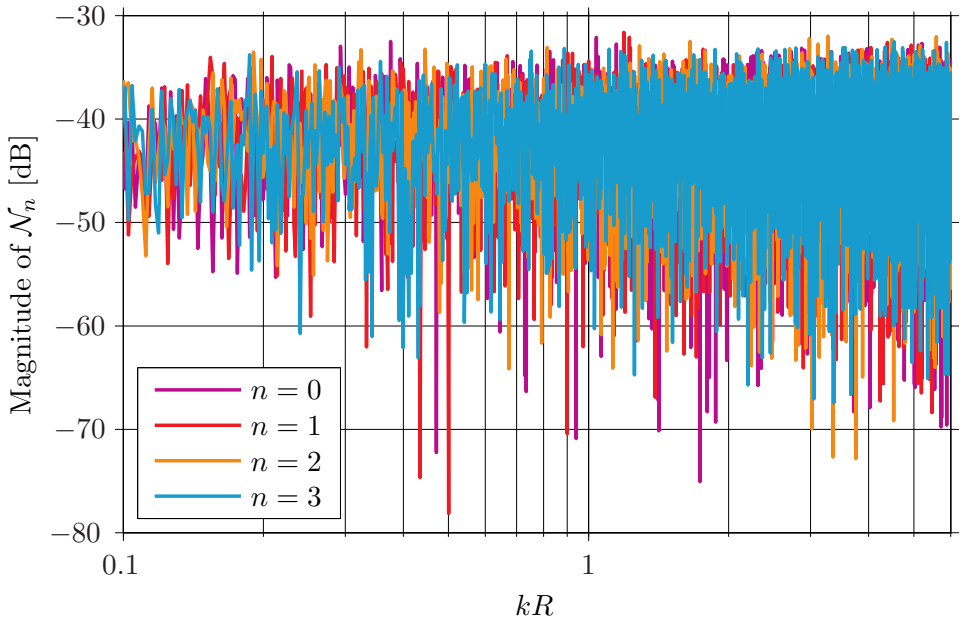

(a)

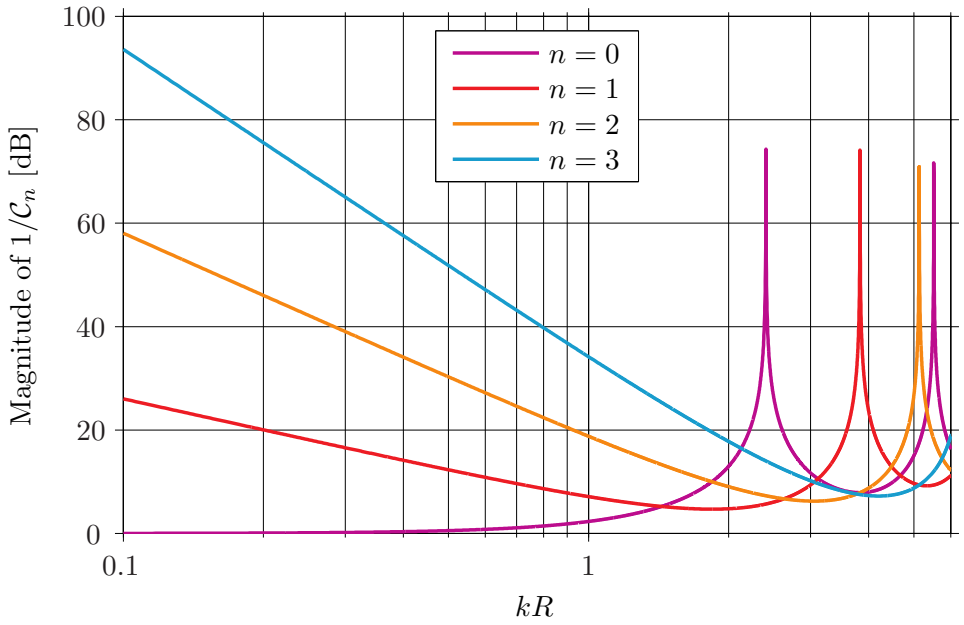

(b)

Figure 5.14: Top panel shows the magnitude of the first four coefficients obtained by decomposing uniformly distributed noise with an unbaffled array of radius of 10 cm and 11 microphones. The noise is designed in order to have 30 dB of SNR at the input of each microphone of the array. The power of the signal of the source in the input of each microphone is −3 dB and the power of the noise is −33 dB. In the bottom panel, the magnitude of the inverse value of the coefficients $\mathcal{C}_n$ are depicted for the first four coefficients. The features of the array are given in table 5.1.

were acceptable. However, if the number of orders is increased, the MSL and the resolution vary considerably. This is shown in figure 5.15 for an unbaffled array of radius 10 cm when the beamforming calculation is done with $N = \lceil kR \rceil$, $N = \lceil kR \rceil + 1$ and $N = \lceil kR \rceil + 2$.

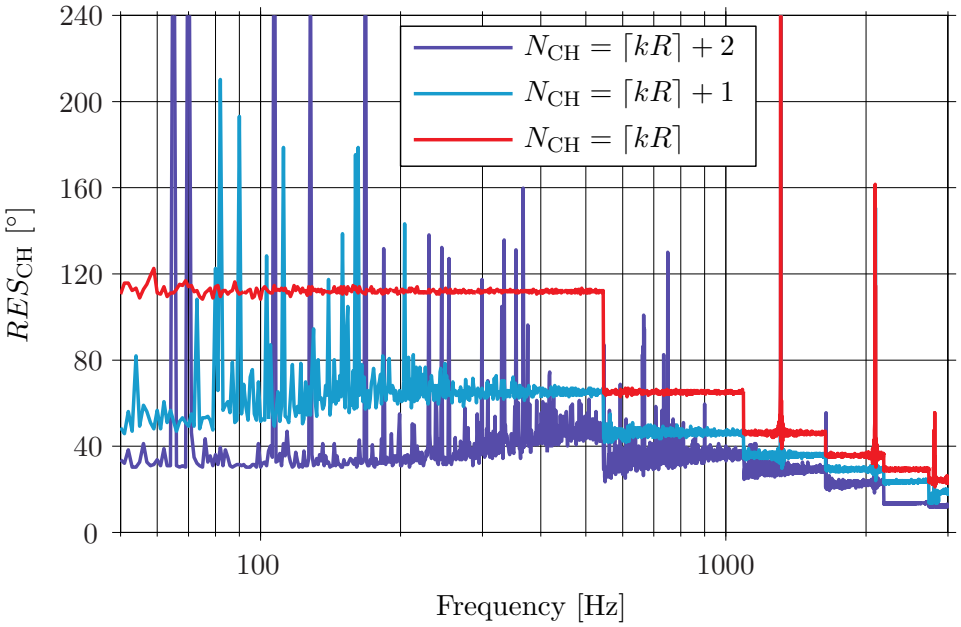

(a)

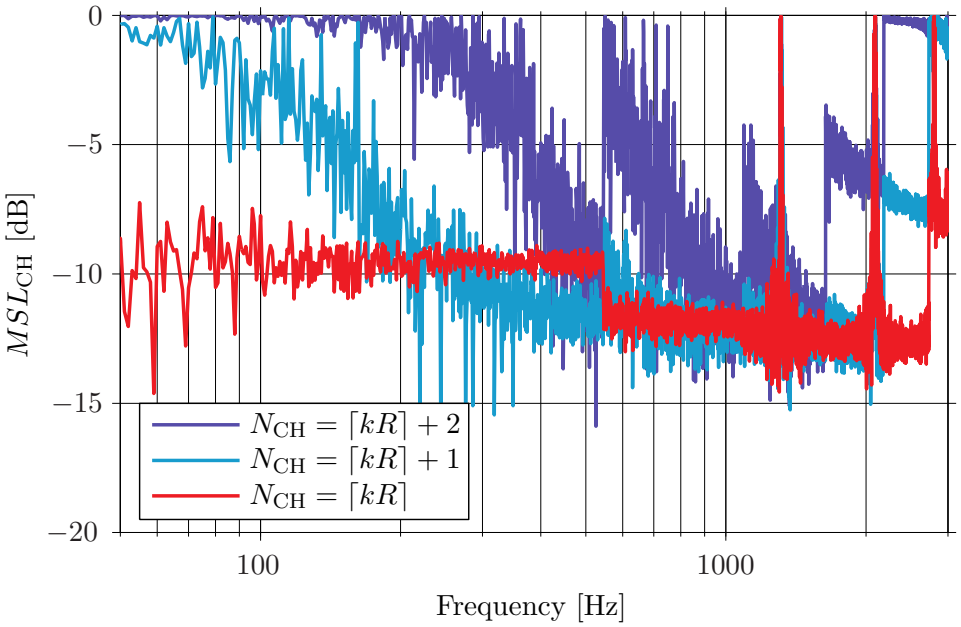

(b)

Figure 5.15: Resolution and MSL obtained with a CH beamformer when an unbaffled array of radius of 10 cm is used and the number of orders for the beamforming processing is $N = \lceil kR \rceil$, $N = \lceil kR \rceil + 1$ and $N = \lceil kR \rceil + 2$. The SNR_m is set to 30 dB.

It can be seen that at low frequencies the resolution and the MSL are more influenced by noise. In addition to this, the influence is stronger when the number of used orders increases. At high frequencies the resolution improves with increasing the number of orders, but at the same time the range where this occurs becomes smaller as the response is polluted with background noise in a wider frequency range. However, the MSL becomes worse in all frequency range when the number of orders increases. Just when $N = \lceil kR \rceil + 1$ the MSL is better or similar to the case of $N = \lceil kR \rceil$ in the range from 300 Hz to 2 kHz. In conclusion, if the array is required to cover a wide frequency range, the best option is to choose $N = \lceil kR \rceil$.

The last feature that is investigated is the influence of the number of microphones in the array. This is exemplified in figures 5.16 and 5.17 for an unbaffled array of 10 cm of radius when the number of microphones is the minimum required plus one more. The reason for choosing only these two different number of microphones is that with these numbers, 11 and 12, the relationship between M and N, i. e. $M > 2N$, admits the same maximum order N in both cases. In other words, as stated in table 5.1 on page 52, the maximum number of orders that can be used with an array of radius 10 cm and 11 microphones is 5. With 12 microphones, the maximum number of orders is still 5. If the number of microphones is increased to 13, the maximum number of orders is then 6, which implies that the response improves towards the higher frequencies with respect to those cases where the maximum number of orders is 5. Therefore, in order to compare the responses in the same conditions in terms of maximum order (and frequency range), the number of microphones can only be 11 or 12.

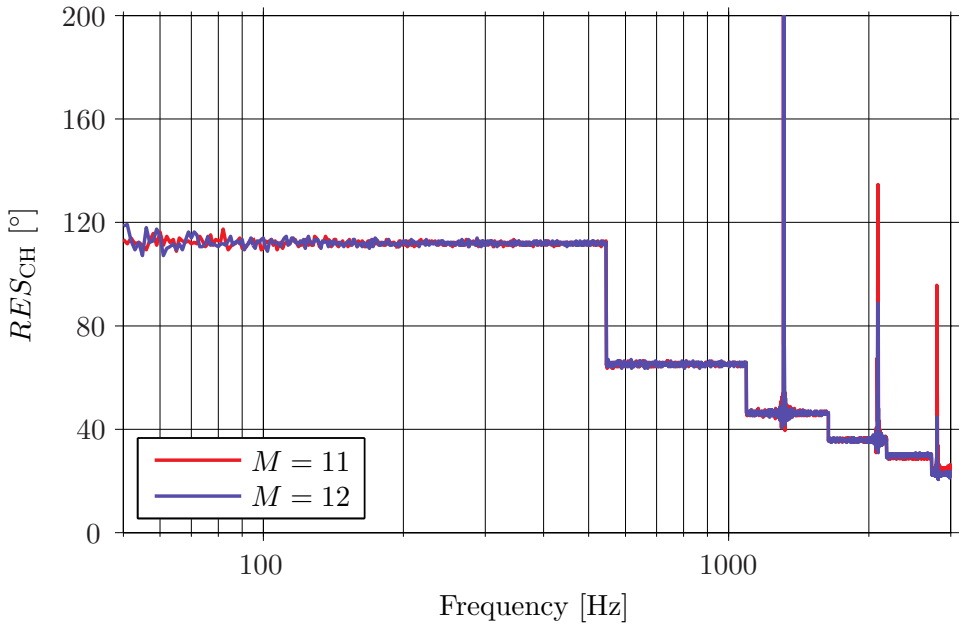

Figure 5.16: Resolution obtained with a CH beamformer when an unbaffled array of radius of 10 cm is used with 11 and 12 microphones. The SNR_m is set to 30 dB.

As can be seen, the result of using one more microphone than the minimum necessary do not have any significant influence in terms of resolution, but the MSL slightly improves at frequencies above $f_{\max}$.

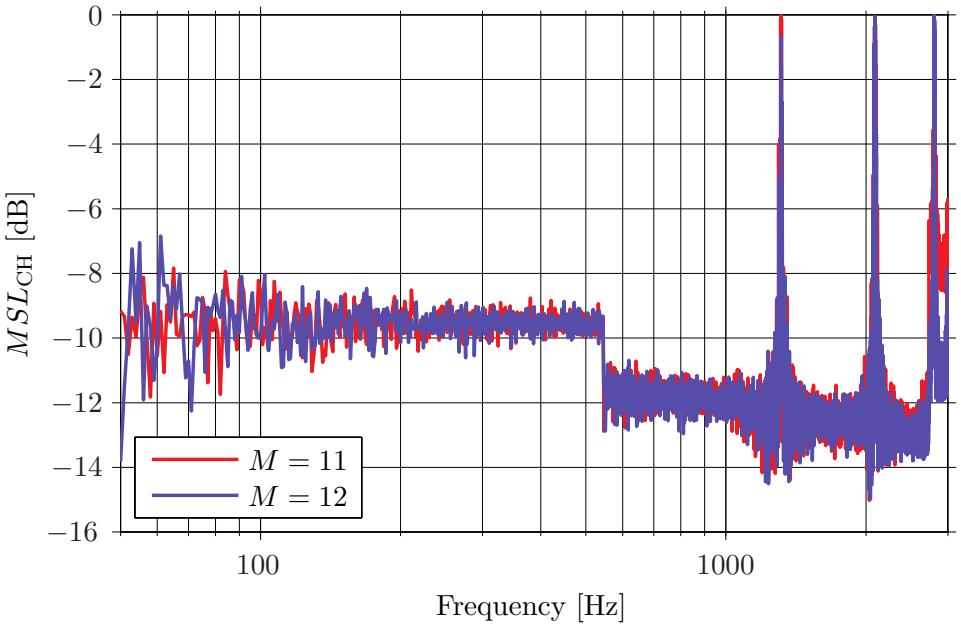

Figure 5.17: MSL obtained with a CH beamformer when an unbaffled array of radius of 10 cm is used with 11 and 12 microphones. The SNR_m is set to 30 dB.

5.3.3 Delay-and-Sum Beamforming

5.3.3.1 Performance in Ideal Conditions

The beampatterns obtained in ideal conditions by means of DSB are shown in figure 5.18, when unbaffled arrays of radius 5, 10 and 20 cm are considered. Note that again, a broadband source placed at 180° has been used. In DSB, the number of orders used for the processing is $N = \lceil kR \rceil + 1$. Later on, the reason for this will be explained.

As can be seen, the patterns are in all cases omnidirectional at low frequencies. With increasing frequency the main beam gets narrower and narrower and the number of side lobes increases. In addition to this, the beampattern becomes more directive when the radius of the array is increased. Approximately below $f_{\max}$, the side lobes gain strength in all cases, meaning that the sampling error arises. However, this error is not as obvious as in CHB. Apart from this, there are other differences from CHB, for instance, the lower frequencies are totally omnidirectional, the output varies continuously with frequency and all high frequencies can be resolved.

The patterns obtained with baffled arrays are shown in appendix A.2.2. In terms of directivity they are similar to the unbaffled case. However, they present some differences that will be analyzed by means of the resolution and the MSL. These two measures are shown in figure 5.19 for both baffled and unbaffled arrays.

As can be seen in all cases, at low frequencies the resolution is 360° and the MSL is non-existent, as the beamformers are omnidirectional. From a certain frequency that depends on the beamformer, the resolution improves continuously until high frequencies. The curves decay in a similar way for both kinds of arrays, but in the baffled case they present very smooth fluctuations. The MSL curves begin in a certain frequency and grow progressively until a maximum level. In the case of unbaffled arrays, this level

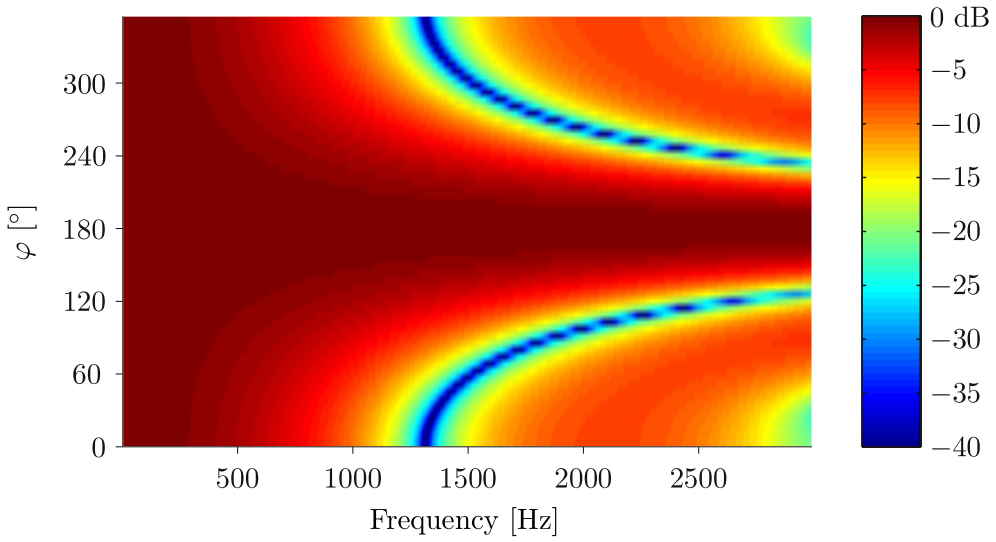

(a) DSB, $R = 5$ cm, Unbaffled.

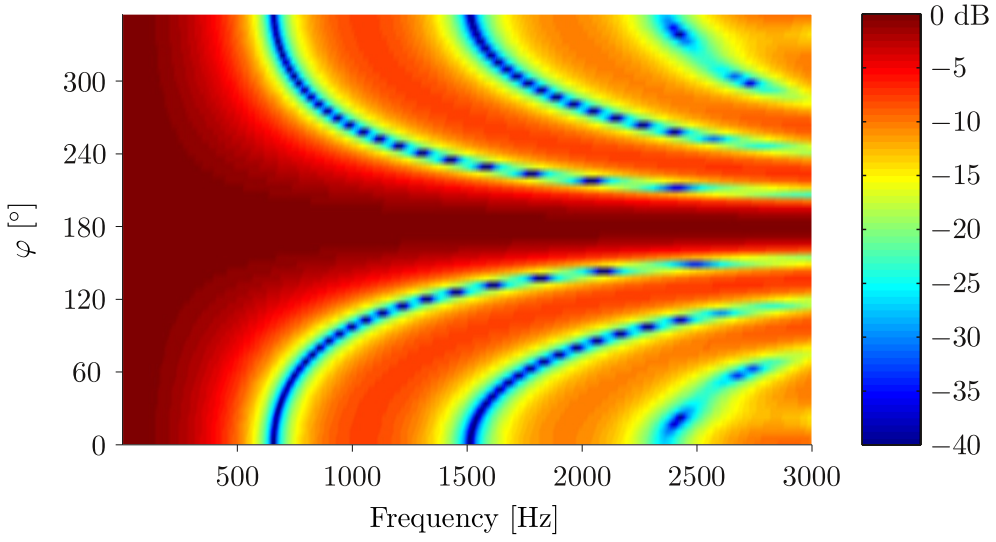

(b) DSB, $R = 10$ cm, Unbaffled.

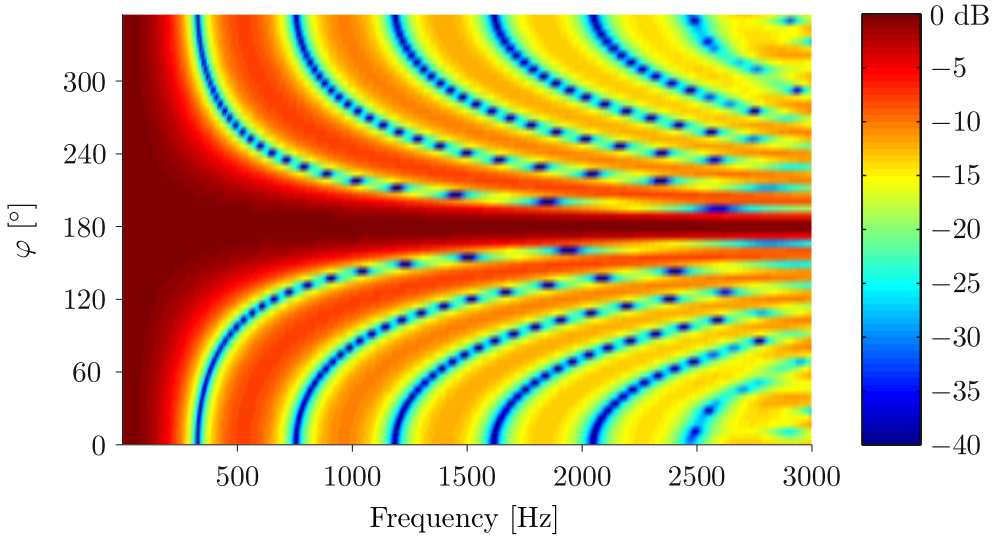

(c) DSB, $R = 20$ cm, Unbaffled.

Figure 5.18: Normalized outputs of three DS beamformers that use unbaffled circular arrays of radius 5, 10 and 20 cm, when a source is placed at 180°. The features of each array are shown in table 5.1.

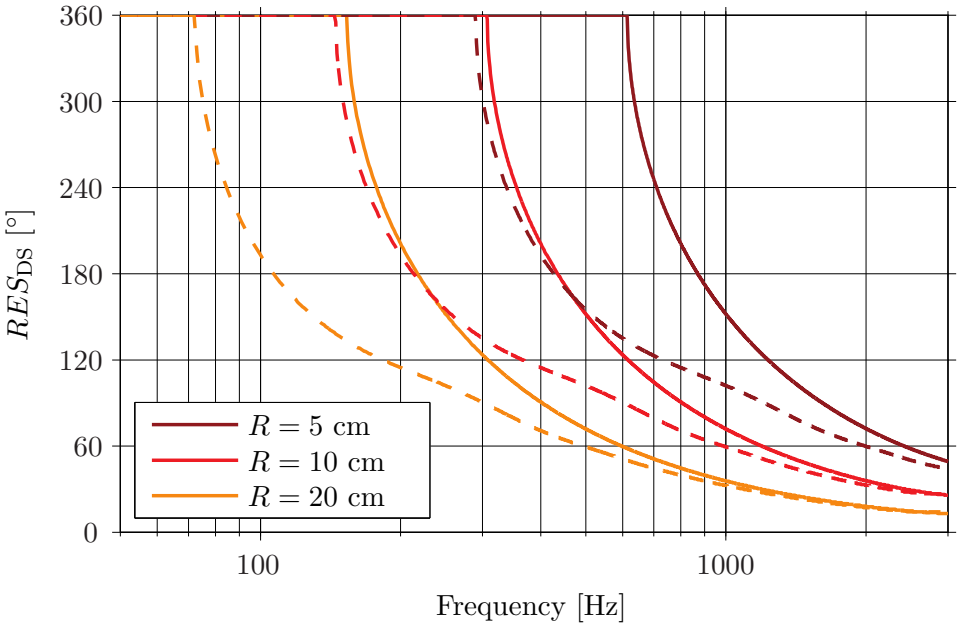

(a)

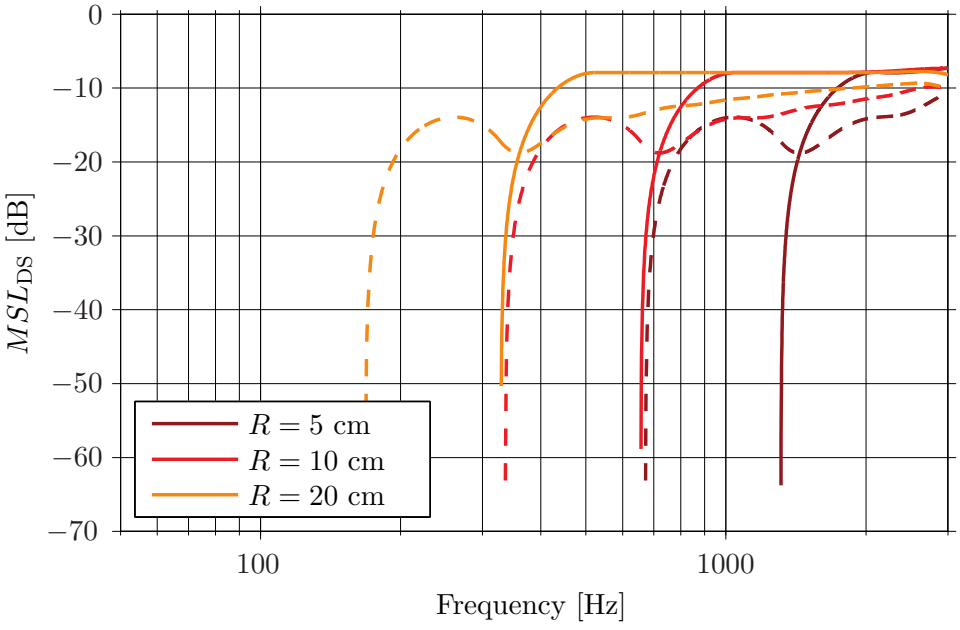

(b)

Figure 5.19: Resolution and MSL of three DS beamformers that use both baffled and unbaffled circular arrays of radius 5, 10 and 20 cm, when a source is placed at 180°. The responses of the unbaffled arrays are the ones with continuous lines, whereas the responses for the baffled arrays are dashed. The features of each array are given in table 5.1.

is kept constant, whereas for baffled arrays the MSL presents smooth ripples while it increases towards high frequencies. Nevertheless, the MSL is better for baffled arrays than for unbaffled.

Independently of baffled or unbaffled arrays, the performance improves with increasing the radius of the arrays and is better in the case of baffled arrays. Furthermore, it can be seen that the baffled array of 5 cm of radius has a resolution similar to the unbaffled array of radius 10 cm, the resolution of the baffled array of 10 cm is similar to the one of the unbaffled array of 20 cm, etc. Therefore, the fact of mounting the array on an infinite baffle makes the array appear to be 'larger' than in the unbaffled case. This tendency can also be observed in the MSL curves. Similar characteristics are found when DSB is applied to spherical arrays [20].

In general, it can be said that the resolution obtained with DSB is much worse than the one obtained with CHB because in that case all the frequency range was 'covered', whereas with DSB only high frequencies are resolved with accuracy but low frequencies are totally unresolved. At high frequencies, the MSL using DSB is worse than in CHB when unbaffled arrays are used. Despite of this, just the opposite occurs when dealing with baffled arrays.

It is interesting to analyze if the resolution and the MSL are independent of the position of the source. Like in the case of CHB, this is done for a specific frequency as a function of φ_s. The resolution and MSL obtained with an unbaffled array of 10 cm are shown in figures 5.20 and 5.21. The frequencies used previously with CHB in figures 5.9 and 5.10 are chosen again. The resolution used for φ_s is 0.005 rad.

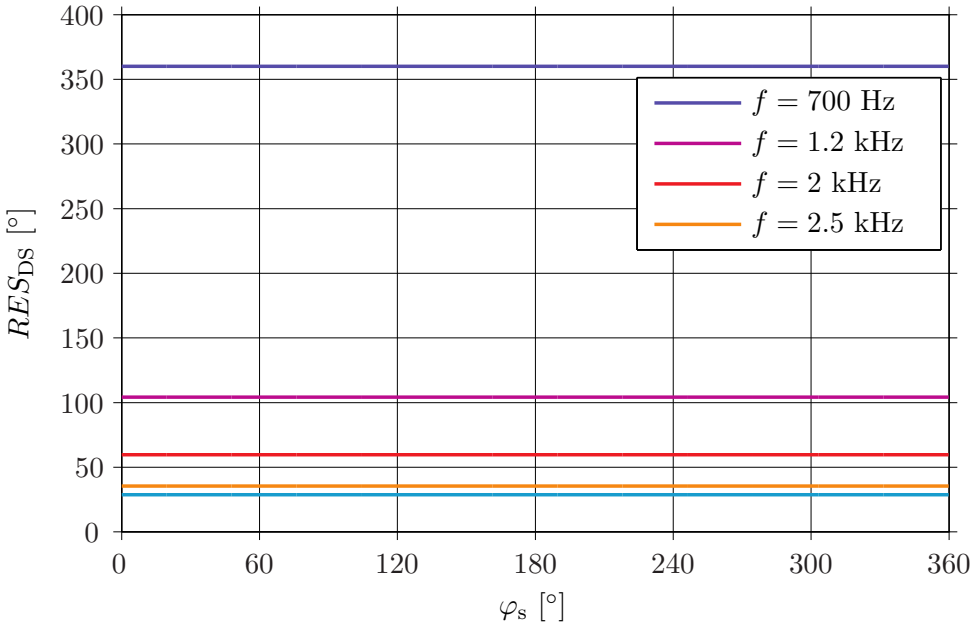

Figure 5.20: Resolution obtained using DSB with an unbaffled array of radius 10 cm at different frequencies as a function of the angular position of the source. The features of the array are given in table 5.1.

These results reveal that the resolution and the MSL are independent of the source position at frequencies up to 2.5 kHz. In the case of a baffled array, which is shown

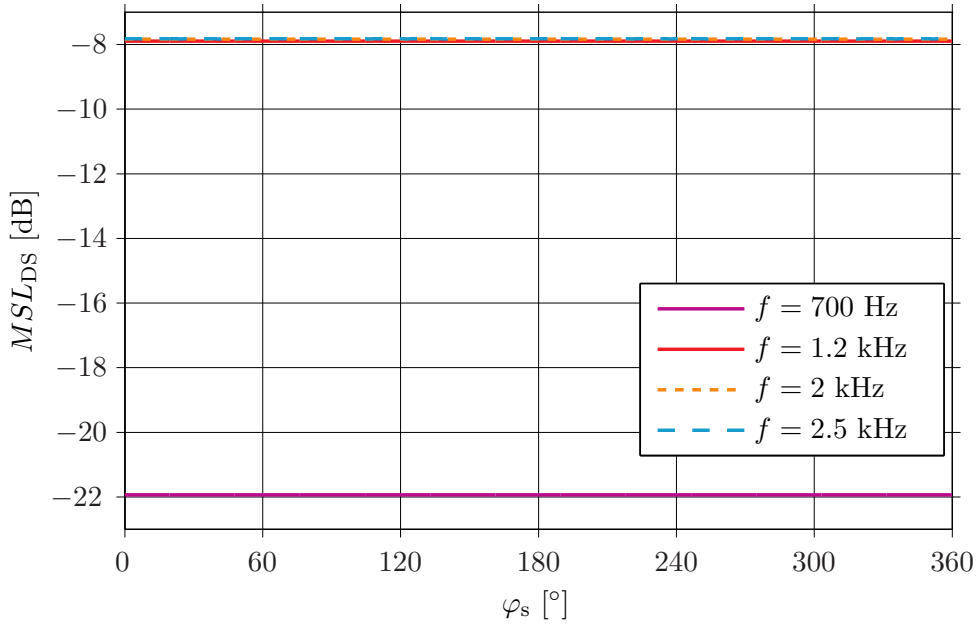

Figure 5.21: MSL obtained using DSB with an unbaffled array of radius 10 cm at different frequencies as a function of the angular position of the source. The features of the array are given in table 5.1.

in figure A.12 in appendix A.2.2, a dependency of the angle can be seen at 2 kHz and 2.5 kHz.

5.3.3.2 Performance with Influence of Background Noise

The performance of DS beamformers must be evaluated in realistic situations that account for background noise. Like in the case of CHB, the SNR at the input of each array microphone (SNR_m) is set to 30 dB.

The resolution and the MSL when background noise is present is given in figure 5.22 when unbaffled arrays are used. As can be seen, the results of both resolution and MSL follow the curves obtained for the ideal case rather accurately. This is also obtained with baffled arrays as can be seen in appendix A.2.2. In contrast with CHB, DSB is more robust to background noise.

Similarly to CHB, the influence of noise on a DS beamformer can be deduced by inserting the relationships found in equations (5.4) and (5.6) into the beamformer output given in equation (4.26) on page 41. This is

$$b_N(kR,\varphi) = \sum_{n=-N}^{N} \tilde{\mathcal{C}}_n(kR,\varphi_{\mathrm{s}})\mathcal{C}_n^*(kR,\varphi) + \mathcal{N}_n\mathcal{C}_n^*(kR,\varphi). \tag{5.7}$$

Assuming $\varphi = \varphi_{\mathrm{s}}$, the first term in the summation is approximately $|\mathcal{C}_n(kR,\varphi_{\mathrm{s}})|^2$ and the second one is random noise that multiplies the coefficients shown in figures 3.3 on page 18 or 3.5 on page 19, depending on the condition of baffled or unbaffled. For orders higher than 0, these coefficients, which present a high-pass filter characteristic

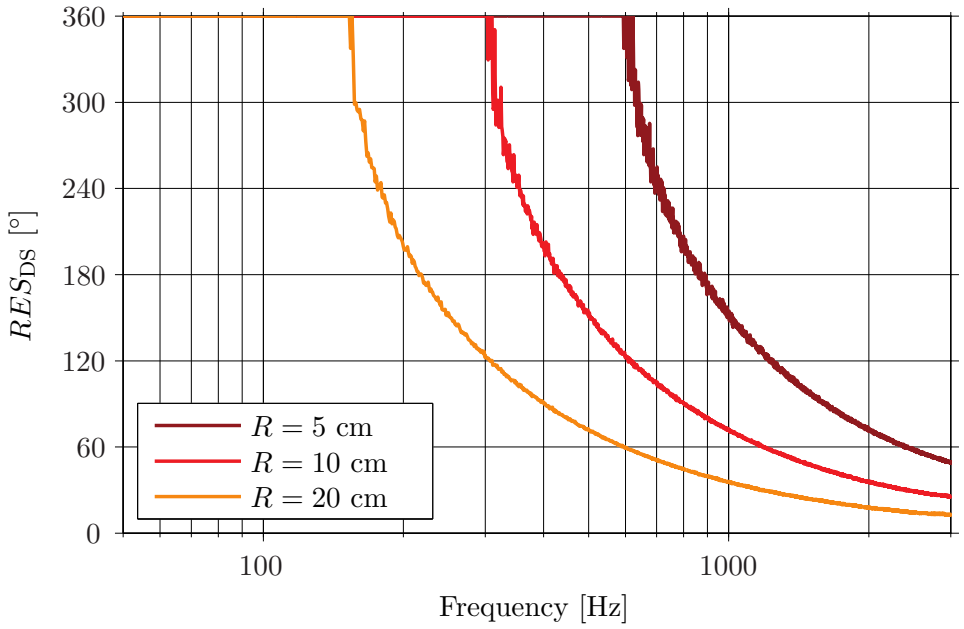

(a)

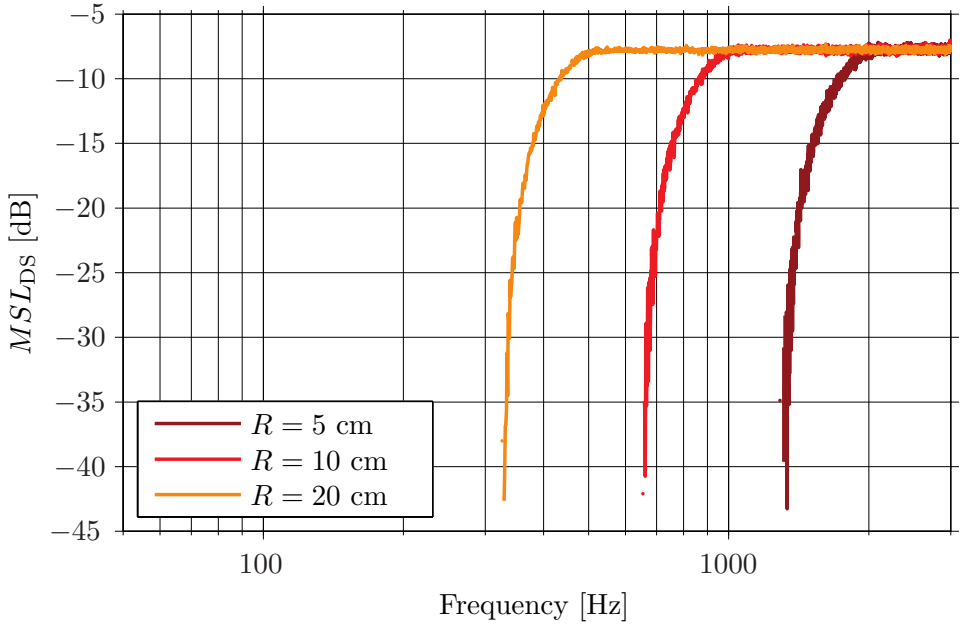

(b)

Figure 5.22: Resolution and MSL of three DS beamformers that use unbaffled circular arrays of radius 5, 10 and 20 cm, when a source is placed at 180° and the SNR in the array microphones is 30 dB. The features of each array are given in table 5.1.

with steeper roll-off as the order increases, attenuate the background noise. This makes the response of the DS beamformer more influenced by the first term (the one that contains the information about the source) than by the noise term.

In contrast to CHB, it becomes obvious from the foregoing reasoning that when the maximum number of orders used for the DS beamformer is increased the noise contribution is practically unaltered. For CHB it turns out that the best option for the processing is when $N = \lceil kR \rceil$, but for DSB this is no longer necessary. In figures 5.23 and 5.24, the resolution and the MSL for the cases $N = \lceil kR \rceil$ and $N = \lceil kR \rceil + 1$ are shown using a DS beamformer. An unbaffled array of 10 cm of radius has been considered.

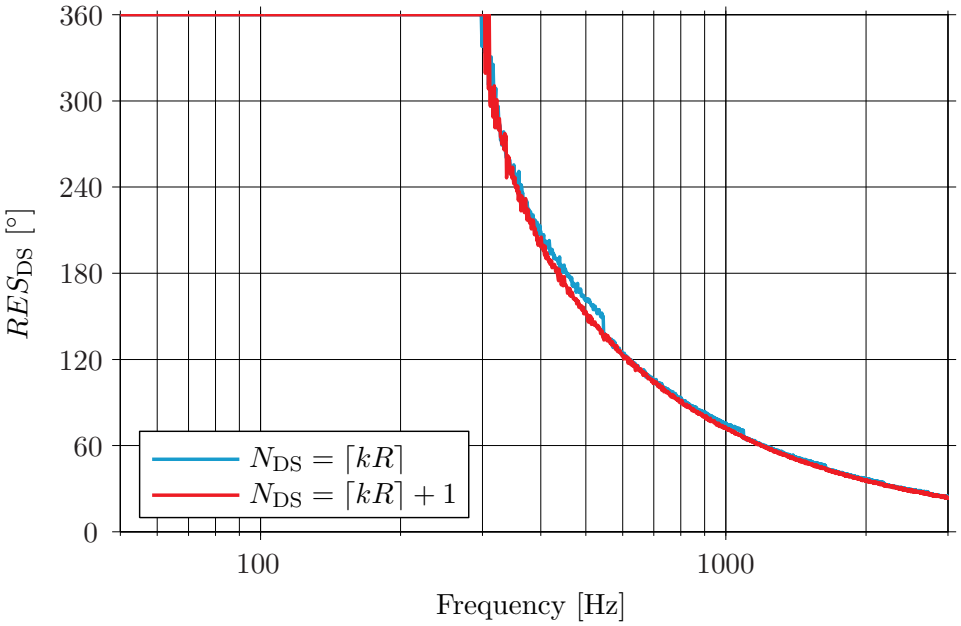

Figure 5.23: Resolution obtained using DSB with an unbaffled array of radius 10 cm when the number of modes used for the beamforming processing is $N = \lceil kR \rceil$ and $N = \lceil kR \rceil + 1$. The SNR_m is set to 30 dB.

As can be seen, the results are very similar for both values of N, but slightly better when $N = \lceil kR \rceil + 1$.

Even though it is not shown here, when the number of orders is further increased no significant improvement with respect to the case of $N = \lceil kR \rceil + 1$ results.[1] For this reason, $N = \lceil kR \rceil + 1$ is preferred for the DSB processing.[2]

Like in the case of CHB, the number of microphones has been increased in order to examine the effect. However, no improvement has been detected. This is illustrated in figure A.13 in appendix A.2.2, where the performance of an unbaffled array of 10 cm with 11 and 12 microphones is shown.

[1] A detailed mathematical proof can be found in appendix A.5.

[2] Note that in all figures of this document that concern DSB, the number of orders have always followed $N = \lceil kR \rceil + 1$.

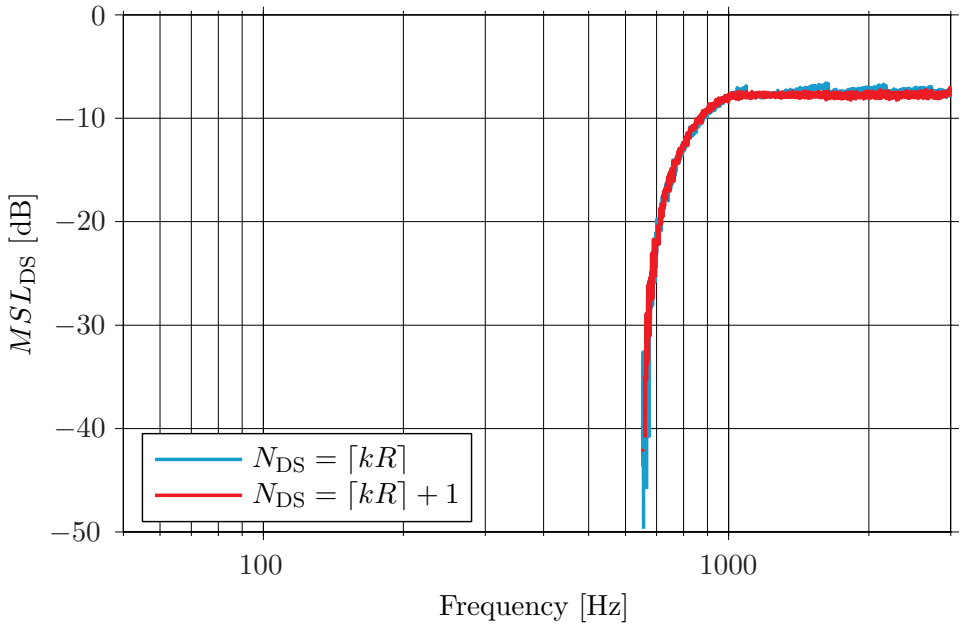

Figure 5.24: MSL obtained using DSB with an unbaffled array of radius 10 cm when the number of modes used for the beamforming processing is $N = \lceil kR \rceil$ and $N = \lceil kR \rceil + 1$. The SNR_m is set to 30 dB.

5.4 Array Design and Prototype Characteristics

From the results of the simulations, it has been seen that in both techniques, DSB and CHB, the larger the array radius the better the performance. In CHB both the resolution and the MSL were fair enough in the frequency range of interest (from 100 Hz to about 3 kHz) for arrays of 10 and 20 cm. However, in the case of DSB a smaller range can be covered with these radius, so an array of much larger radius should be used. Due to the constraints of the array in terms of size and the number of microphones, an array of 10 cm is suggested for the design of the prototype. According to section 3.2.2.2, it is not clear when an array mounted on a finite cylinder can be approximated by an array mounted on an baffle of infinite length. Consequently, it is decided that the prototype must be unbaffled.

Due to technical limitations, the prototype is a circular array with radius of 11.9 cm, instead of 10 cm. The number of microphones can be chosen to be 11 or 12. This implies that the maximum order is $N = 5$ and that the maximum frequency that can be represented without having sampling error is around 2293 Hz, which is smaller than the case of an unbaffled array of 10 cm. To compensate for these differences, the number of microphones is established to be 12, since according to the simulations in section 5.3.2.2 this extends the beamformer performance up to higher frequencies when CHB is used (see figure 5.17). The implemented prototype is shown in figure 5.25.

The resolution and the MSL of the prototype have been simulated using CHB and DSB. The results which account for the influence of background noise are shown in figure 5.26. The number of modes that have been used follows $N = \lceil kR \rceil$ for CHB and $N = \lceil kR \rceil + 1$ for DSB. Although the source considered for the simulations is placed

Figure 5.25: Circular array with radius of 11.9 cm and 12 microphones. Prototype implemented by Brüel & Kjær.

at 180°, the performance obtained with this source can be extrapolated to other source directions as, according to sections 5.3.2.1 and 5.3.3.1, the resolution and the MSL obtained with CHB and DSB are independent of the source position up to frequencies slightly below $f_{\max}$.

As can be seen, at low frequencies the performance is much better with CHB in terms of both resolution and MSL. The resolution is in both cases similar above 1.3 kHz, approximately. However, in this range the MSL using DSB is 5 dB higher than the one obtained with CHB. The approximated values of the resolution and the MSL for the case of CHB are given in table 5.2, where the discontinuities at high frequencies caused by the Fourier coefficients of an unbaffled aperture are also indicated.

Table 5.2: Approximated resolution and MSL when CHB is used with an unbaffled array of 11.9 cm of radius and 12 microphones. The discontinuities where the resolution and the MSL worsen due to the dips in the Fourier coefficients are also given.

Frequency range [Hz]	Resolution [°]	MSL [dB]	Discontinuities
50–458	112	−10	
459–917	65	−12	
918–1376	46	−12	1100 Hz
1377–1834	36	−12	1760 Hz
1835–2293	31	−13	
2294–2752	22	−11	2357 Hz; 2536 Hz

In conclusion, the performance using CHB is more appropriate for the purpose of the array, which is the localization of noise sources in the frequency range from 100 Hz to about 3 kHz. However, in section 5.3.3 it has been seen that DSB is more robust in terms of background noise, and hence this technique should be taken into account in

noisy environments. Furthermore, DSB can be used to resolve those high frequencies where CHB presents discontinuities.

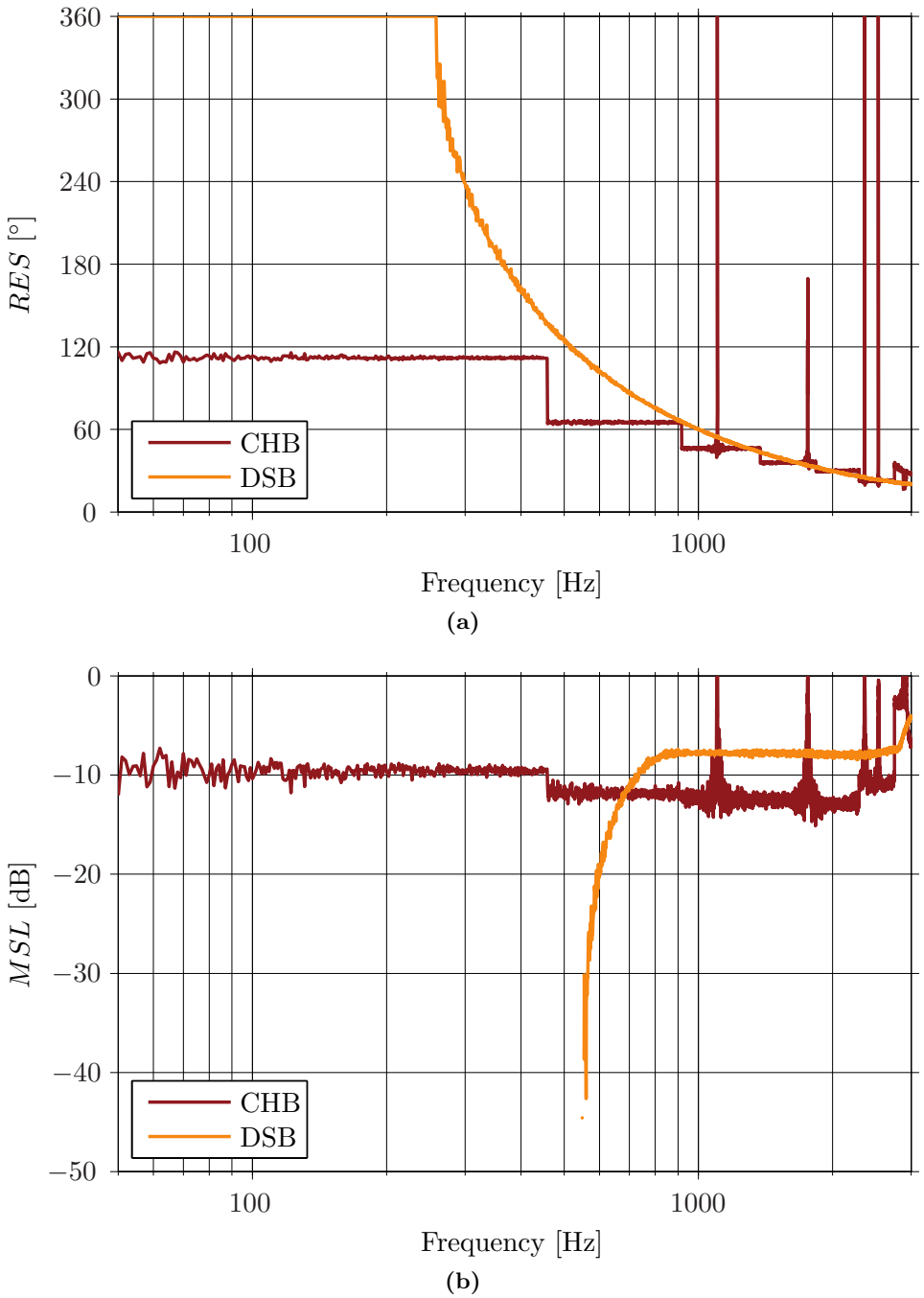

Figure 5.26: Simulated resolution and MSL of an unbaffled array of 11.9 cm of radius and 12 microphones when CHB and DSB are used. A source at 180° has been considered and the SNR_m has been set to 30 dB.

6

Measurement Results and Discussion

6.1 Measurement Setup

A circular array of radius 11.9 cm with 12 equidistant microphones has been tested in an anechoic chamber at the Acoustic Technology Department of the Technical University of Denmark (DTU).

The array is conformed by 1/4 ” microphones *B&K Type 4935* embedded on a circular frame every 30°. In all the measurements, it stands on a turntable *B&K Type 5960*. The turntable is placed on a support that is anchored to the ground of the room which is about 3 m below the support. In figure 6.1, a sketch of the arrangement of the equipment in the anechoic chamber can be seen. The array position is kept along the

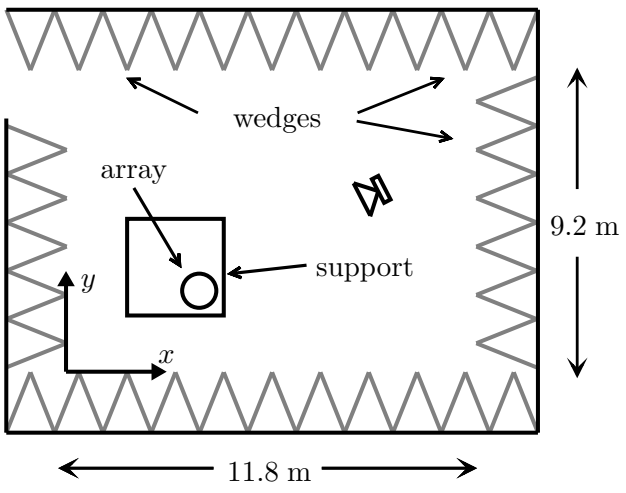

Figure 6.1: Arrangement of the equipment in the anechoic room.

measurements at $x = 4.5$ m, $y = 3.8$ m and $z = 4$ m according to the coordinates given in the sketch. The equipment setup used for the measurements is shown in figure 6.2. The characteristics of all the equipment are described in appendix C.

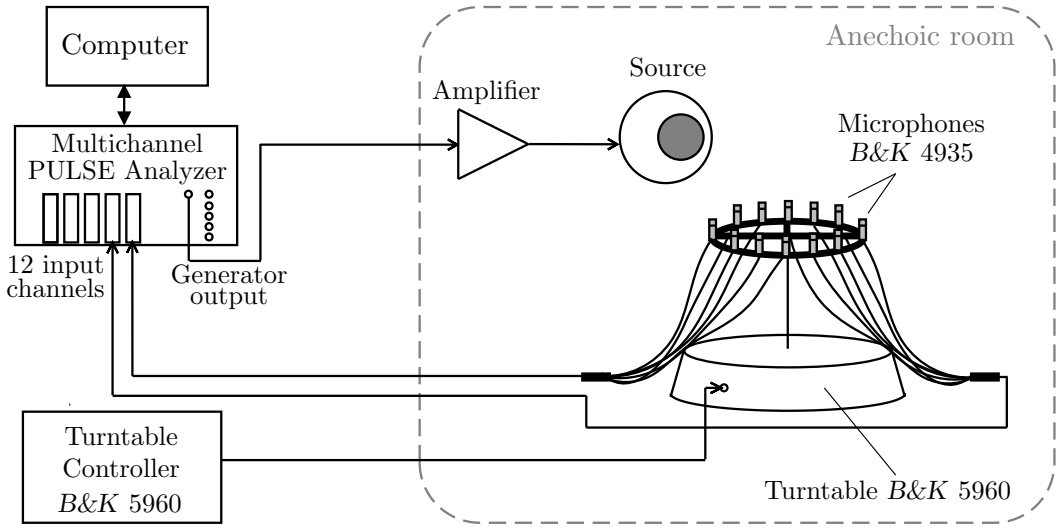

Figure 6.2: Equipment setup. The array and the source are controlled by a PULSE Analyzer and the turntable is managed by its own controller.

The array and the source are controlled by means of a Brüel & Kjær Multichannel PULSE Analyzer that includes various input-channels and one generator output. In all the measurements, the signal from the generator feeds the source after being amplified. In order to excite the entire frequency range of the array in each measurement, the generator signal is pseudorandom noise of 1 s of period, 3.2 kHz of bandwidth and 1 Hz of resolution. The advantage of using pseudorandom noise is that each frequency component has the same amplitude in each period, and hence the average over several periods is not necessary.

The signals captured by the microphones of the array are recorded with the analyzer. Note that these signals are the result of the loudspeaker signal at the measurement point plus background noise. The signals are then processed with the beamforming algorithms DSB and CHB developed in chapter 4. For the processing, an angular resolution of 0.005 rad is used, and the number of orders used to decompose the sound field is $N = \lceil kR \rceil$ for CHB and $N = \lceil kR \rceil + 1$ for DSB.

In all measurements, the source, which is a loudspeaker unit mounted on a sphere, hangs from the ceiling of the anechoic room in order to keep it as static as possible. This can be seen in figure 6.3. The source is placed far enough from the array so the impinging waves are created in the far-field.

To evaluate the performance of the array for different angular directions of the source, the source is kept still at a certain position, whereas the array is moved around its z-axis by means of the turntable. This procedure is very convenient because the direction of the source varies with respect to the array without having to move the source. The rotation can be done with an accuracy of 1°, which corresponds to the resolution of the turntable.

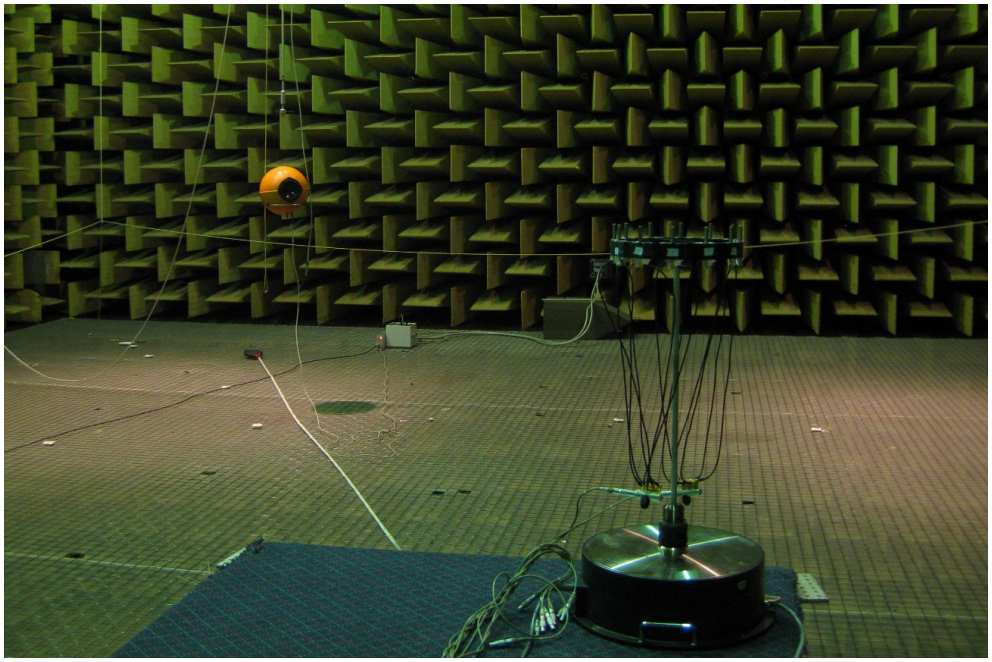

Figure 6.3: Picture of the arrangement of the array and the source in the anechoic chamber used in most of the measurements. The array stands on a turntable and the source hangs from the ceiling.

6.2 Beamformers Output

In this section, the output of the beamformers is analyzed and compared with the simulations. The measurements are performed with the source placed at $x = 8.4$ m, $y = 5.8$ m and $z = 4$ m, so the distance to the center of the array is about 4.6 m. The array is rotated with the turntable in order to have the source at 180°.

The microphone signals are recorded during 1 s, which corresponds to one period of the signal generator. The equivalent sound pressure level $L_{\mathrm{eq},m}$ in each microphone is, in average, 71 dB SPL, whereas the level of the background noise is estimated to be 35 dB SPL during the measurement.

The normalized output obtained with CHB is shown in figure 6.4. For ease of comparison with the theoretical case, the simulated output is also provided in this figure. Note that an SNR of 30 dB due to a uniformly distributed noise at the input of the microphones has been considered for the simulations, according to section 5.3.2.2.

The beampattern agrees fairly well with the simulations and just few differences require to be commented. On the one hand, the side lobes are deformed and blurred compared to the simulations. On the other hand, the output is not only distorted at those frequencies that coincide with the dips in the Fourier coefficients used for the beamforming algorithms (see section 5.3.2), but also at several frequencies in their vicinity. This phenomenon is specially observed around 1.7 kHz.

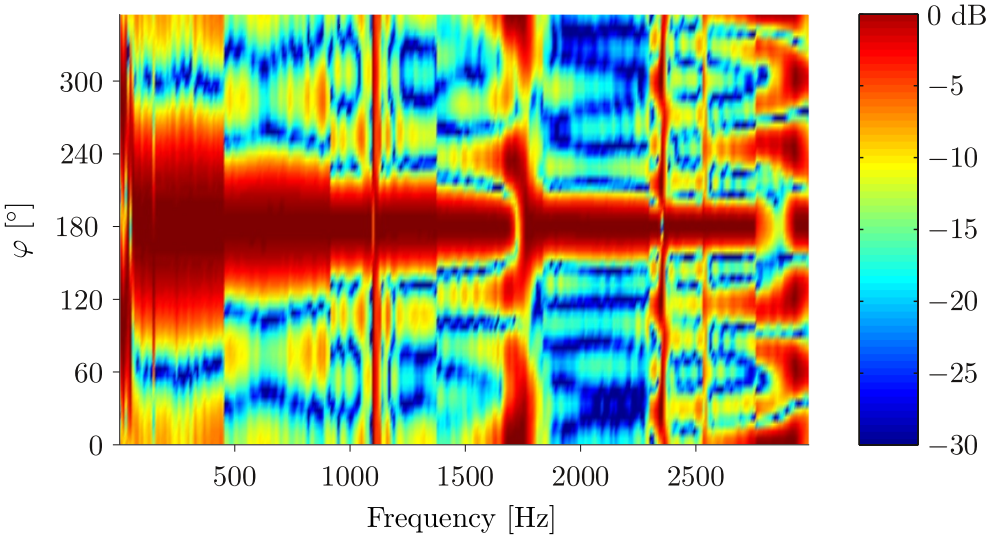

(a) Measurement.

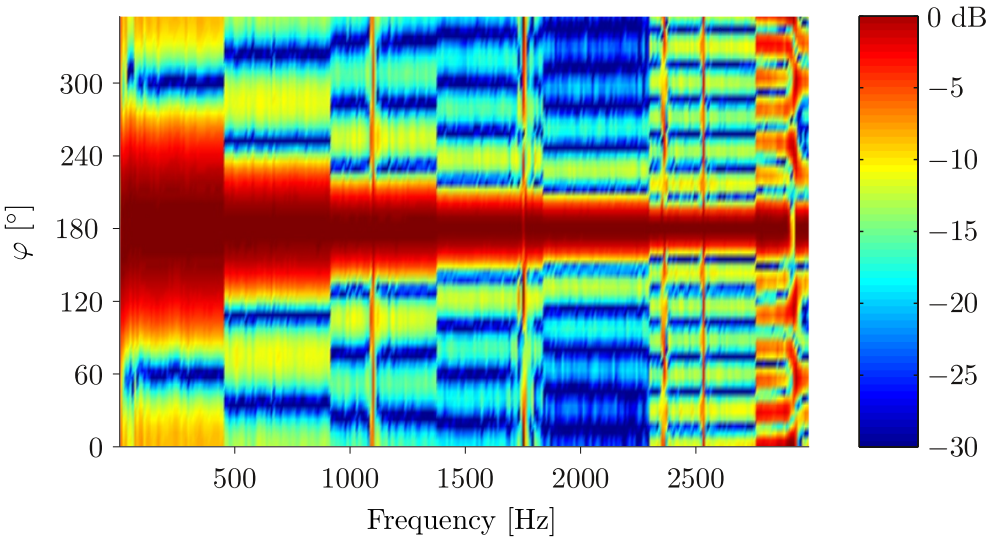

(b) Simulation.

Figure 6.4: Normalized output of a CH beamformer that uses an unbaffled array of 11.9 cm of radius with 12 microphones, when a source is placed at 180°. The top panel shows the measurements performed with a prototype, whereas a simulation is given in the bottom panel. For the simulation an SNR of 30 dB in the input of each microphone has been considered.

These differences are mainly caused by the CH beamformer algorithm itself. As seen in equation (4.19) on page 37, the approximated Fourier coefficients obtained by decomposing the sound field using the array are compared to the theoretical ones by means of a division. When the approximated coefficients match the theoretical ones, the beamformer output yield a similar pattern than the expected in ideal conditions. This is actually the case of the approximated coefficients obtained by means of simulations which are very similar to the theoretical ones as can be seen in figure A.16 in appendix A.3. In figure 6.5, the measured coefficients are shown together with the

theoretical ones. In contrast to the case of the simulations, it can be seen that the theoretical and the measured coefficients are not completely similar, and hence differences between the expected and the measured outputs are observed in figure 6.4. At this point it should be emphasized that the number of orders used for the CH beamformer calculation follows $N = \lceil kR \rceil$. In this sense, the high deviations at low frequencies for orders higher than two, due to the presence of background noise, should not be taken into account for the comparison since these orders are not used for the algorithm at such frequencies. In the frequency range where each order is used, it can be seen that all approximated coefficients present some ripples that are not present in the theoretical case, but in general they follow the same tendency. The most remarkable difference is observed at the dip obtained for the first order as it does not coincide with the theoretical case, see panel (b). In fact, this is the cause that makes the output shown in figure 6.4 present unresolved frequencies in a relatively wide frequency range around 1.7 kHz.

The differences between measurements and simulations can be further examined by studying the resolution and the MSL. These quantities are shown in figure 6.6. The resolution is very similar to the one obtained with the simulation. It can be seen that the response follows the simulation curve rather accurately and even those frequencies that present singularities practically coincide. Just small deviations can be observed at the lowest frequencies, which are attributed to the influence of background noise.

In contrast with the resolution, the MSL deviates somewhat from the simulation. In general, this measure is higher than the expected one and worsens in the surroundings of the singularities. Besides, it is rather high at frequencies below 100 Hz, though this is not a problem since these frequencies are not required for the performance of the array. These deviations from the theoretical case are mainly related to, on the one hand, the influence of background noise and, on the other hand, the difference between the measured Fourier coefficients and the theoretical ones. For example, it can be seen that the ripples at around 300 Hz and 450 Hz coincide completely with the deviations between the measured coefficient of order zero and the theoretical one in the same frequency range.

In chapter 5, it was observed that CHB is rather vulnerable to noise, and this can particularly be seen in the MSL as it is more sensitive measure than the resolution. In addition to this, it can also be stated that the MSL is highly affected by the differences between the measured Fourier coefficients and the expected ones.

In figure 6.7, the normalized output obtained with the DS beamformer is shown. As can be seen, the results agree very well with the theoretical ones. This is also observed with the resolution and the MSL which are provided in figure 6.8. There are only a few differences compared with the simulations. The first one is that the resolution equals 360°, meaning that the main lobe is omnidirectional, up to a frequency 20 Hz higher than expected, see panel (a). The second difference is that the first side lobe appears at 634 Hz instead of 556 Hz as obtained in the simulation, see panel (b). The last main difference is that the MSL is better than expected in the range from 1950 Hz to about 2300 Hz. These differences are again mainly attributed to the differences between the measured Fourier coefficients and the theoretical ones. However, the beampattern as well as the resolution and the MSL, are not that affected by these differences like in the case of CHB. This proves again that DSB is a more robust algorithm.

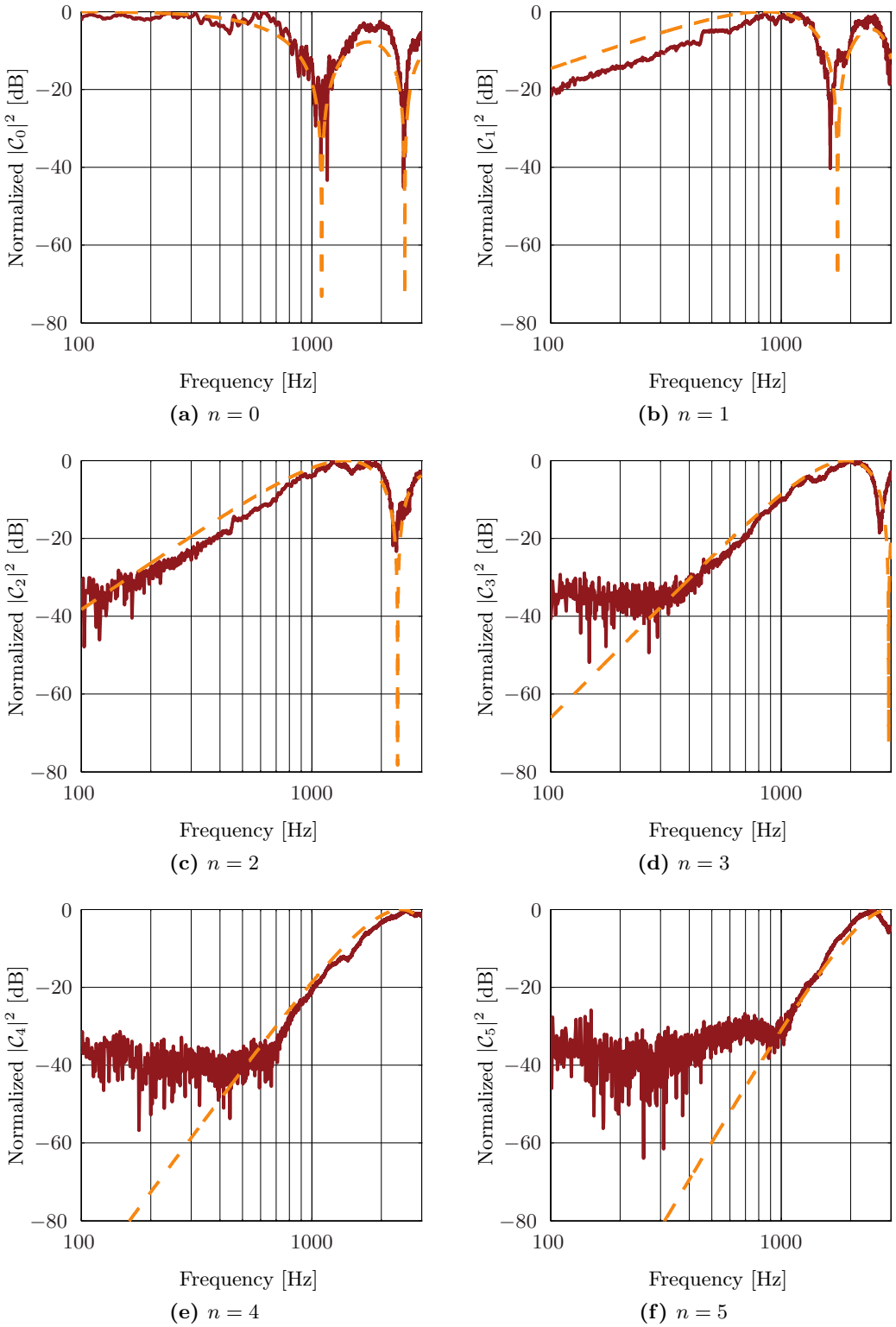

(a) $n = 0$ **(b)** $n = 1$

(c) $n = 2$ **(d)** $n = 3$

(e) $n = 4$ **(f)** $n = 5$

Figure 6.5: Comparison between the theoretical Fourier coefficients (dashed line) and the approximated Fourier coefficients measured with an array of 11.9 cm of radius and 12 microphones (continuous line).

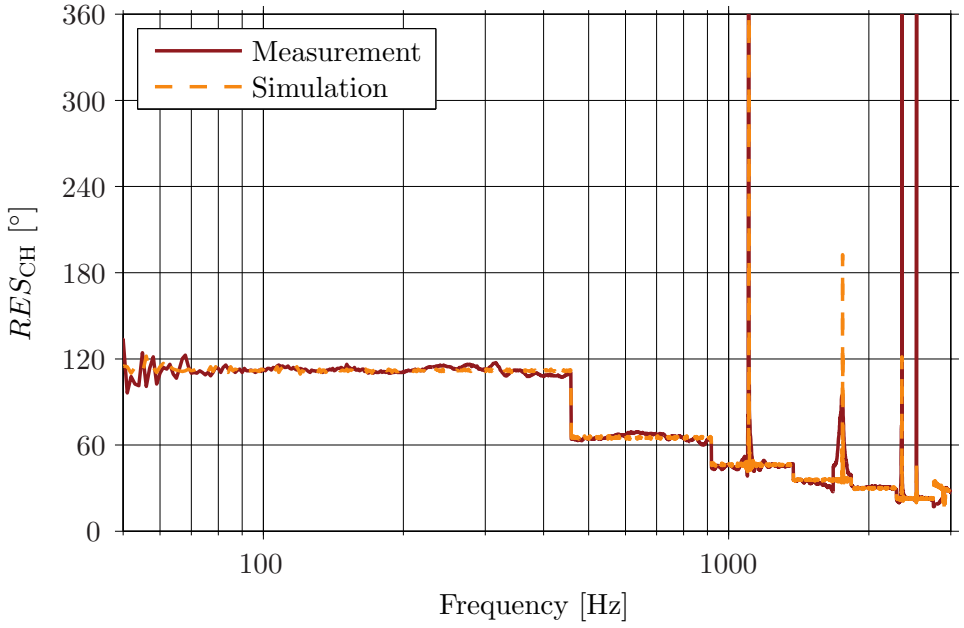

(a)

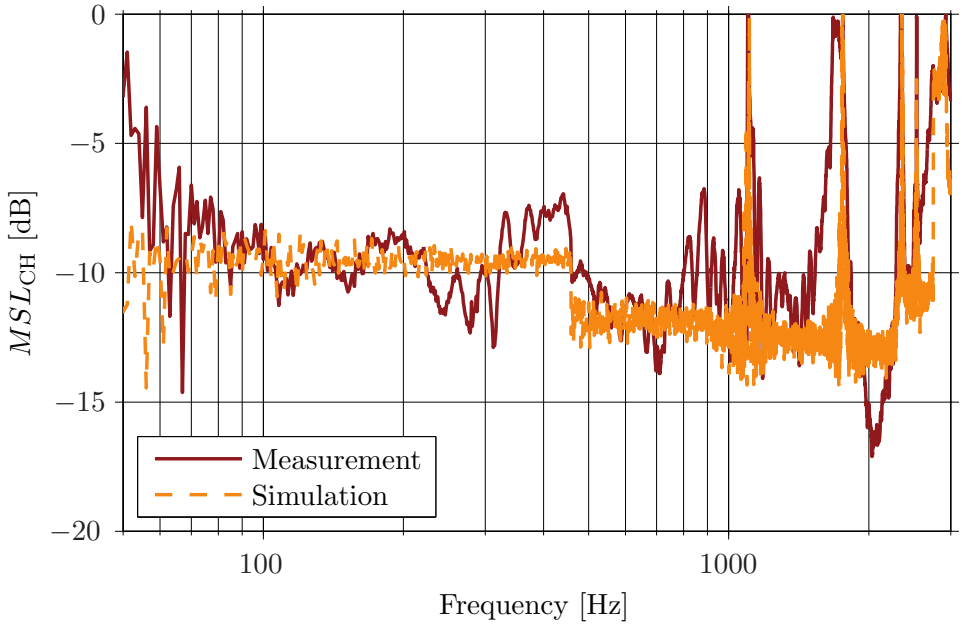

(b)

Figure 6.6: Resolution and MSL of a CH beamformer that uses an unbaffled array of 11.9 cm of radius with 12 microphones, when a source is placed at 180°. The theoretical case obtained by means of a simulation is also displayed. The SNR in each microphone has been set to 30 dB for the simulation.

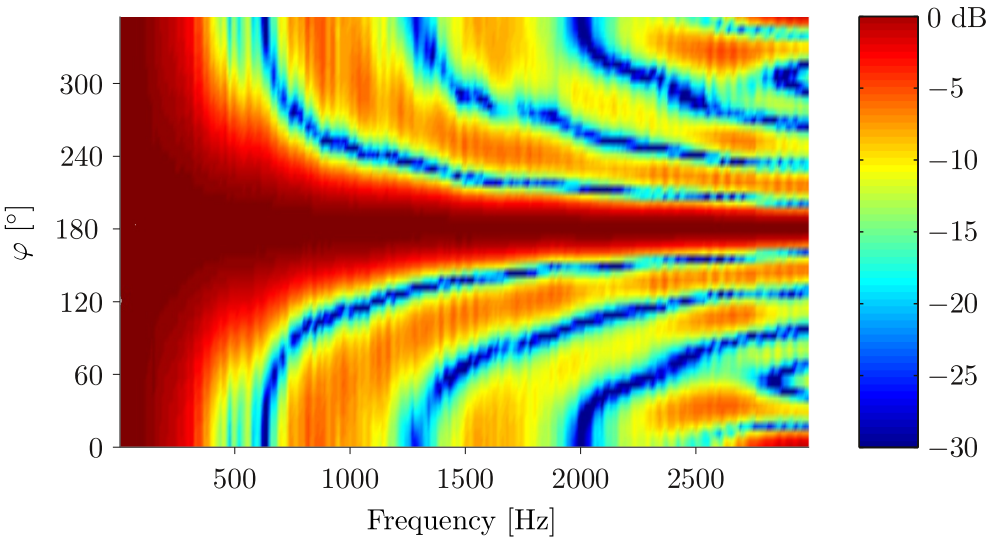

(a) Measurement.

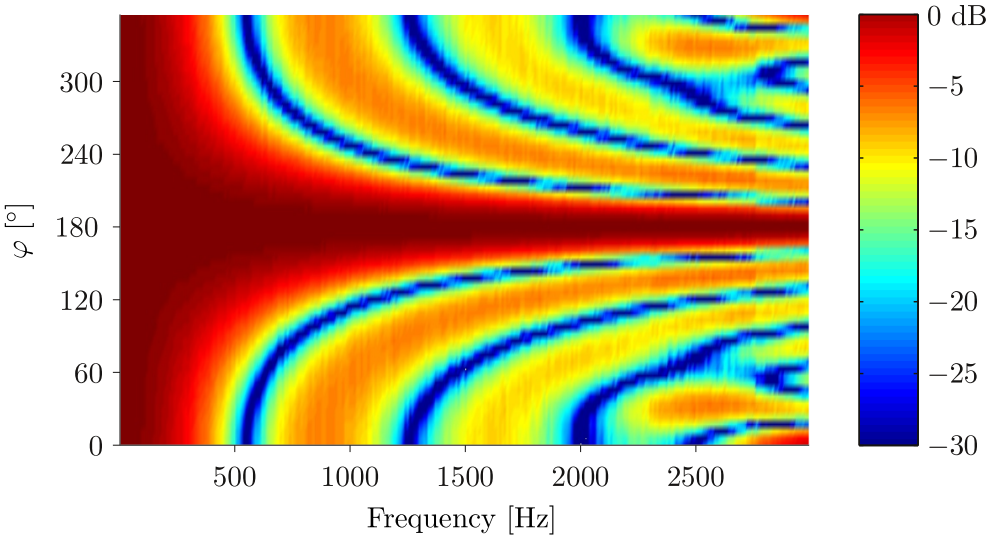

(b) Simulation.

Figure 6.7: Normalized output of a DS beamformer that uses an unbaffled array of 11.9 cm of radius with 12 microphones, when a source is placed at 180°. The top panel shows the measurements performed with a prototype, whereas a simulation is given in the bottom panel. For the simulation an SNR of 30 dB in the input of each microphone has been considered.

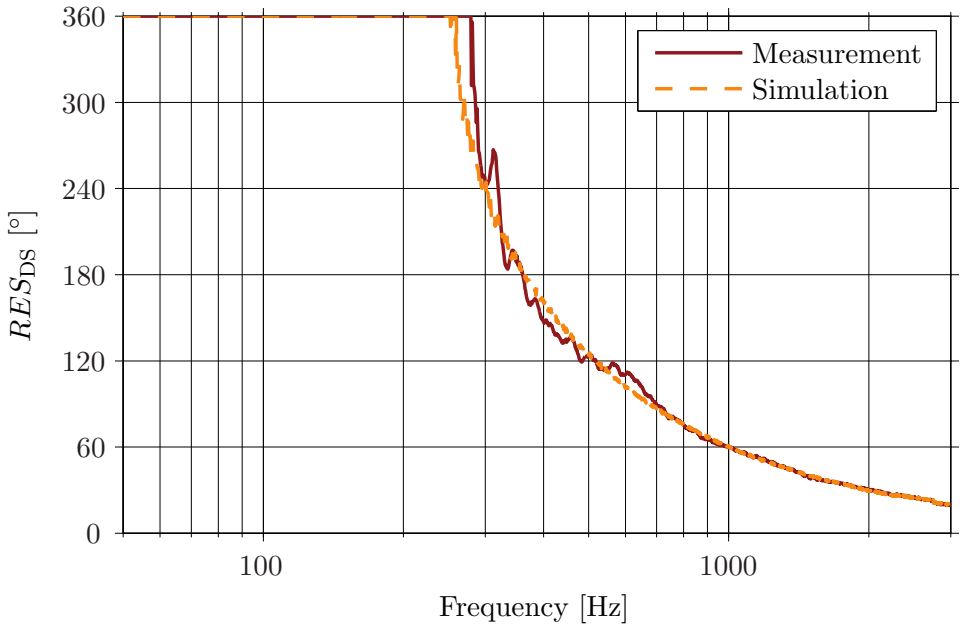

(a)

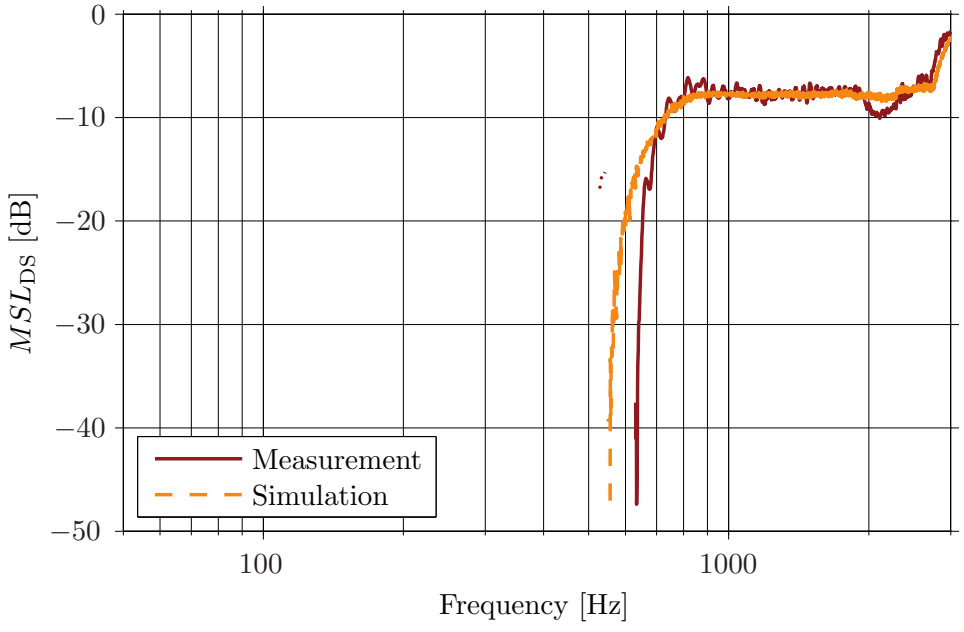

(b)

Figure 6.8: Resolution and MSL of a DS beamformer that uses an unbaffled array of 11.9 cm of radius with 12 microphones, when a source is placed at 180°. The theoretical case obtained by means of a simulation is also displayed. The SNR in each microphone has been set to 30 dB for the simulation.

6.3 Repeatability of the Measurements

In order to analyze the repeatability of the measurements, ten consecutive measurements have been performed with the same conditions. The source has been placed at 180° with respect to the array, at a distance of 4.6 m like in the measurements of the previous section.

Each measurement has been recorded for 2 s, which corresponds to two periods of the generator signal, and has been averaged afterwards over the periods in order to lower the influence of the background noise. The equivalent sound level pressure of the signals at each channel is in average 70.1 dB SPL, and the estimated noise is 32.7 dB SPL. In each measurement the resolution and the MSL have been calculated with both CHB and DSB. The mean values and the standard deviation of these two measures is analyzed in the following.

In figure 6.9, the mean and the standard deviation of the resolution are shown. As can be seen, the mean curves obtained with the two techniques are very similar to the results shown in the previous section where the measurements have been compared to the simulations. For this reason, a separate discussion between the mean and the theoretical values would be redundant. However, the present results can be seen together with the expected ones in figure A.14 in appendix A.3.

Regarding the standard deviation in the case of CHB, some deviations can be observed at frequencies around 100 Hz due to the presence of background noise. At 150 Hz and 250 Hz higher deviations can be observed which are attributed to the influence of the electrical noise (or hum), since these components are placed at odd harmonics of its fundamental frequency (50 Hz). At higher frequencies the deviation is rather small with exception of several peaks that correspond to the singularities due to the unresolved frequencies in the Fourier coefficients. The vicinity of these frequencies also presents small variation.

When dealing with DSB, the higher deviations are found around 257 Hz and 280 Hz which coincide with the beginning of the decrease of the resolution. In addition, smaller deviations can be seen up to 350 Hz. Apart from these deviations, the influence of the hum is also seen through the relatively small peaks at 350 Hz, 450 Hz, 550 Hz, 650 Hz and 750 Hz.

The mean and the standard deviation of the MSL are shown in figure 6.10. In the case of CHB, the deviation is in general fairly small (less than 0.25 dB) except at the lowest frequencies and at some isolated peaks. While the variation at lower frequencies is due to background noise, most of the peaks are the consequence of either the influence of the unresolved frequencies due to the Fourier coefficients or the hum since they appear at odd harmonics of its fundamental frequency.

In general terms, the deviation of the MSL for DSB is smaller than in CHB. The larger variation is found at those frequencies where a side lobe appears for the first time, around 627 Hz and 660 Hz. Also with DSB the influence of the hum is observed.

In conclusion, from these results it is seen that with CHB the results present more variation than with DSB due to the fact that it is less robust with respect to noise.

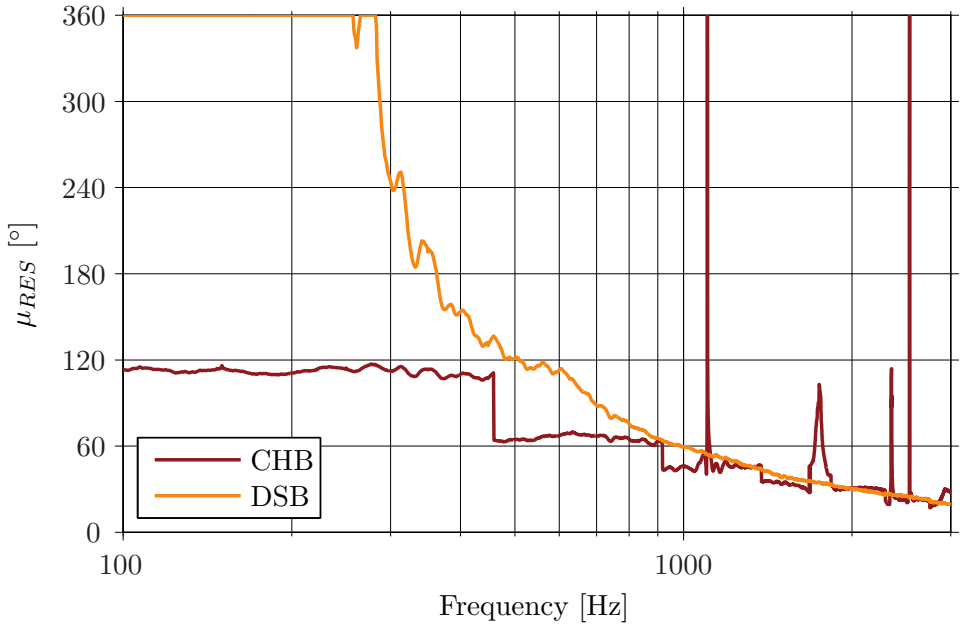

(a)

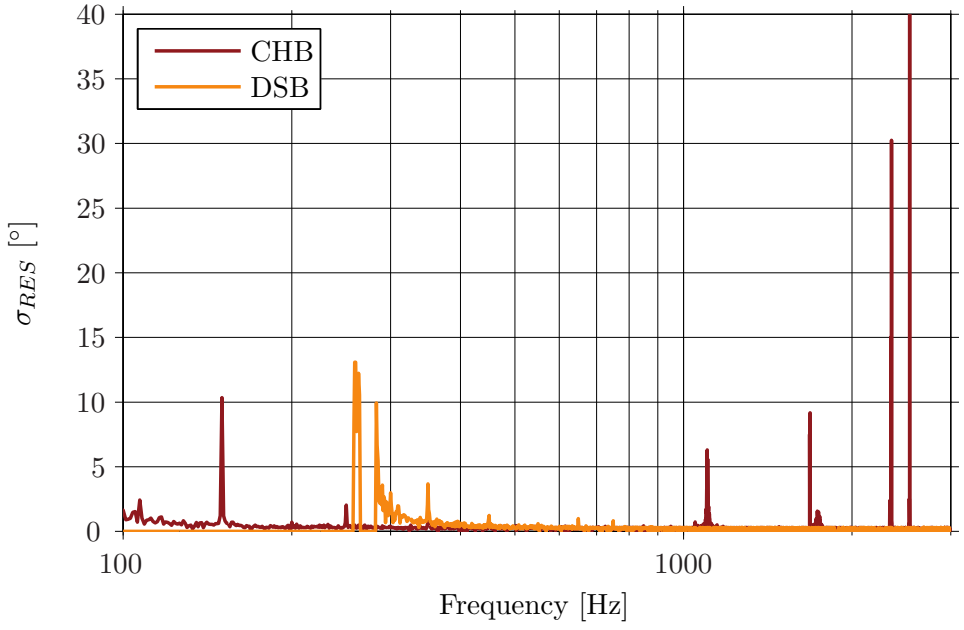

(b)

Figure 6.9: Mean value and standard deviation of the resolution obtained after 10 consecutive measurements. The results follow from using DSB and CHB with a circular array of radius 11.9 cm with 12 microphones, when a source is placed at 180°. Note that the standard deviation has been limited to 40° in order to have a better visibility, even though the last peak obtained with CHB achieves 80°.

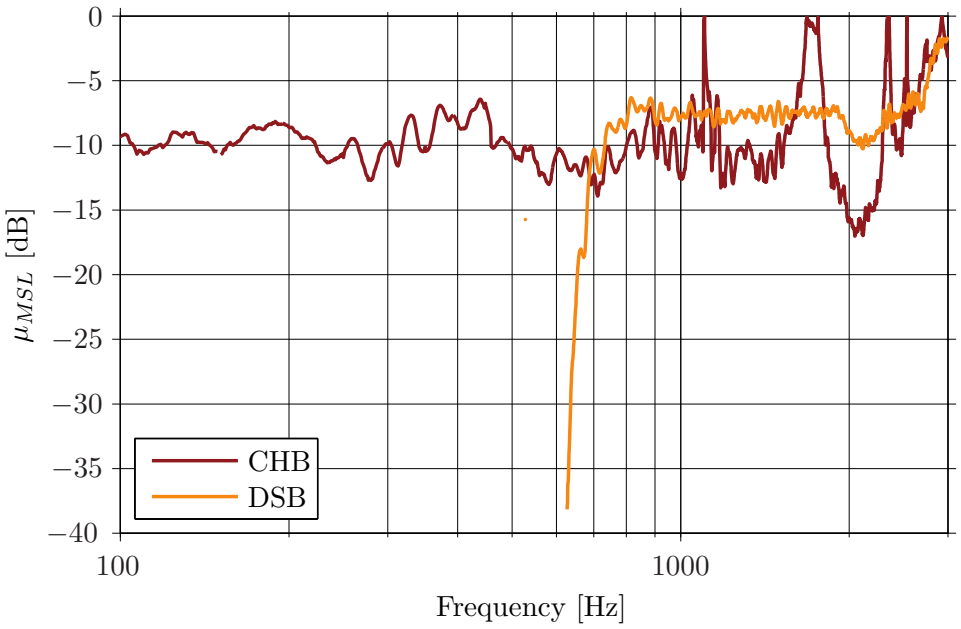

(a)

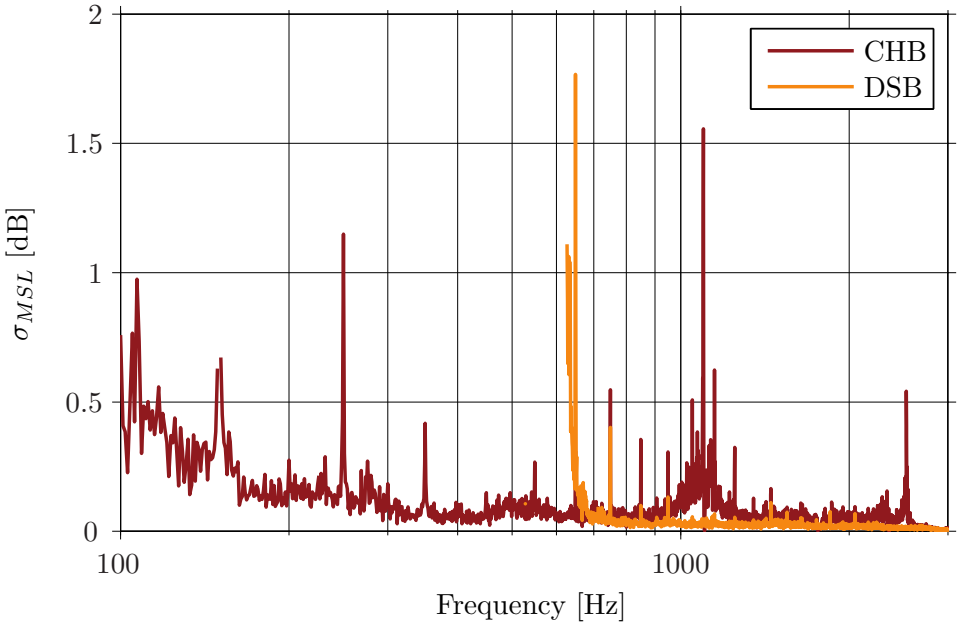

(b)

Figure 6.10: Mean value and standard deviation of the MSL obtained after 10 consecutive measurements. The results follow from using DSB and CHB with a circular array of radius 11.9 cm and 12 microphones, when a source is placed at 180°.

6.4 Influence of the Distance between Source and Array

The influence of the distance between the source and the array is analyzed in this section. The source, initially placed 4.6 m away from the array as in the previous experiment, has been moved back and forth to different positions by means of a rail hanging from the ceiling. In all cases, the source is on-axis with respect to the array, i. e. at 0°.

The generator signal has been kept constant along the measurements. The signal captured by the microphones has been recorded during 2 s, which corresponds to two periods of the generator signal, and has been averaged over the number of periods. The sound pressure level in the microphones as well as the distance between the source and the array are stated in table 6.1. The sound pressure level of the background noise at the microphones is 32.8 dB SPL in average.

Table 6.1: Distance d between the source and the array at each position with the corresponding sound pressure level captured at the microphones in average.

# Position	d [m]	$L_{\mathrm{eq},m}$ [dB SPL]
1	2.6	75.8
2	3.6	72.9
3	4.6	70.9
4	5.6	69.4

The resolution and the MSL obtained with these configurations are shown in figures 6.11 and 6.12 for CHB and DSB, respectively.

In the case of CHB, the resolution is very similar for all distances between array and source. The exception is found at those frequencies that are not resolved with the Fourier coefficients. As can be seen the resolution worsens with increasing distance. When DSB is used, the resolution is practically the same at high frequencies, whereas some differences are seen in the beginning of the decay of the resolution until 600 Hz.

Although the MSL curves for all cases follow the same tendency with both techniques, they do not coincide exactly as this measure is quite sensitive to background noise as mentioned in the previous sections. In this sense, the equivalent sound pressure level of the signal decreases with increasing distance, as shown in table 6.1. This in turn causes the SNR to worsen, and therefore the resulting resolution and MSL suffer more variation. This effect can also be seen in the case of DSB, through some 'unexpected' side lobes that appear between 500 Hz and 600 Hz for the longer distances, due to the low SNR in these measurements.

It is interesting to analyze whether the assumption of far-field is fulfilled with the distances of concern. A common rule of thumb for the approximate distance at which the far-field approximation is valid follows $d \gg \lambda$. Even though this is not fulfilled at the very low frequencies when the distance is 2.6 m, the far-field assumption seems to be still valid since the results have the same tendency as the ones obtained with longer distances.

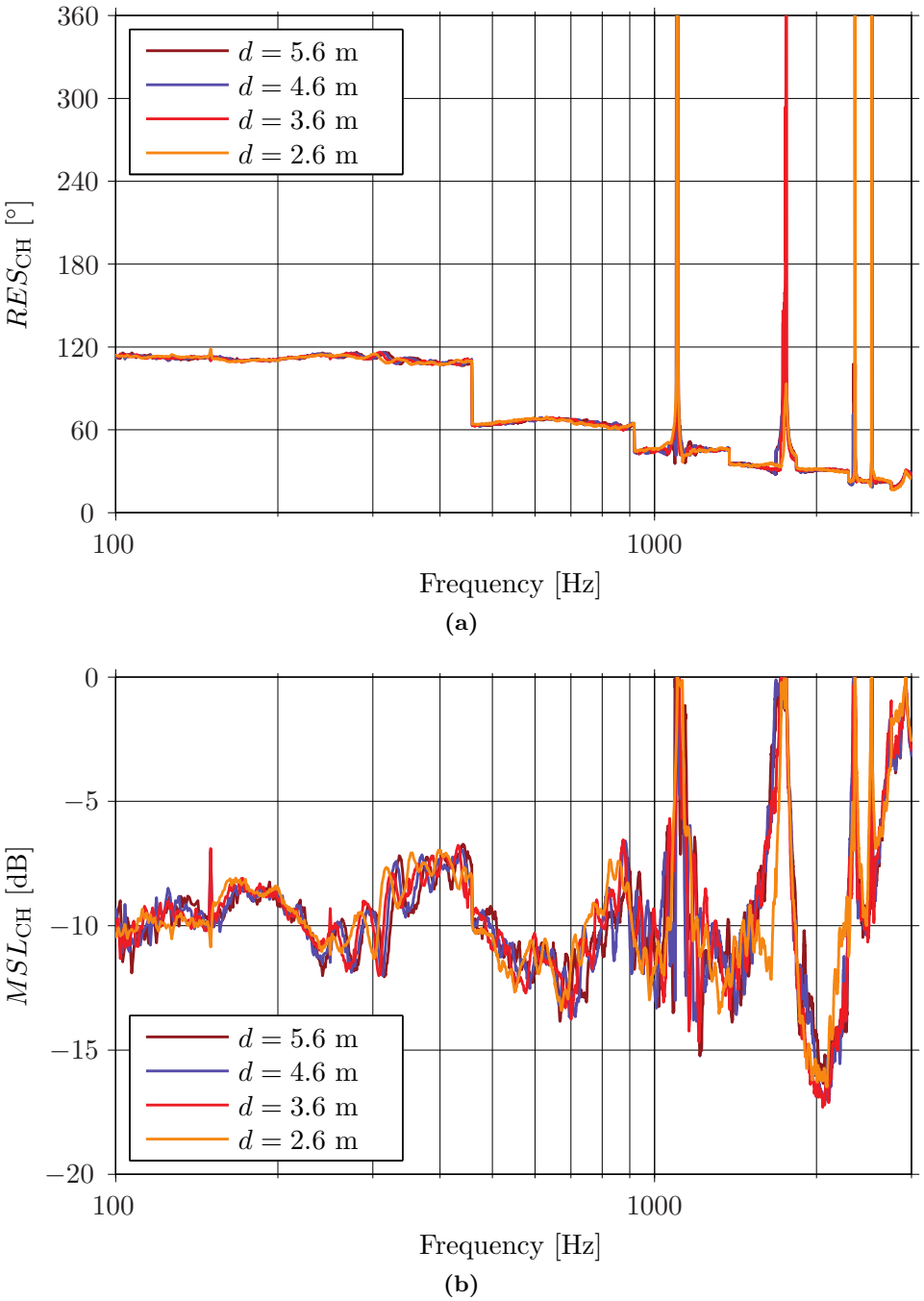

Figure 6.11: Resolution and MSL of a CH beamformer that uses an unbaffled array of 11.9 cm of radius with 12 microphones, for four different distances between the array and the source. In all cases the source is in the direction of 0°.

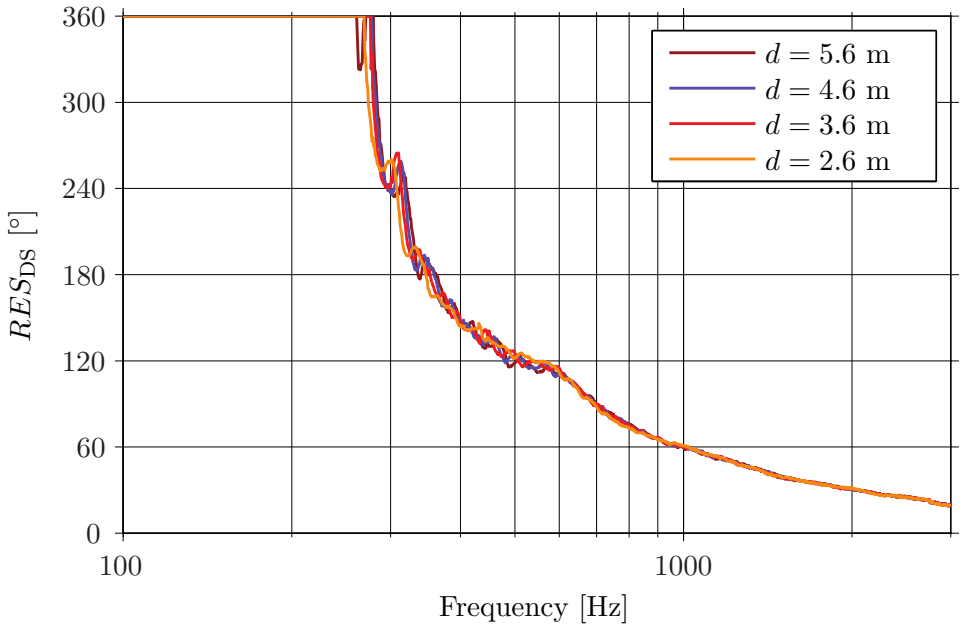

(a)

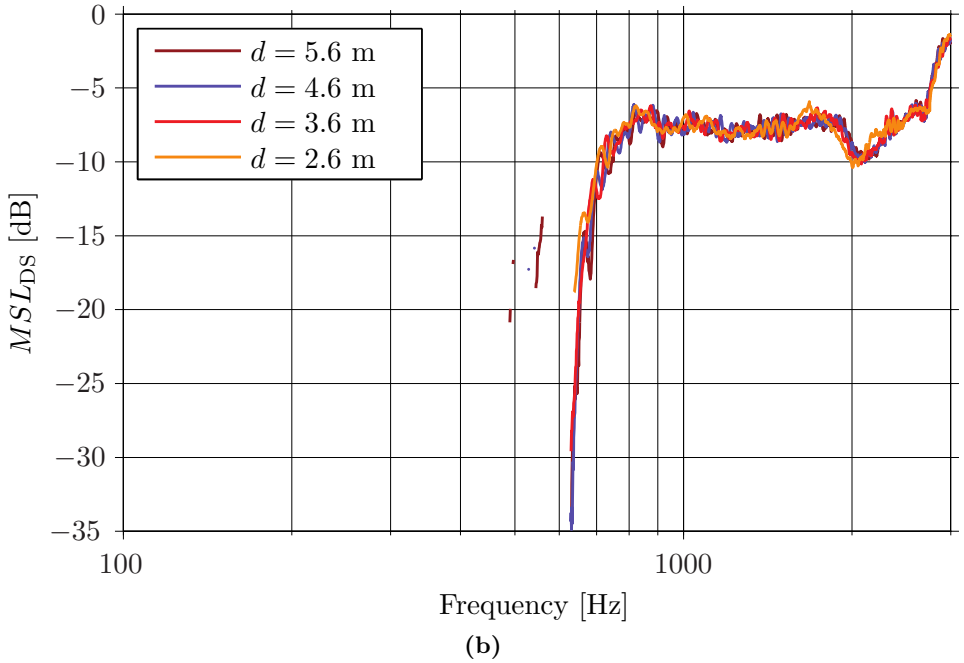

(b)

Figure 6.12: Resolution and MSL of a DS beamformer that uses an unbaffled array of 11.9 cm of radius with 12 microphones, for four different distances between the array and the source. In all cases the source is in the direction of 0°.

6.5 Influence of Background Noise

In the previous sections it has been observed that the resolution and particularly the MSL are influenced by background noise. In this section, further analysis is done by comparing four situations where the SNR at the array microphones is different. For these measurements, the source is placed on-axis with the array at a distance of 4.6 m. In each measurement, the signals captured by microphones have been recorded for 2 s and averaged over two periods, which is the number of periods used in the generator signal. The sound pressure level of the background noise in each channel is estimated to be 31.9 dB SPL, in mean. The level of the generator signal has been varied by means of the amplifier at each measurement. The resulting sound pressure level at the microphones and the corresponding SNR are shown in table 6.2.

The resolution and the MSL obtained from the measurements are depicted in figures 6.13 and 6.14 for CHB and DSB. Obviously, these measures worsen when the SNR decreases, with both techniques. In the case of CHB, the influence of background noise is stronger at low frequencies as can be seen from the resolution and MSL. As analyzed in section 5.3.2.2, this is mainly caused by the CHB algorithm, since it amplifies the noise when multiplying with the terms $1/\mathcal{C}_n$ shown in figure 5.14 on page 61. At high frequencies, these terms do not affect the CH beamformer output, and hence the resolution is rather independent of the SNR.

For DSB, the resolution presents more variation at those frequencies that correspond to the beginning of the decay, between 100 Hz and 600 Hz. At higher frequencies all situations yield practically the same resolution.

The MSL with CHB is polluted with background noise in a wider frequency range than the resolution and also worsen considerably with decreasing SNR. By contrast, with DSB even with the lowest SNR the result is acceptable. The effect of noise in the MSL when dealing with DSB is mainly seen in the 'unexpected' side lobes that appear in the range between 500 Hz and 600 Hz, when the SNR worsens.

With the above ideas two main conclusions can be drawn. On the one hand it has been seen that DSB is more robust to background noise than CHB. On the other hand the MSL appears to be more vulnerable than the resolution with respect to background noise.

Table 6.2: Averaged sound pressure level at the input of the microphones and estimated SNR for each measurement.

# Measurement	$L_{\mathrm{eq},m}$[dB SPL]	SNR [dB]
1	43.3	11.4
2	55.1	23.2
3	65.5	33.6
4	73.5	41.6

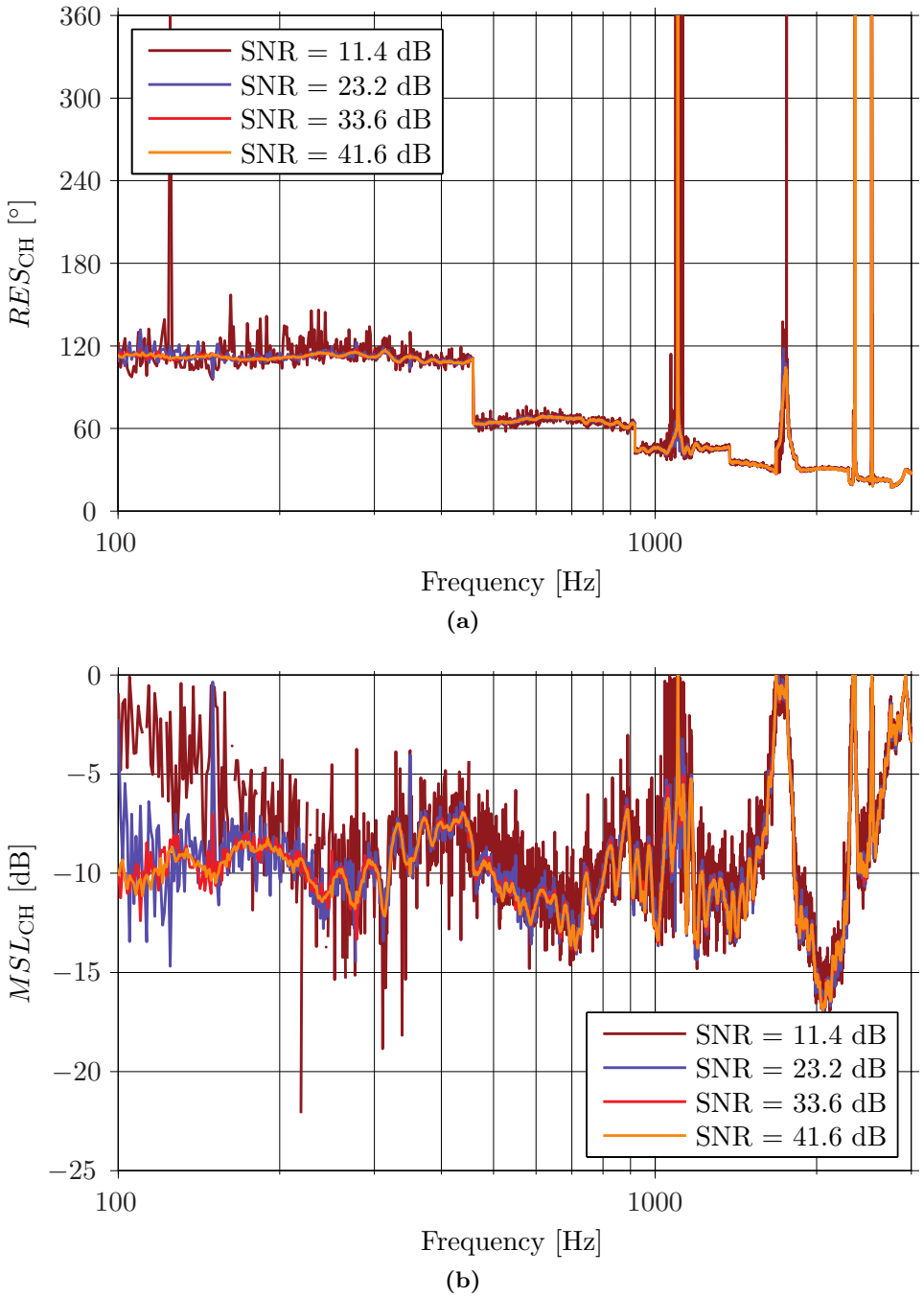

Figure 6.13: Resolution and MSL of a CH beamformer that uses an unbaffled array of 11.9 cm of radius with 12 microphones, for four different SNR. In all cases the source is in the direction of 0° at 4.6 m away from the array.

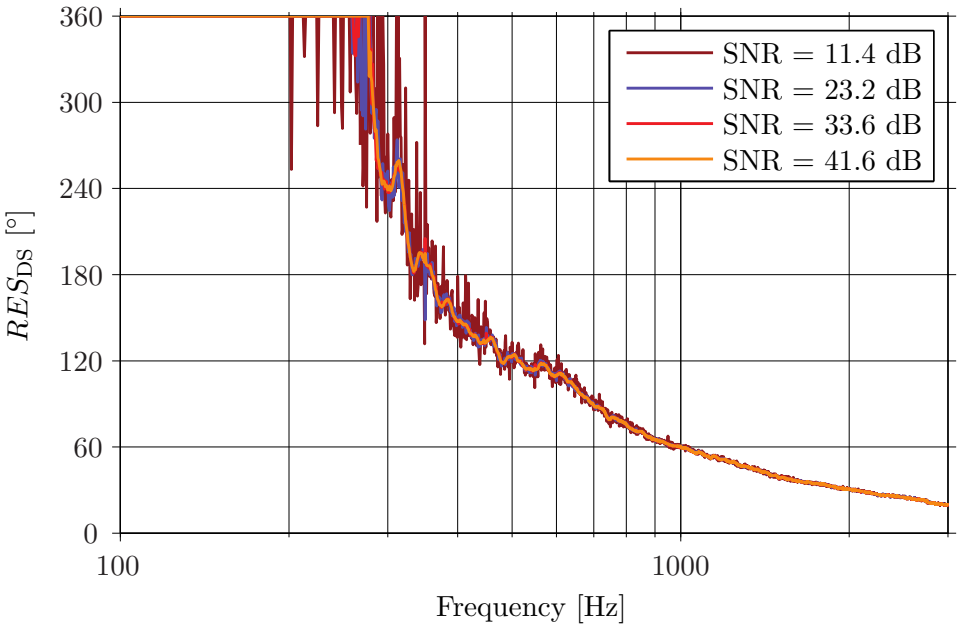

(a)

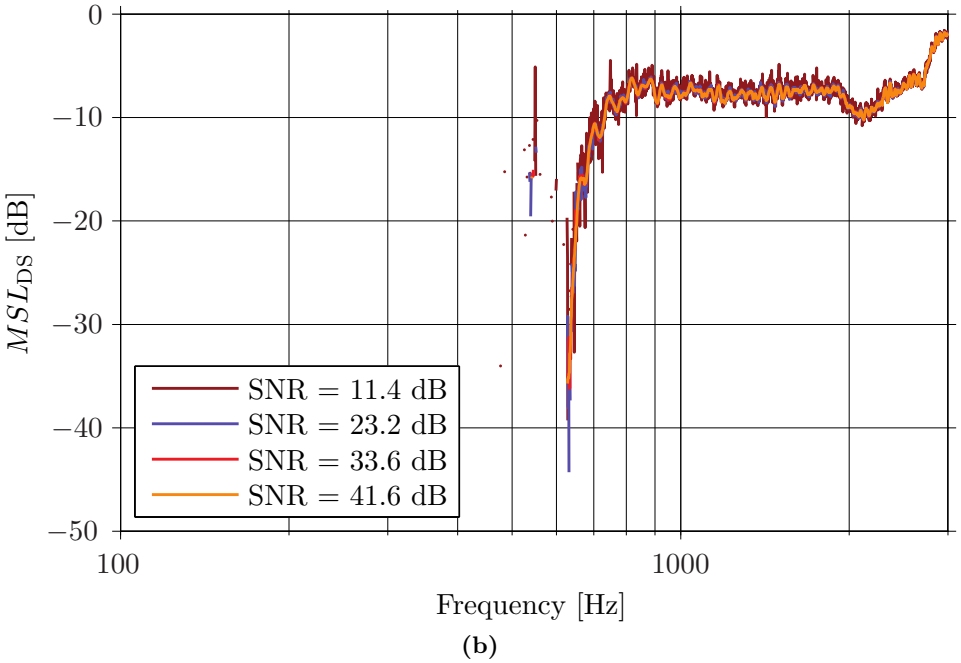

(b)

Figure 6.14: Resolution and MSL of a DS beamformer that uses an unbaffled array of 11.9 cm of radius with 12 microphones, for four different SNR. In all cases the source is in the direction of 0° at 4.6 m away from the array.

6.6 Angle Discrimination

In this section, the array performance is to be analyzed over 360°. The source is kept at the same position along the measurements at 4.6 m away from the array. For the first measurement, the array is focused towards the source, i. e. on-axis, and is rotated by 10° after each measurement until reaching 360°. In this way, 36 different directions of the source with respect to the array are measured. The signals captured by the array microphones are recorded for 2 s and averaged by two, which is the number of periods of the generator signal. The averaged sound pressure level of the signals at each microphone is 71 dB SPL, whereas the background noise is estimated to be 33 dB SPL during the measurements.

According to the simulations shown in sections 5.3.2.1 and 5.3.3.1, in ideal conditions the resolution and the MSL are independent of the source position at low frequencies, whereas at higher frequencies small periodic fluctuations are observed. Furthermore, these fluctuations increase with increasing frequency.

In figures 6.15 and 6.16, the resolution obtained from the measurements is shown at several frequencies as a function of the angle of the source, for CHB and DSB respectively.

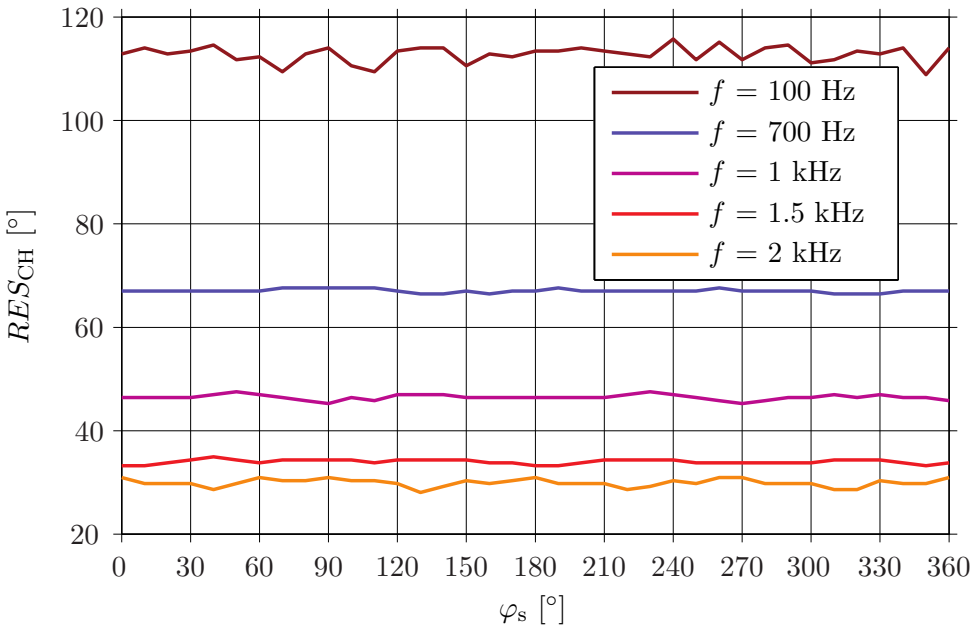

Figure 6.15: Resolution at five different frequencies as a function of the angular position of the source obtained with CHB. A circular array of radius of 11.9 cm with 12 microphones is used. The source is at a distance of 4.6 m from the array.

As can be seen, the resolution is fairly constant for both CHB and DSB and hence it agrees with the simulations. The small fluctuations that are observed at low frequencies are mainly attributed to the influence of background noise. At high frequencies, a periodic pattern is sensed with both techniques.

The MSL obtained with CHB and DSB is shown in figures 6.17 and 6.18. In both cases, the results are not as constant as expected at the lowest frequencies due to the

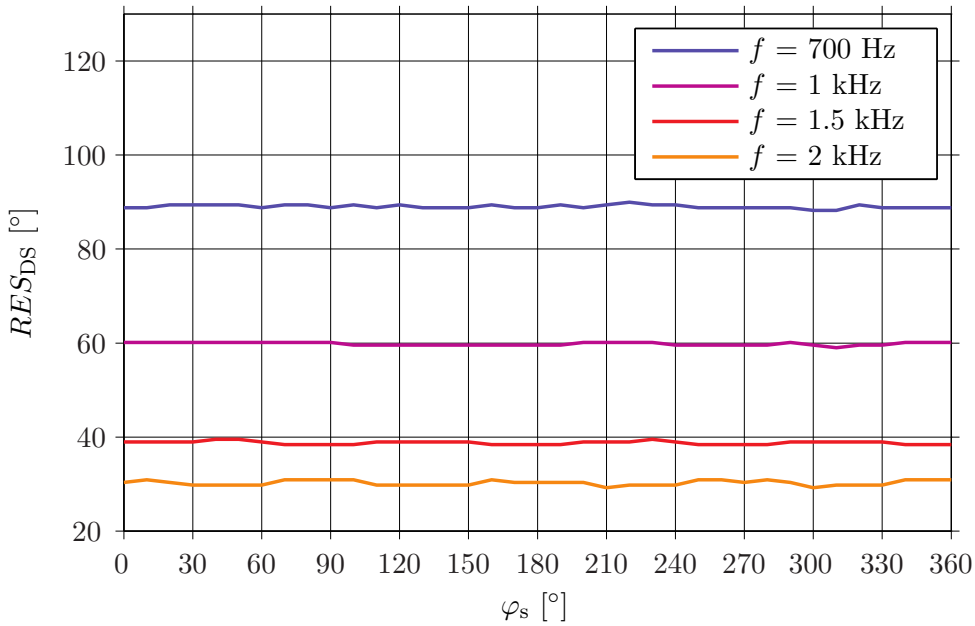

Figure 6.16: Resolution at five different frequencies as a function of the angular position of the source obtained with DSB. A circular array of radius of 11.9 cm with 12 microphones is used. The source is at a distance of 4.6 m from the array.

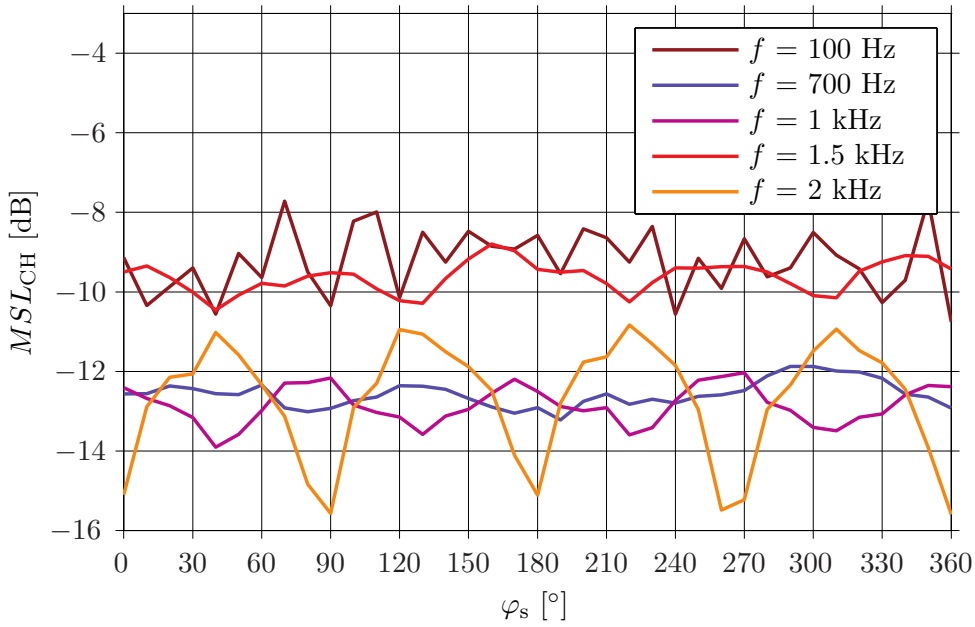

Figure 6.17: MSL at five different frequencies as a function of the angular position of the source obtained with CHB and a circular array with radius of 11.9 cm and 12 microphones. The source is at a distance of 4.6 m from the array.

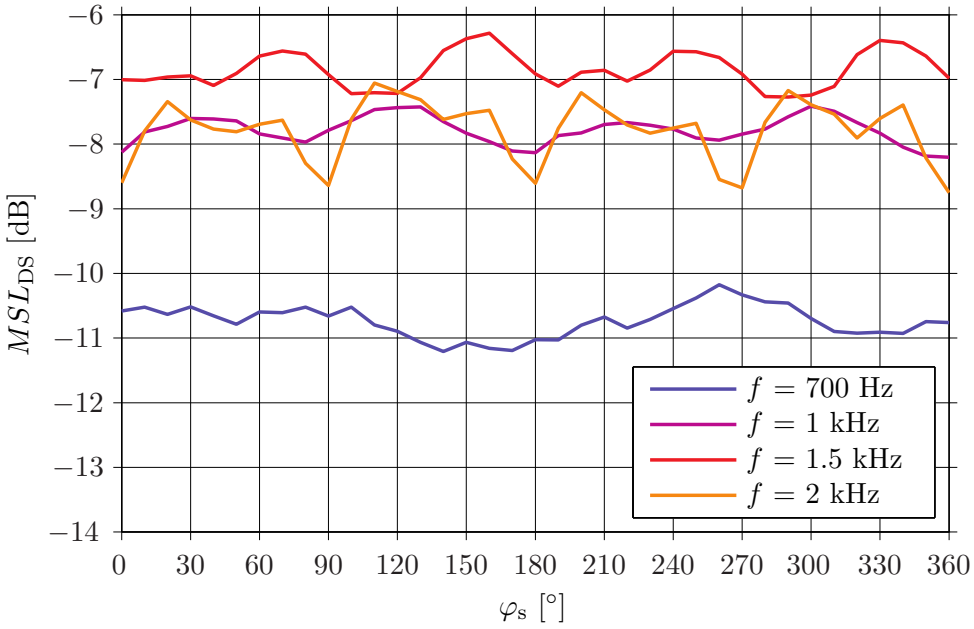

Figure 6.18: MSL at five different frequencies as a function of the angular position of the source obtained with DSB and a circular array with radius of 11.9 cm and 12 microphones. The source is at a distance of 4.6 m from the array.

fact that this measure is more vulnerable to background noise. However, like in the simulations, periodic patterns are obtained at the highest frequencies.

Besides the resolution and the MSL, it is of interest to analyze whether the source is localized at the expected position. This is done by means of averaging the angle at which the beamformers output is maximum and calculating the standard deviation. The frequency range taken into account for these quantities is from 100 Hz to 2750 Hz. In the case of CHB, those frequencies that cannot be properly resolved due to the dips in the Fourier coefficients as well as their vicinity are not used in these calculations. Moreover, in both techniques the values at 150 Hz are also discarded due to the fact that the output can be highly biased by third harmonic of the hum, as seen in section 6.3. All the frequencies that are rejected for the mean and the standard deviation are given in table 6.3.

The resulting mean and standard deviation obtained with both beamforming techniques as well as the expected value of the source position are presented in table 6.4. At first sight, it can be seen that the mean values are very similar to the expected angle. The highest difference between them is 1.7° for CHB and 1.6° for DSB. For ease of comparison, the standard deviation as a function of the mean is depicted in figure 6.19.

Table 6.3: Discarded frequencies for the calculation of the mean and the standard deviation of the maximum value of the beampattern.

Technique	Frequency [Hz]			
CHB	150	1095–1122	1674–1833	2235–2409	2522–2539
DSB	150				

Table 6.4: Localization of the source direction with CHB and DSB. The first column gives the expected angle of the source with respect to the center of the array, whereas the other columns provide the mean and standard deviation for each technique. All units are degrees.

Expected φ_s	CHB		DSB	
	μ_φ	σ_φ	μ_φ	σ_φ
0	0.3	0.79	0.4	0.75
10	10.6	1.05	11.0	0.91
20	20.5	1.86	20.3	0.77
30	30.4	0.97	30.7	0.79
40	40.5	1.29	41.0	0.86
50	51.3	1.35	51.0	0.84
60	61.0	0.98	61.1	0.84
70	70.4	1.71	70.8	0.85
80	80.6	1.20	80.3	0.92
90	90.7	0.91	90.8	0.84
100	100.2	1.21	100.5	0.95
110	110.9	1.92	110.5	0.85
120	120.2	1.21	120.3	0.86
130	130.2	1.44	130.6	0.87
140	141.1	1.44	140.7	0.88
150	150.7	1.01	150.6	0.86
160	161.1	1.74	161.4	0.88
170	171.6	1.21	171.3	0.95
180	180.4	0.87	180.6	0.83
190	190.4	1.16	190.9	0.96
200	201.6	1.89	201.4	0.85
210	210.8	1.07	211.2	0.84
220	221.1	1.27	221.6	0.82
230	231.7	1.33	231.4	0.86
240	241.1	0.92	241.1	0.82
250	251.1	1.68	251.5	0.83
260	261.2	1.11	260.8	0.86
270	271.5	0.90	271.6	0.82
280	281.2	1.12	281.5	0.92
290	291.1	1.89	290.8	0.81
300	300.9	1.11	301.0	0.81
310	310.3	1.39	310.7	0.83
320	320.8	1.42	320.4	0.84
330	330.5	0.91	330.4	0.83
340	340.4	1.77	340.7	0.85
350	351.5	1.20	351.1	0.90
360	359.6	0.88	359.7	0.83

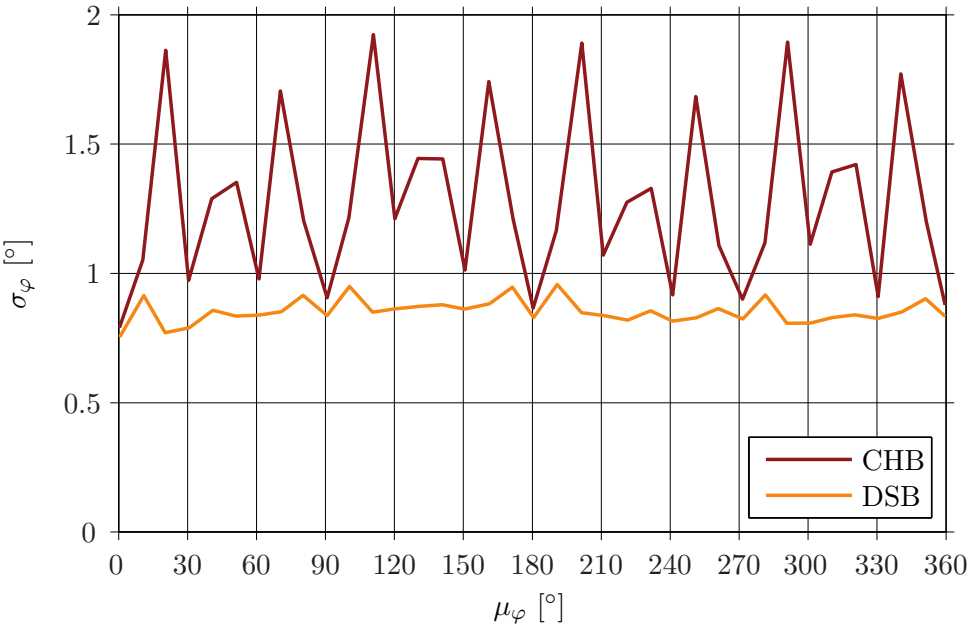

Figure 6.19: Standard deviation as a function of the mean of the direction where the source is localized. These two measures are the result of averaging and calculating the standard deviation of the angles where the beamformers present the maximum output over all the frequency range of interest, i. e. 100 Hz to 2750 Hz, with the exception of those frequencies stated in table 6.3.

The results reveal that the standard deviation using DSB is always smaller than the one obtained with CHB: it is within the range between 0.75° and 0.95° for DSB and between 0.75° and 1.9° for CHB. Therefore, for DSB the standard deviation is rather independent of the position of the source. When dealing with CHB a 'periodic' pattern of 90° can be seen. This pattern alternates between minima at multiples of 30° and maxima in between. Note that the minima coincide with positions of the microphones in the array, which means that with CHB the source can be localized with better accuracy when it is placed in the direction of the array microphones. The fact that the standard deviation is lower with DSB than with CHB proves once more the robustness of the former technique.

6.7 Array Performance with Two Sources

The last experiment deals with the beamformers behavior when two uncorrelated sources are present. To do so, another loudspeaker, a Dynaudio Acoustics *BM 6A*, is placed in the anechoic room apart from the spherical source. It is fed by the generator of a portable Brüel & Kjær PULSE Analyzer. The generator signal consists in pseudorandom noise with frequency content up to 3.2 kHz, resolution of 1 Hz and period of 1 s, as in the case of the signal used for the spherical loudspeaker (see section 6.1). The use of two generators of pseudorandom noise makes the signals of the loudspeakers to be uncorrelated. This is actually a premise for the proper localization of both sources.

Both speakers are placed at about 4.6 m from the center of the array. While the position of the loudspeaker mounted on a sphere is kept at 180° throughout the mea-

surements, the other loudspeaker is placed in the directions: 174°, 151°, 119° and 290°. In this way, both sources are really close to each other in the beginning, and they are progressively getting farther away in the consecutive measurements.

The speakers present a similar sound pressure level at the array when they are driven independently from each other: 70 dB SPL in the case of the spherical source and 70.2 dB SPL for the loudspeaker *BM 6A*. The sound pressure level due to background noise is about 33 dB SPL. These values are obtained after recording the signal during 2 s and averaging over two periods, which corresponds to the number of periods of the generators signal.

The resulting sound field created by both sources being active is captured by the array microphones, recorded during 2 s and averaged over two afterwards. The normalized beamformer outputs obtained from each measurement when CHB is used are shown in figure 6.20.

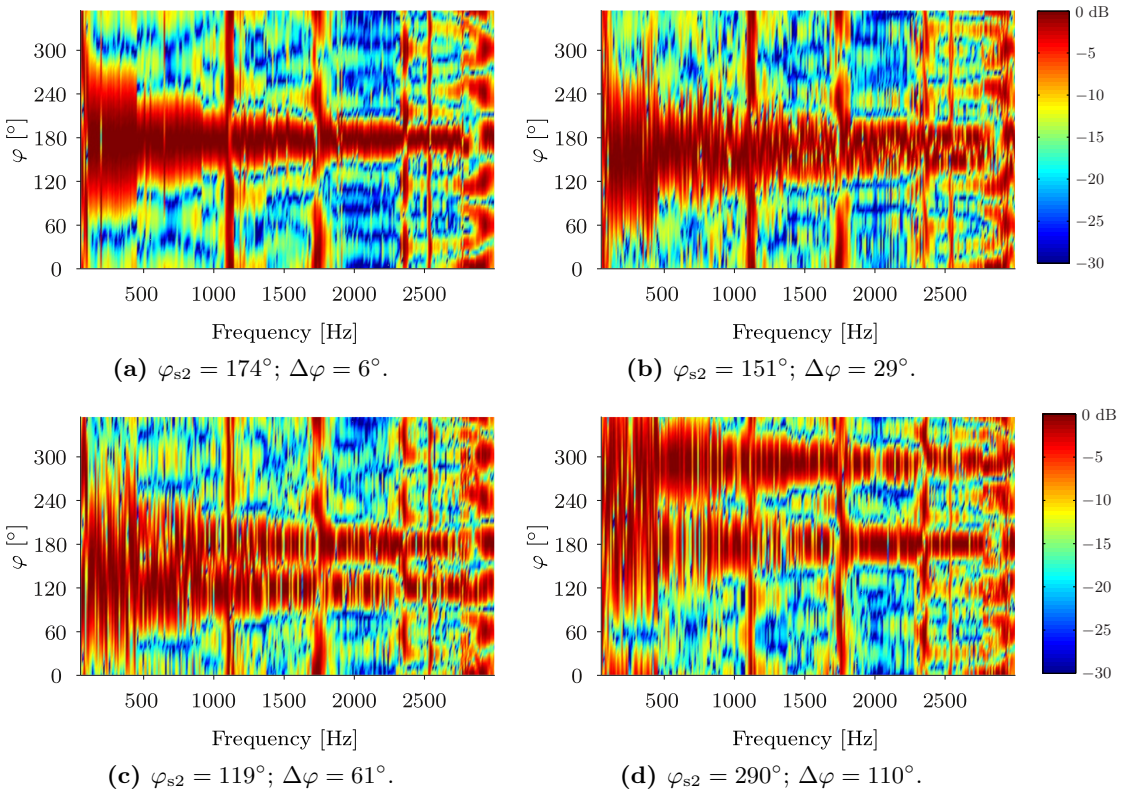

(a) $\varphi_{s2} = 174°$; $\Delta\varphi = 6°$. **(b)** $\varphi_{s2} = 151°$; $\Delta\varphi = 29°$.

(c) $\varphi_{s2} = 119°$; $\Delta\varphi = 61°$. **(d)** $\varphi_{s2} = 290°$; $\Delta\varphi = 110°$.

Figure 6.20: Normalized output of a CH beamformer that uses an unbaffled array of radius 11.9 cm with 12 microphones, when two uncorrelated sources are present. The sources are placed 4.6 m away from the array. While one of them is kept at 180° through all the measurements, the other one is moved to 174°, 151°, 119° and 290°.

In panel (a), the angular distance between the sources is only $\Delta\varphi = 6°$, and as can be seen the beamformer cannot resolve them at all. In panel (b), the beamformer can distinguish between both sources just at really high frequencies. With increasing angular distance between the sources, the beamformer can progressively resolve them in a wider frequency range as shown in panels (c) and (d).

According to section 4.5.1, the definition of the resolution coincides with the minimum distance between to incoherent sources in order for them to be distinguished. It is interesting to see how this is fulfilled in the present experiment. For example, in the frequency range of concern, the resolution is never equal or inferior than 6° as seen in figure 6.6 or as stated in table 5.2 on page 72. Therefore, with a distance of $\Delta\varphi = 6°$ it is not possible to resolve between both sources as observed from figure 6.20. When $\Delta\varphi = 29°$, they can be resolved at those frequencies where the resolution is equal or smaller than 29°. Actually this occurs in the range from about 2.2 kHz up to 2.7 kHz as the resolution is 22° approximately. For each angular distance $\Delta\varphi$, table 6.5 states when this value is equal to or smaller than the resolution and the expected frequency range where it occurs.

In this table, it can be seen that the frequency ranges in which the beamformer is expected to resolve the sources depending on the angular difference between them agree very well with the results shown in figure 6.20.

Table 6.5: Frequency range in which the CH beamformer can distinguish between two sources for a given angular difference $\Delta\varphi$ between them, according to the resolution criterion.

Frequency range	Resolution	$\Delta\varphi$ 6°	29°	61°	110°
100–458 Hz	112°	✗	✗	✗	✗
450–917 Hz	65°	✗	✗	✗	✓
918–1376 Hz	46°	✗	✗	✓	✓
1377–1834 Hz	36°	✗	✗	✓	✓
1835–2293 Hz	31°	✗	✗	✓	✓
2294–2752 Hz	22°	✗	✓	✓	✓

Figure 6.21 shows the beampatterns obtained with DSB. As can be seen, the results show the same tendency as in the case of CHB, that is, with increasing angular distance the beamformer is able to resolve the sources in a wider frequency range. However, the frequency range is equal or smaller than in the case of CHB, since unlike CHB, the DS beamformer is omnidirectional at low frequencies.

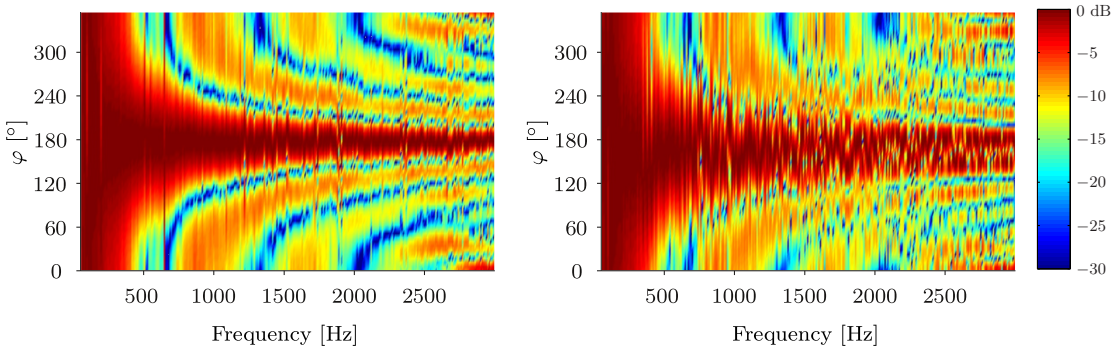

(a) $\varphi_{s2} = 174°$; $\Delta\varphi = 6°$.

(b) $\varphi_{s2} = 151°$; $\Delta\varphi = 29°$.

(c) $\varphi_{s2} = 119°$; $\Delta\varphi = 61°$.

(d) $\varphi_{s2} = 290°$; $\Delta\varphi = 110°$.

Figure 6.21: Normalized output of a DS beamformer that uses an unbaffled array of radius 11.9 cm with 12 microphones, when two uncorrelated sources are present. The sources are placed 4.6 m away from the array. While one of them is kept at 180° through all the measurements, the other one is moved to 174°, 151°, 119° and 290°.

7

Conclusions

7.1 Summary and Conclusions

The localization of environmental noise sources has been investigated with two different beamforming techniques applied to circular arrays. These are a new technique called Circular Harmonics beamforming and the well-known Delay-and-Sum beamforming. One of the main contributions of this work is the complete description of these techniques given in chapter 4. CHB is an adaptation of the Spherical Harmonics beamforming technique to a circular geometry. It is based on the decomposition of the sound field into a series of harmonics, using the principles of the Fourier series. DSB is typically implemented in the time domain. However, in the present work it has been developed in the frequency domain by using matched field processing. The latter makes it possible to use the concepts of the decomposition of the sound field as in CHB.

Concerning the real implementation of these beamformers, two main sources of error arise: the truncation error and the sampling error. The truncation error is due to the fact that a finite number of orders is used for the decomposition of the sound field, when in theory an infinite number of orders should be taken into account. The second error results from the decomposition of the sound field based on the information measured at discrete points. The effect of these errors has been analyzed in chapter 3. It has been shown that they can be minimized when the number of orders follows $N = \lceil kR \rceil$ and the number of array microphones exceeds twice the number of orders, i. e. $M > 2\lceil kR \rceil$.

Environmental noise sources are broadband sources, and hence, an array used for their localization must have a wide operating frequency range. After several measurements, it turns out that an array that covers the range from 100 Hz to about 2.5 kHz is reasonable, since this range represents the major spectral content of the sources of interest. In addition, the array is required to have a maximum radius of 20 cm as it is meant to be portable, and has to be conformed by a moderate number of microphones. Taking these constraints into account, the performance of circular arrays using CHB and DSB has been simulated and evaluated by means of two measures, the resolution

and the MSL.

The following conclusions can been drawn from the simulation results:

- For both CHB and DSB, the larger the radius of the array, the better the performance. In addition, the overall performance also improves with increasing frequency.
- For a given array, CHB has better resolution and MSL in a wider frequency range than in the case of DSB.
- The frequency range is limited at low frequencies by the influence of background noise in the case of CHB and by the fact that the output is omnidirectional for DSB. At high frequencies the limitation is given by the increase of the sampling error, in both cases.
- In the presence of background noise, DSB is more robust than CHB. Besides, the resolution is less contaminated than the MSL.
- CH beamformers present singularities, i. e. frequencies that cannot properly be resolved, when unbaffled circular arrays are used. This problem would be solved if it were feasible to mount the arrays on rigid cylindrical baffles of infinite length.
- The performance of DS beamformers would improve considerably by mounting the arrays on rigid cylindrical baffles of infinite length, but as mentioned previously, this is an unrealistic solution.
- It has been proved that the number of orders used for the beamforming algorithms is optimum when it follows $N = \lceil kR \rceil$ for CHB, and $N = \lceil kR \rceil + 1$ for DSB.

The results of the simulations reveal that the performance considerably improves just by mounting the array on a rigid cylindrical baffle of infinite length, though it is obvious that in real implementations the length of the cylindrical baffle must be finite. In chapter 3, an approximation of a cylinder of infinite length using a finite length cylinder given in the literature has been further examined. Unfortunately, the results have shown that this approximation is not really reliable. Consequently, an unbaffled array has been proposed for the implementation of a prototype. Considering the results of the simulations and the requirements previously mentioned, it has been recommended to use a radius of about 10 cm and 11 microphones.

The final prototype, with a radius of 11.9 cm and 12 microphones, has been tested in anechoic conditions. Very satisfactory results have been obtained as the beampatterns, the resolution and the MSL present extremely good agreement with the simulations, for both CHB and DSB.

Therefore, we can assert that the proposal of such prototype used in combination with the designed beamforming techniques for the localization of environmental noise sources is not only feasible but also very effective in terms of resolution and MSL, in most of the frequency range of interest. In this sense, it is recommended to use CHB for all the frequency range with exception of those high frequencies that cannot be properly resolved due to the nature of this technique. At such frequencies, it is convenient to use DSB instead. In addition to this, DSB should not be underestimated in environments with poor SNR due to its robustness.

Finally, it must be pointed out that even though the array has been designed for the localization of environmental noise sources, this work can be used as a guideline for other scenarios where circular arrays are applicable.

7.2 Future Work

The fact that the prototype yields successful results could encourage us to work for the improvement of such device. The following suggestions for further work are given:

- It has been seen that by mounting the array on a rigid cylindrical baffle of infinite length the output using DSB improves significantly compared to the unbaffled case. In fact, just by mounting the array on the infinite baffle, the performance is very similar to the one of an unbaffled array with twice the radius of the baffled array. In other words, the baffled array appears to be twice as large as an unbaffled array with the same radius. For real implementations the length of the cylindrical baffle must be finite, but it would be very convenient to find which length could be regarded as infinite. In chapter 3, an approximation given in the literature has been found not to be reliable. For this reason, it would be very useful and challenging to find an appropriate approximation.
- Although at low frequencies the CH beamformer presents better performance than the DS beamformer, the resolution is still rather coarse (about 110°), and hence it gives us a very rough estimation of the direction of the source. In many situations, it would be desirable to have better accuracy at such low frequencies. However, the only solution taking into account CHB and DSB lays on the design of a larger array, but this does not fulfill the requirements previously mentioned. Therefore, the solutions imply either the use of other beamforming techniques applied to circular arrays, or a completely different approach by using other array geometries.

A

Further Information

A.1 Bessel Functions

This section provides the characteristics of the Bessel functions frequently used in this document. All the equations are taken or adapted from [22, 23, 24].

The Bessel's differential equation of order $n \geq 0$ follows

$$x^2 \frac{\partial^2 w}{\partial x^2} + x \frac{\partial w}{\partial x} + \left(x^2 - n^2\right) w = 0. \tag{A.1}$$

The general solution to the Bessel's equation can be written as

$$w = A\mathrm{J}_n(x) + B\mathrm{Y}_n(x), \tag{A.2}$$

where $\mathrm{J}_n(x)$ is the Bessel function of the first kind and order n and $\mathrm{Y}_n(x)$ is the Neumann function (or Bessel functions of the second kind) and order n. The Bessel functions can be defined as

$$\mathrm{J}_n(x) = \frac{1}{2\pi} \int_0^{2\pi} \mathrm{e}^{\mathrm{j}(x \sin \varphi - n\varphi)} \mathrm{d}\varphi. \tag{A.3}$$

Alternatively, after applying the change of variable $\varphi = \alpha + \pi/2$ in the previous equation, $\mathrm{J}_n(x)$ can be written as follows

$$\mathrm{J}_n(x) = \frac{1}{2\pi \mathrm{j}^n} \int_0^{2\pi} \mathrm{e}^{\mathrm{j}(x \cos \varphi + n\varphi)} \mathrm{d}\varphi. \tag{A.4}$$

The Neumann functions are defined as,

$$\mathrm{Y}_n(x) = \begin{cases} \dfrac{\mathrm{J}_n(x)\cos(n\pi) - \mathrm{J}_{-n}(x)}{\sin(n\pi)} & n \neq 0, 1, 2, \ldots \\ \lim\limits_{p \to n} \dfrac{\mathrm{J}_p(x)\cos(p\pi) - \mathrm{J}_{-p}(x)}{\sin(p\pi)} & n = 0, 1, 2, \ldots \end{cases} \tag{A.5}$$

Figure A.1 shows the first five orders of $\mathrm{J}_n(x)$ and $\mathrm{Y}_n(x)$.

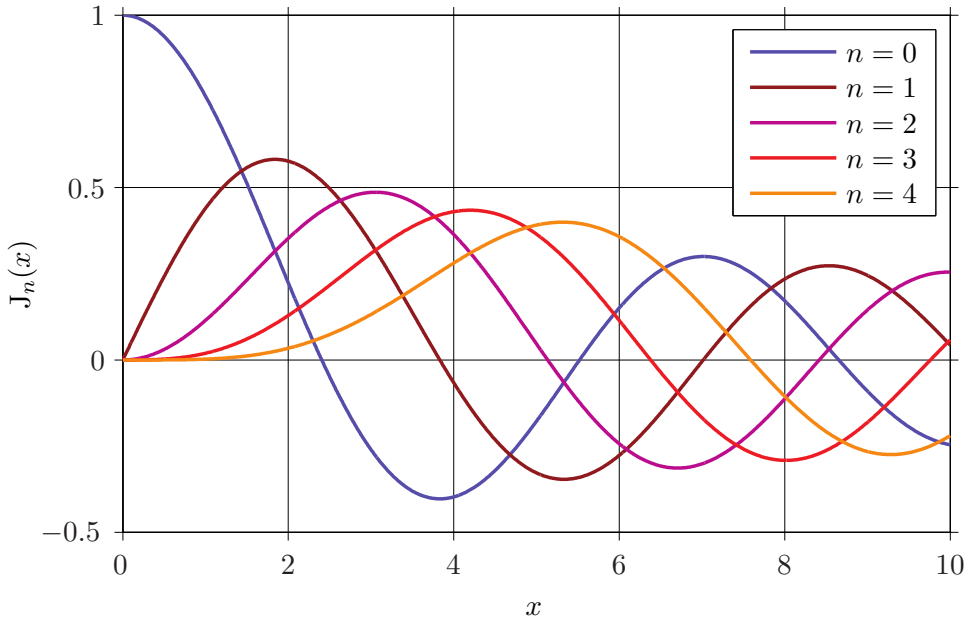

(a) Bessel functions.

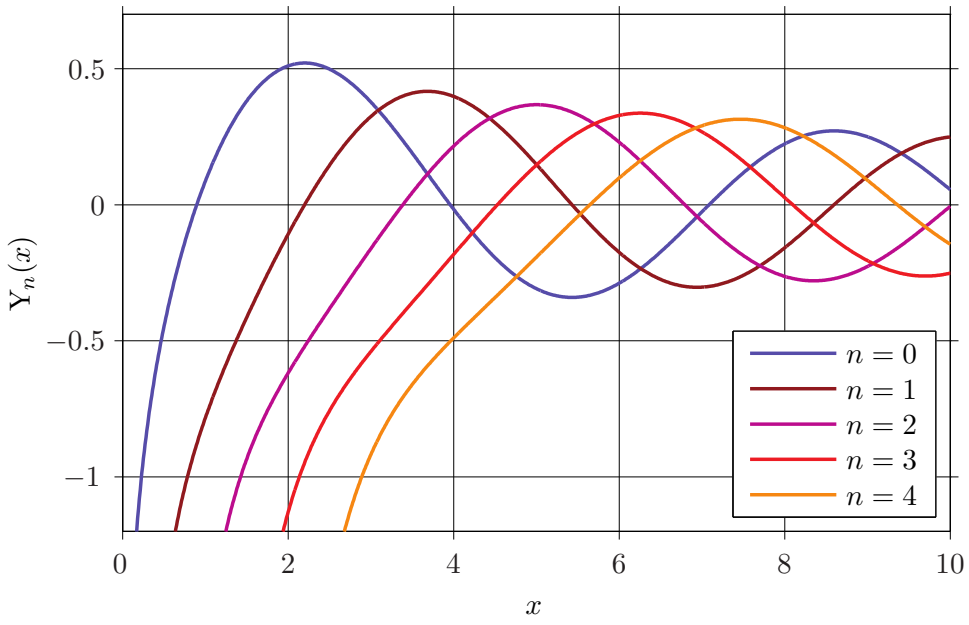

(b) Neumann functions.

Figure A.1: Bessel and Neumann functions for $n = 0, 1, 2, 3$ and 4.

Important properties of these functions are

$$\mathrm{J}_{-n}(x) = (-1)^n \mathrm{J}_n(x) \qquad n = 0, 1, 2, \ldots \tag{A.6}$$

$$\mathrm{Y}_{-n}(x) = (-1)^n \mathrm{Y}_n(x) \qquad n = 0, 1, 2, \ldots \tag{A.7}$$

$$\mathrm{J}'_n(x) = \frac{1}{2}\Big(\mathrm{J}_{n-1}(x) - \mathrm{J}_{n+1}(x)\Big), \tag{A.8}$$

$$\mathrm{Y}'_n(x) = \frac{1}{2}\Big(\mathrm{Y}_{n-1}(x) - \mathrm{Y}_{n+1}(x)\Big). \tag{A.9}$$

A.2 Further Simulations

A.2.1 Circular Harmonics Beamforming

In figure A.2, the normalized outputs of three CH beamformers that use arrays mounted on a rigid cylindrical baffle of infinite length can be seen. Their resolution and MSL, obtained in ideal conditions are depicted in figures A.3 and A.4. The influence of the source position on the resolution, MSL and number of side lobes when baffled arrays are used are shown in figures A.5, A.6 and A.7.

When background noise is taken into account, the resulting resolution and the MSL that result can be seen in figures A.8 and A.9.

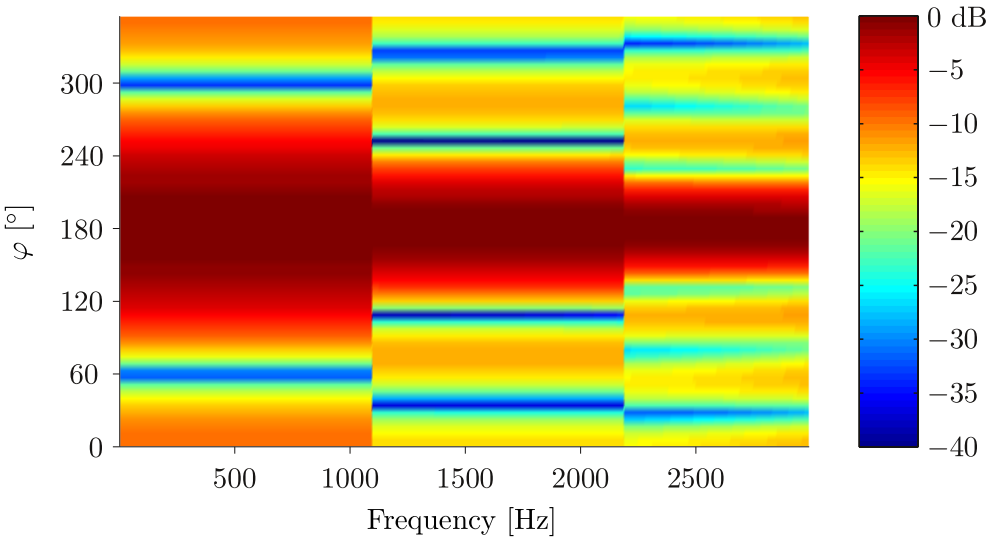

(a) CHB, $R = 5$ cm, Baffled.

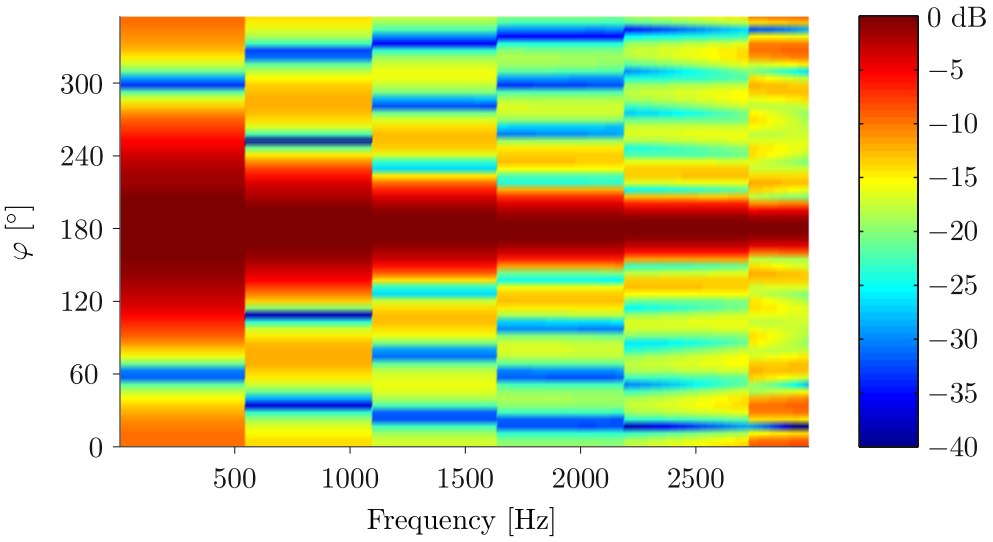

(b) CHB, $R = 10$ cm, Baffled.

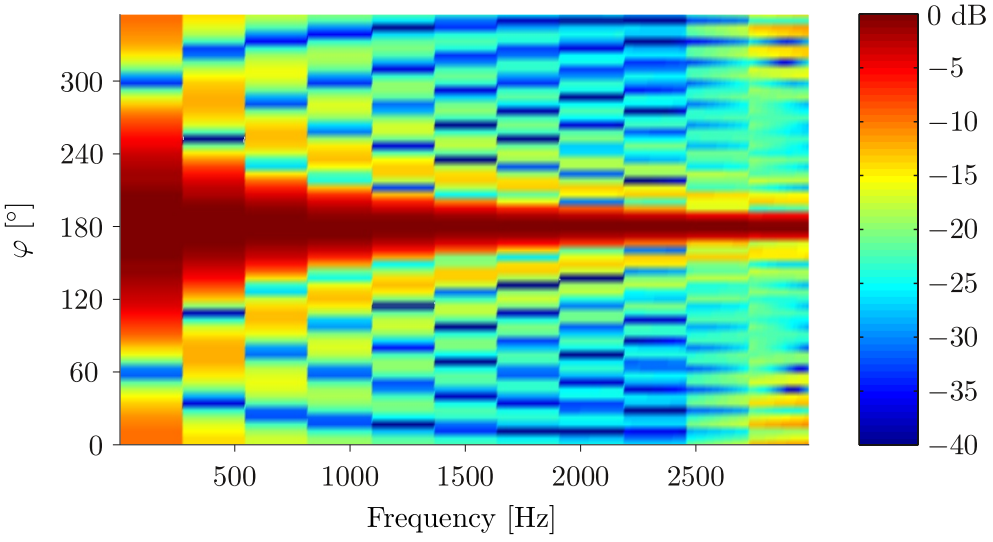

(c) CHB, $R = 20$ cm, Baffled.

Figure A.2: Normalized outputs of three CH beamformers that use circular arrays mounted on a rigid cylindrical baffle of infinite length of radius 5, 10 and 20 cm, when a source is placed at 180°. The features of each array are shown in table 5.1 on page 52.

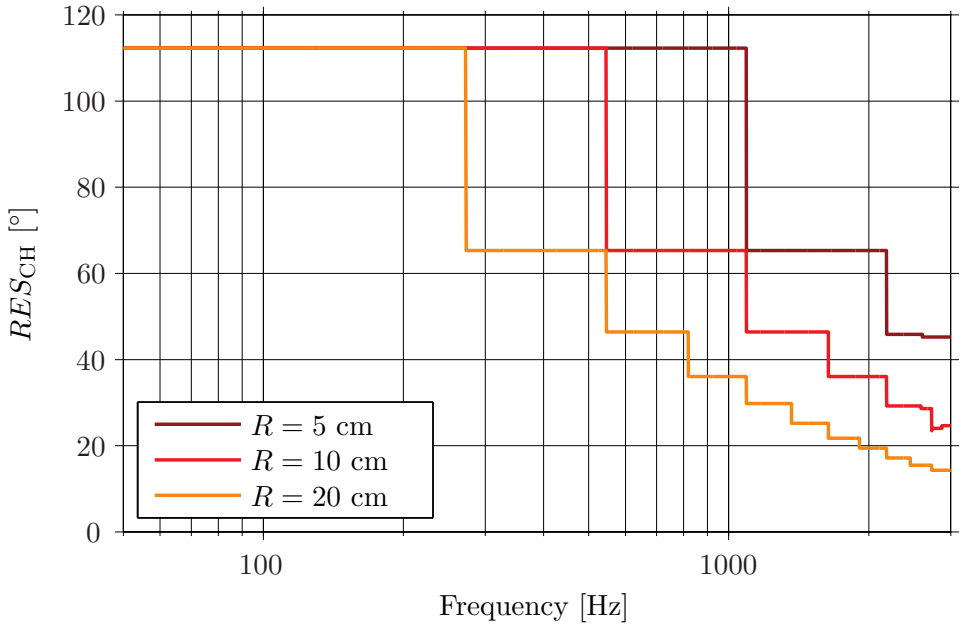

Figure A.3: Resolution of three CH beamformers that use circular arrays mounted on a rigid cylindrical baffle of infinite length of radius 5, 10 and 20 cm, when a source is placed at 180°. The features of each array are given in table 5.1.

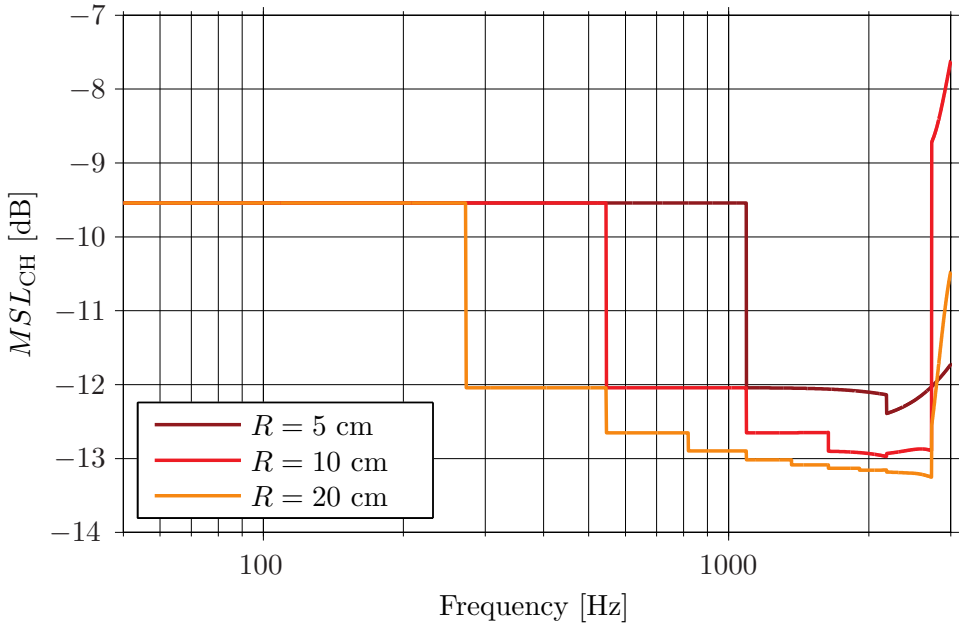

Figure A.4: MSL of three CH beamformers that use circular arrays mounted on a rigid cylindrical baffle of infinite length of radius 5, 10 and 20 cm, when a source is placed at 180°. The features of each array are given in table 5.1 on page 52.

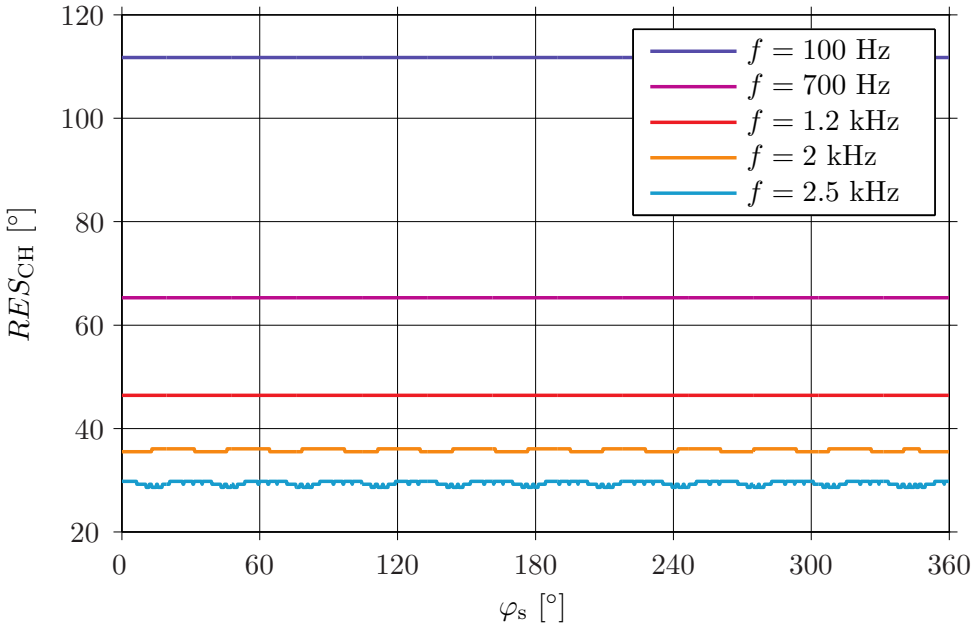

Figure A.5: Resolution as a function of the angular position of the source obtained with CHB and a circular array mounted on a rigid cylindrical baffle of infinite length of radius 10 cm at five different frequencies. The features of the array are given in table 5.1 on page 52.

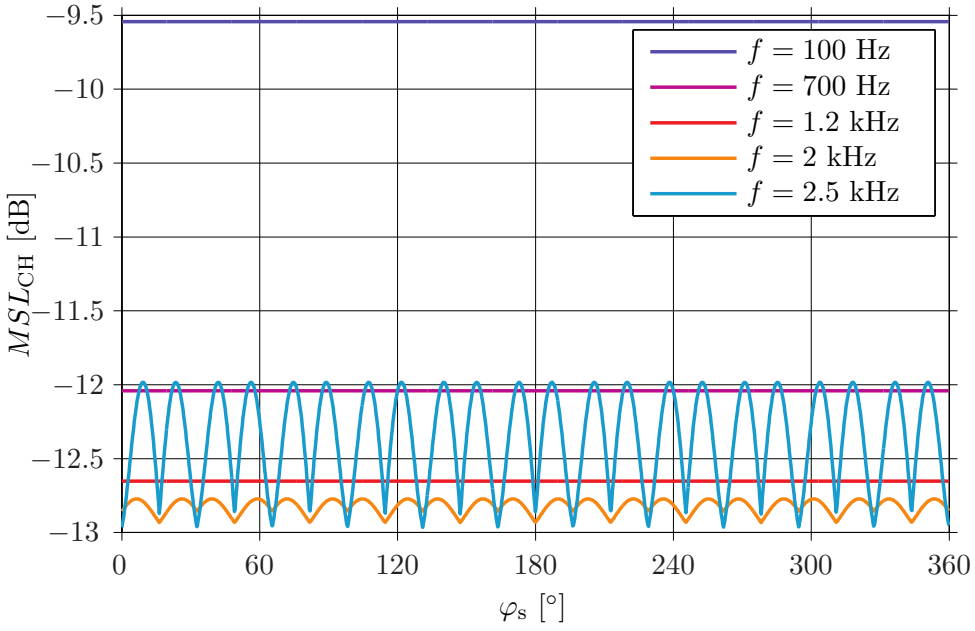

Figure A.6: MSL as a function of the angular position of the source obtained with CHB and a circular array mounted on a rigid cylindrical baffle of infinite length of radius 10 cm at five different frequencies. The features of the array are given in table 5.1 on page 52.

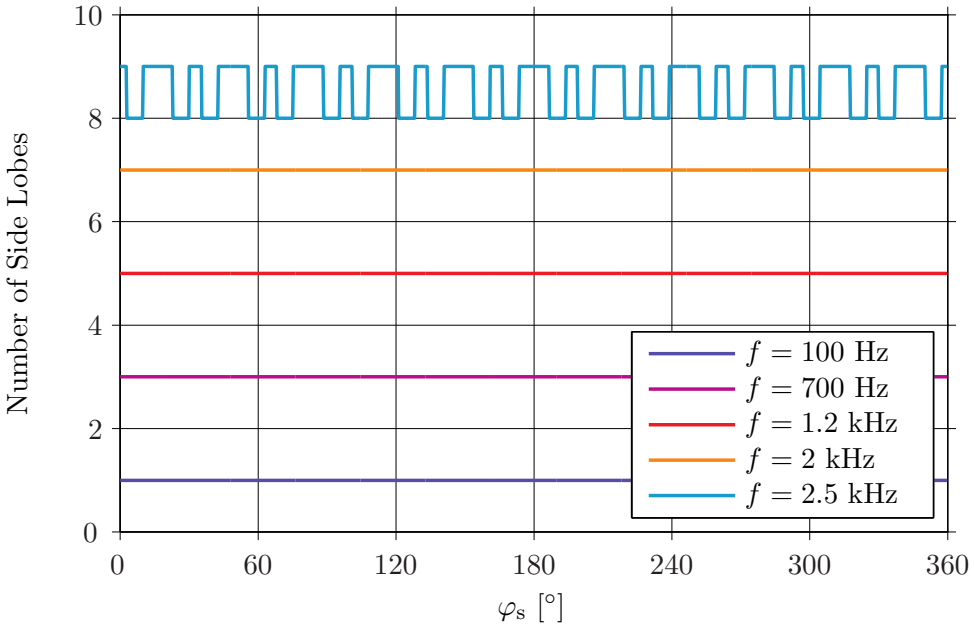

Figure A.7: Number of side lobes as a function of the angular position of the source obtained with CHB and a circular array mounted on a rigid cylindrical baffle of infinite length of radius 10 cm at five different frequencies. The features of the array are given in table 5.1 on page 52.

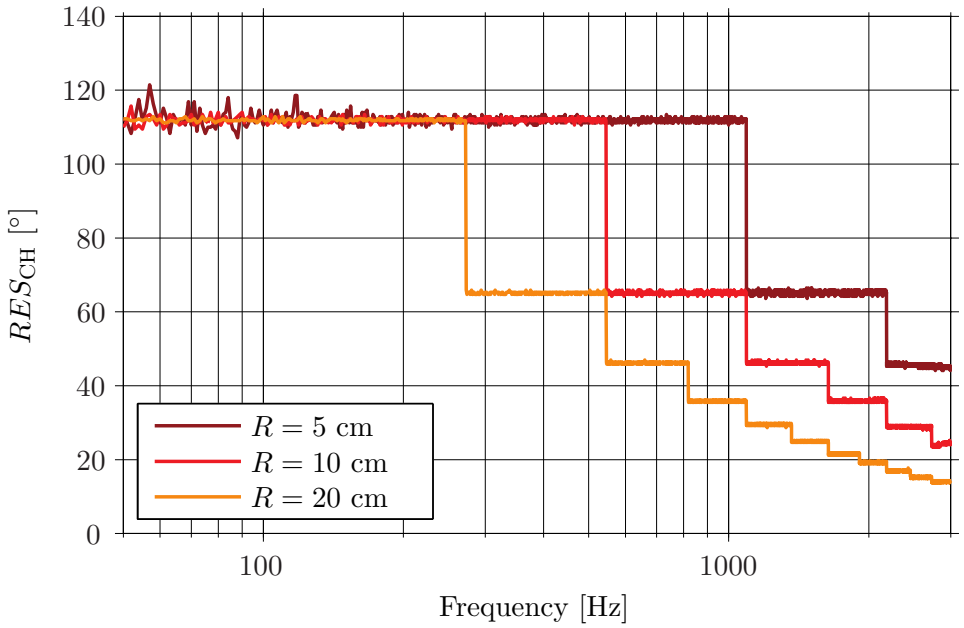

Figure A.8: Resolution of three CH beamformers that use circular arrays mounted on a rigid cylindrical baffle of infinite length of radius 5, 10 and 20 cm, when a source is placed at 180° and the SNR in the array microphones is 30 dB. The features of each array are given in table 5.1 on page 52.

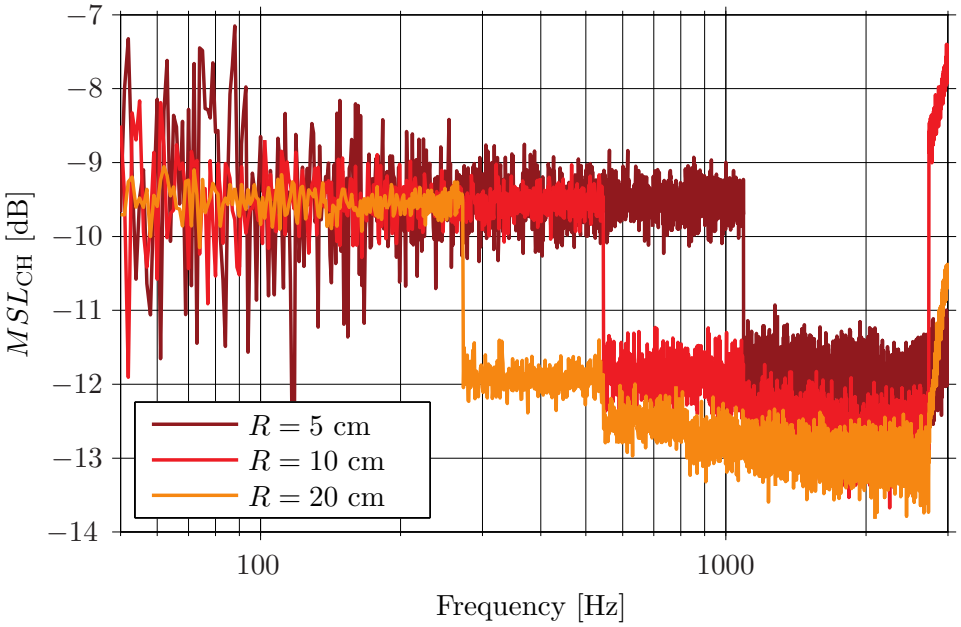

Figure A.9: MSL of three CH beamformers that use circular arrays mounted on a rigid cylindrical baffle of infinite length of radius 5, 10 and 20 cm, when a source is placed at 180° and the SNR in the array microphones is 30 dB. The features of each array are given in table 5.1 on page 52.

A.2.2 Delay-and-Sum Beamforming

The normalized outputs of three DS beamformers that use arrays mounted on a rigid cylindrical baffle of infinite length can be seen in figure A.10. Ideal conditions and a source placed at 180° have been considered for these simulations. The influence of the source position on the resolution and the MSL is shown in figure A.10 for a baffled array of 10 cm of radius.

The resolution and the MSL of three DS beamformers that use baffled arrays can be seen in figure A.12, when background noise is present.

In figure A.13, the resolution and the MSL are shown for an unbaffled array of 10 cm of radius when 11 and 12 microphones are used.

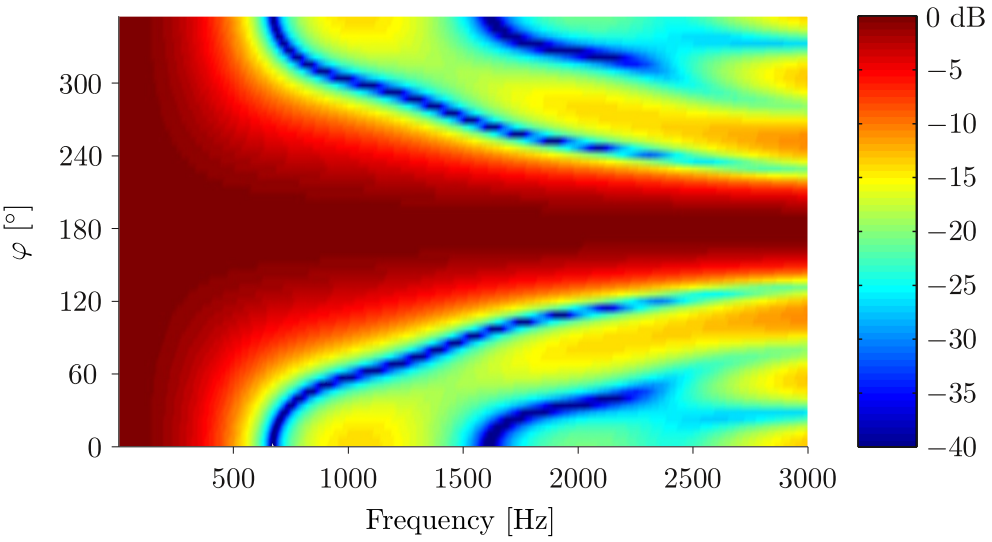

(a) DSB, $R = 5$ cm, Baffled.

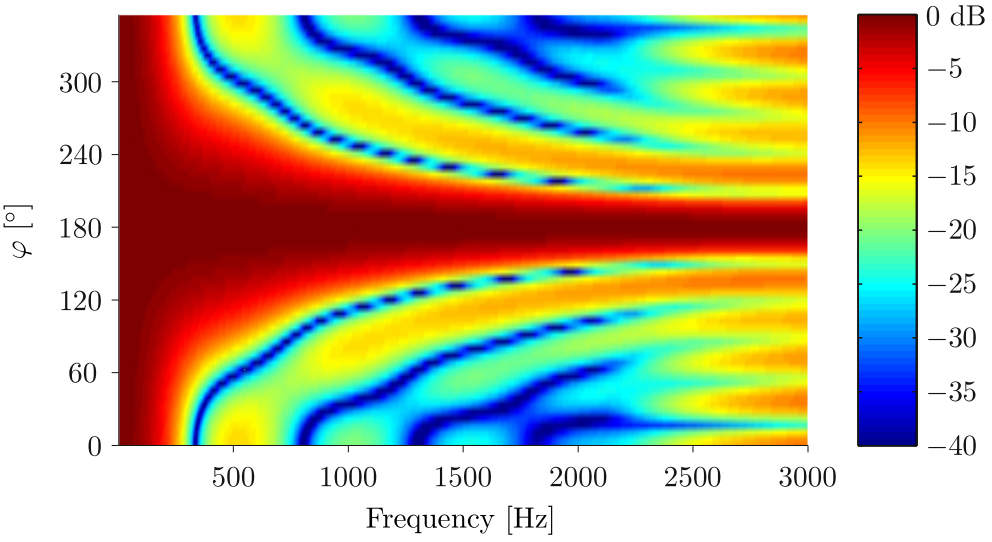

(b) DSB, $R = 10$ cm, Baffled.

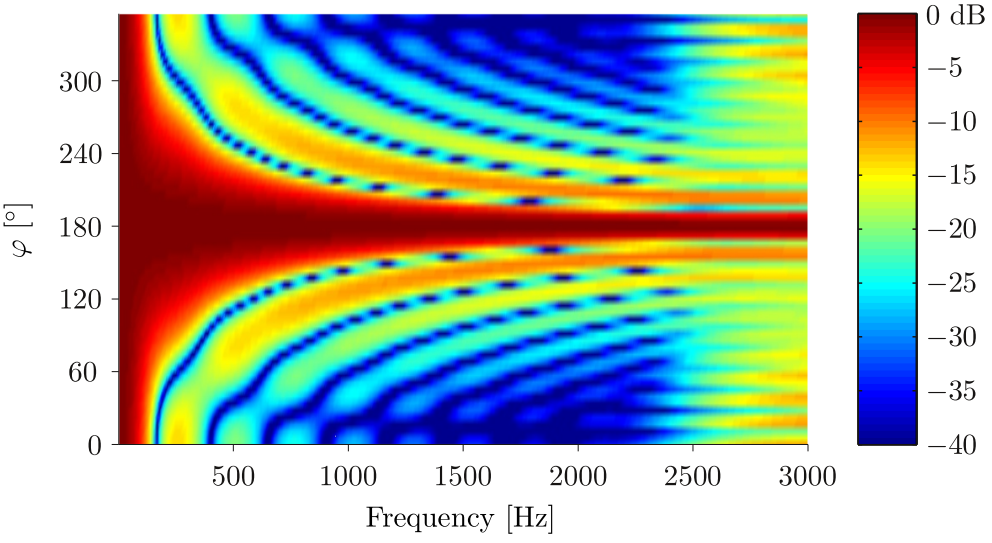

(c) DSB, $R = 20$ cm, Baffled.

Figure A.10: Normalized outputs of three DS beamformers that use circular arrays mounted on a rigid cylindrical baffle of infinite length of radius 5, 10 and 20 cm, when a source is placed at 180°. The features of each array are shown in table 5.1 on page 52.

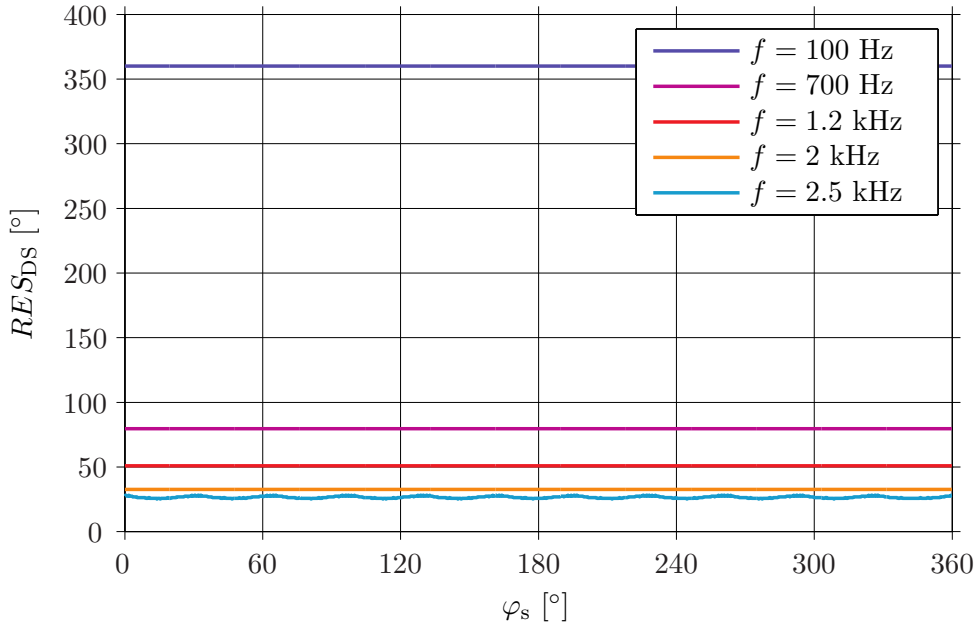

(a)

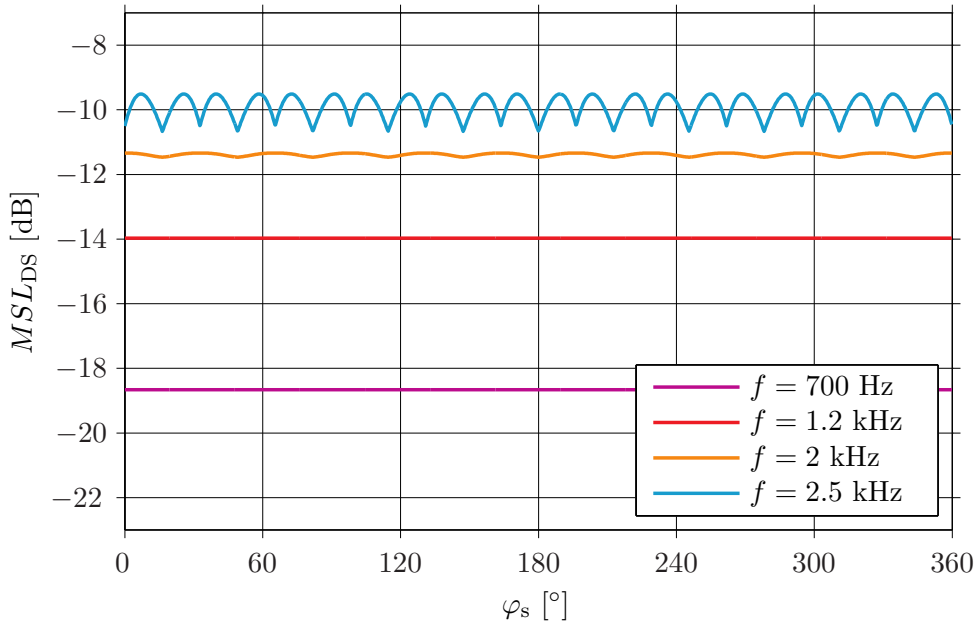

(b)

Figure A.11: Resolution and MSL as a function of the angular position of the source obtained with CHB and a circular array mounted on a rigid cylindrical baffle of infinite length of radius 10 cm at five different frequencies. The features of the array are given in table 5.1 on page 52.

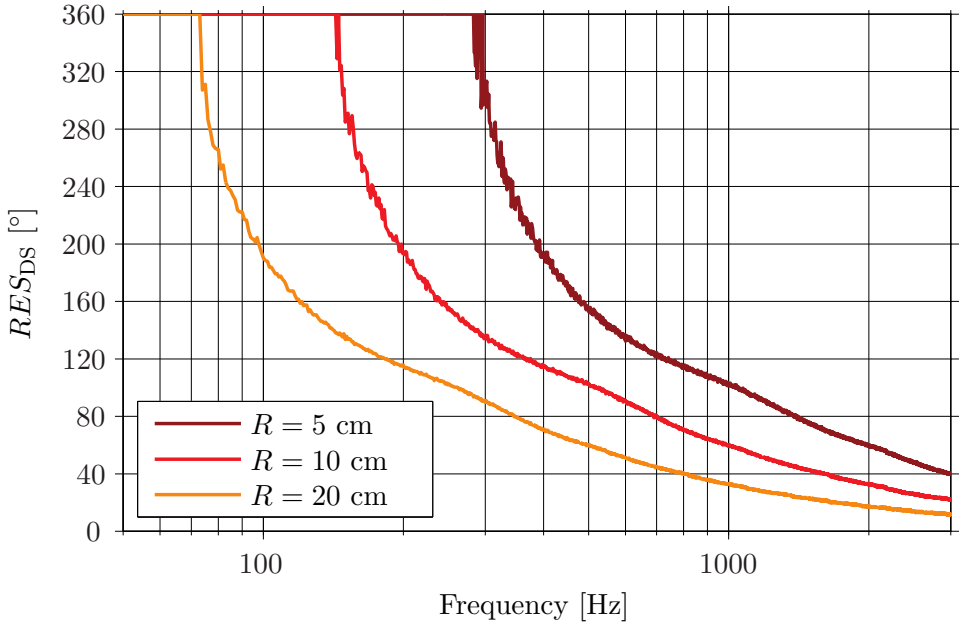

(a)

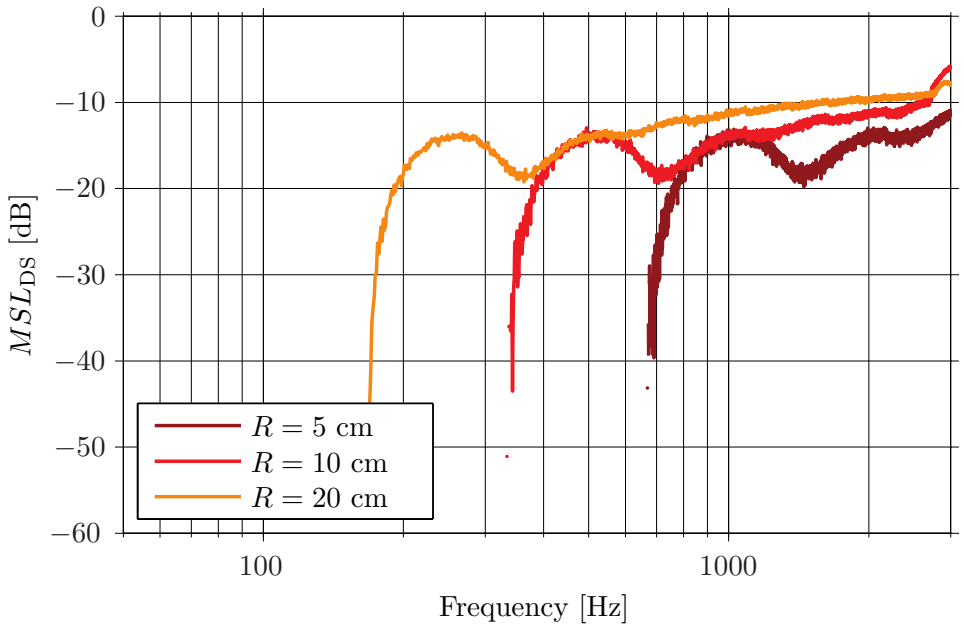

(b)

Figure A.12: Resolution and MSL of three DS beamformers that use circular arrays mounted on a rigid cylindrical baffle of infinite length of radius 5, 10 and 20 cm, when a source is placed at 180° and the SNR in the array microphones is 30 dB. The features of each array are given in table 5.1 on page 52.

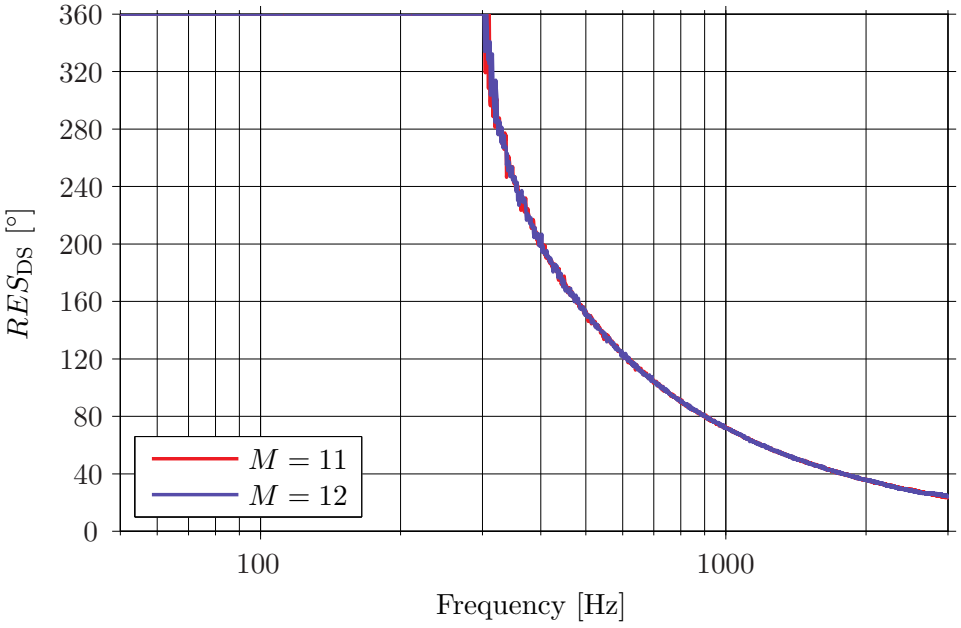

(a)

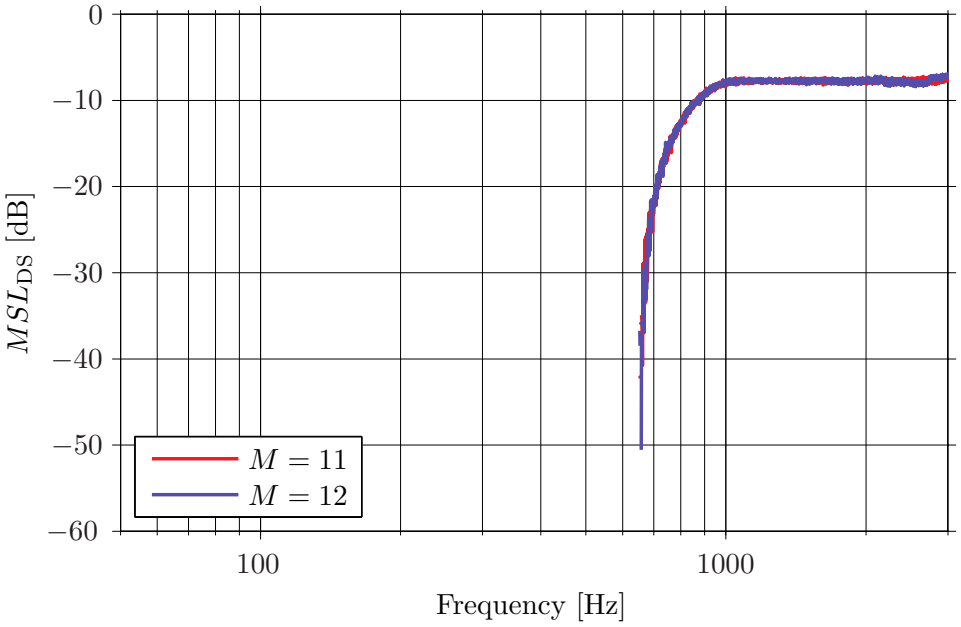

(b)

Figure A.13: Resolution ans MSL obtained with a DS beamformer when an unbaffled array of radius of 10 cm is used with 11 and 12 microphones. The SNR at the input of the microphones is set to 30 dB. The features of the array are given in table 5.1 on page 52.

A.3 Further Results

In figures A.14 and A.15, the mean values of both the resolution and the MSL obtained with CHB and DSB are compared to the results obtained by means of simulations.

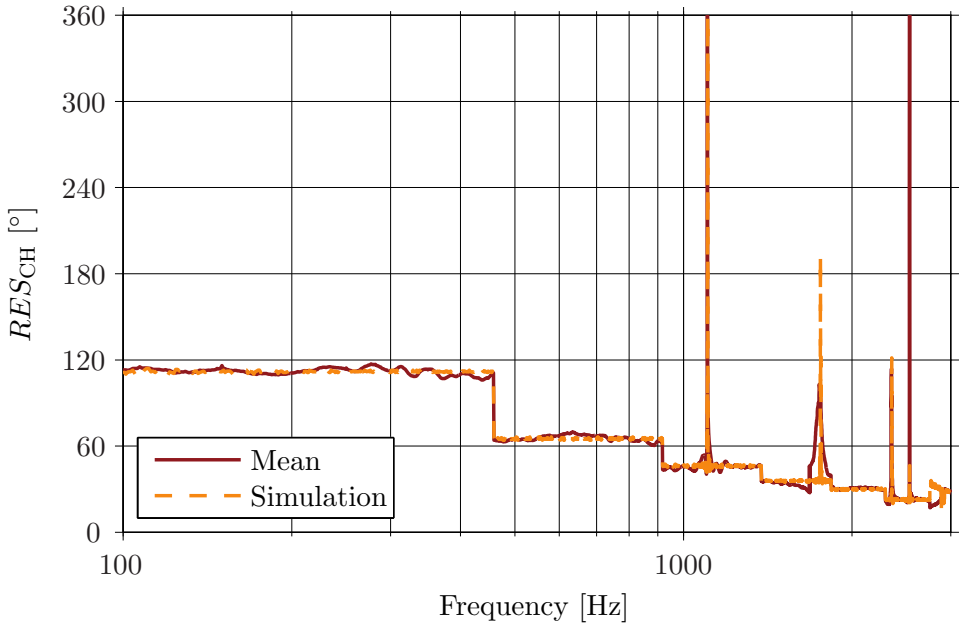

(a)

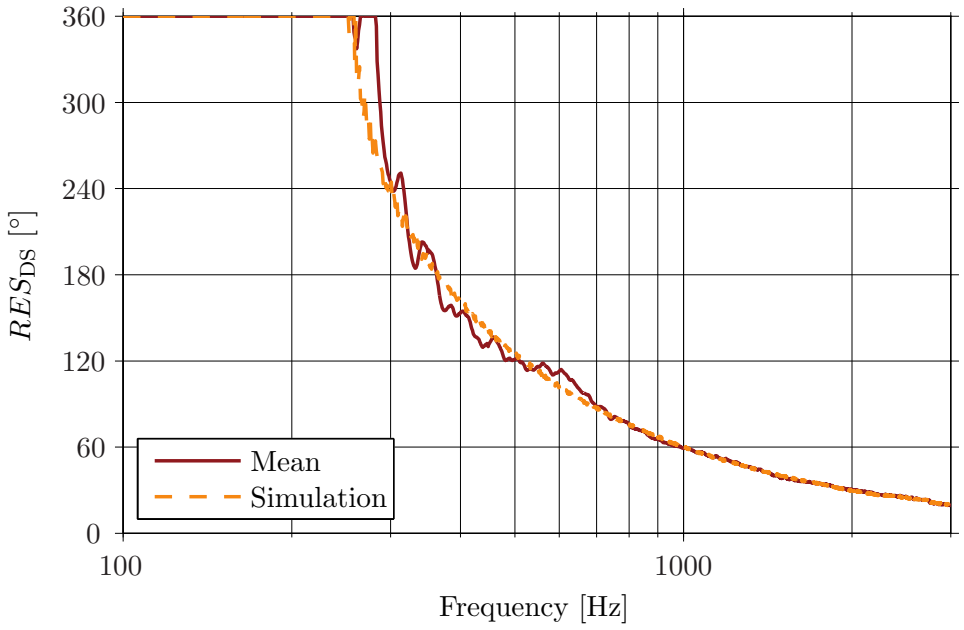

(b)

Figure A.14: Comparison of the mean value of the measured resolution and the simulated response when DSB and CHB are used with a circular array of radius 11.9 cm with 12 microphones. The source is placed at 180°. The mean is obtained after 10 consecutive measurements and the SNR assumed for the simulation is 30 dB at the input of each microphone.

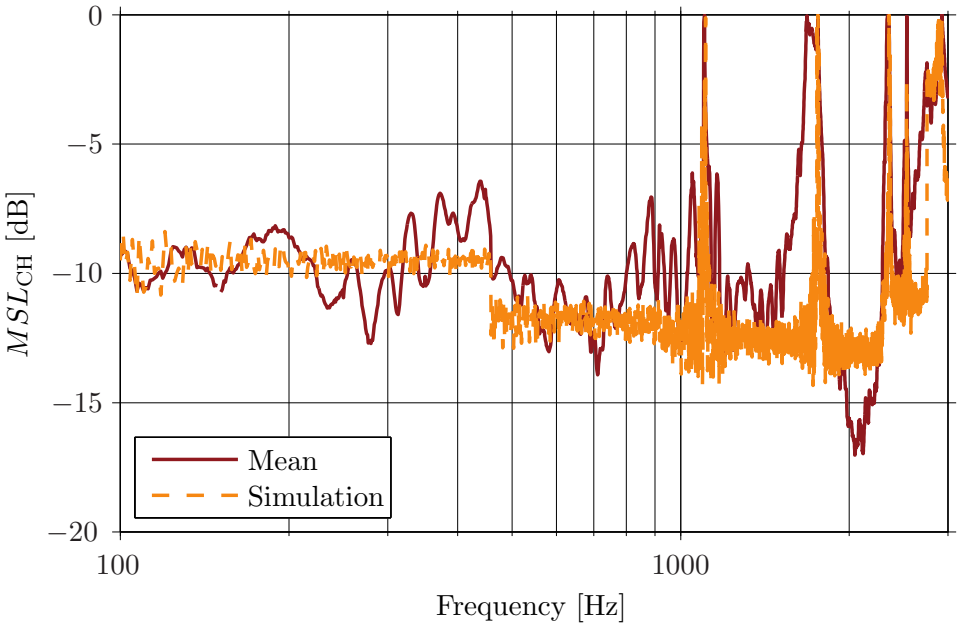

(a)

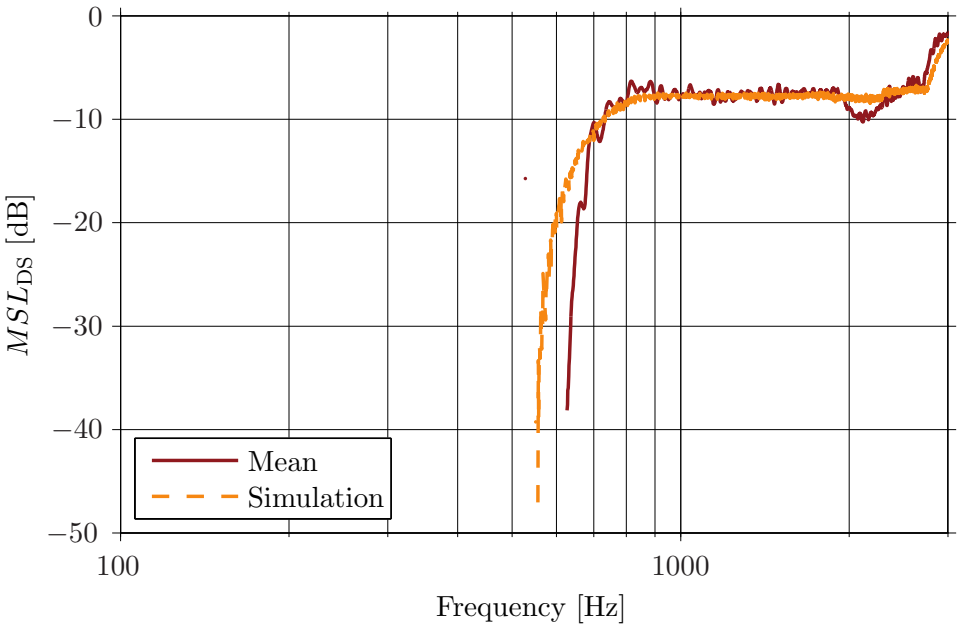

(b)

Figure A.15: Comparison of the mean value of the measured MSL and the simulated response when DSB and CHB are used with a circular array of radius 11.9 cm with 12 microphones. The source is placed at 180°. The mean is obtained after 10 consecutive measurements and the SNR assumed for the simulation is 30 dB at the input of each microphone.

Figure A.16 shows the comparison between the theoretical Fourier coefficients and the simulated ones used for the calculation of the beamformers outputs with CHB and DSB.

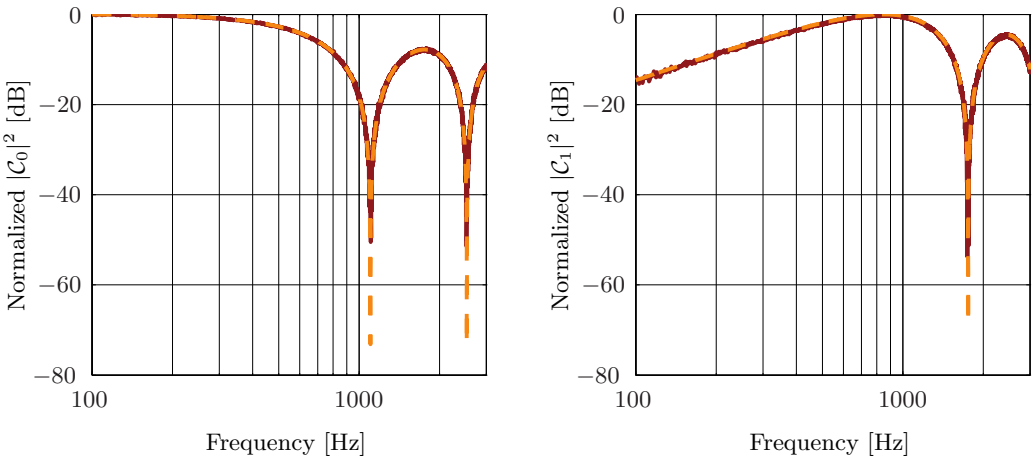

(a) $n = 0$

(b) $n = 1$

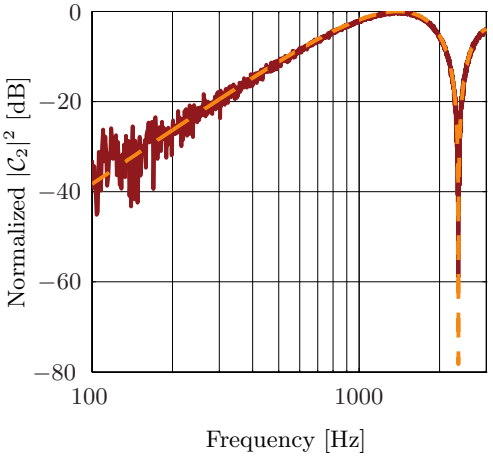

(c) $n = 2$

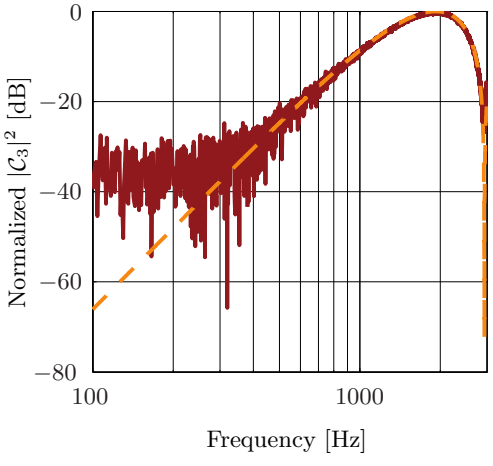

(d) $n = 3$

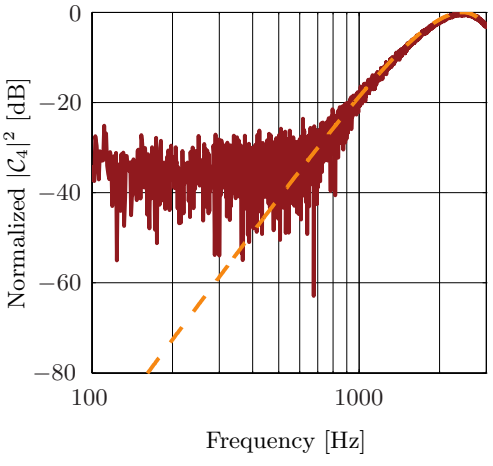

(e) $n = 4$

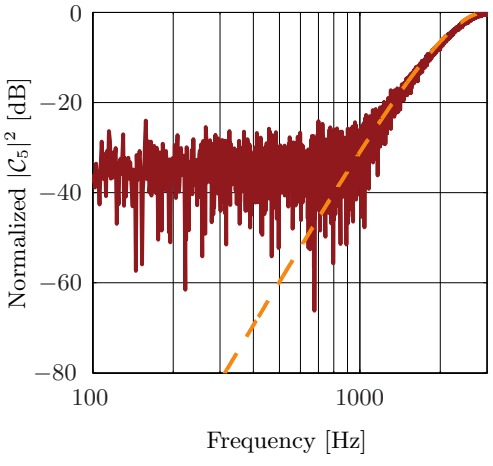

(f) $n = 5$

Figure A.16: Comparison between the theoretical Fourier coefficients (dashed line) and the approximated Fourier coefficients simulated with an array of 11.9 cm of radius and 12 microphones (continuous line). Note that the number of orders used for the algorithm follows $N = \lceil kR \rceil$ for CHB and $N = \lceil kR \rceil + 1$ for DSB. Therefore, the differences at low frequencies for orders higher than one should not be taken into account for the comparison.

A.4 Noise Spectrum of Trains

Figure A.17 shows the averaged equivalent sound pressure level of trains arriving and leaving a station, with and without A-weighting.

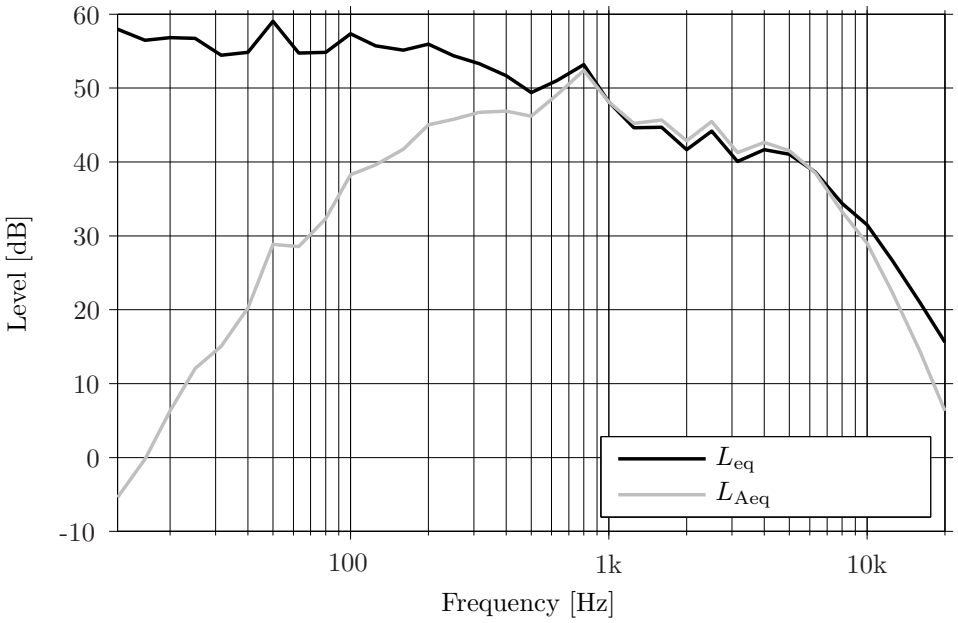

(a) Trains arriving to a station.

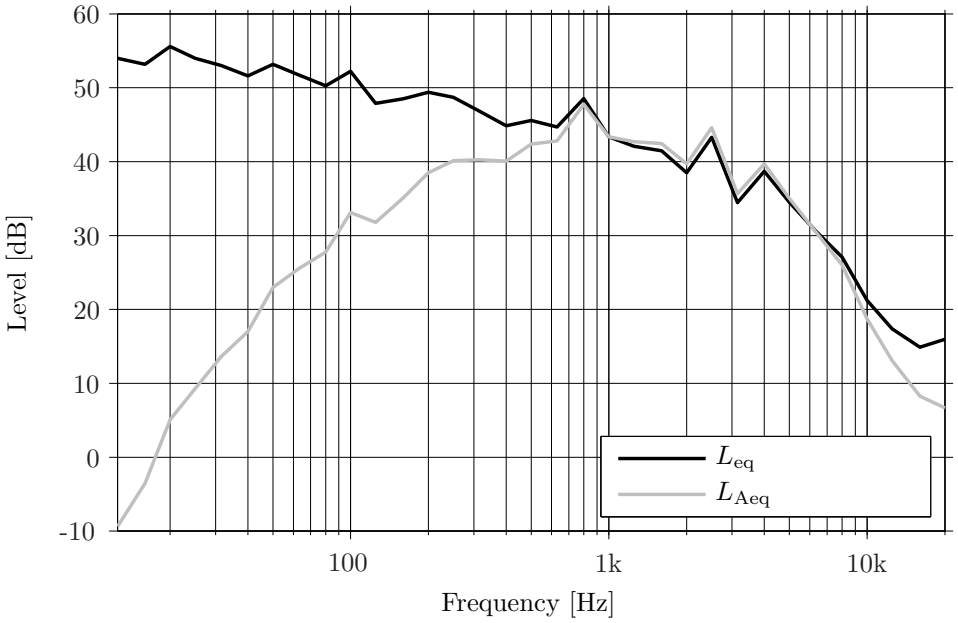

(b) Trains leaving a station.

Figure A.17: Equivalent sound pressure level of trains arriving and leaving a station. This is the result of averaging 10 measurements of 10 min each.

A.5 Selection of the Number of Orders for Delay-and-Sum Beamforming

In section 5.3.3.2, it was seen that the DS beamformer output improves when the number of orders used for the algorithm is $N = \lceil kR \rceil + 1$. But the question is whether the output would improve with increasing the number of orders, or not.

It was seen that the noise term in equation (5.7) on page 68 remains practically unaltered with increasing the number of orders. Hence, the only factor that could enhance the beamformer output is the term $\tilde{\mathcal{C}}_n(kR, \varphi_\mathrm{s})\mathcal{C}_n^*(kR, \varphi)$. In theory, this term can be rewritten using equation (3.22) on page 25,

$$\tilde{b}_{N,DS}(kR, \varphi) = \sum_{n=-N}^{N} \mathcal{C}_n(kR, \varphi_\mathrm{s})\mathcal{C}_n^*(kR, \varphi) + \mathcal{C}_{\mathrm{e},n}(kR, \varphi_\mathrm{s})\mathcal{C}_n^*(kR, \varphi), \tag{A.10}$$

where the coefficients $\mathcal{C}_{\mathrm{e},n}$ represent the error due to sampling. The tilde on top of b is used to emphasize that this is not completely the output of the beamformer as the noise term has been removed. To simplify the analysis, let us assume that $\varphi = \varphi_\mathrm{s}$. Then,

$$\tilde{b}_{N,DS}(kR, \varphi_\mathrm{s}) = \sum_{n=-N}^{N} |\mathcal{C}_n(kR, \varphi_\mathrm{s})|^2 + \mathcal{C}_{\mathrm{e},n}(kR, \varphi_\mathrm{s})\mathcal{C}_n^*(kR, \varphi_\mathrm{s}). \tag{A.11}$$

Let us analyze the example used to illustrate the influence of the number of orders in section 5.3.3.2, where an unbaffled array of 10 cm of radius and 11 microphones was used. With such number of microphones, the maximum value of kR is 5, in order to avoid the sampling error as much as possible (see equation (3.26) on page 26).

The expression given for $\mathcal{C}_{\mathrm{e},n}(kR, \varphi_\mathrm{s})$ can be simplified, recalling that the Bessel functions can be neglected when the order exceeds the argument,

$$\begin{aligned} \mathcal{C}_{\mathrm{e},n}(kR, \varphi_\mathrm{s}) &= \sum_{q=1}^{\infty} (-\mathrm{j})^g \mathrm{J}_g(kR)\mathrm{e}^{\mathrm{j}g\varphi_\mathrm{s}} + (-\mathrm{j})^h \mathrm{J}_h(kR)\mathrm{e}^{-\mathrm{j}h\varphi_\mathrm{s}} \\ &\approx \sum_{q=1}^{\infty} (-\mathrm{j})^g \mathrm{J}_g(kR)\mathrm{e}^{\mathrm{j}g\varphi_\mathrm{s}}, \end{aligned} \tag{A.12}$$

where $g = Mq - n$ and $h = Mq + n$. Inserting this result into equation (A.11) yields

$$\tilde{b}_{N,DS}(kR, \varphi_\mathrm{s}) \approx \sum_{n=-N}^{N} |\mathcal{C}_n(kR, \varphi_\mathrm{s})|^2 + \sum_{q=1}^{\infty} (-\mathrm{j})^g \mathrm{J}_g(kR)\mathrm{e}^{\mathrm{j}g\varphi_\mathrm{s}}\mathcal{C}_n^*(kR, \varphi_\mathrm{s}). \tag{A.13}$$

At the lower frequencies, kR is small and as seen in section 3.3, a few number of modes are needed to represent the sound field. For example, at those frequencies that satisfy $\lceil kR \rceil = 1$, equation (A.11) results in

$$\tilde{b}_{1,DS} = |\mathcal{C}_0|^2 + 2\left(|\mathcal{C}_1|^2 + 0 \cdot \mathcal{C}_0^* + 0 \cdot \mathcal{C}_1^*\right), \tag{A.14}$$

when $N = 1$. Note that the error due to sampling can be neglected according to equation (A.12), since the argument of the Bessel functions is much smaller than the order. When $N = 2$,

$$\tilde{b}_{2,DS} = |\mathcal{C}_0|^2 + 2\left(|\mathcal{C}_1|^2 + |\mathcal{C}_2|^2 + 0\cdot\mathcal{C}_0^* + 0\cdot\mathcal{C}_1^* + 0\cdot\mathcal{C}_2^*\right) \approx \tilde{b}_{1,DS}. \tag{A.15}$$

The approximation follows from the fact that at low frequencies the coefficients have smaller amplitude with increasing order, as seen in chapter 3. Therefore, it can be seen that using more orders at low frequencies do not provide a better beamformer output.

At high frequencies, say at those frequencies where $\lceil kR \rceil = 4$, the output is, when $N = 4$,

$$\tilde{b}_{4,DS} = |\mathcal{C}_0|^2 + 2\left(|\mathcal{C}_1|^2 + |\mathcal{C}_2|^2 + |\mathcal{C}_3|^2 + |\mathcal{C}_4|^2 + 0\cdot\mathcal{C}_0^* + \ldots + 0\cdot\mathcal{C}_4^*\right). \tag{A.16}$$

This will be the output when N is chosen to follow $N = \lceil kR \rceil$. When the number of modes is increased by one, following $N = \lceil kR \rceil + 1$, i. e. $N = 5$,

$$\tilde{b}_{5,DS} = |\mathcal{C}_0|^2 + 2\left(|\mathcal{C}_1|^2 + |\mathcal{C}_2|^2 + |\mathcal{C}_3|^2 + |\mathcal{C}_4|^2 + |\mathcal{C}_5|^2 + 0\cdot\mathcal{C}_0^* + \ldots + 0\cdot\mathcal{C}_5^*\right). \tag{A.17}$$

Unlike the case at low frequencies, $\tilde{b}_{5,DS}$ cannot be approximated to $\tilde{b}_{4,DS}$ because the term $|\mathcal{C}_5|^2$ is still comparable to the term $|\mathcal{C}_4|^2$, as at high values of kR, more modes gain strength and their magnitudes become similar, see figure 3.3 on page 18. Therefore, $\tilde{b}_{5,DS}$ presents an extra term compared to $\tilde{b}_{4,DS}$ that will contribute in the improvement of the response with respect to the case when $N = \lceil kR \rceil$. If the number of modes is further increased,

$$\begin{aligned}\tilde{b}_{6,DS} = |\mathcal{C}_0|^2 + 2\big(&|\mathcal{C}_1|^2 + |\mathcal{C}_2|^2 + |\mathcal{C}_3|^2 + |\mathcal{C}_4|^2 + |\mathcal{C}_5|^2 + |\mathcal{C}_6|^2 + \\ &0\cdot\mathcal{C}_0^* + \ldots + 0\cdot\mathcal{C}_5^* + (-\mathrm{j})^5\mathrm{J}_5(kR)\mathrm{e}^{\mathrm{j}5\varphi_s}\mathcal{C}_6^*\big).\end{aligned} \tag{A.18}$$

Note that the error due to sampling is present through the last term of the equation. $\mathcal{C}_6^*$ is in fact a Bessel function (see equation (3.9) on page 17), in which the order considerably exceeds the argument. Therefore, it can be neglected, and consequently the error is canceled. Likewise, the term $|\mathcal{C}_6|^2$ can also be neglected. So the output will be similar to the one obtained with $N = 5$,

$$\tilde{b}_{6,DS} \approx \tilde{b}_{5,DS}. \tag{A.19}$$

This means that there is no difference between the outputs when $N = \lceil kR \rceil + 1$ and $N = \lceil kR \rceil + 2$. In the same way, when more orders are added the result will be the same as the one obtained with $N = \lceil kR \rceil + 1$.

In conclusion, in DSB, the number of orders used up to a spatial frequency kR can be chosen to be $N = \lceil kR \rceil$ like in CHB, but the output is improved in the same frequency range just by adding another order, $N = \lceil kR \rceil + 1$. However, it is shown that when more orders are taken into account the output remains like in the case of $N = \lceil kR \rceil + 1$.

B

Source Code

B.1 Modal Response using a Circular Aperture mounted on a Cylindrical Baffle of Finite Length

The following script has been used to implement the modal response using an aperture mounted on a rigid cylindrical baffle of finite length.

```
1: global k R n L;
2: kanalysis = 1:250; % k values under analysis
3: R = 4e-2; % radius of the array
4: n_total = [0 1 2 3]; % order
5: L = 1; % half the length of the baffle
6: for s = 1:length(n_total)
7:      n = n_total(s);
8:      for ii = 1:length(kanalysis)
9:          k = kanalysis(ii);
10:         % Calculation of the integral. The indeterminations at -k and k
11:         % are avoided. The limits of the integral are +/- infinity but
12:         % they are truncated at -400 and 400, because above this range
13:         % the function under the integral diverges.
14:         [Q_temp,t_temp] = gaussq(@int_finite_baffle,[-400 -k+1 k+1],[-k-1 k-1
                400]);
15:     % value of the coefficient for a certain order n
16:         C(s,ii) = 1i^n*(besselj(n,k*R)-k*L/pi*besselj_prime(n,k,R).*Q(ii));
17:     end
18:  end
```

The function `@int_finite_baffle` in line 14 follows

```
1: function y = int_finite_baffle(x)
2:
3: global k R n L;
4: y = hankel1(n,sqrt(k^2-x.^2)*R).*sin(x*L)./(x*L)./(sqrt(k^2-x.^2).*
       hankel1_prime(n,sqrt(k^2-x.^2),R));
```

B.2 Beamforming Techniques

B.2.1 circular_harm_beamformer.m

```
function [bn, b] = circular_harm_beamformer(k,R,N,P,phi,phi_M,condition)
% bn: normalized value of the beamformer output;
% b: beamformer output
% k: wavenumber
% R: radius of the array
% N: number of harmonics used to decompose the sound field
% P: sound pressure captured in the microphones
% phi: angles in the array plane
% phi_M: angles of the microphones position
% condition: 'baffled' if the array is mounted on a cylindrical
% baffle of infinite length or 'unbaffled' if it is unbaffled.

A = 1; % Scaling factor
b = 0;
for n = -N:N
    if strcmpi(condition,'unbaffled')
        Rn = R_unbaffled(n,k,R);
    elseif strcmpi(condition,'baffled')
        Rn = R_baffled(n,k,R);
    end
    b = b + sum(1/length(phi_M)*P.*exp(-j*n*phi_M.')*exp(j*n*phi)/((-1)^n*Rn)
        ,1);
end
b = A*b;
bn = b/max(abs(b));
```

B.2.2 delay_and_sum_beamformer.m

```
function [bn,b] = delay_and_sum_beamformer(k,R,N,P,phi,phi_M,condition)
% bn: normalized value of the beamformer output;
% b: beamformer output
% k: wavenumber
% R: radius of the array
% N: number of harmonics used to decompose the sound field
% P: sound pressure captured in the microphones
% phi: angles in the array plane
% phi_M: angles of the microphones position
% condition: 'baffled' if the array is mounted on a cylindrical
% baffle of infinite length or 'unbaffled' if it is unbaffled.

A = 1/length(phi_M); % Scaling factor
b = 0;
for n = -N:N
    if strcmpi(condition,'unbaffled')
        Rn = R_unbaffled(n,k,R);
    elseif strcmpi(condition,'baffled')
        Rn = R_baffled(n,k,R);
    end
    b = b + sum(1/length(phi_M)*P.*exp(-j*n*phi_M.')*exp(j*n*phi)*conj(Rn*(-1)
        ^n),1);
end
b = A*b;
bn = b/max(abs(b));
```

B.2.3 Complementary Functions

```
function Rn = R_baffled(n,k,R)
% n: order
% k: wavenumber
% R: radius

Rn = i^n*(besselj(n,k*R)-besselj_prime(n,k,R).*hankel1(n,k*R)./hankel1_prime(n
    ,k,R));
```

```
function Rn = R_unbaffled(n,k,R)
% n: order
% k: wavenumber
% R: radius

Rn = i^n*besselj(n,k*R);
```

B.3 Resolution and Maximum Side Lobe Level

B.3.1 resolution.m

```
function res = resolution(b,phi,f)
% res: output of the function in radiant
% b: beamformer output
% phi: angles used for the calculation of the beamformer output
% in radiant
% f: frequency at which the beamformer is tuned

b_db = 20*log10(abs(b));
idx1 = find(b_db == max(b_db));
phi_max = phi(idx1(1));
val_3db = max(b_db)-3;
% From the position of the max to the end it looks for positions
% in which the magnitude has decreased by -3dB with respect to the maximum
idx2 = find(b_db(idx1(1):end) < val_3db);
if isempty(idx2)
    idx3 = find(b_db(1:idx1(1)) < val_3db); % looks the -3dB positions from
                        % the begining until the max
    if isempty(idx3) % Omnidirectional case
        res = '';
        disp(sprintf('Resolution warning: f = %1.1f Hz not resolved!!!',f));
    else
        phi_3db_approx = phi(idx3(end));
        res = 2*abs(phi_max - phi_3db_approx);
    end
else
    phi_3db_approx = phi(idx1(1)+idx2(1)-1);
    res = 2*abs(phi_max - phi_3db_approx);
end
if res > 2*pi
    res = 2*pi;
end
```

B.3.2 msl.m

```
function msl_output =  msl(b,phi)
% b: beamformer output
% phi: angles used for the calculation of the beamformer output
% mls_output: returns the maximum side lobe level in dB

b = 20*log10(abs(b));
[pos_max, pos_min] = find_max_min(b, phi);
if pos_max == 0 % Omnidirectional case
    msl_output = NaN;
elseif pos_min == 0 % Omnidirectional case
    msl_output = NaN;
else
    maxima = b(pos_max);
    minima = b(pos_min);
    max_val = max(maxima);
    % Position of the absolute maximum
    idx_max_abs = pos_max(find(b(pos_max) == max_val));
    % Position of the relative maxima
    idx_rel_max = find(maxima < max_val);
    rel_max = sort(maxima(idx_rel_max));
    if isempty(rel_max)
        msl_output = NaN; % Any side lobe
    else
        msl_output = rel_max(end); % maximum side lobe
    end
end
```

The function `find_max_min.m` follows

```
function msl_output =  msl(b,phi)
% b: beamformer output
% phi: angles used for the calculation of the beamformer output
% mls_output: returns the maximum side lobe level in dB

b = 20*log10(abs(b));
[pos_max, pos_min] = find_max_min(b, phi);
if pos_max == 0 % Omnidirectional case
    msl_output = NaN;
elseif pos_min == 0 % Omnidirectional case
    msl_output = NaN;
else
    maxima = b(pos_max);
    minima = b(pos_min);
    max_val = max(maxima);
    % Position of the absolute maximum
    idx_max_abs = pos_max(find(b(pos_max) == max_val));
    % Position of the relative maxima
    idx_rel_max = find(maxima < max_val);
    rel_max = sort(maxima(idx_rel_max));
    if isempty(rel_max)
        msl_output = NaN; % Any side lobe
    else
        msl_output = rel_max(end); % maximum side lobe
    end
end
```

B.4 Other Functions used for the Simulations

B.4.1 plane_wave.m

```
function p = plane_wave(k,R,phi_s,phi_M,condition)
% k = wavenumber
% R = array radius
% phi_s = position of the source
% phi_M = position of the microphones
% condition = 'unbaffled' or 'baffled' for an array mounted on a cylindrical
    rigid baffle of infinite length

N = 60;  % maximum order that avoids NaN in the range from 1 Hz to 3000 Hz
if strcmpi(condition,'unbaffled')
    p = (exp(-j*k*R*cos(phi_M-phi_s))).';
elseif strcmpi(condition,'baffled')
    p = 0;
    for n = -N:N
        p = p + (-i)^n*(besselj(n,k*R)-besselj_prime(n,k,R).*hankel1(n,k*R)./
            hankel1_prime(n,k,R))*exp(j*n*(phi_M-phi_s));
    end
    p = p.';
end
```

B.4.2 random_noise.m

```
function n = random_noise(Ps,SNR)
% n = random_noise(Ps,SNR)
% Ps = Power signal
% SNR = SNR in dB
% random_val = randn(size(Ps)) + j*randn(size(Ps));
% n = (sqrt(Ps./(SNR*abs(random_val).^2/2)).*random_val);

SNR = 10^(SNR/10);
abs_n = sqrt(2*Ps/SNR); % Noise magnitude
phase_n = 2*pi.*rand(size(Ps)); % Phase uniformly distributed from 0 to 2*pi
n = abs_n.*exp(j*phase_n);  % Noise in complex notation
```

C

Facility, Device and Software List

Table C.1: Used facilities, devices and software.

Type	**Manufacturer**	**Model/name**	**Description/notes**
Anechoic Chamber		Large anechoic room in building 354 (room 027) at DTU	Free space volume of about 1000 m^3. Lower limiting frequency of about 50 Hz.
Circular Array	Brüel & Kjær	Prototype	Circular array with a radius of 11.9 cm. It contains 12 equispaced microphones, all of them being Brüel & Kjær 1/4 " microphones *B&K Type 4935*.
Controllable Turntable	Brüel & Kjær	*B&K Type 5960*	Turntable capable to rotate with an accuracy of 1°.
Turntable Controller	Brüel & Kjær	*B&K Type 5997*	Remote controller for the turntable.
Multichannel Portable PULSE	Brüel & Kjær		The front-end includes 5 sets of 12-channel Input Module *B&K Type 3038 B*, a Power-Supply Module *B&K Type 2826* and a 5/1-channel Input/Output Controller Module *B&K Type 7539 A*.
Portable PULSE	Brüel & Kjær		The front-end includes a 4/2-channel Input/Output Module *B&K Type 3109* and a LAN Interface Module *B&K Type 7533*
Amplifiers			Homemade amplifiers.
Spherical Loudspeaker			Loudspeaker unit mounted on a sphere.
Loudspeaker	Dynaudio Acoustics	*BM 6A*	Two-way loudspeaker system.

Continued on the next page...

Table C.1: Used facilities, devices and software (continued).

Type	**Manufacturer**	**Model/name**	**Description/notes**
Calibrator	Brüel & Kjær	*B&K Type 4230*	Produces 94 dB at 1 kHz. Used with an adapter for 1/4 ” microphones.
Sound Level Meter	Brüel & Kjær	*B&K Type 2250*	Hand-held sound level meter set with the template ‘Frequency Analyzer’ to measure environmental noise.
Software	Brüel & Kjær		Software for the PULSE system. The template ‘NS-STSF Irregular Array’ of the environment ‘Noise Source Identification’ is used to acquire the data from the array.
Software	Brüel & Kjær	*B&K BZ5503*	Utility software for the sound level meter *B&K Type 2250*.
Software	The MathWorks	*Matlab* Version 7.6.0.324 (R2008a)	Among others including the Signal Processing Toolbox.
Computer			Used for the software of the Multichannel Portable PULSE, and for *Matlab*.
Laptop			Used for the software of the Portable PULSE.

Abbreviations and Symbols

Abbreviations

CHB	Circular Harmonics beamforming
CH	Circular harmonics
DSB	Delay-and-Sum beamforming
DS	Delay-and-Sum
MSL	Maximum side lobe level
SNR	Signal-to-noise ratio

Greek Symbols

φ	Azimuthal angle in the xy-plane
φ_i	φ coordinate of the wavenumber vector $\vec{k_\mathrm{i}}$
φ_m	Angular position of the m'th microphone in a circular array
φ_s	Angular position of a source
ω	(Angular) Frequency [rad/s]
ρ_0	Equilibrium density of the medium ($\approx 1.204\ \mathrm{kg/m^3}$ for air at 20°)

Roman Symbols

$\bar{b}_{N,\mathrm{CH}}$	Normalized output of a CH beamformer
$\bar{b}_{N,\mathrm{DS}}$	Normalized output of a DS beamformer
c	Speed of sound (≈343 m/s for air at 20°)
$\mathcal{C}_n^\bullet$	Fourier coefficient of order n for a circular aperture mounted on a rigid cylindrical baffle of infinite length
$\tilde{\mathcal{C}}_n^\bullet$	Fourier coefficient of order n for a circular array mounted on a rigid cylindrical baffle of infinite length
$\mathcal{C}_n^\mathrm{L}$	Fourier coefficient of order n for a circular aperture mounted on a rigid cylindrical baffle of length $2L$
$\mathcal{C}_n^\circ$	Fourier coefficient of order n for an unbaffled circular aperture
$\tilde{\mathcal{C}}_n^\circ$	Fourier coefficient of order n for an unbaffled circular array
f	Frequency [Hz]

$\mathrm{H}_n^{(1)}(x)$	Hankel function of first kind and order n with argument x
$\mathrm{H}_n^{(2)}(x)$	Hankel function of second kind and order n with argument x
$\mathrm{H}_n'(kR)$	Derivative of $\mathrm{H}_n(kr)$ with respect to r, evaluated at $r = R$
j	Imaginary unit, $\mathrm{j}^2 = -1$
$\mathrm{J}_n(x)$	Bessel function of order n with argument x
$\mathrm{J}_n'(kR)$	Derivative of $\mathrm{J}_n(kr)$ with respect to r, evaluated at $r = R$
k	Wavenumber
$\vec{k}_\mathrm{i}$	Wavenumber vector of an incident plane wave
L	Half the length of a cylinder ($2L$).
M	Number of microphones that conform an array
MSL	Maximum side lobe level
N	Maximum order used to decompose the sound field with circular harmonics
$\hat{p}$	Sound pressure in complex notation
R	Radius of a cylinder, circular array or circular aperture
RES	Resolution
SNR_m	Signal-to-Noise ratio at the input of each microphone of a circular array
$\mathrm{Y}_n(x)$	Neumann function of order n with argument x

Bibliography

[1] **Maynard, J., Williams, E.** and **Lee, Y.**, *Nearfield Acoustic Holography: I. Theory of Generalized Holography and the Development of NAH*, J. Acoust. Soc. Am., Vol. 4, No. 78, pp. 1397–1413, October 1985.

[2] **Hald, J.**, *Basic Theory and Properties of Statistically Optimized Near-field Acoustical Holography*, J. Acoust. Soc. Am., Vol. 4, No. 125, pp. 2105–2120, April 2000.

[3] **Hald, J.**, Handbook of Signal Processing in Acoustics. Chapter 9., Springer New York, 2008.

[4] **Johnson, D.** and **Dudgeon, D.**, Array Signal Processing Concepts and Techniques, Prentice Hall, 1993.

[5] **Brandstein, M.** and **Ward, D.**, Microphone Arrays. Signal Processing Techniques and Applications, Springer, 2001.

[6] **Meyer, J.** and **Elko, G.**, *A Highly Scalable Spherical Microphone Array based on an Orthonormal Decomposition of the Soundfield*, *IEEE International Conference on Acoustics, Speech and Signal Processing (CASSP'02)*, Vol. 2, pp. 1781–1784, 2002.

[7] **Rafaely, B.**, *Plane-wave Decomposition of the Sound Field on a Sphere by Spherical Convolution*, J. Acoust. Soc. Am., Vol. 116, No. 4, pp. 2149–2157, October 2004.

[8] **Hald, J.**, *Spherical Harmonics Beamforming*, Brüel & Kjær internal paper.

[9] **Teutsch, H.** and **Kellermann, W.**, *Acoustic Source Detection and Localization based on Wavefield Decomposition using Circular Microphone Arrays*, J. Acoust. Soc. Am., Vol. 120, No. 5, pp. 2724–2736, November 2006.

[10] **Jacobsen, F.**, Propagation of Sound Waves in Ducts, Acoustic Technology, DTU Electrical Engineering, August 2006, lecture Note 31260.

[11] **Pierce, A.**, Acoustics: An Introduction to its Physical Principles and Aplications, McGraw-Hill, 1981.

[12] **Jacobsen, F.** and **Juhl, P.**, Radiation of sound, Acoustic Technology and Institute of Sensors, Signals and Electrotechnic, DTU Electrical Engineering and University of Southern Denmark, April 2007.

[13] **Morse, P.** and **Feshbach, H.**, Methods of Theoretical Physics, McGraw-Hill, 1953.

[14] **Morse, P.** and **Ingard, K.**, Theoretical Acoustics, McGraw-Hill, 1968.

[15] **Teutsch, H.**, Modal Array Signal Processing: Principles and Applications of Acoustic Wavefield Decomposition, Springer, 2007.

[16] **Hartmann, W.**, Signals, Sound, and Sensation, Springer, 1997.

[17] **Williams, E.**, Fourier Acoustics: Sound Radiation and Nearfield Acoustic Holography, Academic Press, 1999.

[18] **Van Trees, H.**, Optimum Array Processing. Part IV of Detection, Estimation, and Modulation Theory, John Wiley & Sons, 2002.

[19] **Elko, G.** and **Meyer, J.**, Springer Handbook of Speech Processing. Part I. 50, Springer, 2008.

[20] **Jourdan, J.** and **Marschall, M.**, *Comparison of Beamforming Techniques on a Sphere*, Tech. rep., Acoustic Technology – DTU Elektro, October 2008.

[21] **Christensen, J.** and **Hald, J.**, *Technical Review*, Tech. rep., Brüel & Kjær, 2004.

[22] **Spiegel, M., Liu, J.** and **Abellanas, L.**, Schaum. Fórmulas y Tablas de Matemática Aplicada, McGraw-Hill, 2005.

[23] **Asmar, N.**, Partial Differential Equations, Prentice Hall, 2nd edn., 2000.

[24] **Skudrzyk, E.**, The Foundations of Acoustics, Springer-Verlag/Wien, 1971.